

SENSORLESS CONTROL OF SINGLE PHASE PM BRUSHLESS DC MOTOR DRIVES

Teză destinată obținerii
titlului științific de doctor inginer
la
Universitatea "Politehnica" din Timișoara
în domeniul INGINERIE ELECTRICA
de către

Ing. Liviu Ioan Iepure

Conducător științific: prof.univ.dr.ing. Ion Boldea
Referenți științifici: prof.univ.dr.ing. Mircea Radulescu
prof.univ.dr.ing. Lorand Szabo
conf.univ.dr.ing. Lucian Tutelea

Ziua susținerii tezei: 15.10.2010.

Seriile Teze de doctorat ale UPT sunt:

- | | |
|------------------------|---|
| 1. Automatică | 7. Inginerie Electronică și Telecomunicații |
| 2. Chimie | 8. Inginerie Industrială |
| 3. Energetică | 9. Inginerie Mecanică |
| 4. Ingineria Chimică | 10. Știința Calculatoarelor |
| 5. Inginerie Civilă | 11. Știința și Ingineria Materialelor |
| 6. Inginerie Electrică | |

Universitatea „Politehnica” din Timișoara a inițiat seriile de mai sus în scopul diseminării expertizei, cunoștințelor și rezultatelor cercetărilor întreprinse în cadrul școlii doctorale a universității. Seriile conțin, potrivit H.B.Ex.S Nr. 14 / 14.07.2006, tezele de doctorat susținute în universitate începând cu 1 octombrie 2006.

Copyright © Editura Politehnica – Timișoara, 2010

Această publicație este supusă prevederilor legii dreptului de autor. Multiplicarea acestei publicații, în mod integral sau în parte, traducerea, tipărirea, reutilizarea ilustrațiilor, expunerea, radiodifuzarea, reproducerea pe microfilme sau în orice altă formă este permisă numai cu respectarea prevederilor Legii române a dreptului de autor în vigoare și permisiunea pentru utilizare obținută în scris din partea Universității „Politehnica” din Timișoara. Toate încălcările acestor drepturi vor fi penalizate potrivit Legii române a drepturilor de autor.

România, 300159 Timișoara, Bd. Republicii 9,
tel. 0256 403823, fax. 0256 403221
e-mail: editura@edipol.upt.ro

Preface

This thesis represents an approach to single phase PM brushless DC motor drives. In-depth characterization through finite element method, advanced dynamical modeling and sensorless control strategies of this type of motor are treated in this thesis.

Study motivation

The development of power electronics, digital control through digital signal processors (DSP) and permanent magnet technology has led to a widespread use of PM-BLDC motors in various fields of applications. This type of electrical motors is used in a wide variety of equipment including residential applications, automobiles, medical and healthcare equipment, drives on Personal Computers etc. An important part of the used energy by these types of applications is represented by fractional horsepower motors, ranging in size from a few watts up to about one horsepower.

Mass production and market competition of small electric drives demand decrease of production costs. Meanwhile, the output characteristics have to remain the same or even increase. It seems that in the field of small power, small starting torque applications, the single phase PM brushless DC motor presents a growing interest, especially in the residential and automotive industry, where it is more efficient than rival motors. It is used in order to cut the costs of the power electronics converter for variable speed, by reducing the number of power switches and the number of Hall sensors.

Also, sensorless control is essential for low-cost variable speed applications such as fans and pumps, and so, there is a growing interest in "sensorless" schemes for single phase PM-BLDC motors, in which position information is derived by on-line analysis of the voltages and currents in the machine windings.

Considering the above, the scope of this thesis is to give a detailed approach on single phase PM-BLDC motor drives, through FEM based analysis and dynamical modeling, and to bring new contributions in the sensorless control methods research area for this type of motor.

ACKNOWLEDGEMENTS

I wish to express my gratitude to my supervisor Prof. Ion Boldea, from University Politehnica of Timisoara, Faculty of Electrical Engineering, whose support and guidance made this work possible. Dr. Eng. Dorin Iles, former head of R&D department at EBM-Papst GmbH&CO, St. Georgen, Germany, deserves my special gratitude.

I want to thank also to Prof. Frede Blaabjerg and Prof. Remus Teodorescu, from the Institute of Energy Technology, Aalborg University, Denmark for their support during my reasearch period in Aalborg.

Many thanks to Prof. Gheorghe Daniel Andreescu from the Faculty of Automation and Computers, University Politehnica of Timisoara.

I would like to express my special gratitude also to Assoc. Prof. Lucian Tutelea for our cooperation so far. Also, I want to thank to all who contributed to my engineering education and also to my colleagues from Intelligent Motion Control Laboratory at Faculty of Electrical Engineering , Timisoara. Eng. Alin Stirban and Eng. Robert Antal deserves my special gratitude.

Finally, I want to thank and express my love to my family for their priceless and endless support offered when it was most needed.

Iepure, Ioan Liviu

Sensorless control of single phase PM brushless dc motor drives

Teze de doctorat ale UPT, Seria 6, Nr. 20, Editura Politehnica, 2010, 192 pagini, 162 figuri, 4 tabele.

ISSN:1842-7022

ISBN: 978-606-554-183-2

Keywords: brushless dc motor, permanent magnet, finite element analysis, tapered airgap, flux estimator, sensorless control

Abstract,

A comprehensive approach by FEM analysis and experimental measurements is done in order outline the peculiarity of single phase PM-BLDC motor and to deliver machine parameters necessary for further simulations and control tasks. A detailed approach of modeling a single phase PM-BLDC motor for control purpose is presented and an advanced digital simulation model of the motor control system is developed.

Two motion sensorless control methods for single phase permanent magnet brushless d.c. (PM-BLDC) motor drives, based on flux estimation are introduced. The first one is based on a prior knowledge of the PM flux/position characteristic while the second one is based on a fictitious orthogonal flux system. Both method are detailed, illustrated by simulation results and validated by experiments. In order to obtain an enhanced sensorless control system the regenerative braking is also implemented under sensorless control.

Table of Contents

Objectives of the thesis	8
Outline of the thesis	8
Chapter 1 Fractional horsepower applications	9
1.1. Introduction	9
1.2. Permanent magnet synchronous motor at a glance.....	11
1.3. Efficiency increasing by PM-BLDC motors	12
1.4. Low-cost solutions for fractional horsepower applications	14
1.4.1. Single phase PMSM/ PM-BLDC motor	15
1.4.1.1. Fundamentals and theory of operation	15
1.4.1.2. Interior vs. exterior rotor	19
1.4.2. Single phase PMSM classification	20
1.4.3. Single phase PM-BLDC drive	25
1.4.4. Single phase PM-BLDC motor sensorless control	28
1.5. Conclusions	30
Chapter 2. Single phase PM-BLDC motor: In-depth characterization by FEM analysis and experiments	33
2.1. Introduction	33
2.2. FE analysis	35
2.2.1. Materials selection.....	36
2.2.2. Field distribution	37
2.3 No load flux linkage and BEMf	45
2.4. Phase inductance	47
2.5. Cogging torque and total torque analysis	48
2.5.1. Maxwell stress tensor method	50
2.5.2. Virtual work method	50
2.5.3. Cogging torque: FEM results	51
2.6. Electromagnetic torque	53
2.7 Starting torque and torque pulsations analysis.....	55
2.8. Experimental measurements	57
2.8.1. BEMF coefficient validation	57
2.8.2. Inductance validation	58
2.8.3. Static torque measurement	59
2.8.4. Starting torque validation	60
2.8.5. Dynamic torque measurement	61
2.9. Conclusions	62
Chapter 3. Motor dynamical modeling and control	65
3.1. Introduction	65
3.2 Single phase PM-BLDC motor: mathematical model	66
3.3 Single phase PM-BLDC motor control system	68
3.3.1. Close loop speed control	68
3.3.2. Power electronic converter	70
3.4. Matlab-Simulink simulation model	71
3.4.1. Single phase PM-BLDC motor model validation by hysteresis current control.....	71

6 Table of Contents

3.4.2. Advanced Simulink/PSIM digital simulation control system mode.....	79
3.4.2.1. Speed and torque close loop control	81
3.4.2.2. Simulation results	86
3.5. Speed and position calculation from Hall sensor signal	91
3.6. Conclusions	94
Chapter 4. Motion sensorless control of single phase brushless DC PM motor drive based on prior knowledge of PM flux vs. position ..	97
4.1. Introduction.....	97
4.2. PM flux estimator	98
4.3. FEM based position estimator	102
4.4. Speed estimator	107
4.5. Experimental validation of the proposed state observer.....	108
4.5.1. PM flux estimator: experimental results	108
4.5.2. Estimated position: experimental results	109
4.5.3. Estimated speed: experimental results	112
4.6. motion sensorless control based on FEM assisted state observer	115
4.6.1. Control system overview	115
4.6.2. Experimental results	116
4.7. Conclusions	122
Chapter 5. Motion sensorless control of a single phase brushless D.C. PM motor drive based on a fictitious orthogonal flux system... 	125
5.1. Introduction	125
5.2. Proposed state observer structures	126
5.3. PM flux estimator	127
5.4. Orthogonal PM flux system generator	127
5.5. Offline Fourier analysis based position refining and speed estimator	129
5.5.1. Fourier analysis and state observer implementation	129
5.5.2. Experimental results	132
5.6. PLL based position refining and speed observer	135
5.6.1. PLL behavior analysis	135
5.6.2. Experimental results	139
5.6.3. Offline Fourier analysis based state observer vs. PLL based state observer: short experimental comparison	143
5.7. Hybrid I-f starting and observer based motion sensorless control: experimental results	144
5.8. Experimental results	145
5.9. Conclusions	155
Chapter 6. Enhanced motion sensorless control including regenerative braking.....	157
6.1. Introduction	157
6.2. Braking methods for single phase PM-BLDC motor	158
6.3. Current control with soft switching PMM mode	159
6.4. Regenerative braking modes	160
6.4.1. Regenerative braking using only the BEMF	160
6.4.2. Improved regenerative braking by complementary PWM signals	166
6.4.2.1 Analysis of current control during motor and braking mode	166
6.4.2.2. Phase voltage estimation when using complementary PWM	169
6.5. Experimental results	173

6.6. Conclusions	179
Chapter 7 Experimental setup	181
7.1. Tested motor	181
7.2. Measuring laboratory equipment	182
7.3 Experimental platform	183
7.4. Software implementation	185
7.5. Conclusions	186
Chapter 7 Conclusions and contributions.....	187
Author's papers related to Ph.D. thesis	189
Author's CV.....	190

Objectives of the thesis

The main objectives of the thesis are:

- Offer an overview of the single phase permanent magnet brushless dc electric machines applications, topologies and control methods.
- Realize a comprehensive analysis using finite element method and outline the peculiarities of a single phase PM brushless dc motor.
- Develop a complete simulation model for dynamical modeling of a single phase PM brushless dc motor together with its control as close as possible to reality.
- Find a sensorless control strategy for a single phase PM brushless dc motor drive.
- Simulation and experimental implementation of the proposed sensorless control methods.
- Implementation of an enhanced sensorless control method which to contain the regenerative braking also.

Outline of the thesis

The thesis is organized in 8 chapters as follows:

The *first chapter* presents a comprehensive overview of actual and proposed applications of single phase permanent magnet brushless dc electric machines. Different topologies are presented and Hall based control and the sensorless control is discussed.

In the *second chapter* the characterization of a single phase PM brushless dc motor by finite element method and by laboratory measurements is presented.

The *third chapter* presents an accurate dynamical motor model obtained by using the obtained parameters from FEM. A complete simulation model containing the motor and the control is detailed.

The *forth chapter* introduces a sensorless control method for a single phase PM brushless dc motor based on a real time flux estimator and a prior knowledge of PM flux vs. position characteristic of the motor.

The *fifth chapter* presents a sensorless control method for a single phase PM brushless dc motor based on a real time flux estimator and a generated orthogonal PM flux system.

The *sixth chapter* describes the possibility to obtain the regenerative braking for a single phase PM brushless dc motor and an enhanced sensorless control method which includes the regenerative braking is presented.

In the *seventh chapter* the test setup used for the experimental work is presented and in the *eighth chapter* contains the thesis conclusions and contributions.

1. FRACTIONAL HORSEPOWER APPLICATIONS

1.1. Introduction

Electrical motors are used in a wide variety of equipment including residential applications and commercial refrigerating and air conditioning (HVAC) systems, as well as industrial processes of all sorts. Motors account for more than 50% of total electricity use in the United States [1] and it is not expected to be less at international level. The majority of motor energy use is due to integral-horsepower (i.e., 1 hp or greater), three-phase alternating current (AC), induction motors which are regulated by efficiency standards. However, integral-horsepower motors are substantially outnumbered by fractional-horsepower (less than 1 hp) motors. These motors are produced in both single and polyphase configurations, and are ubiquitous in commercial and residential applications from small pumps and fans, to compressors and conveyors. In the industrial sector, estimates of the proportion of drive energy represented by fractional-horsepower motors range from 0.5 to 1.5% [2].

According to [3], the US residential sector account for 37% of the electricity used nationally (Fig. 1a).

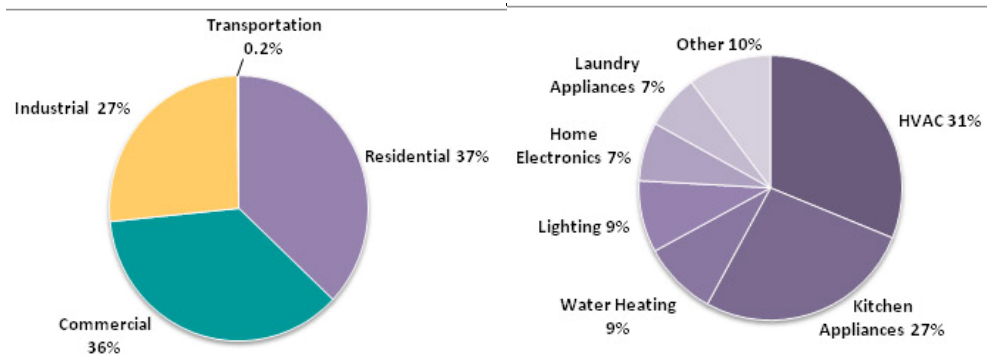


Figure 1. Graphic of electricity consumption by a) sectors, b) by type of appliance

In the residential sector, heating, ventilation, air conditioning and kitchen appliances (e.g., refrigerators and dishwashers) together account for more than half of household electricity use (see Figure 1b) [3]. On the other hand almost three-fifths of the motor energy use in the residential and commercial sector is by fractional horsepower motors, ranging in size from a few watts up to about one horsepower [4].

Other notorious applications for low power electric drives are those on automobiles (Fig. 1.1), medical and healthcare equipment, drives on Personal Computers etc.

10 1. Fractional horsepower applications

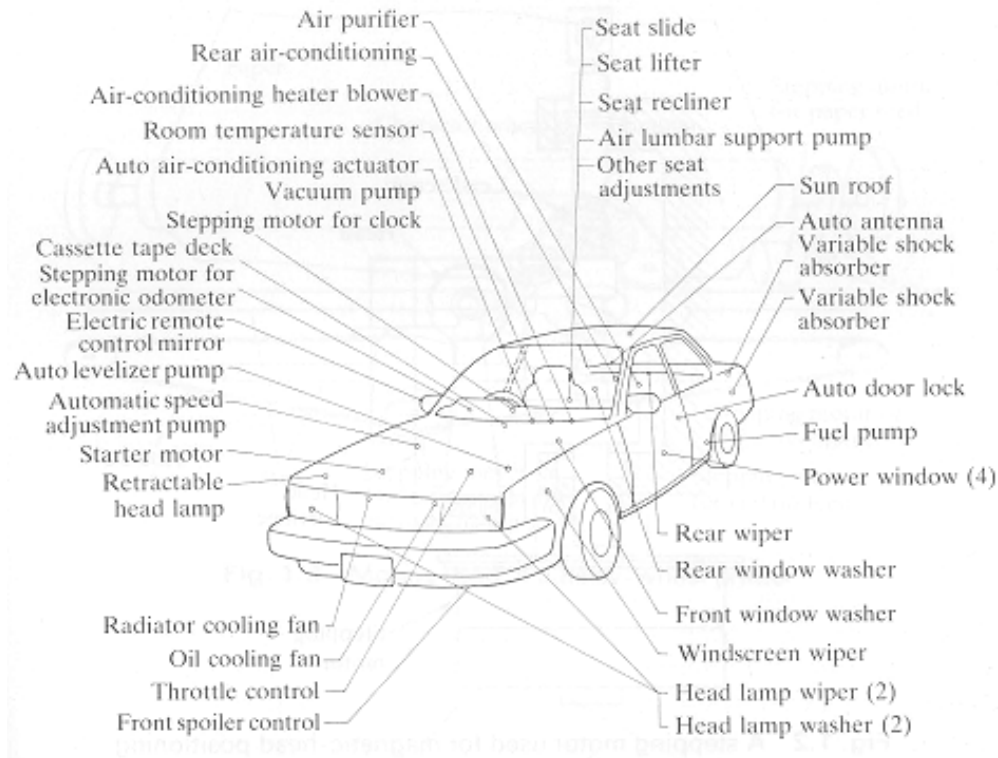


Fig. 2. Small motor drives on automobiles

Electrical appliances such as computers, printers, fax machines, copy machines, have relatively small power, and therefore, also small electricity demand per unit of equipment. But as their number is significantly growing, their electricity consumption it is considerable in the total consumption of a typical office building.

The dominant motors type used in the residential sector are:

- Universal AC motors are commonly used for sporadic applications where high speed is needed (vacuum cleaners, washing machines, drills, etc.). Such Universal motor drives-with triac variacs – have resulted in low cost low power drives but the presence of the mechanical commutator with all its reliability and safety problems limits their applications and thus the trend is to gradually reduce their market share, application by application.
- DC brush PM motor drives – with diode rectifier and single IGBT (MOSFET) dc-dc converter – is yet another low cost low power drive still dominant in automobile auxiliaries or in some home appliances. Again the cost is moderately low but the reliability (maintenance) and safety of brush - commutators seems the reason for their gradual replacement by brushless motion drives.
- Single-phase induction motors are used for operating household appliances like refrigerator compressors and washing machines and have been traditionally used to drive fans and pumps of small power. Recently the inverter control of a split phase capacitor IM for such purposes has been thoroughly investigated while the motor efficiency was slightly improved by

using a copper cage in the rotor. The 6,4,2 leg PWM IGBT (MOSFET) voltage source inverter have all been investigated thoroughly [6,7] with the aim of reducing the drive costs with a split-phase capacitor IM.

The above presented motors represent low cost solutions for these low power applications and they aren't very efficient. Since the residential motor load is a very large portion of the energy used in the world, it could greatly benefit from more efficient motor drives.

1.2. Permanent magnet synchronous motor at a glance

The development of power electronics, digital control through digital signal processors (DSP) and permanent magnet technology has led to a widespread use of PM synchronous motors in various fields of applications.

The PMSM is a doubly excited motor where the dc supplied excitation winding from the rotor is replaced by PMs. The usage of PM instead of copper winding for excitation has the following advantages comparing with the conventional electrically excited synchronous machine:

- -higher efficiency due to eliminate copper losses in the rotor
- -elimination of slip-rings and extra DC supply voltage
- -low-volume and low-weight due to permanent magnet excitation
- -more compact construction

As main drawbacks of the PM excitation we can mention:

- -high cost of the PM
- -the PM may be demagnetized by excessive armature reaction, by excessive temperatures or by excessive mechanical shock
- -additional control effort for field weakening operation [8]

Based on the wave shape of their induced emf, the PMSM are classified in brushless ac motors (sinusoidal bmf and distributed stator winding) and brushless dc motors (trapezoidal bmf and concentrated stator winding).

The differences between those two types of motors can be summarized in the following:

The BLAC motor:

- -is supplied with sinusoidal currents
- -all three phases are conducting at a time
- -a smooth torque is obtained
- -it needs a higher computational effort to obtain the same control capabilities as a high performance DC motor drive, by using the field oriented control.
- -needs an high resolution position information

The BLDC motor:

- -is supplied with rectangular current
- -only two phases are conducting in the same time
- -torque pulsations are unavoidable due to the phase commutation
- -it approximates the operation of PM dc motor with power electronics taking place of the brushes using a simpler control system compared with PMSM
- -low resolution position information suffices

The PMSM are a class of electrical machines with probably a greater diversity in size, shape, geometry and configuration than any other type of machines. [9] So, one of the best advantage of the PM machine compared to conventional ones is that it can be constructed in many non-standard sizes and shapes, which often compensates the higher cost.

1.3. Efficiency increasing by PM-BLDC motors

While the demand for electricity is expected to grow in the future, the requirement for higher efficiency devices pushes industry to increasingly adopt the PMSM both in the constant speed applications (to improve efficiency and power factor in comparison to induction and wound-rotor synchronous motors) and in variable speed drives. [10]

In the field of constant speed application, for line start capability, the PMSM is designed with a squirrel-cage winding on the rotor to provide the torque from standstill to near-synchronous speed.

The increasing interest for adjustable speed drives in recent years made the PMSM a top competitor for a full range of motion control applications. In this type of applications a power electronic converter and a position feedback is needed in order to achieve stable and self starting motor operation. In literature this type of drive is often called self synchronous PMSM.

The main advantages which have to be considered when choosing between adjustable-speed and fixed-speed motors drives are:

- energy savings
- velocity or position control
- transients amelioration [9] [11]

The use of PM-BLDC motor in adjustable speed drives can prove its merits in various applications. For example, in the field of air moving applications it is often possible to reduce average energy costs by 50% or more by using adjustable-speed drives, which eliminate the throttling or recirculation loss. The adjustable-speed drive may be more expensive, but its capital cost can be offset against energy savings and the reduction of maintenance requirements on mechanical components [5].

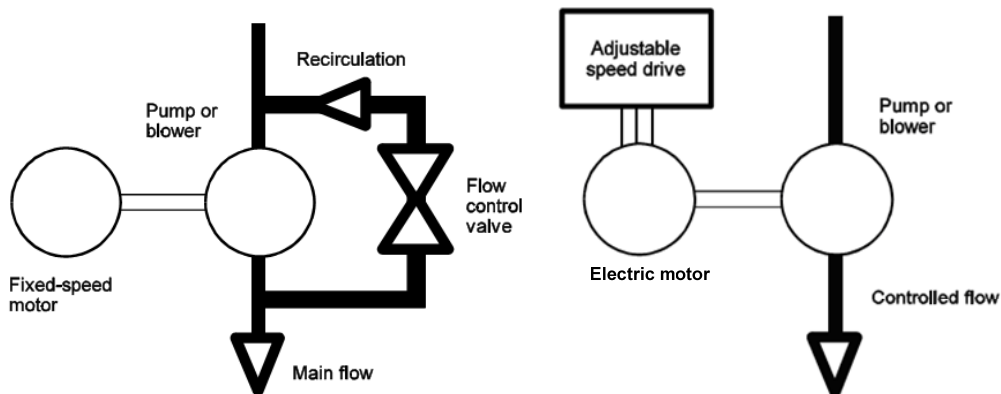


Figure 3. Flow process control under: a) fixed speed, b) variable speed

Since the efficiency and power factor of induction motors falls off in small sizes. In the fractional and low integral-horsepower range the complexity of the AC drive is a drawback, especially when dynamic performance, high efficiency, and a wide speed range are among the design requirements. [5]

Due to the increasing requirements for lower energy consumption, the different types of 1 (2) speeds ac mains-supplied induction motors or DC motors are gradually replaced by variable speed inverter fed motors, mostly of the PM-BLDC

type [12]. Such examples are the washing machine and the refrigerators applications.

In a conventional washing machine, a DC or an induction motor drives the drum via a belt and pulleys (Figure 2.a). Substituting these machines with a BLDC motor gives also another advantage over the previous mentioned ones: by using such a motor a direct-drive washing machine (Figure 2.b) is obtained by suppressing of the belt, pulley and eventual brushes of the DC motor. Indeed, these elements are the weak parts of the washing machine and are often the cause of failures [13].

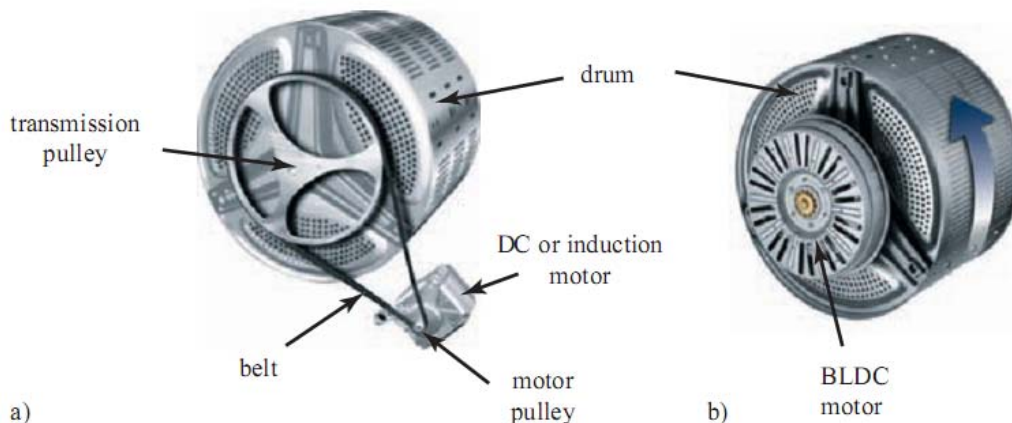


Figure 4. a) Conventional washing machine; b) LG's direct-drive washing machine

A washing-machine motor for home appliance rates usually less than one kilowatt. The drum of the machine rotates approximately at 50 rpm during the washing process, up to approximately 1500 rpm or higher during the drain [14]. Therefore, the direct-drive motor of the washing machine should run over a large speed range. Figure 2 shows a direct-drive washing machine for home appliances produced by LG [15]. The motor, directly-connected to the drum, is a 3 phase brushless DC (BLDC) PM motor with trapezoidal back-EMF waveforms and it is supplied with rectangular current.

Also, if we consider the residential refrigerators and freezers which can have up to 5 motors, we would obtain great reduction in energy consumption by introducing the PM-BLDC motor. The compressor is normally an AC single-phase induction motor. The use of an adjustable speed PM-BLDC motor drive, would be a great improvement over current practices in which the compressor motor runs at full speed until the desired temperature is meet then cycles on and off between full speed and off.

In the automotive industry due to the drawback of the used DC motor and in the given electrical trends to develop the 42V automotive power supply systems, will help to make brushless motors more acceptable by reducing the current levels and therefore the size and cost of MOSFETs required in the drive[5]. Here, PM-BLDC motors are already used in fuel pumps, steering systems and fan controllers for air conditioning systems and engine cooling.

14 1. Fractional horsepower applications

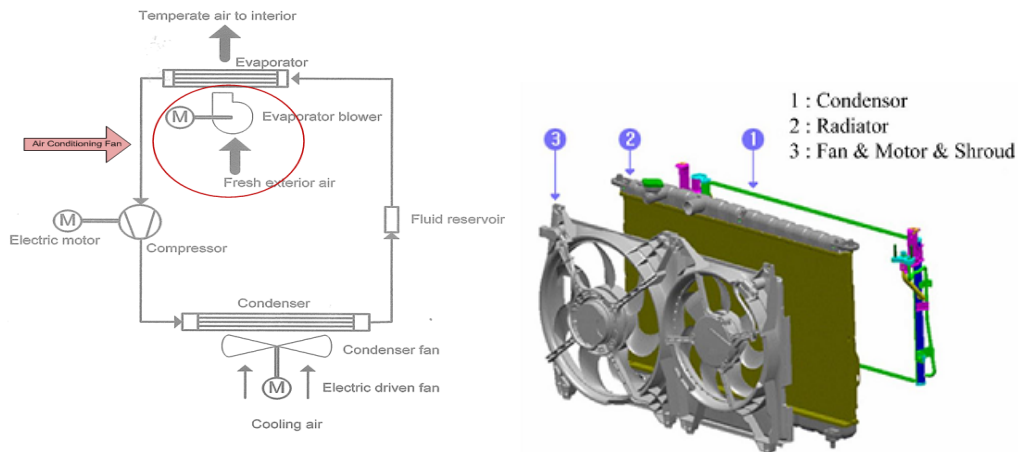


Figure 5. Engine cooling fan module [16]

Because it has the same control capabilities like a DC motor but it has the advantage of brush removal resulting in higher reliability, lower noise and the possibility to be used in other mediums where the dc motor wasn't proper due to the produced commutation sparks, PM brushless DC motors are one of the motor types rapidly gaining popularity and are used in other fields such as Aerospace, Medical, Industrial automation equipment and instrumentation etc.

1.4. Low-cost solutions for fractional horsepower applications

When referring to low power electrical application, compared with the industrial sector, it is more feasible to introduce more efficient motor drives, because the life spans of household appliances and gadgets are generally shorter than the life spans of large industrial machines and so there are more opportunities to replace inefficient motors. Also, the price difference between higher efficiency motor drives and typical motor drives is smaller at the residential level than it is at the industrial level, but here the cost is also an important factor.

So, considering the above, a compromise between the desired performance and the cost must be done.

As previously seen the 3 phase PM-BLDC is increasingly adopted in various drives in the field of low power applications. Since at this level of applications the cost is often a decisive criterion, cost minimization of the PM-BLDC motor drive is very important. Due to the high volume nature of these applications, cost minimization is of a great importance, not only to save materials and labor, but also for the fact that, without such a cost minimization, many of these applications with variable speed drives may not be realized. One place for cost reduction is the converter and its associated controller requirement. So in order to cut the cost, the half bridge converter, the four switch converter or the C-dump converter with $n+1$ switches for an n -phase machine are sometimes used [17][40].

In order to further reduce the cost, in applications which require performances not as high as those given by the 3 phase BLDC motors, but higher than those given by the existing ones, synchronous motors with two or one phase are used.

1.4.1 Single-phase PMSM/PM-BLDC motor

Mass production and market competition of small electric drives demand decrease of production costs. Meanwhile, the output characteristics have to remain the same or even increase. It seems that in the field of small power, small starting torque applications, the single phase brushless DC motor presents a growing interest, especially in the residential and automotive industry, where it is more efficient than rival motors [18][19]. It is used in order to cut the costs of the power electronics converter for variable speed, by reducing the number of power switches and the number of Hall sensors.[12]

If we restrict out the domain of interest at low power fans, blowers and pumps, which stand out as a good part of this market of electric drives, we can use the fact that the torque depends essentially only on speed and that in general enjoy low torque starting conditions, to use the single phase PMSM. Consequently, their control may be simplified to a great extent. The consequence of this action is notably lower system costs.

1.4.1.1 Fundamentals and Theory of Operation

A single-phase brushless DC motor consists of a rotor with permanent magnets and a stator with windings as shown in fig.6.

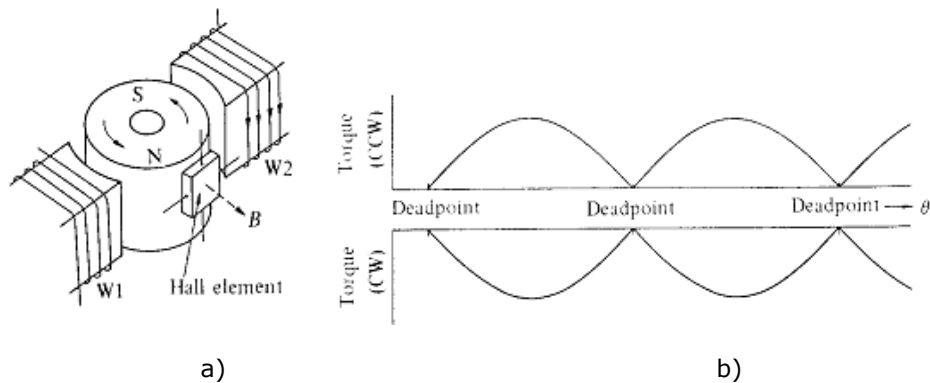


Figure 6. Basic single phase PMSM: a) components, b) generated torque [20]

It can be seen that the rotor has two wound salient poles and the rotor is no salient. Because of the stator construction the rotor always tends to stop in the position below the stator's pole because there is the minimum reluctance value when the winding is unexcited.

In this position the electromagnetic torque is zero and this is a real problem for starting and not only. If such a dead point, where the developed torque is zero, exists in single-phase brushless DC motors, there is a possibility that the motor will stop at the dead-point and be unable to start again when it carries a frictional load. When the load is small, the rotor may be able to pass through the dead point due to inertia.

The basic solutions for obtaining a smoother torque are the increase of the phase number or the use of space harmonic magnetic field.

16 1. Fractional horsepower applications

An ideal theoretical solution with the role of outlining the principle behind the use of space harmonic magnetic field, is presented in figure 7. It consist in an additional four pole magnet coupled to the rotor, and an additional four pole magnet coupled to the stator[20].

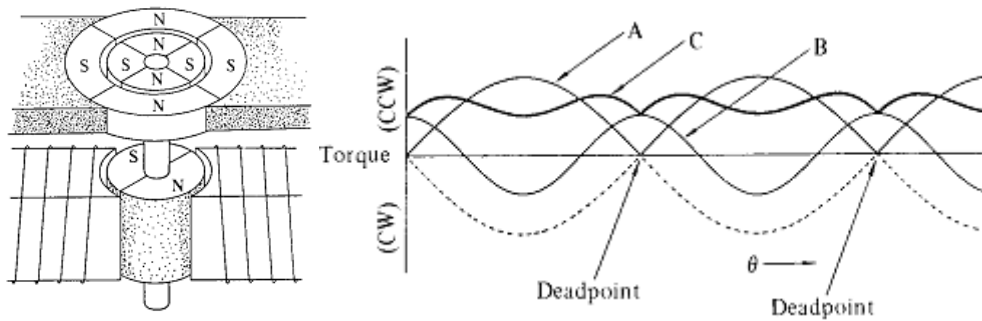


Figure 7. Principle of torque dead-points elimination [20]

Torque curve A is given by the two pole magnets, curve B is represents the produced torque by the four pole introduced magnets and curve C depicts the resultant torque. It goes without saying, that in order to obtain the continuous curve A, a method for phase commutation should be used.

The presented example is an ideal case of a smooth torque. For simplicity issues, the torque produced by the two pole magnets at zero current, named cogging torque, is not considered here.

Since this is not a practical solutions, an applied solution which exploits the above presented principle of introducing a complementary torque component is the usage of an parking magnet who has the role of creating a spatial shifting between the stator and rotor magnetic axes. In this way there is a angle between the rotor and stator fields before starting and so there is a starting torque. [12].

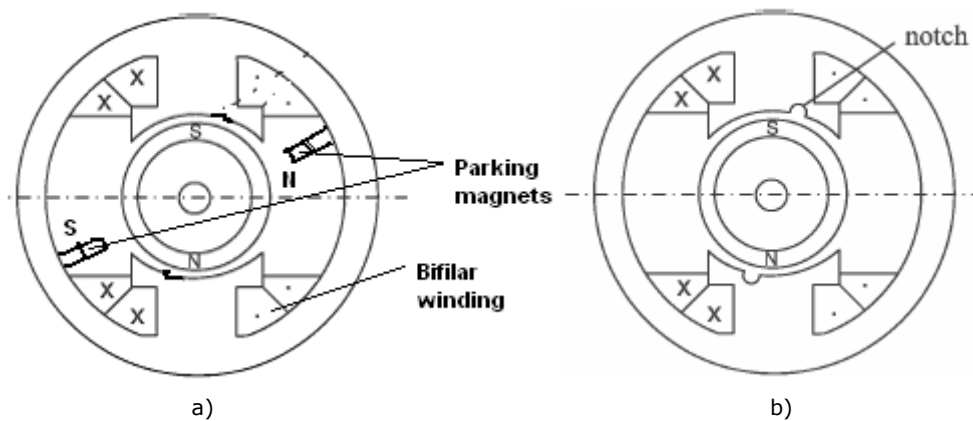


Figure 8. Solution for self-starting capability: a) parking magnets, b) stator notch

In order to eliminate the extra cost of the parking magnet, other solutions exploits the existence of the torque produced by the PMs at zero current. Those are based on a modified stator shape which has the role of modifying the previous existing cogging torque which made the rotor to align at the zero starting torque

position. One of these solutions is to make a notch in the stator poles, this making the rotor to align with stator at an angle different from zero thanks to the variable reluctance below stator's poles.

To realize the airgap asymmetry, a salient pole PM synchronous motor can also be designed as a self-starting motor implying a nonuniform air gap, (wider at one end of the pole shoe than at the opposite end) by using the two solutions presented in figure 9: an uneven (tapered) airgap or a stepped airgap [21].

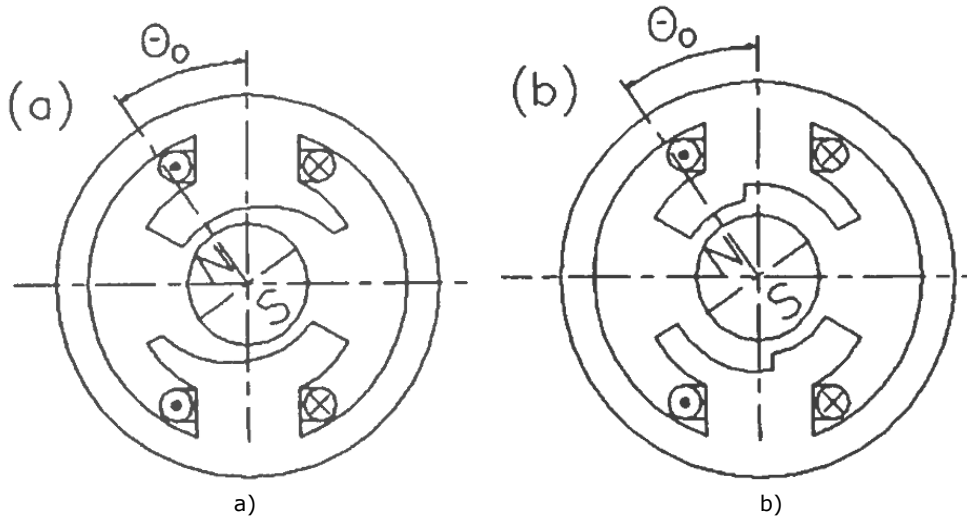


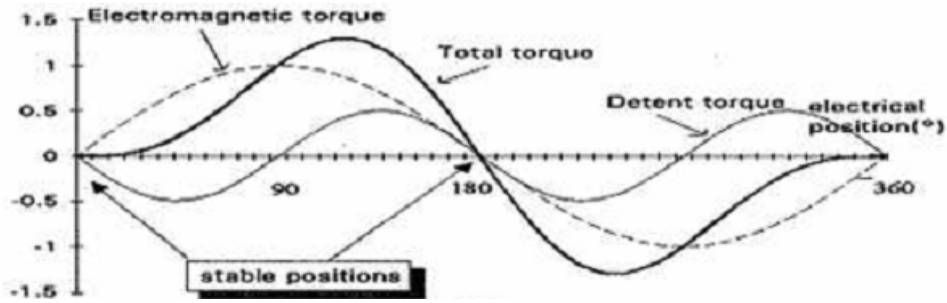
Figure 9. Solution for selfstarting capability: a) tapered-airgap, b) stepped airgap

In figure 9 the rest angle θ_0 is the angle between the center axis of the stator poles and the axis of the PM rotor flux when the phase current is zero. This motors are self-starting when, with a zero value phase current, the angle $\theta_0 \neq 0$.

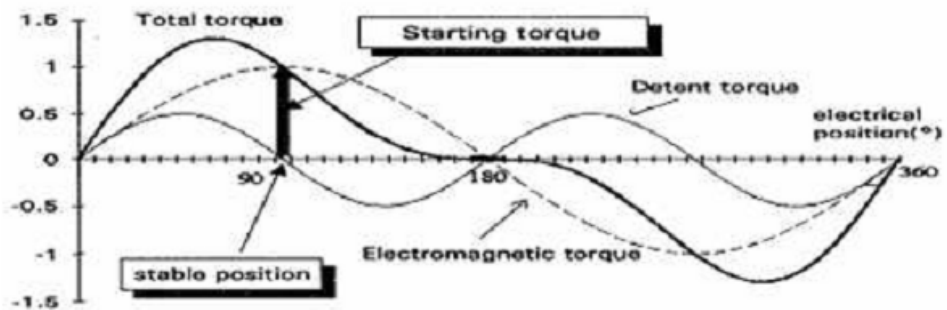
Ideally the largest starting torque is achieved when the rest angle $\theta_0 = \pm 90^\circ$.

In figure 10.a it is visible that with a smooth airgap, the single-phase excitation produces zero starting torque because the detent position is under the stator salient poles. An exaggerated and ideal case of a modified cogging torque is shown in figure 10.b. Here the detent position corresponds to 90 electrical degrees where the starting torque is maximum. In practice it is hard to obtain such a large misalignment between the stator and the rotor. An intermediate detent position between those shown in figure 10.a and 10.b is usually achieved.

18 1. Fractional horsepower applications



a)



b)

Figure 10. Torque components for : a) smooth airgap, b) uneven airgap

If the stator and the rotor of the above presented motors are inverted an outer rotor motor is obtained (Fig. 11). The BLDC outer motor is often used, especially for the single phase motor in order to increase the inertia and so to reduce the speed fluctuations which can be caused by the torque pulsations.

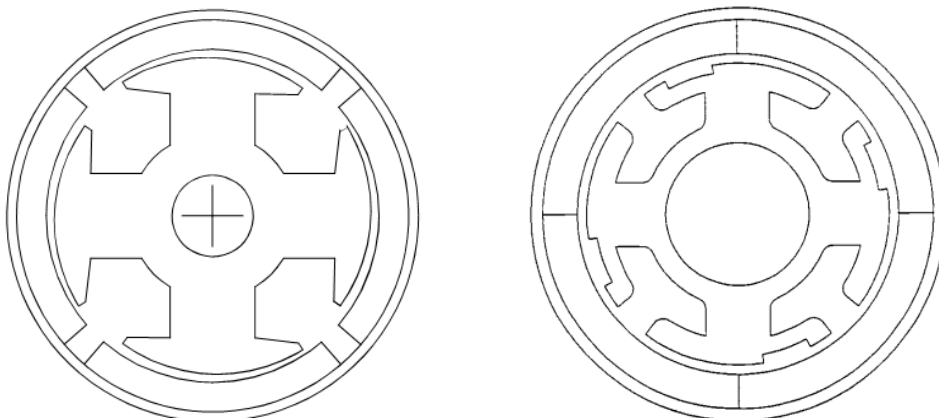


Figure 11. Outer rotor topologies for selfstarting: a) tapered airgap, b) notch in the stator pole

1.4.1.2 Interior vs. Exterior rotor

Single phase brushless DC motors can be classified, according to their structure, as follows:

- ┆ Outer-rotor motors
- ┆ Inner-rotor motors
- ┆ Special-configuration motors (axial flux motors)

The basic differences, which have to be considered in the design process, between inner and outer rotor motors, are summarized below:

- The outer-rotor motor has more magnetic material than the inner-rotor device, which means it is capable of more flux when the identical materials are used. It would be necessary to use a higher-energy-product magnet to get the same performance from an inner-rotor motor.[22]
- A SMPM motor with an outer rotor has usually a larger airgap diameter than a SMPM motor with inner rotor having the same external diameter. The length and thus the weight of the machine can be decreased for a machine with an outer rotor. The outer-rotor SMPM motors approximately 15% lighter than the motors with an inner rotor, if only the active weight is considered.
- In the case of non-overlapping concentrated windings, PMSMs with outer rotors are easier to wind.
- If the rotor is internal, the centrifugal forces tend to detach the PMs and a bandage or other protection is often necessary. However in the case of an external rotor, the PMs are pressed on the rotor iron by the centrifugal forces, making their detachment more improbable.[13]

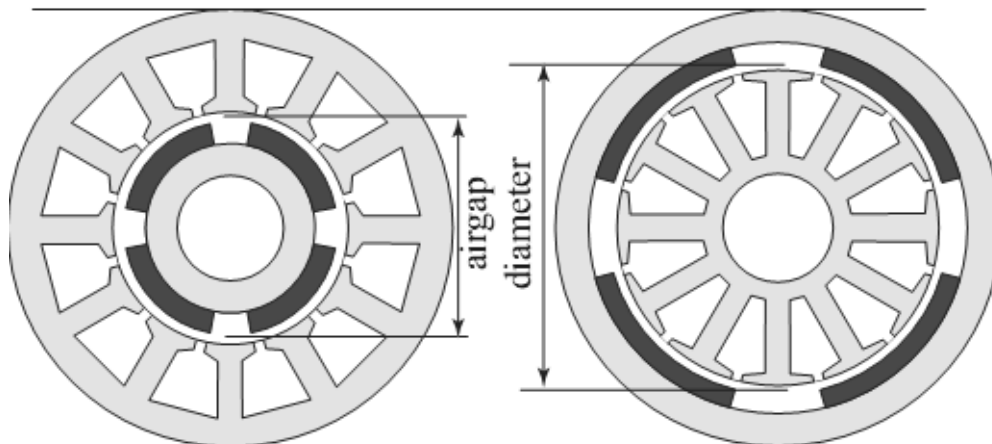


Figure 12. Inner and outer-rotor PMSMs with same external diameter.

- Also the outer motor results in shorter end turns which yields lower inductance and less copper loss.
- The inertia of the inner-rotor motor is lower because of its smaller rotor diameter. Therefore, it accelerates more rapidly than the outer-rotor motor.
- The main source of losses, the windings, is located in the stator, therefore, in the case of an outer rotor, the cooling would be less efficient [22].

1.4.2 Single phase PMSM classification

If in the area of large drives, the motor is always chosen from one of the classical types, the field of relatively small power applications is more spectacular due to the variety of motor types and topologies that can be used. The interest for the single phase PMSM is evident if we look at the research work and publications done in this field. Different topologies of such motors are proposed for various low cost low power applications.

With regard to the magnetic circuit, the 1 ph. PMSM can be classified as:

- Radial flux machine with :
 - the U shape stator core
 - the round stator core
- Axial flux : disk type motors
- Transverse flux machine : the claw pole stator core

Based on the PM placement the single phase can be with:

- PM on the rotor
- PM on the stator

For low cost low power applications a class of nonclassical motors has known an increasing development.

The U shape stator core (Fig. 13.a) has been proven inferior to the standard round stator core in terms of weight for same performance [19]. But it is still used due to the reduced cost and easy manufacturing of the stator [23]. Figure 13.b illustrates the simple assembly process for this type of topology.

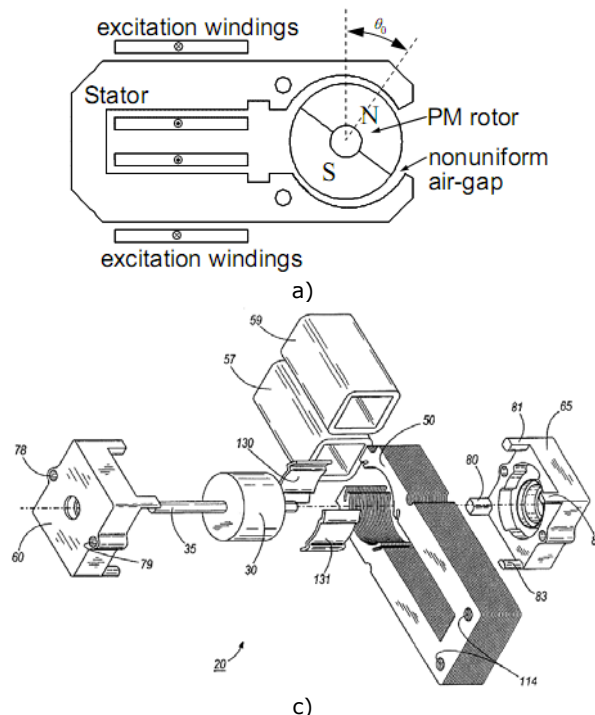


Figure 13. The U frame stator: a) the self-starting geometry with tapered airgap, b) Component parts assembly [23]

The C frame shape (Fig.14) is used at very low power where it proved to be more efficient than the used shaded pole induction motor [24].

In [25] a single phase PM BLDC motor is obtained using the stator frame of a shaded pole induction motor, with the short-circuited coil removed, and a ring PM ferrite rotor (Fig. 15). In this case the airgap asymmetry, and so the self starting, is given by the slot where the short-circuited coil was. In this case, the efficiency of the obtained BLDC motor was measured to be more than four times higher than that of the commercial shaded pole motor. This proves that using the existing technology for producing the shaded pole IM, higher efficiency single phase motors could be obtained with a reduced manufacture cost, compare with the shaded pole motor, due to the simpler construction of the PM rotor.

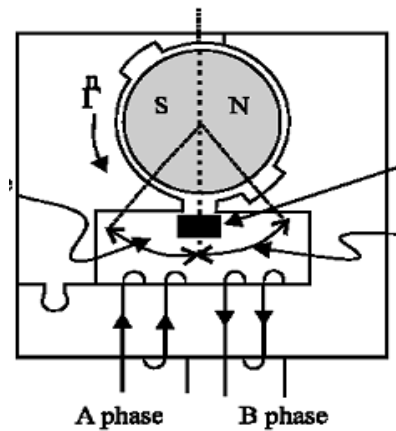


Figure 14. The C-frame type brushless DC motor

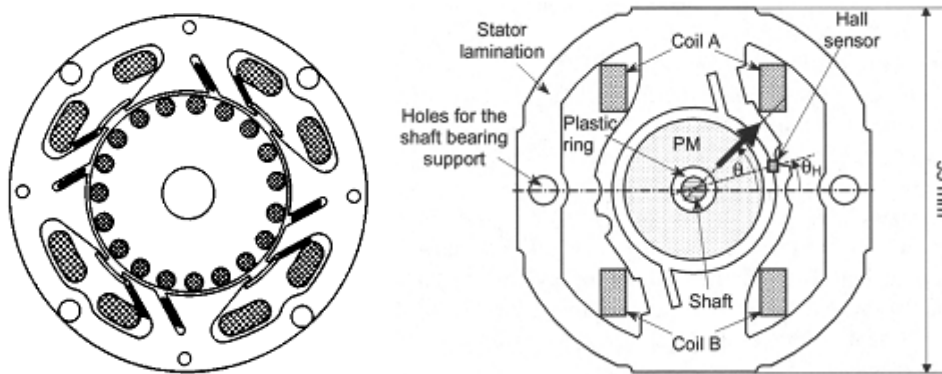


Figure 15 From shaded pole motor to single phase PM brushless dc motor
a) single phase shaded pole motor, b) single phase PM-BLDC motor

With regard to the axial flux motor, in [26] a single phase disc-type PM-BLDC motor with salient-pole stator is introduced as a direct drive for a water pump with so-called wet rotor. The stator consists of radial laminated cores and coils wound on them. The cores are placed axially and distributed uniformly on the stator circumference. They can be glued together by means of synthetic resin. The rotors

22 1. Fractional horsepower applications

are placed on both sides of the stator (figure 16.a). They are steel discs with permanent magnets glued onto their surfaces. The single-phase connection is shown in figure 16.b.

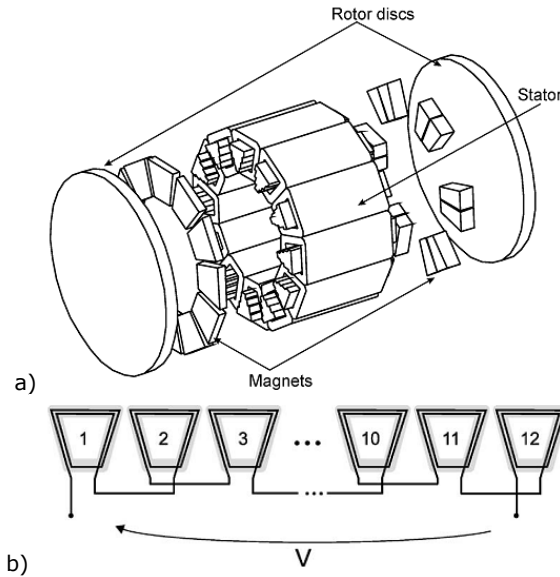


Figure 16. Axial flux motor: a) Structure of a single-phase disc motor, b) Single-phase connection of coils.

In order to assure the self-starting capability, the authors propose the solution of rearranging the position of permanent magnets on the surface of one of the rotor discs as shown in Fig. 17.

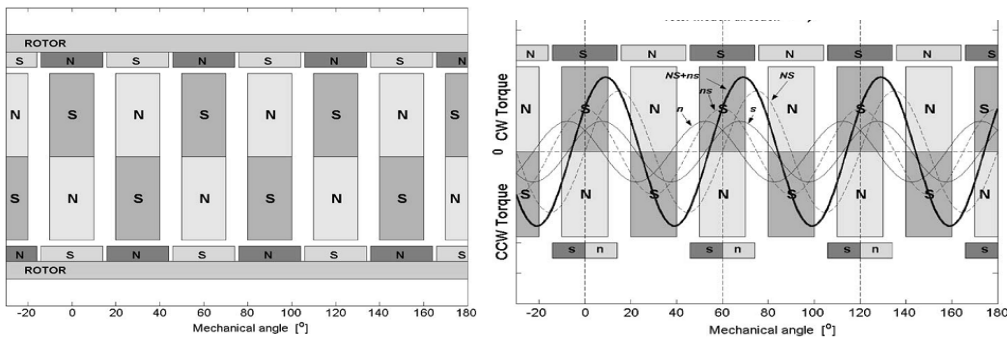


Fig.17 Magnet rearrangement and torque components at constant current

In [27], [28] the transverse flux construction is introduced for a single phase spindle motor for DVD applications, respectively for a small fan application. The single phase claw pole PM-BLDC motor is yet another solution for low cost applications. The construction of this type of motor can be made of lamination or of soft magnetic composite (SMC). The powder core motor will be most profitable for the high volume low cost applications, for the motor structures that are unpractical

to make of conventional laminated steel. By using a single circular winding has the advantage of low cost and ease of manufacturing [29]. The stator can be made of three distinct parts easy to assembly (Figure 18).

The solutions for self-starting are the same presented for the radial flux motors.

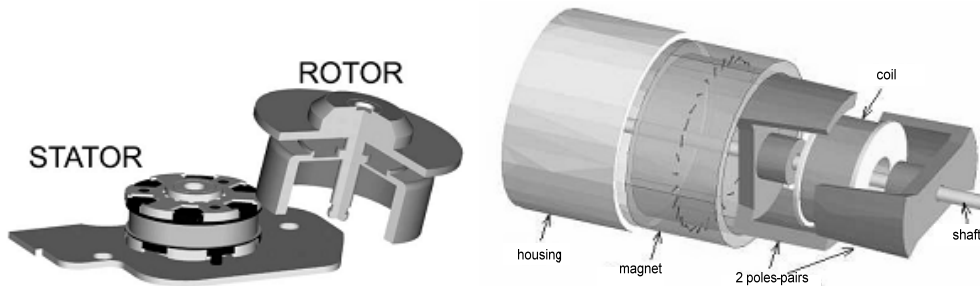


Figure 18. a) Pancake-type spindle motor, b) Single phase claw pole PMSM [29]

In [30], a brushless doubly-salient PM machine (Fig. 19) was proposed with the aim of combining the advantages of the SRM and the PM-BLDC motor into one machine as an attractive solution for a low cost high speed generator. Due to its numerous advantages such as simple construction, low inertia, high power density, robustness, and due to the fact that is suitable for high speed application (the permanent magnets are on the stator pole) it was proposed as a viable solution to replace the claw pole pole alternator.

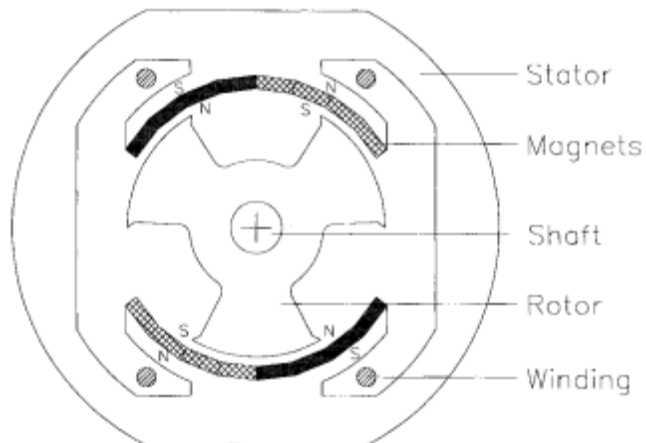


Figure 19. Single phase flux reversal machine

Since in [30] the FRM was explored like a generator, in [31] the FRM is proposed as a motor for a vacuum cleaner. The geometry from figure 18 had to be modified in order for the motor to start when the winding is energized. Figure 20 illustrates the alternative topologies of FRM for self-starting [32].

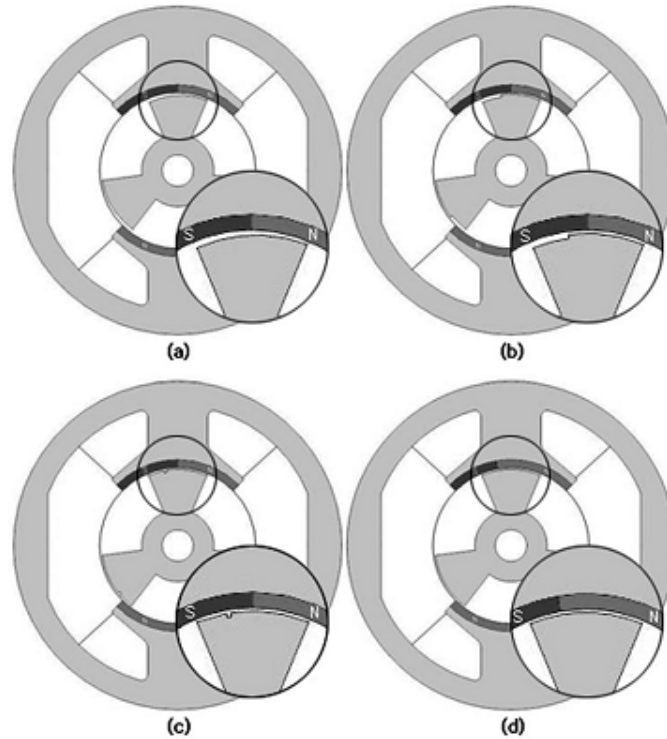


Figure 20. Self-starting solutions for a flux reversal motor: a) tapered airgap, b) stepped airgap, c) slotted teeth, d) asymmetric PM width

Another unconventional single phase PM-BLDC motor is the flux-switching permanent magnet motor [33] [34]. Here the permanent magnets are placed in the stator, and both the stator and the rotor have salient poles. The rotor poles have to be asymmetric designed in order assure the starting (figure 21).

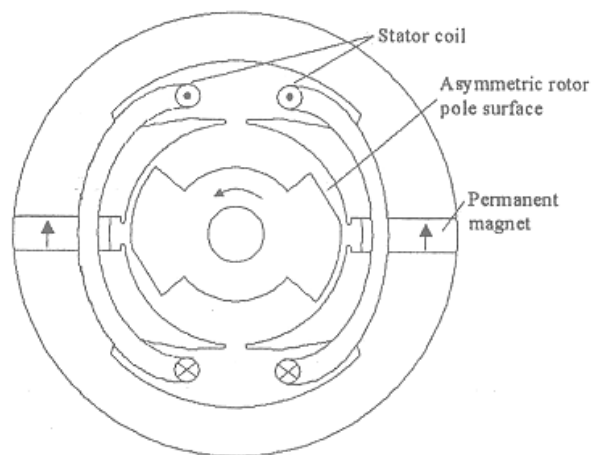


Figure 21. Single phase PM Flux switching motor topology

1.4.3 Single phase PM-BLDC drive

As compared to a conventional DC brush motor, brushless DC (BLDC) motors are DC brush motors turned inside out, so that the field is on the rotor and the armature is on the stator. As explained before, field excitation of BLDC motor is provided by a permanent magnet and commutation is achieved electronically instead of using mechanical commutators and brushes. In the case of single phase PM BLDC motor, in order to rotate, a pulsating magnetic field which interacts with PM field need to be produced by a power electronic converter which supplies the phase winding.

By far, the most used single phase PM-BLDC motor is the one with nonsalient surface magnet rotor, due to its simplicity and to the strong research background work done until now.

This motor will be considered further for a brief description of the existing solutions for hall based control, respectively for sensorless control.

With regard to the winding configuration the single phase PM-BLDC motor can have a unifilar winding or a bifilar winding (sometimes called two phase motor).

The bifilar winding motor consist of two semi-coils opposite wounded on each stator pole. The obtained two phase windings are alternatively energized by two unipolar current pulses.

Despite of their disadvantages like low winding utilization and additional copper cost, it is still used for reducing the number of electronic components and so the cost and the commutation losses. Also another advantage of the bifilar winding is the easy possibility of sensorless control by sensing the emf in the nonconducting phase.

A typical single phase PM-BLDC motor with bifilar winding is shown in figure 22. For obtaining a high magnetic coupling between the two coils, these must be wound as figure 21.a) shows.

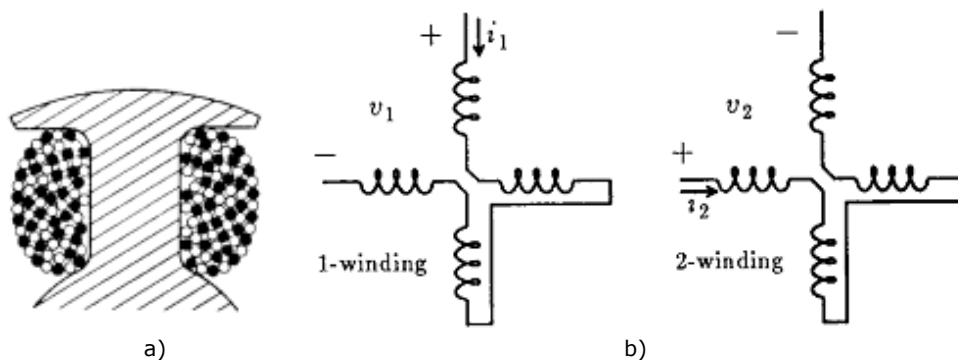


Figure 22. Typical single phase PM-BLDC motor with bifilar windings: a) tooth winding, b) electrical connections

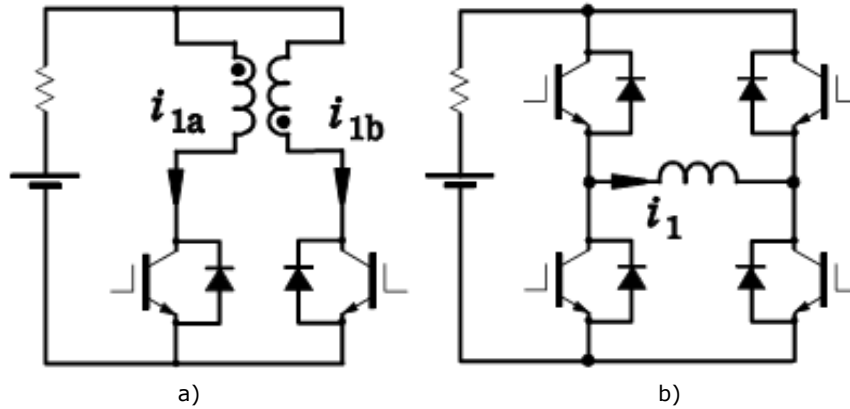


Figure 23. Simple commutation circuit for single phase PM-BLDC motor: a) unifilar winding, b) bifilar winding

Figure 23.a shows a simplified electronic commutation circuit for the bifilar winding. Each phase of a BLDC motor is energized by commutating the two transistors in order to maintain the synchronism. Complementary switching is used with the transistors controlling the two windings: normally each conducts for half a cycle in any full cycle. When one switches off, the current ideally transfers immediately to the other, but in practice the mutual coupling between the two paths is imperfect and the resulting leakage inductance retains a fraction of the inductive energy, which must be dissipated. There is also an overvoltage on the outgoing transistor, which may cause avalanching if a snubber is not used [5].

To decrease the energy consumption of a single phase PM-BLDC motor, it is greatly recommended that the motor stator be wound with a unifilar winding. Since the unifilar-wound stator has a single-wire winding which is simpler to manufacture, the increased reliability and reduced manufacturing cost and time are important gained advantages.

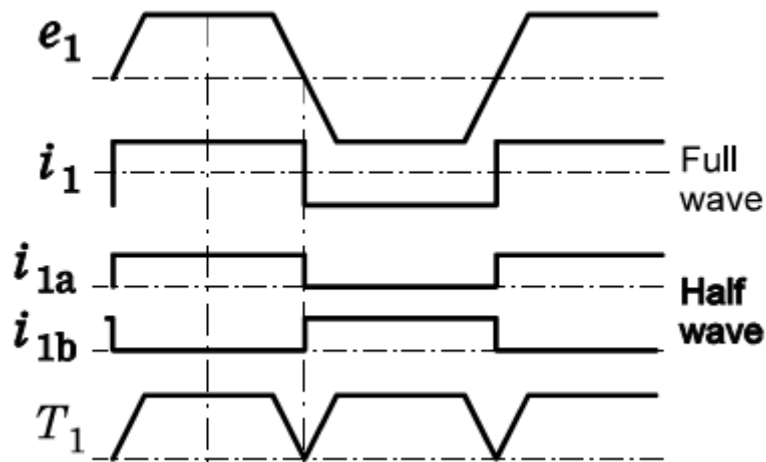


Figure 24. Unifilar and bifilar winding single phase PM-BLDC motor waveforms

In order to commutate this type of motor a bipolar current is now needed in order to alternate the produced magnetic field. For this purpose a full bridge converter as figure 23.b shows is used.

A graphical comparison for the unipolar and bipolar current electronic converters is presented next (Figure 24). The halfwave or "unipolar" current i_{1a} flows in one path for half a cycle; then it is switched off and the current i_{1b} flows in the other path. For the bipolar drive the current i_1 is switching sign every half cycle. Therefore, the torque generated is basically the same as with a one-phase or two-phase motor. The torque produced by the interaction of e_1 and i_1 (or i_{1a} , i_{1b}) is shown as T_1 . The EMF and the current both require a finite time to change from positive to negative, and this results in a dip in the torque waveform every half-cycle, i.e., at twice the fundamental frequency.

If a variable speed drive is needed, the speed of the BLDC fan is efficiently controlled by using the PWM technique. In this method, the speed is controlled by the duty cycle of the PWM that drives the one or two winding coils in the BLDC fan independently. In PWM controlled converter, another advantage of the full bridge converter reveals: the efficiency can be further improved with the use of the higher cost H-bridge switching driver maintaining the energy in the stator winding. The H-bridge drive method also eliminates the need for snubbing inductive energy at commutation transitions and allows for recirculation of inductive winding current to maintain energy in the motor while PWM switching occurs. [35].

Another power electronics converter with 2 low cost thyristor power switches was proposed in [36] for the bifilar winding motor (Fig. 25). It uses a single IGBT buck dc.-dc. converter to shape (control) the stator phase current and two low cost thyristors just to turn on and off at fundamental frequency the two bifilar windings of the stator phase. The bifilar winding provides for elimination of the level shifting in the thyristors control circuit and because the winding is off for half a period it may be used for e.m.f. estimation and this for motion-sensorless control. The side effect is the reduction of motor efficiency.

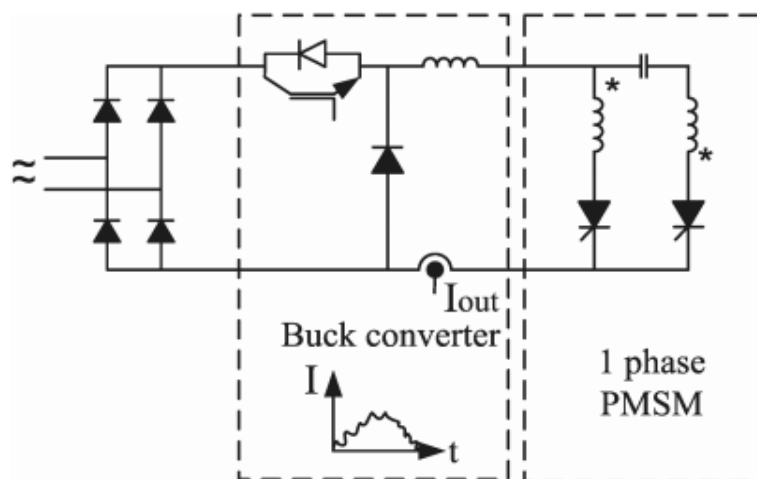


Figure 25. The chopper current inverter drive for single phase (bifilar winding) PMSM

1.4.4 Single phase PM-BLDC motor sensorless control

The current in the windings of a brushless permanent-magnet (PM) machine must be synchronized to the instantaneous position of the rotor in order to produce constant torque as the one shown in figure 24. Therefore, it is important to know the rotor position in order to understand which transistor has to be commutated. The most common method of sensing in a BLDC motor is using hall-effect position sensors.

The Hall sensor is, as all components, a cost added, but especially because there is a need to be mounted rather accurately to provide good feedback to commutate at the right moment. Also other advantages like less wire, more compact drive and the possibility to be used in hostile environments, including temperature, must be mentioned.

The three phase BLDC motors have for a long time been controlled in sensorless mode, eliminating the need for Hall sensors. Because sensorless control is essential for low-cost variable speed applications such as fans and pumps, there is a growing interest in "sensorless" schemes for single phase PM-BLDC motors also, in which position information is derived by on-line analysis of the voltages and currents in the machine windings.

Figure 26 illustrates simplified sensorless control diagram where the outlined position estimation block is used instead of the Hall sensor.

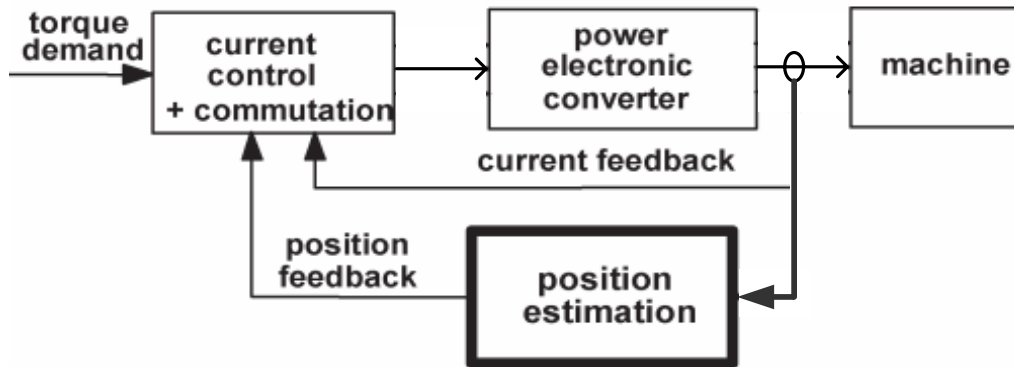


Figure 26. Simplified sensorless control diagram

Two main sensorless control methods for single phase PM-BLDC motor were proposed until now.

In [36], [37], [38] a sensorless control solution for the motor with bifilar winding is proposed. The method is based on the bembf sensing in the nonconducting winding. The difference is that in [36] the current control is done by the dc-dc converter, while in the other the current control is done by the two transistors that are also used for phase commutation. A resistance divider may be used to measure the voltage of the nonconducting coil, V_{off} .

The PM flux Ψ_{PM} is thus given by equation 1:

$$\Psi_{PM}^{\theta_r} = \int V_{off} \cdot dt \approx \Psi_{PM} \cdot \cos \theta_r \quad (1)$$

To control the machine with e.m.f. in phase with current it means to turn on (off) the phase when Ψ_{PM} is maximum or when e.m.f. is zero. So, when the e.m.f. (V_{off}) is zero the phase coils are turned on and off. For trapezoidal current control, only zero crossing of the e.m.f. in the off stator coils with amplitude control by the current regulator suffice.

At very low speeds the e.m.f. signal is not available and thus a selfstarting sequence is required.

In [39] a sensorless control based on the winding time-sharing method for a unifilar winding single phase PM-BLDC motor is applied for a small fan. It consist in a method of bemf sensing combined with the current commutation pulse control (figure 27). During the time interval of half electrical period, first the winding is energized for torque production and then the supply voltage is made zero and after a time interval needed for current decay the back emf is measured. Off course, there is the possibility to measure the bemf before or after the zero crossing.

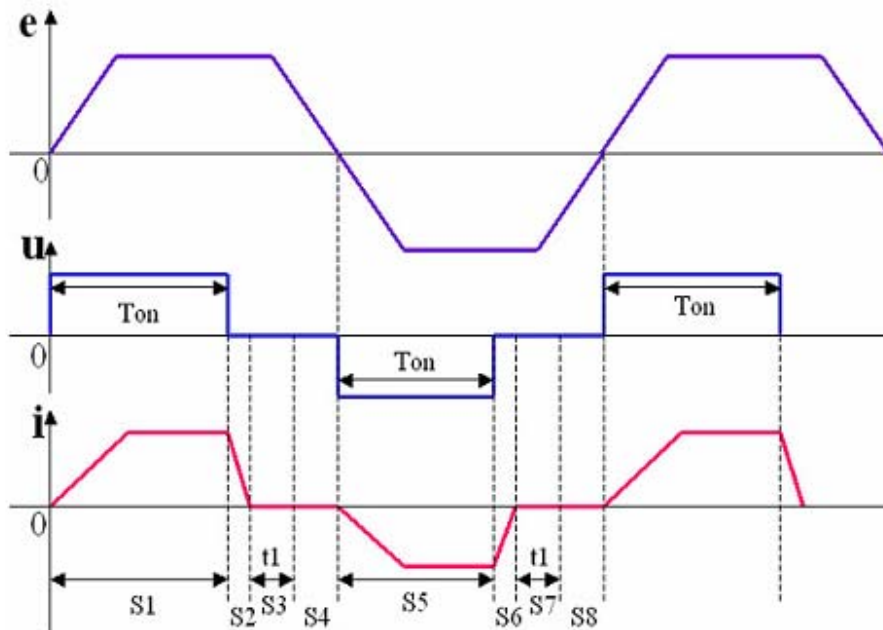


Figure 27. The ideal waveforms of $e(t)$, $u(t)$ and $i(t)$ for winding time-sharing method sensorless control

Since the cost of microcontrollers has decreased, and many BLDC motors applications start using microcontrollers in their products, a class of intelligent variable speed control BLDC motor control system can become widely used even for low power applications. Considering the above, it seems more and more convenient to include also the sensorless control feature.

Since both of the above mentioned sensorless control methods have their drawbacks like high torque pulsations and no possibility to reduce them by current shaping, the estimator based sensorless control can be used in order to obtain a better performance

1.5 Conclusions

The field of fractional horsepower applications presents an important part from total energy consume over the world. The literature overview was done and it rendered that, in spite of their small power, the mass production of fractional horsepower motors (which usually have not a very high efficiency) makes them a not negligible at all energy consumers.

The main motor types that currently apply on low power applications were reviewed and their drawbacks were outlined.

A short overview over the PM synchronous motor is done and the advantages given by the introduction of such motors in variable speed drives and not only are presented and illustrated by literature examples.

The single phase PM brushless dc motor is an important candidate for low cost applications. A simplified theoretical approach of this type of motor is presented and an overview over the main low cost single phase PM motors topologies is done further.

The power electronics converter topologies and their control for torque production are presented and then the main sensorless control methods, existing in the literature, for a single phase PM BLDC motor were pointed out.

References

- [1] T.Kubo, H. Sachs, S. Nadel, "Opportunities for new appliance and equipment efficiency standards: energy and economics savings beyond current standards programs", ACEEE-A016, Washington, D.C.:American Council for an Energy-Efficient Economy.
- [2] Electric Power Research Institute. 1992. "Electric Motors: Markets, Trends, and Applications", TR-100423. Palo Alto, Calif.: Electric Power Research Institute.
- [3] "Electricity Overview", <http://www.pewclimate.org/technology/overview/electricity>.
- [4] Arthur D. Little, "Opportunities for Energy Savings in the Residential and Commercial Sectors with High-Efficiency Electric Motors", Washington, D.C.: Arthur D. Little, Inc.1999.
- [5] T.J.E. Miller, "SPEED's electric motors", University of Glasgow, 2002
- [6] H. Kragh, "Modelling, Analysis and Optimization of Power Electronics Circuits for Low Cost Drives", PH. D. Thesis, Aalborg University, 2000
- [7] B. M. Gordon, R. A. McMahon, "Comparison of Two Low Cost Small Induction Motor Drive Configurations", Record of EPE - 1997, Trondheim,Vol. 3, pp. 724 - 729
- [8] D. Iles-Klumpner, "Automotive Permanent Magnet Brushless Actuation technologies", Ph.D. dissertation, University Politehnica of Timisoara, 2005.
- [9] S.A. Nasar, I. Boldea, L.E. Unnewehr, "Permanent Magnet, Reluctance, and Self-Synchronous Motors", CRC Press, 1993.
- [10] R. Krishnan, "Electric motor drives: Modeling, Analysis and Control", Prentice Hall, 2001.
- [11] T.J.E. Miller, "Brushless Permanent-Magnet and Reluctance Motor Drives", Clarendon Press, Oxford, 1989.
- [12] I. Boldea, S. Nasar, „Electric Drives (2nd ed.)", Boca Raton, FL.:Taylor & Francis (CRC Press), 2005.

- [13] F. Meyer, "Permanent magnet synchronous machines with non-overlapping concentrated windings for low-speed direct-drive applications", Ph.D. dissertation, Royal Institute of Technology, Stockholm, 2008.
- [14] A. Bianchi and L. Buti, "Three-Phase A.C. Motor Drive and Controller for Clothes Washers", in Int. Appliance Technical Conference, available on www.appliancemagazine.com, 2003.
- [15] LG Electronics, www.lge.com.
- [16] J.H. Choi, I.S. Jung, J. Hur, H.G. Sung, B.K. Lee, "On the feasibility of the brushless DC (BLDC) motor and controller for 42V automotive cooling fan system", Proc. Of Electric Machine and Drives Conference, May 2007, pp.1349-1354.
- [17] R. Krishnan, "PM brushless DC motor drive with a new power-converter topology", Transactions on Industry Applications, vol. 33, No.4, July/August 1997, pp.973-982.
- [18] E.C. Protas "Energy saving by means of a new drive conception", Proceedings of International Aegean Conference on Electrical Machines and Power Electronics (ACEMP 95), 5-7 June 1995, Kusadasi (Turkey), pp. 303-308.
- [19] Vlado Ostovic "Performance comparison of U-Core and round-stator single-phase permanent-magnet motors for pump applications", IEEE Transactions on Industry Applications, Volume 38, Issue 2, Mar/Apr 2002 Page(s):476 – 482.
- [20] T. Kenjo, S. Nagamori, "Permanent magnet and brushless DC motors", Clarendon Press, Oxford, 1985.
- [21] J.F. Gearas, M. Wing, "Permanent magnet motor technology", Marcel Dekker, Inc., New York, 2002.
- [22] W. H. Yeadon, A. W. Yeadon "Handbook of small electric motors", McGraw Hill, 2001.
- [23] D.M. Ionel, B. Branecky, A.E. Lesak, "Electrical machine and method of manufacturing the same", US Patent 6,975,049, Dec. 2005.
- [24] D. Ionel, "High-efficiency variable-speed electric motor drive technologies for energy savings in the US residential sector", in Proc. 12th Int. Conf. on Optimization of Electrical and Electronics Equipment, Brasov., Romania, May. 20-22, 2010, pp. 1403-1413.
- [25] M. adriollo, M. De Bortoli, G. martinelli, A. Morini, A. Tortella, "Performance Assessment of a Single-Phase PM Synchronous Motor for Small Fan Appliances", Proc. of international Conference on Electrical Machines, sept. 2008, pp. 1-6.
- [26] Ernest A. Mendrela, Mariusz Jagiela, "Analysis of Torque Developed in Axial Flux, Single-Phase Brushless DC Motor With Salient-Pole Stator" IEEE Transactions on Energy Conversion, Vol. 19, no. 2, June 2004, pp.271-277.
- [27] D.R. Huang, T.F. Ying, L.T. Kuo, S.J. Wang, H.C. Huang, C.Y. Huang, "A single phase spindle motor design for DVD applications", Journal Mater. Sci. Technol., vol.16, no2, 2000, pp 251-255.
- [28] Min-Fu Hsieh, Mi-Ching Tsai, Alex Horng, "An Efficient Approach for Cogging Torque Analysis of Motors with Three-Dimensional Flux Distribution" Trans. On Magnetics, Oct. 2006, Issue 10, pp. 3464-3466.
- [29] A. Reinap, "Design of Powder Core Motors", Ph.D. Dissertation, Lund University, 2004.
- [30] R. P. Deodhar, S. Andersson, I. Boldea, T. J. E. Miller, "The Flux-Reversal Machine: A New Brushless Doubly-Salient Permanent-Magnet Machine", Trans. On Industry Applications, vol. 33, no. 4, July/August 1997, pp. 925-934.

32 1. Fractional horsepower applications

- [31] K. B. Jang, S. H. Won, T. H. Kim, Ju Lee, "Starting and High-Speed Driving of Single-Phase Flux-Reversal Motor for Vacuum Cleaner", *Trans on Magnetics*, vol. 41, no. 10, Oct. 2005, pp. 3967-3969.
- [32] S. H. Won , T. H. Kim, K. B. Jang, S.K. Choi, W.S. Oh , Ju Lee, "Effect of design variables on starting torque of single phase flux-reversal machine", *Journal of Applied Physics*, 1999.
- [33] Y. Chen, S. Chen, Z.Q. Zhu, D. Howe, Y.Y. Ye, " Starting torque of single-phase flux-switching permanent magnet motors", *Trans. On Magnetics*, Oct 2006, vol.42, Issue 10, pp. 3416 – 3418.
- [34] Yi Cheng , Charles Pollock, Helen Pollock, "A Permanent Magnet Flux Switching Motor For Low Energy Axial Fans", *Record of Industry Applications Conference*, Oct. 2005, vol.3, pp. 2168 – 2175.
- [35] T.C. Lun, "Microcontroller for Variable Speed BLDC Fan Control System", *Freescale Semiconductor, Inc.*
- [36] G. Iliescu, L. Tutelea, I. Boldea, "Performance of a Single-Phase Self-Starting PM Brushless Motor Fed by a Chopper-Controlled Current-Source Thyristor Inverter", *record of OPTIM-2006*, Vol.2, May 2006, pp.85-90.
- [37] "AVR440: Sensorless Control of Two-Phase Brushless DC Motor", *Atmel, Application note.*
- [38] M. M. Radulescu, Z. Biro, C. M. Pop, "Two - Phase Electronically - Commutated PM Small Motor Without Position Sensor", *Record of ELECTROMOTION - 1999*, Patras, Greece, Vol. 2, pp. 529 – 532
- [39] Weizi Wang Zhigan Wu Wanbing Jin Jianping Ying "Sensorless control technology for single phase BLDCM based on the winding time-sharing method", *record of Industrial Electronics Society*, Nov 2005, pp. 1732-1736.
- [40] C. Tsung Lin, Chung-Wen Hung, Chin won Liu, "Sensorless control for four switch three phase BLDC motor drives", *Trans. On Industrial Applications*,

2. SINGLE PHASE PM-BLDC MOTOR:IN-DEPTH CHARACTERIZATION BY FEM ANALYSIS AND EXPERIMENTS

Abstract

For accurately solving original problems containing partial differential equations or integral equations an effective computer program based on the finite element method (FEM) is a useful tool. For the electromagnetic design of electrical machines the finite element analysis can be considered to be a well-established design method. Due to the various nonclassical motor topologies design that applies in low power applications the FEM analysis is a necessary step due to the existing difficulties in finding a unified analytical approach.

In this chapter, a detailed electromagnetic analysis is done and parameters such as phase inductance, back emf, cogging torque and total torque with respect to rotor position are obtained by Finite Element Method (FEM). To verify this analysis, the obtained parameters are compared with experimental measurements.

The comprehensive approach by FEM analysis and experimental measurements has the scope to deliver machine parameters necessary for further simulations and control tasks.

Also, the FEM software can become a necessary tool in the process of designing a sensorless drive for low power applications, from the electromagnetic design to the final sensorless drive, given the strong connection between the motor design, power electronic converter and the adopted sensorless control. It can be used for mass production drives where it could lead to an overall cost decrease, or even for customized applications where the FEM analysis is a very good tool for an in-depth understanding of the machine behavior.

2.1 Introduction

Finite element analysis, in general, provides more accurate results than the analytical magnetic equivalent circuit approach because it considers a large number of flux paths compared to the magnetic equivalent circuit method.

By using the FEM any PM motors of any geometry and materials can be analysed with no need to analytically calculate reluctances, leakage factors or the operating point on the recoil line. But to understand and use FEM software tools efficiently the user must have the fundamental knowledge of electromagnetic field theory [1].

A four pole single phase BLDC motor with PM outer rotor, and salient stator poles with concentrated windings is chosen for FEM analysis and then for sensorless control implementation.

As presented in Chapter 1, one of the peculiarities of single phase PMSM is the fact that it requires a solution for self starting in order to eliminate the dead

points where the net torque is zero and thus the motor is unable to start. Some solutions are presented in [2].

For the analyzed motor the adopted solution is the tapered airgap which creates a variable reluctance under each pole that introduces a reluctance torque component which assists the interaction torque and results in a net unidirectional total torque, irrespective of rotor position. Also, using this solution for selfstarting will result in a smoother cogging torque waveform than other common structures [2].

Fig. 1 illustrates the described geometry

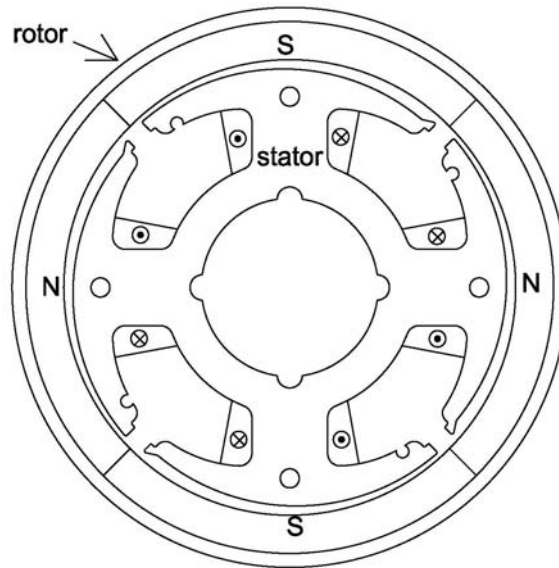


Figure 1 Analyzed BLDC motor geometry

Table 1 contains the main motor geometrical dimensions.

TABLE I
Motor Dimensions

Stator diameter	35 mm
Stator axial length	10mm
PM thickness	3mm
Exterior rotor diameter	40mm
Rotor axial length	17mm
Maximum air gap value	1 mm
Minimum air gap value	0.4 mm

2.2 FE analysis

The software used to realize electromagnetic finite element analysis is FEMM 4.2. It consist in a suite of programs which helps solving electromagnetic problems on two-dimensional planar and axisymmetrical domains.

The first step in preparing the FEA is to develop the machine model to accurately reflect the analysed real machine in terms of geometry, materials, magnet properties, and electrical current in the stator slots. Once the geometry is precisely defined, it is meshed as shown in Fig. 2 to permit the integration calculations of the elements.

Figure 2 presents a 2D cross section of the motor geometry with materials and circuits definition and Dirichlet's defined boundary condition. This conditions implies that the nodes at the boundary are constrained with a fixed potential value, usually zero. This means that there is no leakage flux beyond the analysis area.

Whenever a mesh is generated, it is important to consider the requirements of the different regions. A fine mesh in the regions around the airgap is required:

- The part of the rotor nearest to the airgap (including the magnet).
- The stator teeth
- The airgap: A fine mesh in and around the airgap will produce higher accuracy on the force and torque computation.

The automatic mesh generator usually produces an adequate mesh in terms of quality, accuracy and size. However it is better to adjust and control the density of the mesh with a specific mesh generator.

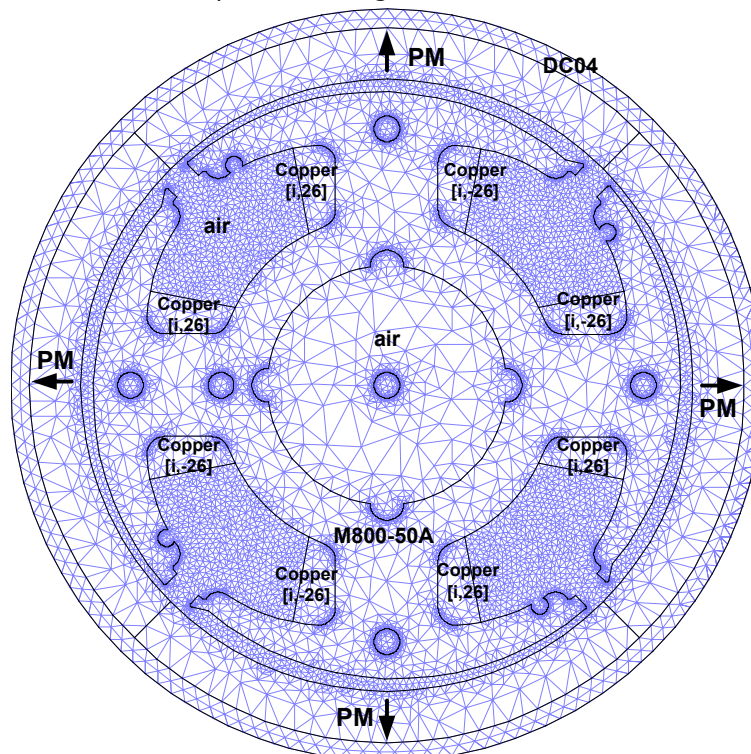


Figure 2. FE model with materials and circuit definition

For an accurate analysis of electromagnetic field, a mesh containing 30215 nodes was elaborated in order to have at least 4 layers under the stator pole region where the airgap is minim.

In the presented two dimensional model shown in Figure 2, the winded coil is modeled as two separated rectangles, and current density is applied as opposite directions.

2.2.1 Materials selection

With regard to the material selection, for PM materials, barium and strontium ferrites are broadly used in fractional horsepower motors. Ferrite magnets are widely used, even though they have low remanence, coercivity, and power product due to the following aspects:

- very cheap compared to rare-earth material magnets and Alnico,
- ferrite magnets are electrically non conducting so eddy current losses are therefore much less of a problem in ferrites, and this is the fundamental reason why they are used in higher frequency applications
- are easy to manipulate and are easy to magnetize; is popular for use in complex shapes because is composed of fine particles made from iron oxide, Fe_2O_3 , with barium (Br) or Strontium (Sr)
- not affected by corrosion
- ferrite magnets are less dependent on the change of temperature[1][3]

The magnet has a practically linear demagnetization curve with a low remanence and coercive force.

The main disadvantage is that using this type of magnet it result in higher motor volume and weight.

The choice of magnetic material depends on the physical properties of material, the application conditions, the price but also on the required shape, magnetization and dimensions.

In order to maintain the low cost, ferrite magnets with remanent flux density of 0.24 T and the recoil permeability off 1.06 are used for the FEM characterized motor. Figure 3 shows the demagnetization characteristic of the used ferrite.

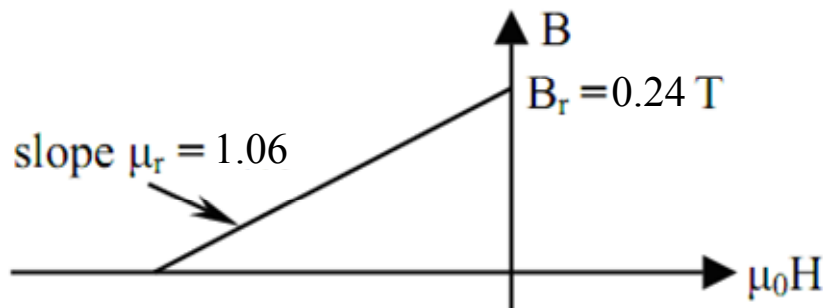


Figure 3. Demagnetization characteristic of the PM

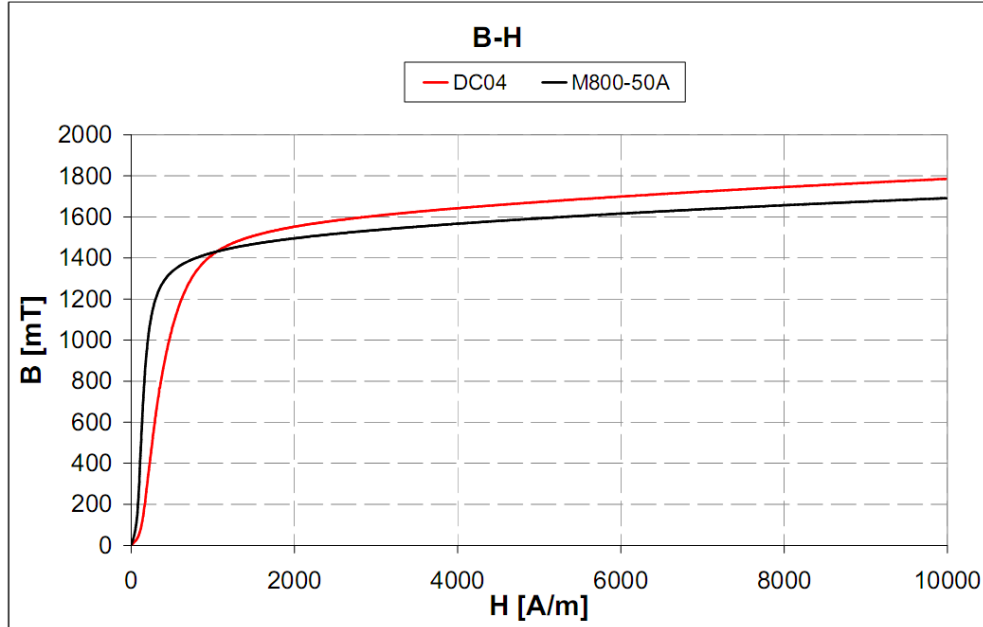


Figure 4. B-H magnetization curve of the used soft magnetic materials

The rotor and stator yoke, which are typically made of steel, are modeled with a nonlinear magnetization curve. For the soft magnetic materials, the M800-50A laminated steel is used for the stator and DC04 solid steel for the rotor and their magnetization curve is illustrated in figure 4.

2.2.2 Field distribution

The accurate knowledge of the magnetic field distribution is very important for predicting motor's parameters such as cogging torque, back emf and self inductance.

The magnet shape has always been recognized as an important factor, but the magnetization direction of the motor is equally important. The variation of the magnetization within a magnet is being considered and analyzed in [4]-[6]. In all these analytical approaches the tangential component of magnetization was neglected and the authors concentrated only on radial component.

In practice, the tangential component of magnetization is almost unavoidable [7] and has to be taken into account in the design process.

In [8] both the radial and tangential components of magnetization are considered in the analysis of the PM field within a 3 phase brushless dc. motor. The effect of the magnetization orientation in single phase PMSMs is referred to in [2] and [9].

The relation between field vectors B and H in a permanent magnet is given in (1):

$$\vec{B} = \mu_0 \mu_r \vec{H} + \mu_0 \vec{M} \quad (1)$$

For linear demagnetization characteristic of PM, the amplitude of magnetization vector M is:

$$M = \frac{B_r}{\mu_0} \quad (2)$$

and its orientation depends on the amplitudes of radial and tangential components, in polar coordinates:

$$\vec{M} = M_r \cdot \vec{r} + M_\theta \cdot \vec{\theta} \quad (3)$$

In this chapter, in the finite element characterization of the presented geometry the influence of the magnetization direction at pole transition was noticed.

First ideal radial magnetization was considered but, since both the cogging torque and bemf were affected by the magnetization direction, a closer to reality magnetization pattern was found by using the trial and error method. By repetitive comparisons between the measured and the finite element computed cogging torque, the magnetization direction was changed in the FEM model. Figure 5 presents the actual magnetization from FEM.

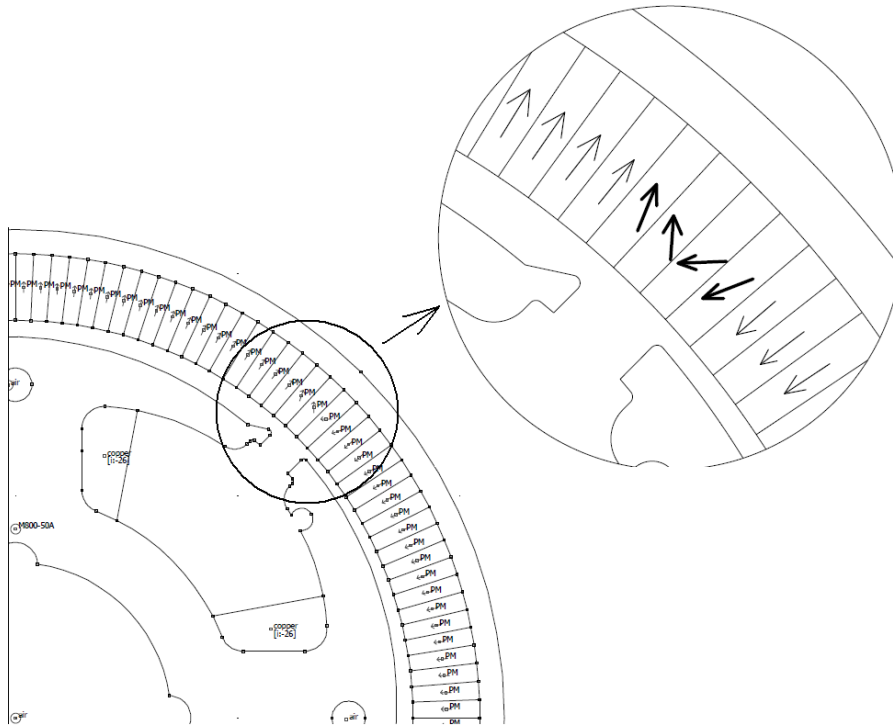


Figure 5. FE model with actual magnetization orientation

The four magnets were divided in 40 equal pieces. The difference from the ideal radial magnetization is that at the ends of each magnet a tangential component for the magnetization vector was inserted.

Since obtaining the correct value of flux density and magnetic field remains an important issue for designing an electric machine which is hardly accomplished by analytical means, the field distribution at no load and under load is the first step in a FE analysis and is important for checking the saturation of flux density in each part of the machine.

First a comparison between the ideal radial magnetization and the practical determined magnetization pattern is done with regard to the field distribution and flux density map at no load.

Figure 6 and 7 presents the field distribution and the saturation level for the ideal radial magnetization at no load while figure 8 and 9 illustrates the same things for the modified magnetization pattern.

The difference in the field distribution is noticed at the region where the permanent magnet is changing the polarity.

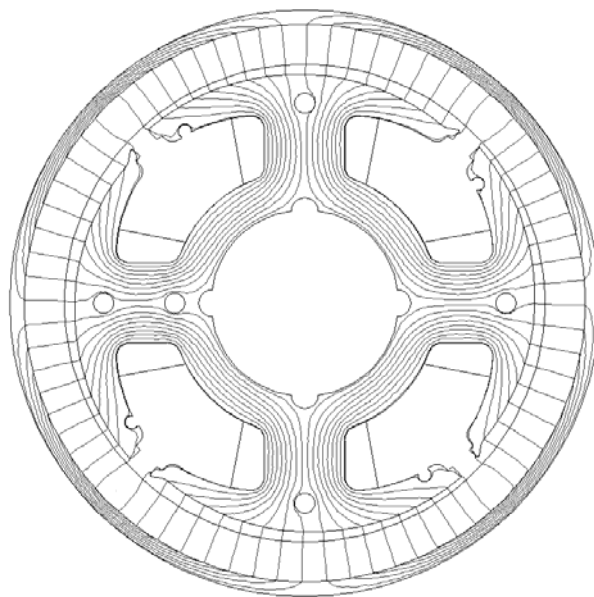


Figure 6. Field distribution for ideal radial magnetization (no load)

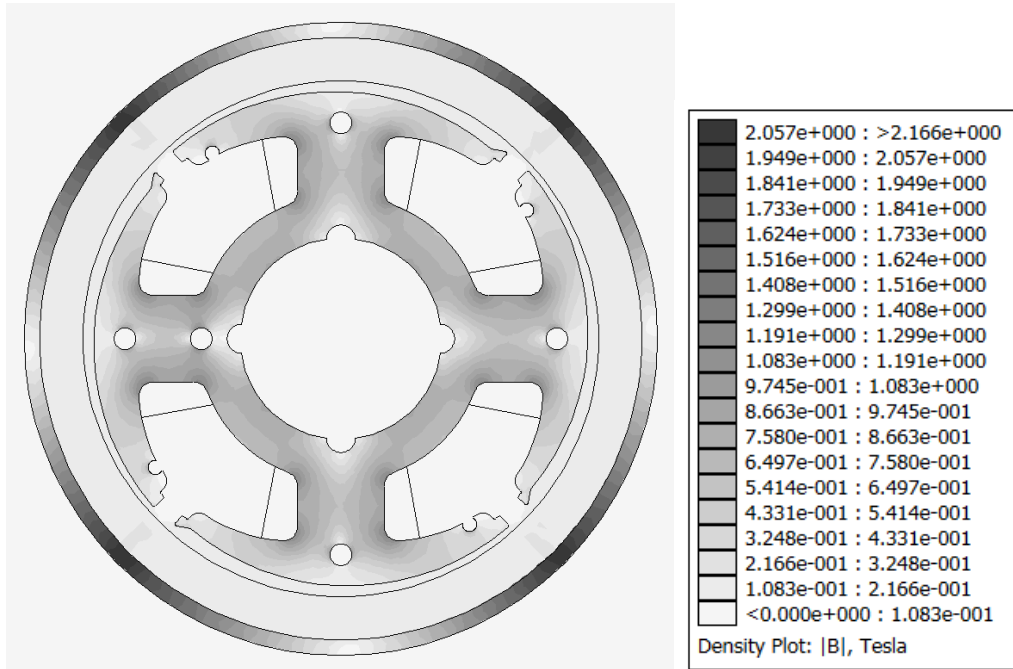


Figure 7. Flux density for ideal radial magnetization (no load)

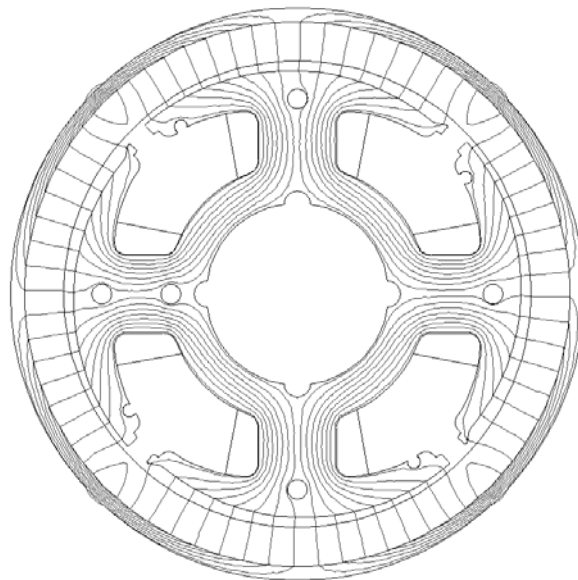


Figure 8. Field distribution for the aligned rotor position (no load) considering the tangential component in the magnetization pattern

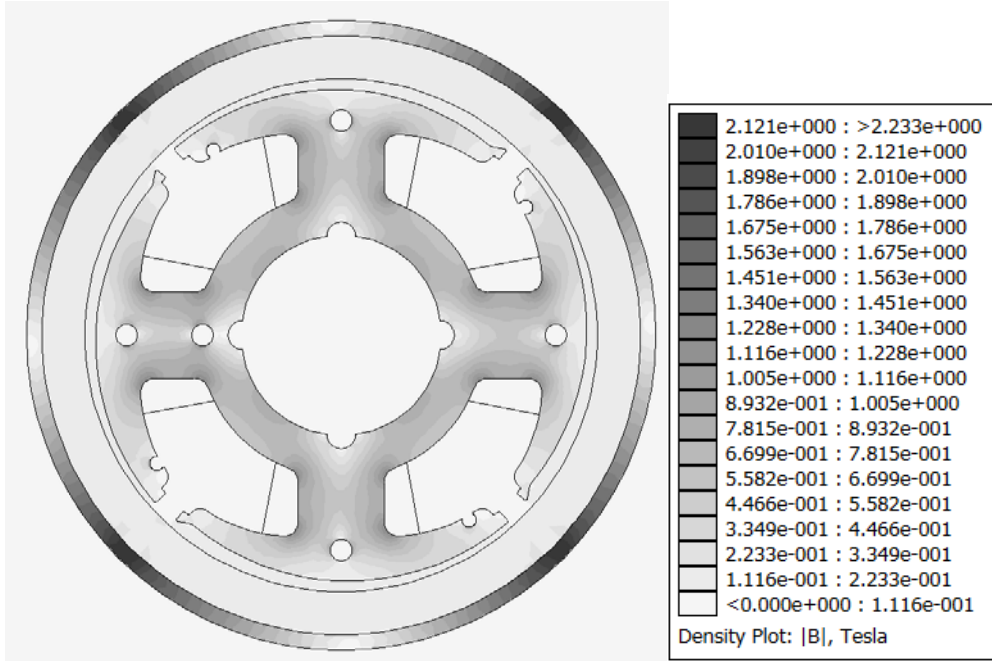


Figure 9. Flux density distribution for the aligned rotor position (no load) considering the tangential component in the magnetization pattern

Figure 10 illustrates the effect of this change on flux density distribution under the rotor's poles.

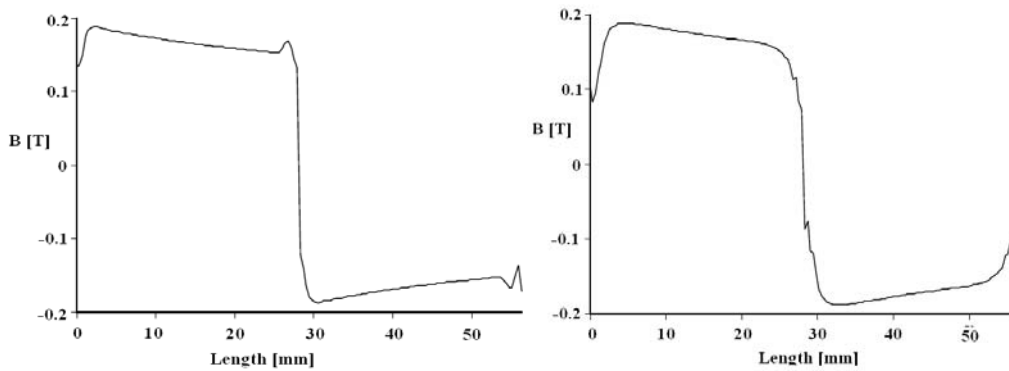


Figure 10. Airgap PM flux density distribution under two stator poles for: a) radial magnetization, b) modified magnetization pattern

It will be shown in the next section how this small difference can influence the cogging torque shape.

To show how the position of the rotor with respect to the stator influences the magnetic flux density distribution in the motor, the field distribution and saturation level were computed for two rotor positions for both no load and 2A load conditions and are presented in parallel. The considered positions are the detent position and the 90 electrical degrees displacement position.

The considered magnetization is the one presented in figure 3, which gives the better correspondence between calculated and measured parameters, as will be shown in the next sections.

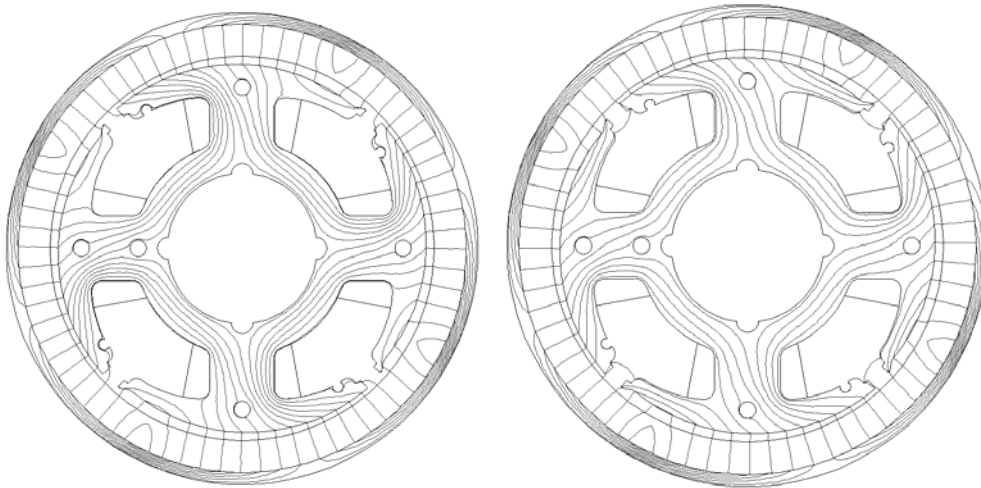


Figure 11. Field distribution at detent position (no load, radial magn) and (load 2 A, radial)

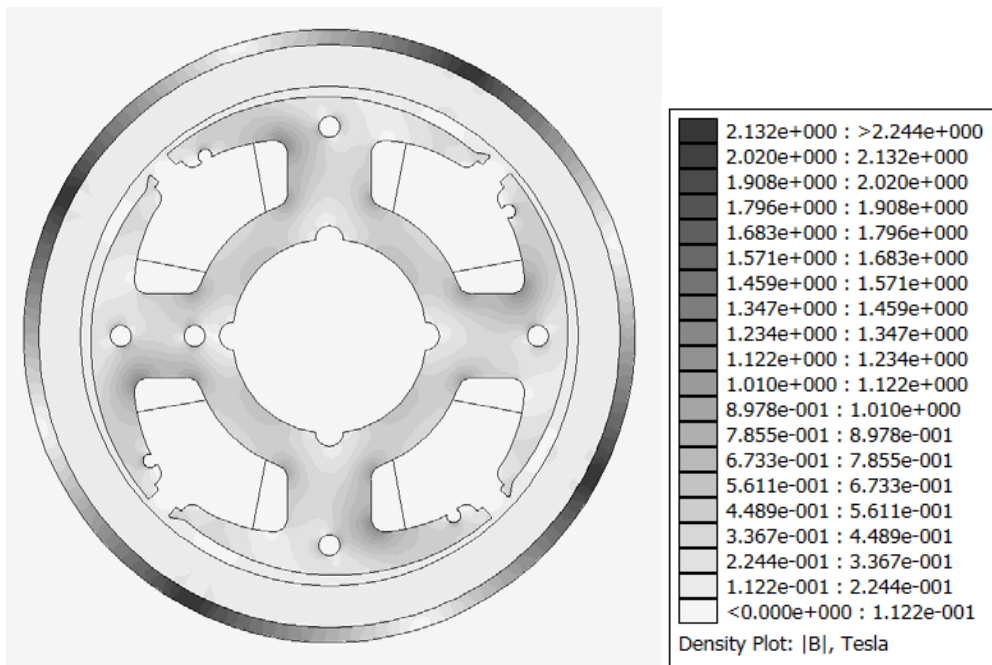


Figure 12. Flux density at detent position (no load)

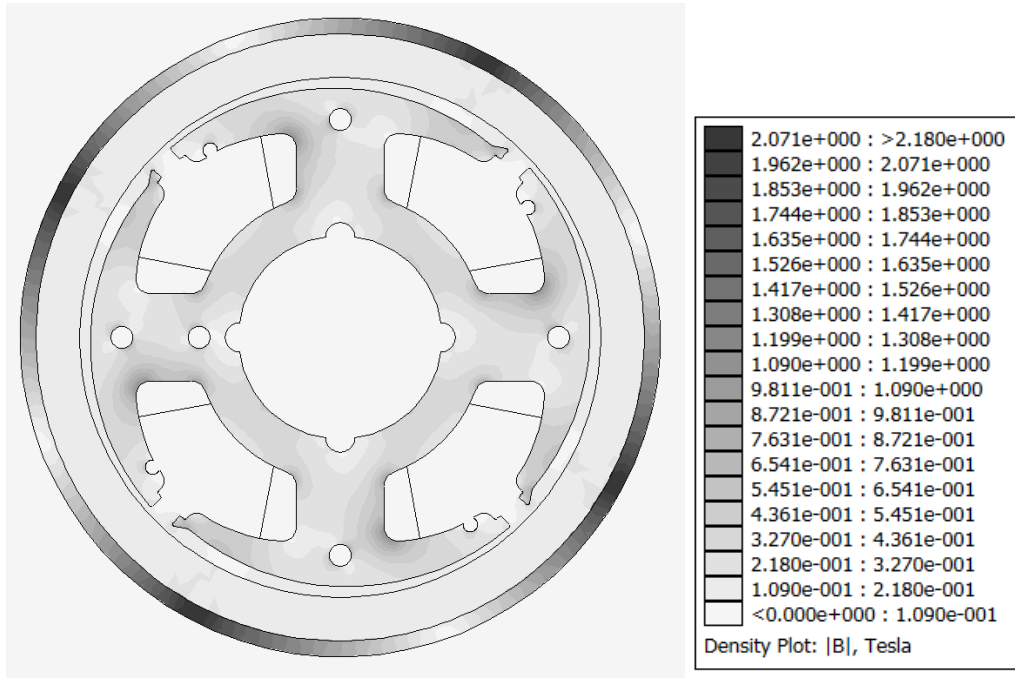


Figure 13. Flux density at detent position (2A load)

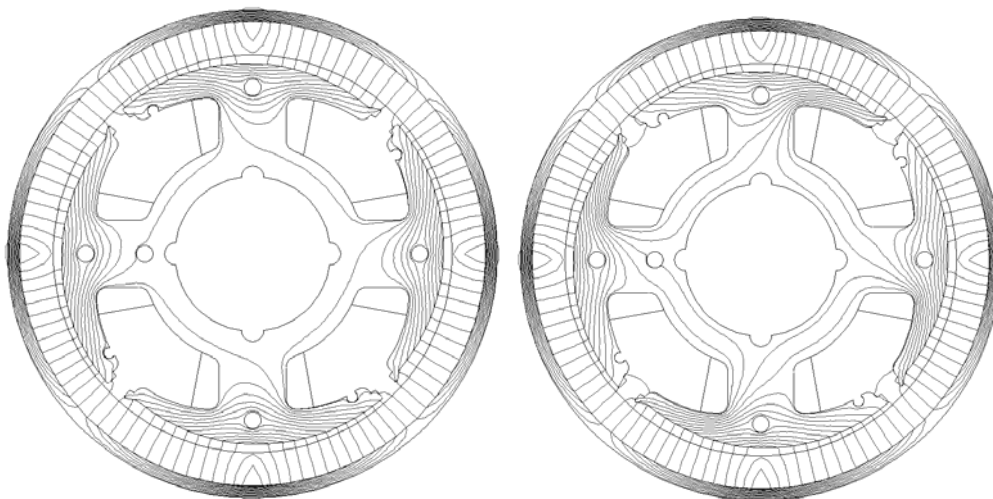


Figure 14. Field distribution at 90 el degrees (no load) and Field distribution at 90 el degree (load 2 A)

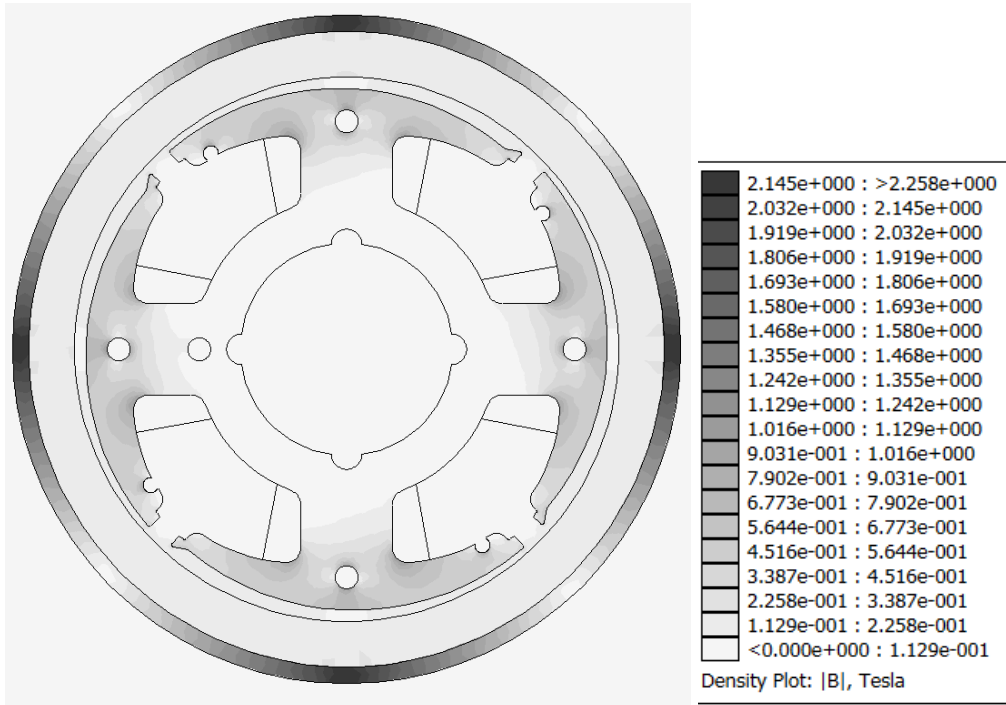


Figure 15. Flux density at 90 el degree (no load)

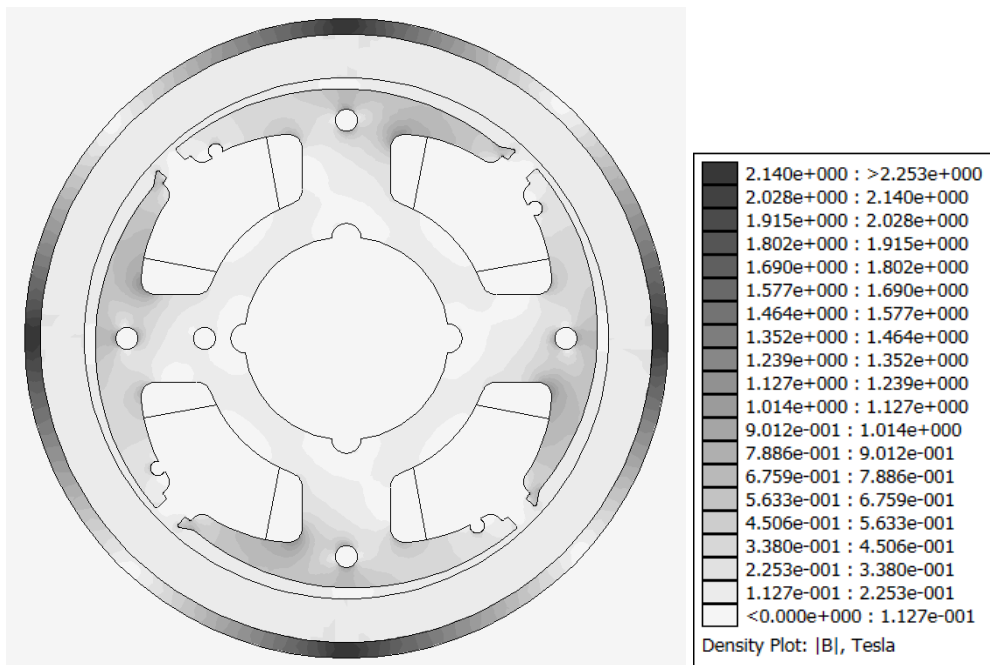


Figure 16. Flux density at 90 el degree (load)

2.3 No load flux linkage and BEMF

To go deeper into the analysis and prediction of the motor constant, more must be known about the exact shape of the back EMF, which depends on the flux distribution. The real bmf is unlikely to be a pure rectangular shape as it is usually used in motor modelling.

There are many factors that influence the shape of the back EMF, such as magnet geometry, spacing, fringe effects, steel geometry and materials properties. For the special case of single phase motor, in [10],[11] it was shown by FE results how the bmf is affected by the asymmetric stator structure. Also, in [12], for the motor with tapered airgap, as the one used here, it was proved that the larger the g_{max}/g_{min} is the more different then a rectangular shape the bmf is.

The no load flux linkage versus mechanical rotor position is presented in figure 17.

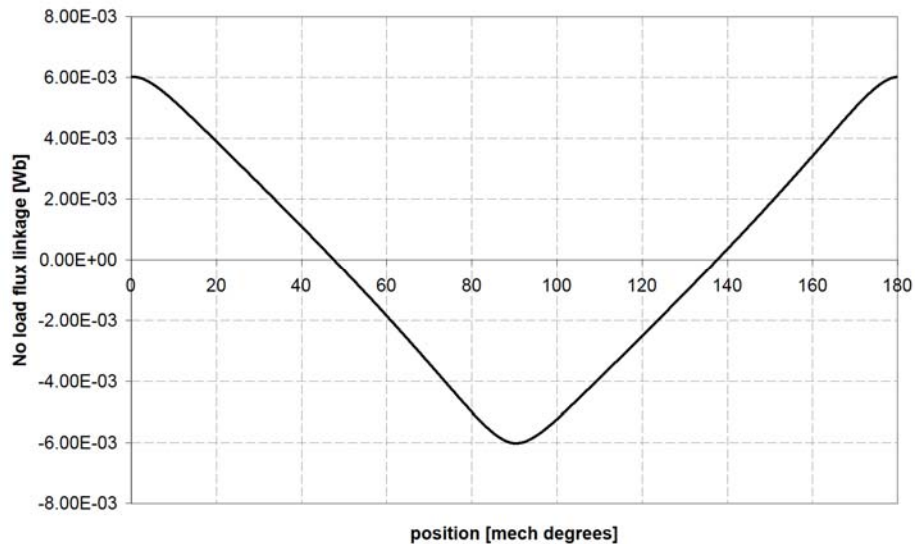


Figure 17. No load flux linkage vs position

The no load flux linkage is determined based on eq ()::

$$\Psi = 2 \cdot p \cdot N_c \cdot \int_S B \cdot ds \quad (4)$$

which based on planer symmetry it is reduced to a line integral in the used software:

$$\Psi = 2 \cdot p \cdot N_c \cdot L_{stack} \cdot \int_l B \cdot dl \quad (5)$$

Where N_c - number of turns per coil, p - number of pole pairs, Ψ - flux density, L_{stack} - the axial length of the motor.

The bmf shape is important for knowing the type of supplied current in order to obtain low torque ripple.

Based on machine voltage equation (6), we obtain the back emf voltage for zero current in the coils.

$$U = R \cdot i + \frac{d(L \cdot i)}{dt} + E \quad (6)$$

The back emf voltage is calculated by using the finite element method to calculate the magnetic flux linkage in the stator phase coils at zero current. The waveform of the back emf can be obtained from the time derivative of the so obtained flux linkage waveform.

The back emf relation is:

$$E = -\frac{d\Psi}{dt} = -\frac{d\Psi}{d\theta} \cdot \frac{d\theta}{dt} \quad (7)$$

$$\frac{d\theta}{dt} = \omega \quad (8)$$

$$\Psi = n_s \cdot N_c \cdot \Phi_{PM} \Rightarrow E = -n_s \cdot N_c \cdot \omega \cdot \frac{\Delta\Phi_{PM}}{\Delta\theta} \quad (9)$$

where n_s -number of slots and N_c -number of coils / pole

The variation of flux is obtained with

$$\frac{\Delta\Phi}{\Delta\theta} = \frac{\Phi_j - \Phi_{j-1}}{\theta_j - \theta_{j-1}} \quad (10)$$

So we denote k_e by:

$$k_e = -n_s \cdot N_c \cdot \frac{\Phi_j - \Phi_{j-1}}{(\theta_j - \theta_{j-1}) \cdot \pi / 180} \quad (11)$$

$$\Rightarrow E = k_e \cdot \omega \quad (12)$$

The FEM calculated and measured bmf coefficient, k_e , variation with position is shown in Fig. 18.

Figure 18 also illustrates how the modified magnetization pattern affects the bmf waveform.

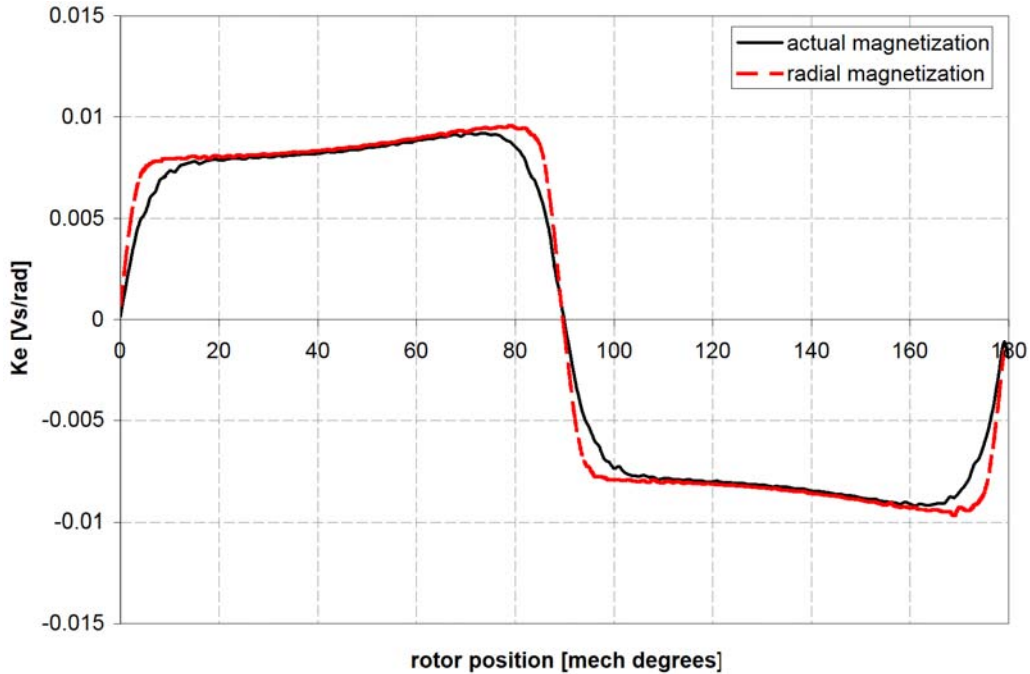


Figure 18. BEMF shape vs. position

2.4 Phase inductance

The inductance is computed using (13), by setting a constant value in the winding and evaluating the flux linkage. For the inductance computation by FEM, the PM residual flux density is replaced with 0 and we keep the recoil permeability to 1.06 P.U. The inductance is calculated as ratio of the flux and current.

$$L = \frac{\Psi}{i} \quad (13)$$

where Ψ - flux linkage, and i - phase current.

The obtained inductance value from FEM using the described method is $L=0.54$ [mH] and it is constant with rotor angle due to no salient rotor poles.

Due to the fact that the PMs affect the electromagnetic field distribution and the flux linkage, the inductance variation with rotor position is also computed by using finite element method which takes this phenomenon into consideration.

Setting a constant current value in the winding and moving the rotor in successive positions from 0 to 180 degrees with an increment of 1 degree, the inductance is calculated using equation (14). The flux linkage produced only by the currents is obtained by subtracting the no load flux linkage from the measured flux with load.

$$L = \frac{(\Phi_{tot} - \Phi_{PM})}{i} \cdot 2 \cdot p \cdot N \quad (14)$$

where Φ_{tot} -the flux produced by both the current in the winding and by the permanent magnets; Φ_{PM} - magnetic flux produced by PM at zero current value;

Figure 19 shows the obtained inductance versus position from FEM calculation. Although the maximum value corresponds with the one obtained from the frozen permeability method, a slight inductance variation with rotor angle is noticed here. This variation can be explained as a slightly saturation effect in the aligned position, caused by the corroboration of permanent magnet and excitation fields.

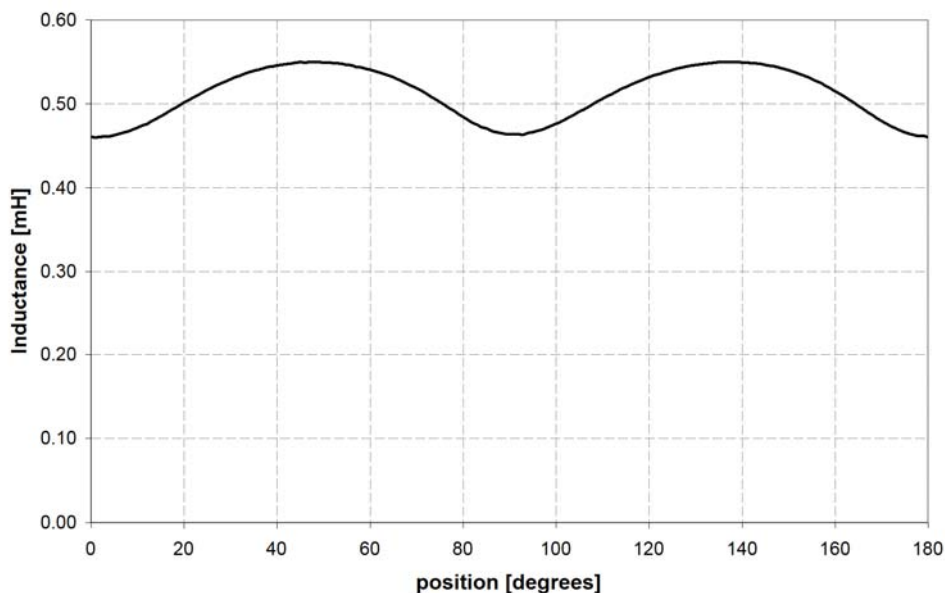


Figure 19. Self inductance versus rotor position

2.5 Cogging torque and total torque analysis

The cogging torque is a particularity of PM motors and is a very challenging problem. Cogging torque is produced by the interaction between the permanent magnets of the rotor and the stator slots at no load [13].

In most brushless permanent magnet motors, this torque is undesirable because it causes additional losses, vibrations and torque oscillations. Comparing with the case of three phase PMSM where torque ripple minimization is an important issue in the motor design, in the field of single phase PMSM another point of view over this torque has to be considered. On the contrary, here the existence of the cogging torque (also called detent torque) for self-starting is an essential characteristic.

The cogging torque is used to assure the starting position of the rotor in which the axis of symmetry of the rotor and the stator magnetic field do not overlap. In this position there is a space shift between the rotor and the stator field which generates torque when current flows through windings.

Here cogging torque cannot always be minimized, it has to be small and in the same time it has to be strong enough to assure the rotor parking in the detent position. In fact the ideal shape of the cogging torque should be as the one given in figure 20.

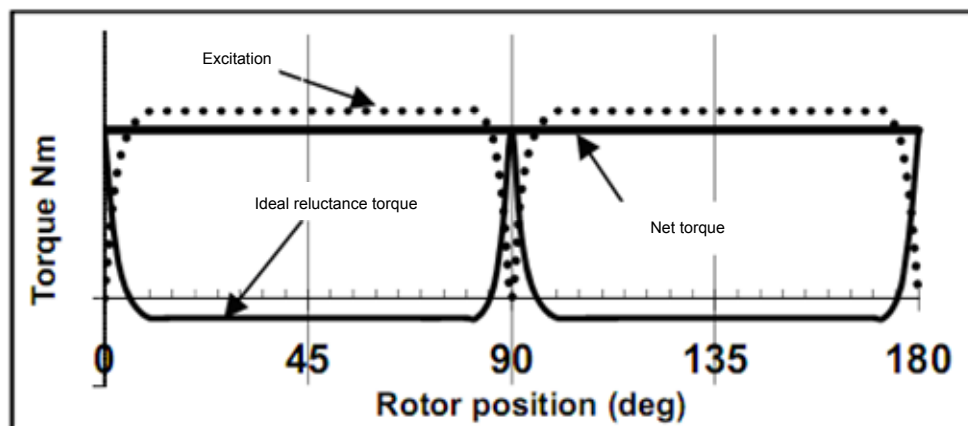


Figure 20. Ideal cogging torque waveform

Considering that the medium value of cogging torque over an eigen period is zero, the shape from figure 10 has sense if we consider the characteristic dead points in the excitation torque which have to be eliminated. So we would like a high as possible positive value and a small and smooth negative value for the cogging torque.

There has been a great research work done regarding the cogging torque in single phase PM motors. In [14]-[16] the impact of different stator pole shapes over the torque was reported. Also, in [17] the improvements of the motor characteristics in cogging torque and torque ripple are proved by the finite element analysis and experimental results for a novel air gap topology which combines the equal and unequal airgaps instead of using only unequal airgaps for all stator poles. The influence of the different solutions for selfstarting on cogging torque, bembf and total torque for a FRM are also reported in [18].

Considering the given interest, we can say that cogging torque is a very challenging problem and a proper calculation is needed for further advanced control tasks.

Although, some analytical approaches to calculate cogging torque are referred to in [19], [20], and the flux-MMF diagram technique is proposed in [10], the more accurate and easy to obtain information is delivered by FEM.

The FEM based computation of cogging torque can be done several ways. The virtual work method [21] and Maxwell stress tensor [4], [22] are the most popular. Also [5] reports a method based on stored energy.

Here, in order to ensure accurate predictions, the cogging torque has been calculated by both Maxwell stress integration and from the rate of change of co-energy.

A short description of the two methods and methodology to apply those is presented in the following paragraphs.

2.5.1 Maxwell stress tensor method

The Maxwell stress tensor method is using the local flux density distribution along a specific integration contour. Using the definition of Maxwell stress tensor, the electromagnetic torque can be determined using equation:

$$T = \int_S \frac{1}{\mu_0} \cdot r \cdot B_n \cdot B_t \cdot ds \quad (15)$$

Based on planar symmetry the use equation in 2D FEA is :

$$T = \frac{L_{stack}}{\mu_0} \cdot \int_l r \cdot B_n \cdot B_t \cdot dl \quad (16)$$

where L_{stack} is the axial motor length, r the distance from the rotation axis to the integration path, B_n and B_t , the normal and tangential components of magnetic density and μ_0 the air permeability.

The accuracy of the results obtained by the Maxwell stress method strongly depends on the model discretization and on the selection of the integration line or contour [1]. The air-gap region requires very careful meshing by using several levels of elements. In order to avoid this drawback an improved Maxwell stress tensor volume integral option available in FEMM software it is used. For this method no special consideration are required, in getting good force or torque results, as opposed to the Stress tensor line integral. Although results tend to be more accurate with finer meshing around the region upon which the force or torque is to be computed[23].

To obtain the cogging torque by using this method is relatively simple and it suppose to move the rotor in successive positions and to compute the Maxwell stress volume integral. No post processing calculation is necessary.

2.5.2 Virtual work method

The virtual work method is based on the principle of conservation of energy or coenergy and the principle of virtual displacement. The magnetic energy and the coenergy are defined in equation (17,18):

$$W = \int_V \left(\int_0^B H \cdot dB \right) \cdot dV \quad (17)$$

$$W' = \int_V \left(\int_0^H B \cdot dH \right) \cdot dV \quad (18)$$

The torque is calculated as the derivative of the stored energy W with respect to a small position displacement at constant flux linkage Φ or as the derivative of the stored coenergy W' with respect to a small position displacement at constant current i .

$$T = \frac{\partial W'(i, \theta)}{\partial \theta} \Big|_{i = \text{const}} = - \frac{\partial W(\Psi, \theta)}{\partial \theta} \Big|_{\Psi = \text{const}} \quad (19)$$

Where W , W' , Ψ and i are the magnetic energy, coenergy, flux linkage and current, respectively[1].

Here, the torque is calculated using the total magnetic coenergy W' of the system when its rotor part is physically displaced. This method is chosen because the constant current condition is more easy to accomplish than the flux linkage constant condition.

To do this the system coenergy is calculated by FEM solver for different displacements of the rotor, keeping the current constant, and then the equation (20) is evaluated using a finite difference approximation.

$$T = \frac{\partial W'(i, \theta)}{\partial \theta} \Big|_{i = \text{const}} = - \frac{\Delta W'}{\Delta \theta} \quad (20)$$

The problem with the finite difference approach is that the most suitable value for angular displacement has to be found using trial and error procedure. If $\Delta \theta$ is too small, rounding-off errors in $\Delta W'$ may appear, because the values of the volume integral of the co-energy are close in two adjacent rotor positions. If $\Delta \theta$ is too large, a less accurate torque information is obtained. Also, when calculating the torque versus position using finite differences the obtained waveform is affected by noise.

To avoid those drawbacks, a curve fitting approach is used to approximate the coenergy variation with rotor position. It is easier to obtain the torque when applying eq 19 to the obtained analytical function $W'=f(\theta)$.

As we can notice, this method has the drawback that it requires a laborious post processing work for obtaining accurate results.

2.5.3 Cogging torque FEM results

Figure 21 shows the numerical results for two periods of cogging torque waveform, by using both the above presented methods for the case of an ideal radial magnetization. It can be noticed that the differences between the obtained results by using both methods were negligible.

The cogging torque period is calculated as:

$$T_{cogg} = \frac{360^{0\text{mech}}}{\text{LCM}(N_p, N_s)} = \frac{360^{0\text{mech}}}{\text{LCM}(4,4)} = \frac{360}{4} = 90^{0\text{mech}} \quad (21)$$

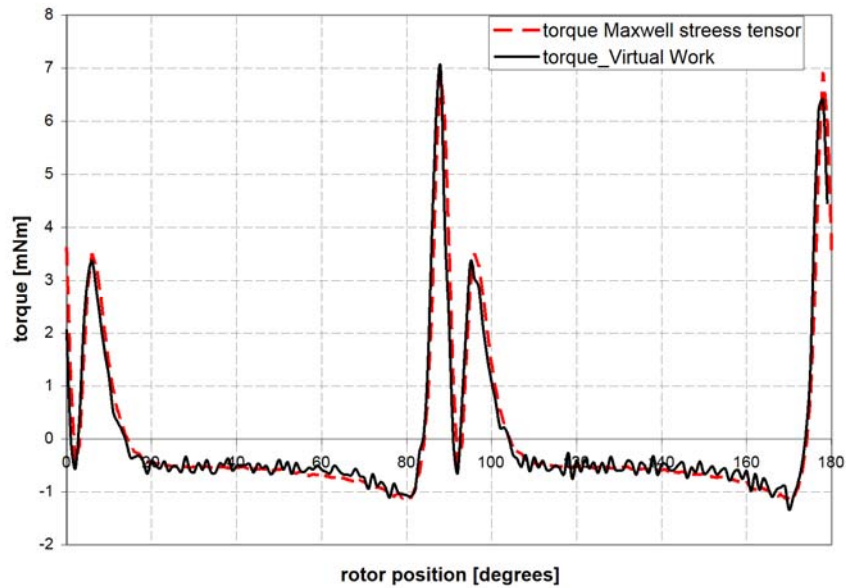


Figure 21. Cogging torque vs. Position (ideal radial magnetization)

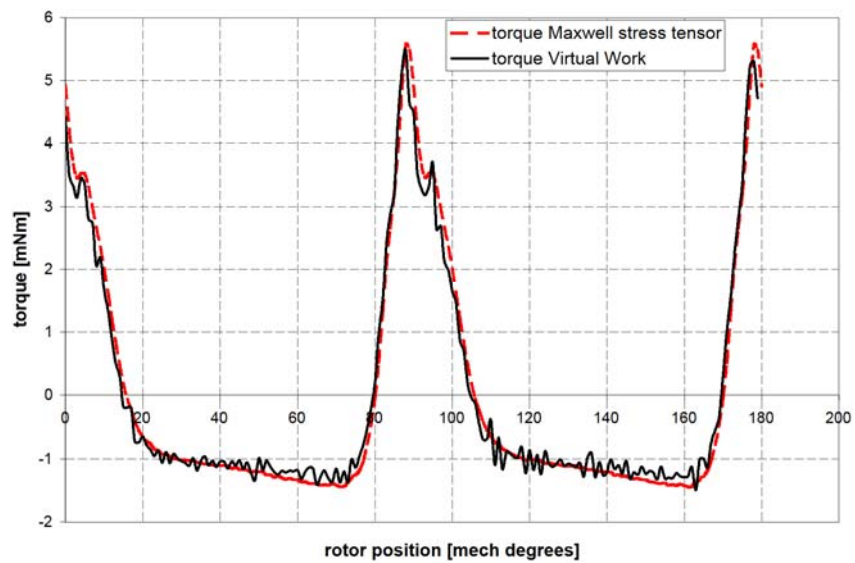


Figure 22. Cogging torque vs. Position (modified magnetization pattern)

The obtained shape for the cogging torque, for a considered ideal radial magnetization has a gap at the approximately 90 mechanical degrees. Because this shape is undesirable, the reason of this gap was searched by using a small parametric variations of the stator geometry around the given CAD motor drawings. By comparing also with the experimental results, the cause was mainly determined

to be the magnetization pattern which is slightly different from the ideal radial magnetization, as shown in figure 5.

The obtained cogging torque waveform after considering the modified magnetization pattern is illustrated in figure 21. Again, a good correspondence between the two obtained waveforms, by using both calculation methods, is visible.

Due to this good agreement between the Maxwell stress tensor and Virtual work methods, only the first one will be used further due to its reduced labor and calculation time.

Figure 23 shows the influence of the magnetization pattern over the cogging torque shape.

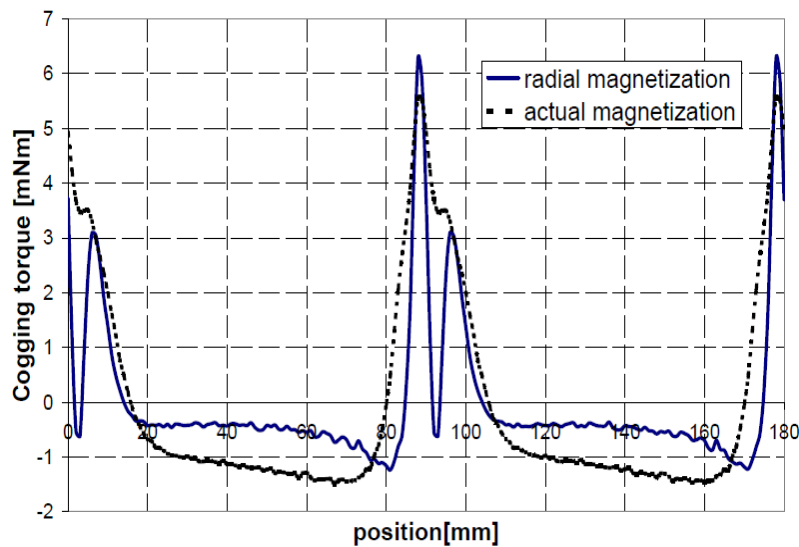


Figure 23. Calculated cogging torque vs rotor position

Since the cogging torque is caused by the airgap magnetic reluctance variation with rotor position it is necessary to mention that the FE analysis was done for an airgap variation given by the max/min airgap equal to 1mm/0.4 mm.

2.6 Electromagnetic torque

The electromagnetic torque appears as the result of the interaction between rotor and stator magnetic fields. Since the distribution of rotor magnetic field and the stator current are both functions of rotor angle, the developed torque will also vary with the relative position between the stator and rotor magnetic fields.

To calculate the produced resultant torque T by the single phase PMSM, using FEM analysis, a constant current value is set in the windings and the same procedure as the one used for cogging torque evaluation applies.

The obtained torque can be written as in equation 22 with respect to the cogging torque and excitation torque components.

$$T = T_{exc} + T_{cogg} \quad (22)$$

$$T_{exc} = K_e \cdot i \quad (23)$$

Figure 24 illustrates the torque components over an electrical period for a constant current of 1 A in the phase winding. The electromagnetic torque produced only by excitation T_{exc} is obtained using equation (22).

It can be noticed that the excitation torque has the same shape as the bmf, as expected from equation (23).

Also, the torque distortions caused by the cogging torque in the resultant torque are visible.

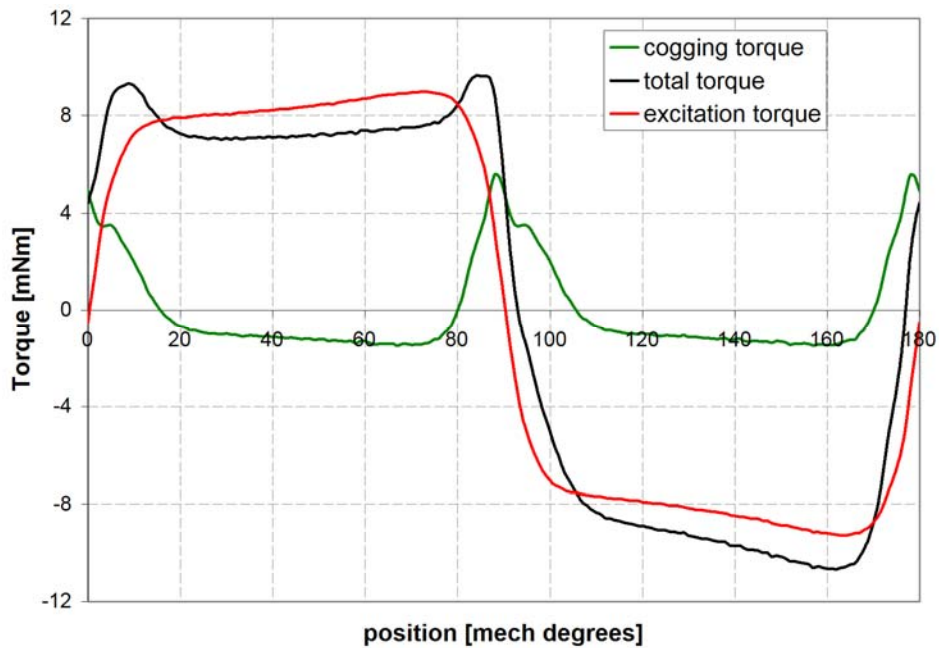


Figure 24. Torque components obtained from FEM at a 1 A constant current value

The cogging torque essential role in removing the dead points from the excitation torque can be noticed in figure 25. Here positive and then negative current values are supplied and the developed torque is evaluated for successive rotor positions using the maxwell stress tensor method.

The cogging torque components develops an approximately 5 mNm which complements the excitation torque at the position where the latter becomes zero (approx. 90 degrees).

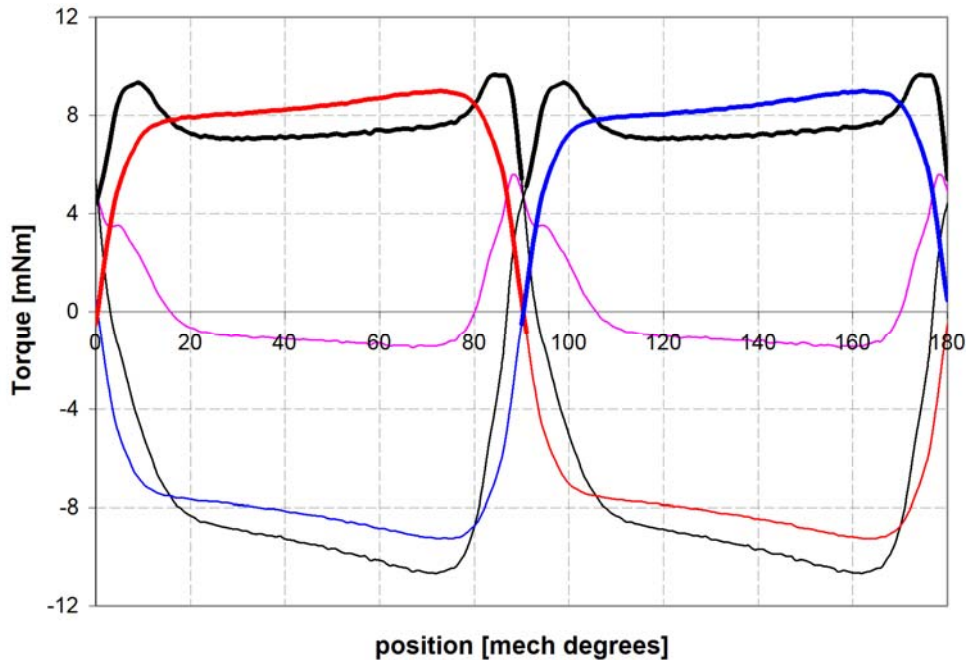


Figure 25. Torque components at positive and negative 1A current value

2.7 Starting torque and torque pulsations analysis

The starting torque represents one of the basic problems of single phase PM-BLDC motors. As presented in Chapter 1 there is no starting torque in case of symmetrical airgap geometry. For the tapered airgap, a modified cogging torque is the intentional result of the stator asymmetry which drives the unexcited motor to a position at which sufficient electromagnetic torque is developed to start the motor when it is energized.

Since the torque vary with rotor angle, for a proper and onest determination of the starting torque the starting position must be specified. For the starting torque analysis done here, the starting position is considered the detent position ($T_{cogg}=0$) at no load. For this case, in order that the cogging torque to be able to put the rotor in the starting position, the load torque should heavily depend on speed.

For this case, it can be easily seen from figure 24 and equation (22) that the starting torque is the developed torque by the excitation current (T_{exc}). Because the excitation torque also varies with position it is obvios that the starting torque will also be dependent on the same factors that influences the cogging torque.

Furter, for an easy understanding of the starting torque evaluation procedure, the stability analysis of the positions where $T_{cogg}=0$ is necessary.

For a symmetric airgap, the positions where the cogging torque is zero corresponds to the positions where the magnet is aligned with the stator pole, respectively at the halfway between two stator poles. When the magnet is aligned with the poles, any small disturbance will cause the magnet to restore in the same position, this is the stable position with $T_{cogg}=0$. Contrary, when the magnet is

halfway between the stator poles, any small disturbance will cause the rotor to move and to leave this position. For uneven airgap those zero cogging torque positions differ and a graphical analysis is done.

In figure 26, considering the point A, if a small disturbance moves the rotor to the right, a negative torque is developed which brings it back. If a small disturbance moves the rotor to the left a positive torque will bring it back to the right. This is the stable position. If we consider the point B, if a small disturbance moves the rotor to the right, a positive torque will cause the rotor to move to the right, if a small disturbance moves the rotor to the left a negative torque will drag it to the left.

The rest position in the cogging torque waveform is defined by :

$$T_{cogg} = 0 \quad (24)$$

$$\frac{dT_{cogg}}{d\theta} < 0 \quad (25)$$

The starting torque is extracted from figure 26, considering the above defined detent position. It is visible that the starting torque depends on the current. For the 1A the smaller pulsations are obtained in the torque envelope because the way that cogging torque complements the excitation torque. At higher current values the gap in the produced torque becomes greater, but usually it is not sensed due to the high inertia of the rotor.

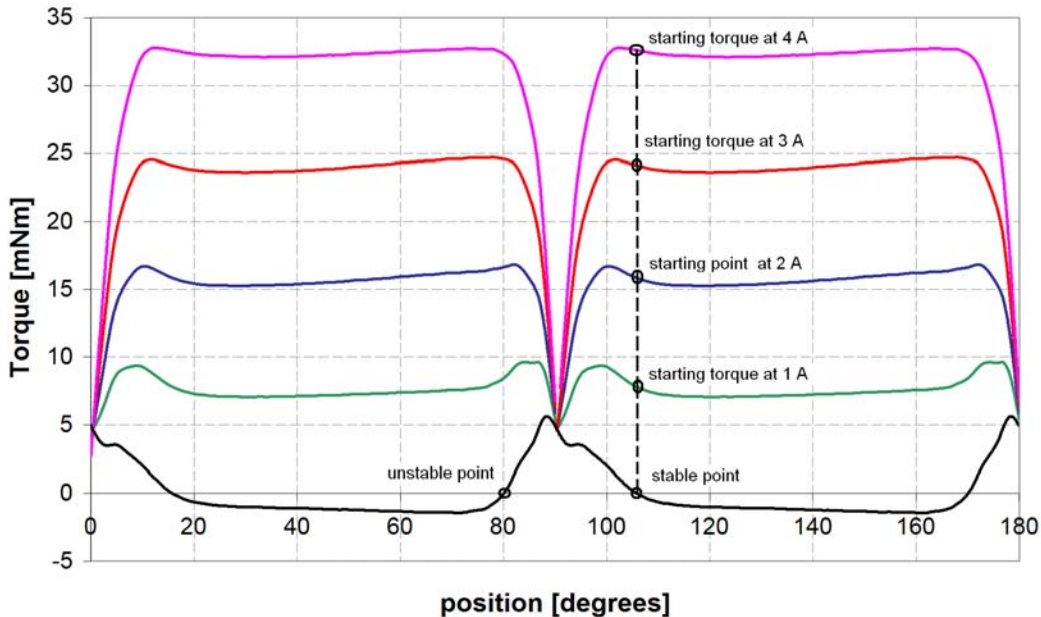


Figure 26. Detent position and Starting torque explicative drawing

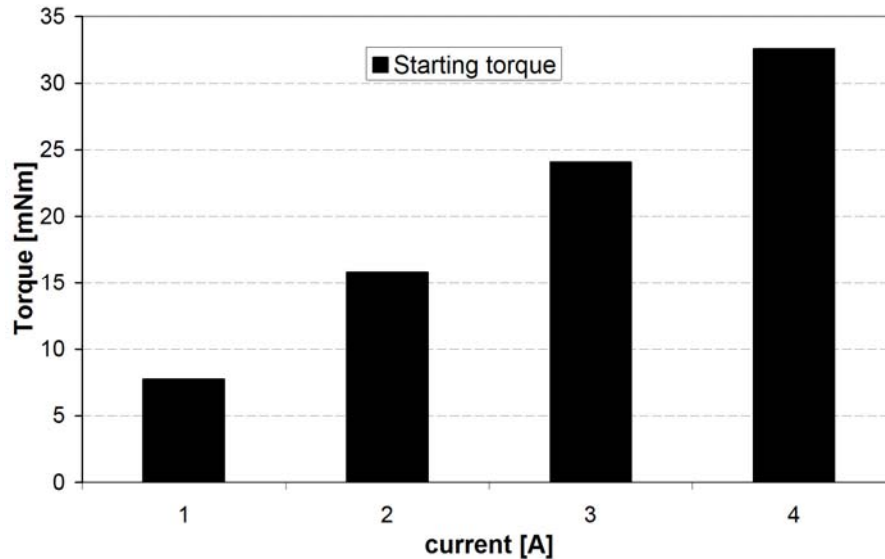


Figure 27. Starting torque for different currents

2.8 Experimental measurements

To verify the FE analysis, measurements were performed and parameters obtained by both methods were compared.

2.8.1 BEMF coefficient validation

The BEMF coefficient K_e was measured by driving the motor as a generator at a fixed small speed and the BEMF was measured using dedicated test equipment and the Labview software from NI.

Figure 28 shows a comparison between the FEM based and the measured BEMF waveforms.

Acceptable agreement is visible while the rather differences may be attributed to:

- inexact knowledge of axial PM flux contribution, only approximated here because 2D FEM was used,
- to airgap mechanical tolerances
- the real motor has small differences in the geometry and in the materials properties in comparison with the FE model
- to inexact knowledge of PM magnetization pattern.
- some inaccuracy of the geometry of the real motor
- numerical errors in FE analysis

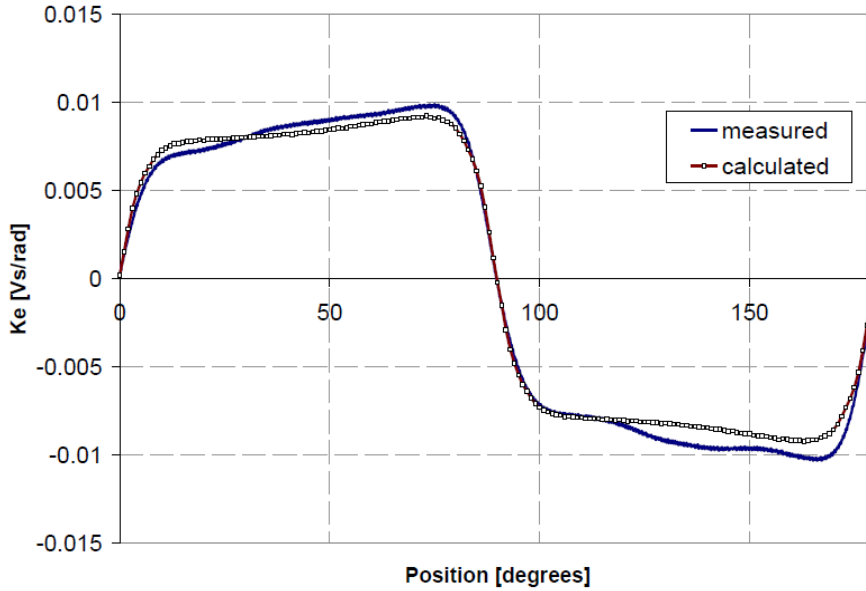


Figure 28. BEMF shape vs. position

2.8.2 Inductance validation

The inductance variation with rotor position was measured using an RLC bridge. The rotor was positioned in successive positions using a dedicated mechanical device. Figure 29 shows a comparison between the measured and calculated inductance variation with position.

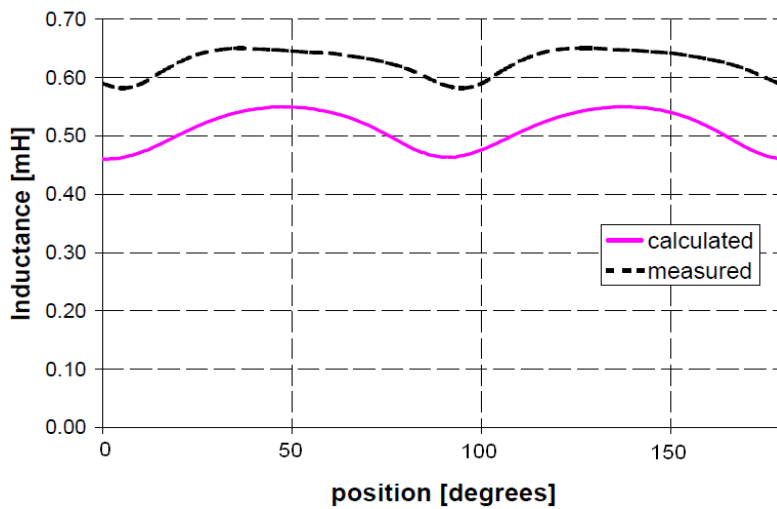


Figure 29. Calculated and measured inductance

The difference between the two waveforms may be explained by the fact that the calculated inductance from FEM considered all the flux useful without considering the end winding leakage inductance.

Phase Resistance calculation and measurement

The winding resistance is analytically determined based on (26).

$$R = \rho_{\text{Co-20}} \cdot \frac{l_c \cdot N_t}{A_{\text{wire}}} \quad (26)$$

where l_c - medium length of one coil turn, N_t - total turns, A_{wire} - wire cross section area.

Table 2 contains the computed and measured resistance values.

TABLE II
Resistance value

Computed resistance value	Measured resistance value
0.23 Ω	0.27 Ω

2.8.3 Static torque measurements

In order to validate the computed torque waveforms, torque measurements were done under the same conditions. The tested motor was driven at a constant very low speed (7 rpm) by a speed controlled drive. The torque was measured with a torque sensor, while for synchronization of the torque information with rotor position an incremental encoder was used.

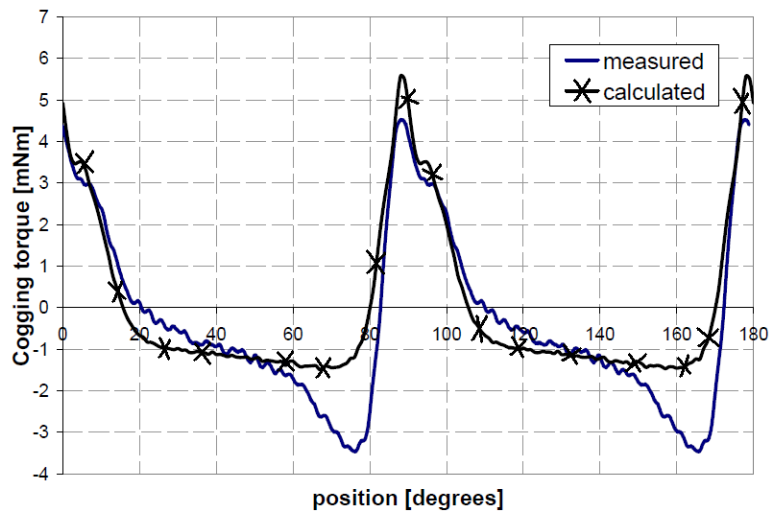


Figure 30. Cogging torque vs. position

Figure 30 shows the rotor angle dependence for both the measured and calculated cogging torque. The differences between those two shapes may be again explained by the fact that we didn't measure the actual magnetization curve and

pattern of the PMs and by the differences between the real and assumed airgap along rotor periphery.

For the total electromagnetic torque the same procedure was used, but now the motor winding was fed with constant value dc current. Figure 31 presents a comparison between the measured and calculated by FEM total electromagnetic torque.

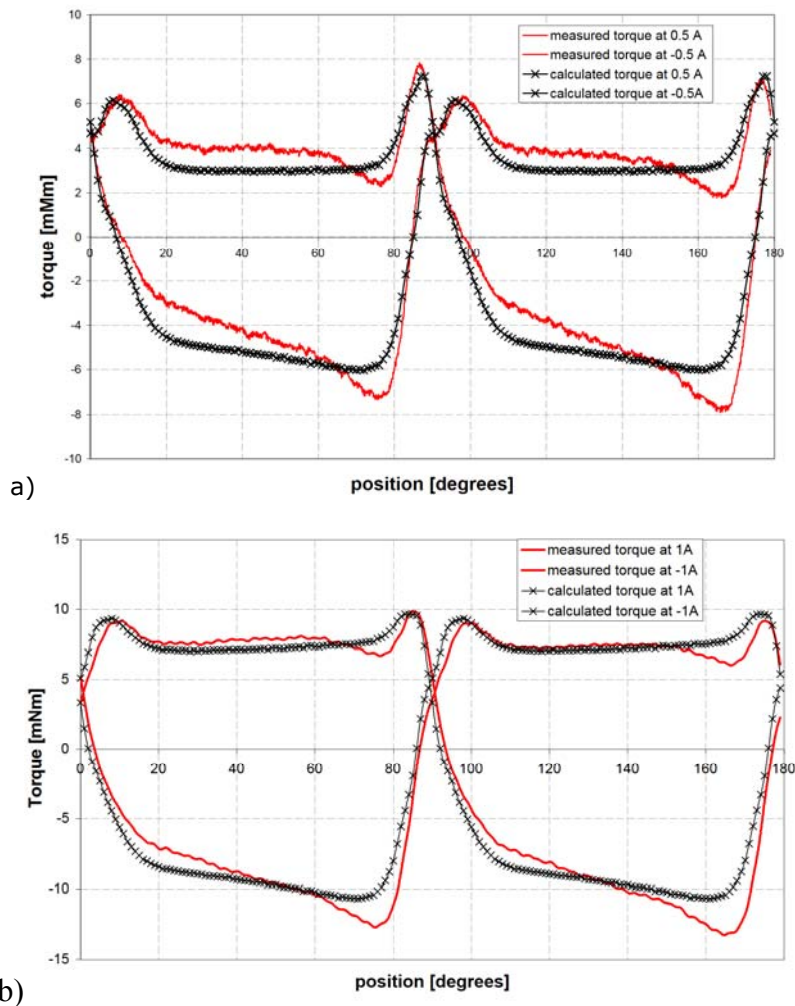


Figure 31. Torque vs. Position at : a) 0.5 A, b) 1A

A good correspondence between the FEM and measured torque waveforms is visible, especially at 1 A. The torque tends to become smoother with current increase.

2.8.4 Starting torque validation

For self starting capability the detent position should correspond to an enough electromagnetic torque in order to overcome the load torque. Here, in the case of a fan, blower type load, this is represented only by mechanical friction. The

experimentally determined starting torque is extracted from the measured static characteristics of torque/position as figure 32 shows.

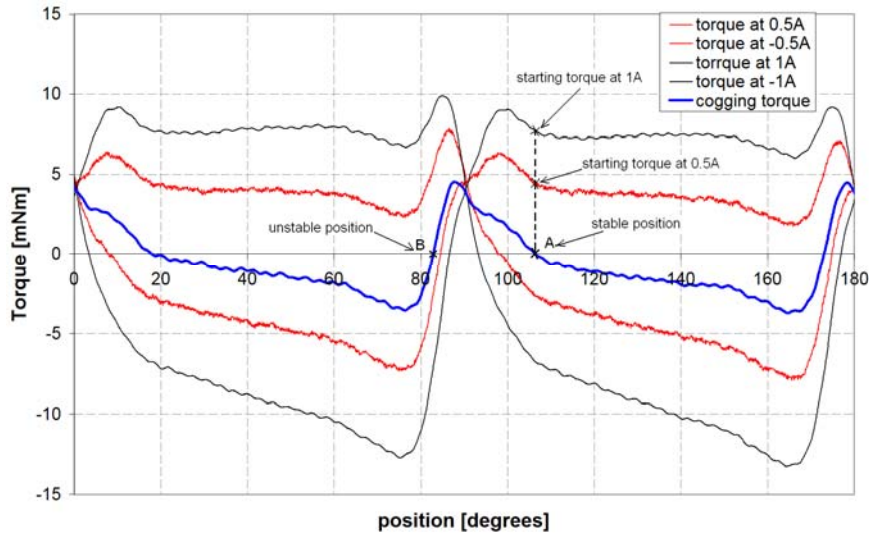


Figure 32. Detent position and Starting torque explicative drawing

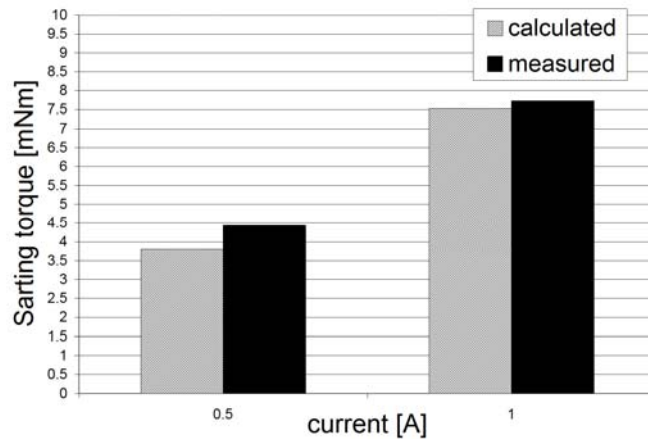


Figure 33. FEM vs. Measured starting torque for 0.5 A and 1A

Figure 33 presents a comparison between the obtained starting torque values by FEM and test measurements. Only the starting torque values for 0.5 A and 1 A are compared due to the technical limitation of the test equipment.

2.8.5 Dynamic torque measurement

The analyzed motor so far was also tested as driven with current commutated based on the Hall sensor signal and a PWM technique using the dSpace 1104 equipment.

The motor was driven in close loop current control with the reference set at 2A and it was loaded using a dedicated test rig with a load device based on eddy currents principle.

Figure 34 shows the measured current and torque waveforms at 110 rpm and 220 rpm. At this relatively low speed the torquemeter was still able to measure the torque pulsations. The torque rated frequency oscillations are mainly due to the single phase character of torque interactions while the lower frequency torque oscillations are due to mechanical coupling with the motor driven in speed open loop control mode.

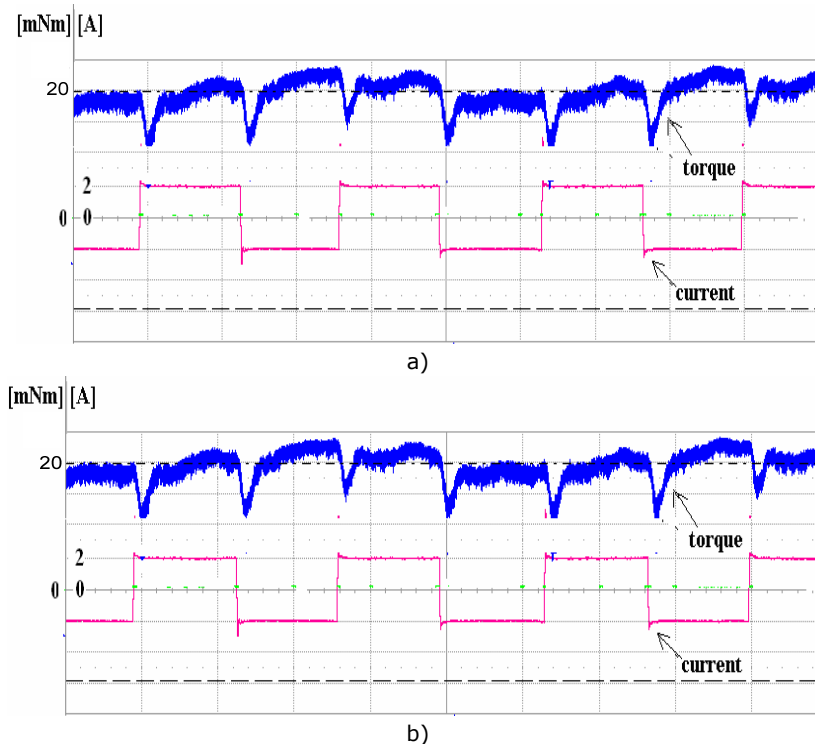


Figure 34. Torque and current at a) 110 rpm; b) 220 rpm

The torque obtained on dSpace platform is in good correspondence with the one measured with dc. current. For a rectangular bipolar current of 2A the torque pulsations are rather acceptable, approximately 50% of maximum value. Besides the current switching torque pulsations, figure 34 show some smaller high frequency pulsations due to the PWM commutation. At higher speeds, dynamical effects cause the measured electromagnetic torque to deviate from the static torque because the torquemeter inertia did not allow us to measure the torque pulsations (figure 35).

2.9 Conclusions

Since the identification of actual parameters in a system is essential in designing a high performance motor drive system, an objective of this chapter was the introduction of a 2D FE analysis approach as a preliminary methodology for characterization of single phase PM-BLDC motrs.

FEA-based simulations have been performed to compute the main parameters of a single phase PM-BLDC motor.

An overview of the existing research work on single phase PM-BLDC motor design and FEM analysis was done. It was concluded that the motor parameters which are further needed for modelling and control purposes, are strongly affected by stator and rotor geometry. Finite element magnetostatic solvers can include these effects, resulting a more accurate estimate of the motor bEMF and excitation torque constant, phase inductance, cogging torque and flux linkage. This parameters are very important aspect when a simulation model as close as possible to reality is desired.

The importance of mesh generation, materials selection and field distribution was also outlined.

A detailed approach by FEM on flux linkage, BEMF constant and phase inductance was presented and the obtained results were illustrated.

An in-depth analysis of the cogging torque, electromagnetic torque and starting torque was done in order to predict the selfstarting capability and torque pulsations. For this, FEA-based simulations have been used to compute the torque waveforms of a PM brushless dc motor under different excitations from 0 A to rated current.

In order to validate the obtained parameters from FEM calculation, test measurements have been done. All the above parameters were also measured under static tests and the obtained results were compared with the measured ones. Although there were some differences, the results from FE analysis were in close agreement with the experimental ones.

Also dynamic torque measurements with close loop torque control have been done in order to accomplish the experimental part.

When determining motor parameters, in detail, the need to have a good knowledge of real magnetization direction for the ferrite permanent magnet ring was demonstrated. Here, a closer to reality magnetization pattern was determined by comparing the FEM obtained and the test measured BEMF and cogging torque. So, a closer to reality magnetization, with a tangential component at the transition between poles was considered.

It was concluded that the correct prediction of single phase PMSM parameters is influenced by the corroboration of the geometry and magnetization direction.

References

- [1] J.F. Gieras, M. Wing, "Permanent magnet motor technology", Marcel Dekker, Inc., New York, 2002.
- [2] S. Bentouati, Z. Q. Zhu, D. Howe, "Influence of Design Parameters on the Starting Torque of a Single-Phase PM Brushless DC Motor", *Trans on Magnetics*, vol. 36, no. 5, September 2000, pp. 3533-3536.
- [3] F. Meyer, "Permanent magnet synchronous machines with non-overlapping concentrated windings for low-speed direct-drive applications", Ph.D. dissertation, Royal Institute of Technology, Stockholm, 2008.
- [4] D. M. Ionel, M. Popescu, M. I. McGilp, T. J. E. Miller, and S. J. Dillinger, "Assessment of torque components in brushless permanent-magnet machines through numerical analysis of electromagnetic field," *IEEE Trans. Ind. Appl.*, vol. 41, no. 5, pp. 1149-1158, Sep./Oct.2005.
- [5] D. G. Dorrell, M. Popescu, and M. I. McGilp, "Torque Calculation in Finite Element Solutions of Electrical Machines by Consideration of Stored Energy", *IEEE Transactions on magnetics*, vol.42, no.10, October 2006

- [6] R.P. Deodhar, D.A. Staton, T.M. Jahns, T.J.E. Miller, "Prediction of cogging torque using the flux-MMF diagram technique", IEEE Trans Industry Applications, Vol. 32, pp. 569 - 576, May-June 1996.
- [7] K. F. Rasmussen, "Analytical prediction of magnetic field from surface mounted permanent magnet motor," in Proc. Int. Electrical Machines and Drives Conf.. Seattle, WA, 1999, pp. 34-36.
- [8] K.F. Rasmussen, J.H. Davies, , T.J.E Miller, M.I. McGelp, M.Olaru, "Analytical and numerical computation of air-gap magnetic fields in brushless motors with surface permanent magnets", , IEEE Transactions on Industry Applications, Volume 36, Issue 6, Nov/Dec 2000 Page(s): 1547 - 1554
- [9] L. Iepure, L. Tutelea, I. Boldea, "FEM analysis and control of a tapered airgap single phase PMSM", record of OPTIM-2008, pp 241-248.
- [10] S. Ahmed, P. Lefley, "Development of a Single Phase PM BLDC Motor from a Novel Generic Model", AEDIE 2009.
- [11] Yin-Kwang Lin, Der-Ray Huang, Shin-Lu Chen, Kuo-Chi Chiu, Tai-Fa Ying, Chung-I G. Hsu, "Back electromotive force enhancement for a new single-phase synchronous motor", Journal of Applied Physics, vol.85, no. 2, april 1999, pp.4907-4909
- [12] Chun-Lung Chiu, Yie-Tone Chen, Wun-Siang Jhang, "Properties of Cogging Torque, Starting Torque, and Electrical Circuits for the Single-Phase Brushless DC Motor", Trans. On Magnetics, vol. 44, no. 10, oct. 2008, pp.2317-2323.
- [13] D. C. Hanselman, "Brushless permanent-magnet motor design", McGraw-Hill, Inc., 1994.
- [14] Anton Hamler, Boiidar Hribernik , "Impact of Shape of Stator Pole of One Phase Brushless Motor on Cogging Torque", Trans. On Magnetics, vol. 32, no.3, May 1996, pp.1545-1548
- [15] Lizhi Sun, Qi Feng, and Jing Shang, "Drive of Single-Phase Brushless DC Motors Based on Torque Analysis", Trans. On Magnetics, vol 43, no. 1, January 2007, pp.46-50.
- [16] Der-Ray Huang, Tai-Fa Ying, Shyh-Jier Wang, Chi-mou Zhou, Yin-Kwang Lin, Kai-Wen Su, Chung-I G. Hsu, "Cogging torque reduction of a single-phase brushless dc motor", Trans. On Magnetics, vol 34, no 4, July 1998, pp.2075-2077.
- [17] Byung-Il Kwon, Byoung-Yull Yang, Seung-Chan Park, Young-Sun Jin, "Novel Topology of Unequal Air Gap in a Single-Phase Brushless DC Motor",Trans. On Magnetics, vol/ 36, no. 5, sept. 2001, pp.3723-3726.
- [18] S. H. Won , T. H. Kim, K. B. Jang, S.K. Choi, W.S. Oh , Ju Lee, "Effect of design variables on starting torque of single phase flux-reversal machine", Journal of Applied Physics, 1999.
- [19] K. Lu, P. O. Rasmussen, Ewen Ritchie, "An Analytical Equation for Cogging Torque Calculation in Permanent Magnet Motors", record of ICEM 2006.
- [20] H.B.Ertan, B.Dag, G.Capolino, "Calculation of some parameters of Single Phase PM Motor for Design Optimization", OPTIM-2002, vol.2, pp. 351-356.
- [21] J.L.Coulomb, G. Meunier, "Finite element implementation of virtual work principle for magnetic or electric force and torque computation," IEEE Transactions on Magnetics. Vol. MAG-20, pp. 1894-1896, 1984
- [22] M. Popescu, D.M Ionel,. T.J.E. Miller, S. Bellinger, M. I. McGilp, "Improved finite element computations of torque in brushless permanent magnet motors", Second International Conference on Power Electronics, Machines and Drives, 2004 (PEMD 2004), Volume 2, Issue , 31 March-2 April 2004, Page(s):540-545,Vol.2.
- [23] David Meeker, "Finite Element Method Magnetics, User's Manual, 2009

3. MOTOR DYNAMICAL MODELING AND CONTROL

Abstract

In this chapter a detailed approach of modeling a single phase PM-BLDC motor for control purpose is presented. First, an accurate digital motor model is developed by using the previous FEM based obtained characteristics. Then, the digital PM-BLDC motor model is validated by simulations under hysteresis current control.

An overview of the speed closed loop control possibilities is presented and a short description of the used power converter topology is done. Important aspects as sampling frequency, switching frequency, soft switching or hard switching commutation methods are referred to for both simulation and practical implementation purposes.

Considering the above mentioned important aspects, an advanced digital simulation model of the motor control system is developed. This digital model allows to accurately model the machine and also permits an in depth simulation of the control. The digital control simulation is as close as possible to the real hardware implementation on dSpace platform.

Also, in spite of the fact that it is not the primary objective of this chapter, a short description of the Hall based control for a single phase PM-BLDC motor is done. The possibility to obtain the speed and a high resolution position information from the Hall sensor signal is explored. This information will be further used for validating the proposed sensorless control.

3.1. Introduction

A well defined mathematical model of an electrical motor is an important part in the development process of a performant motor control drive, sensed or sensorless.

Usually ideal bmf, excitation torque, cogging torque and constant inductance are used in modeling the machine. Consequently, the motor drive control system simulation is usually carried out in system simulators, like SIMULINK, using very simple analytical models for electrical machines, which does not always give the accurate results.

For more accuracy the FE time stepping analysis coupled with circuit model [1]-[9], electronic converter [10]-[12] and control model [13]-[16], is increasingly studied, the prove being the numerous paper related to this field. Although there is a great interest in coupling the finite element analysis with circuit simulation and eventually with closed loop control, this method has a reduced popularity due to some drawback like:

- Long computation time
- Need of knowledge about the coupling mechanism is required

- Implementing a feedback loop into the time-stepping analysis is a rather complex task. It is necessary to synchronize the time steps with the control system, which, in turn, controls the switching components of the converter [17].
- The commercial FEM software with possibilities of coupling the field analysis with circuit model and closed loop control are not always suitable due to unaffordable license fees and confidential computational algorithms and program code.
- The control systems, on the other hand, are nowadays based on complex estimators and feedback loops. For simulation, it is a laborious work to implement those in a FE based software, and the use of a software tool like Simulink, with a lot of dedicated features for control purposes is usually more advantageous.

This chapter proposes the simulation of electrical machines, external circuits and control systems, by using an intermediate solution between the above presented ones. This avoids the disadvantages of the coupling solution and gives more accurate results than a simple dynamical model.

Since the identification of actual parameters in a system is essential in designing a high performance controller, this chapter will concentrate in modeling the motor behavior using the FEM determined and experimentally validated parameters, as functions of rotor position, from chapter 2. This way, the particularities given by stator geometry, airgap asymmetry and local saturation are taken into consideration. Similar approaches to motor modeling are addressed in [18]- [22]. For the machine modeling, the Laplace transformation is applied and the Matlab/Simulink software package is used.

3.2. Single phase PM-BLDC motor: mathematical model

A brushless dc motor can be considered a dc motor turned inside out, so that the field is on the rotor and the armature is on the stator.

The electromagnetic torque, T_{em} , is linearly proportional to the armature current, while the back-emf in a BLDC motor is linearly proportional to the rotational speed of the shaft.

In order to have a proper operation of the motor, it is necessary to synchronize the phase current with the phase back-emf. Since the PM-bl dc motor has a trapezoidal back emf, for maximum torque/ current a square wave current is supplied to the stator windings. By keeping the square top of the current aligned with the square top of the back EMF, the obtained torque is optimum. To control the machine with EMF in phase with the current it means to switch the current through the stator phase when the magnetic flux is maximum or when the EMF is zero. This is achieved by the use of a Hall position sensor which detects the position of the rotor field, and hence the position of the rotor shaft, or by means of a sensorless observer.

So, considering the above, a brushless dc motor is actually a permanent magnet ac motor whose torque-current characteristics are similar with those of the dc motor. Instead of commutating the armature current using brushes, electronic commutation is used.

Based on this similitude with DC motor, the machine equations are simple and similar with those of a dc motor.

The single phase PM-BLDC motor can therefore be represented by the equivalent circuit shown in Fig. 2.

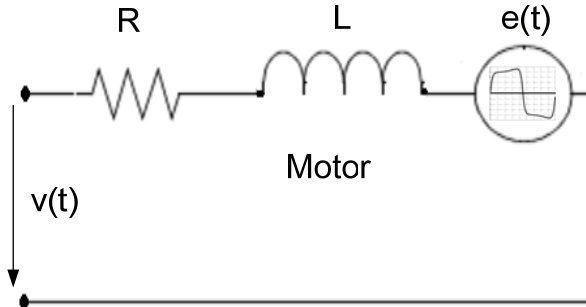


Figure 1. Equivalent circuit for stator winding

The differential equations used for describing the dynamic behavior of a single phase BLDC motor are further used for creating the machine model.

The voltage equation for the equivalent circuit from figure 1 is:

$$v(t) = R \cdot i(t) + L(i, \theta_{er}) \cdot \frac{di(t)}{dt} + e(t) \quad (1)$$

where $v(t)$ is the phase voltage input, R , L are the phase resistance respectively the phase inductance and $e(t)$ is the BEMF. The BEMF is proportional with the phase current through $k_e(\theta_r)$:

$$e(t) = k_e(\theta_{er}) \cdot \omega_r(t) \quad (2)$$

$$\theta_{er}(t) = \int p \cdot \omega_r(t) \cdot dt \quad (3)$$

In the above equations, $\theta_{er}(t)$ is the electrical angle and $\omega_r(t)$ is the rotational speed, p - number of pole pairs, while $k_e(\theta_{er})$ is the instantaneous emf function dependent of angular position.

The motion equation is:

$$T(t) = J \cdot \frac{d\omega_r(t)}{dt} + B \cdot \omega(t) + T_L(t) \quad (4)$$

Where J - the inertia moment, B - viscous frictional coefficient, $T_L(t)$ - load torque and $T(t)$ is the total developed electromagnetic torque given as the sum of the cogging torque $T_{cog}(t)$ and excitation torque $T_e(t)$ (eq.5).

$$T(t) = T_e(t) + T_{cog}(\theta_{er}) \quad (5)$$

$$T_e(t) = k_e(\theta_{er}) \cdot i(t) \quad (6)$$

In eq. (1)-(6), the parameters inductance, back EMF and torque coefficient $k_e(\theta_{er})$ and cogging torque component are explicitly written as functions of rotor position. The inductance term $L(i, \theta_{er})$ will also be reduced only to position dependence $L(\theta_{er})$ due to the fact that, after a FE analysis, the inductance doesn't modify when motor supplied with current values in the range of 0-4 A.

In spite of its simple construction the single phase BLDC motor control is not an easy task. The developed motor model will be further used for the development of sensorless control methods. The sensorless control strategies are first explored by digital simulations and only then validated by experiments. For this, an accurate motor model is needed.

Making use of the Laplace transformation the motor dynamical model in operational domain is built in figure 2.

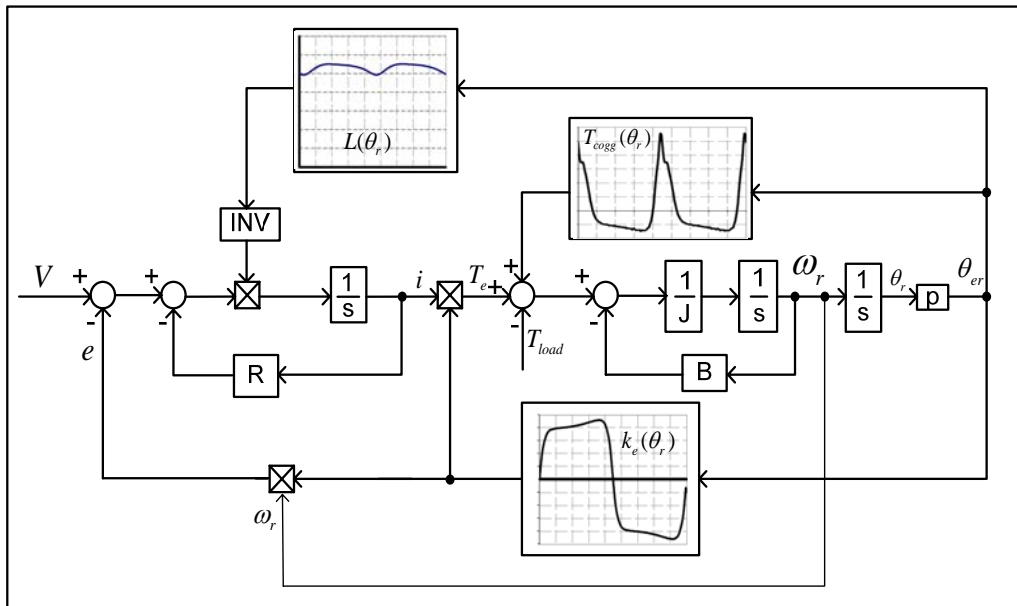


Figure 2. Block diagram of the single phase PM-BLDC motor

3.3. Single phase PM-BLDC motor control system

3.3.1 Closed loop speed control

There are many different implementations methods for a single phase PM-BLDC motor control, from a simple commutation method of a fixed voltage using a

Hall sensor to drive the fixed speed motor, to more complex speed control methods. This implies the modifying of the supply voltage by means of PWM or hysteresis control, combined with phase advance commutation angle at high speed. [22]-[24]

To control the speed, a speed controller may directly determine the duty cycle of a pulse width modulator (PWM), Fig. 3, or a cascaded control with an outer speed and an inner current control loop may be employed.

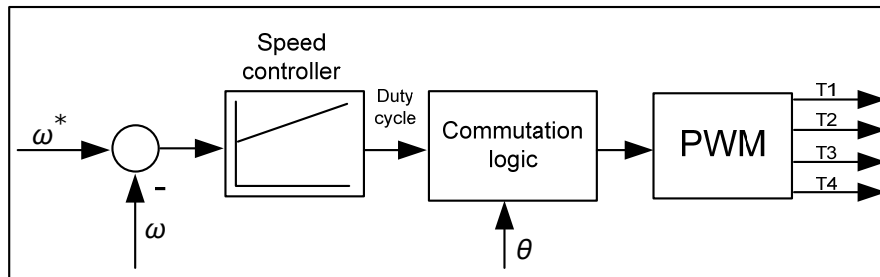


Figure 3. Speed control with PWM

When the phase voltage is controlled to regulate the speed, the current response is delayed by the electrical time constant $T=L/R$ of the motor. To obtain a better current (torque) response time, an inner closed loop current control is employed here. The performance of the outer speed loop is dependent on how tight the current is regulated. Also, another advantage of current regulation is the fact that reduces the sensitivity to non-linearities like dead-time effect, friction, power switch voltage drop or disturbances like BEMF.

To control the current, a hysteresis controller can be used (figure 5). In the hysteresis-type current regulator, the power transistors are switched off and on according to whether the current is greater or less than a reference current. The error is used directly to control the states of the power transistors.

The advantages of the hysteresis controller are fast transient response and simple implementation.

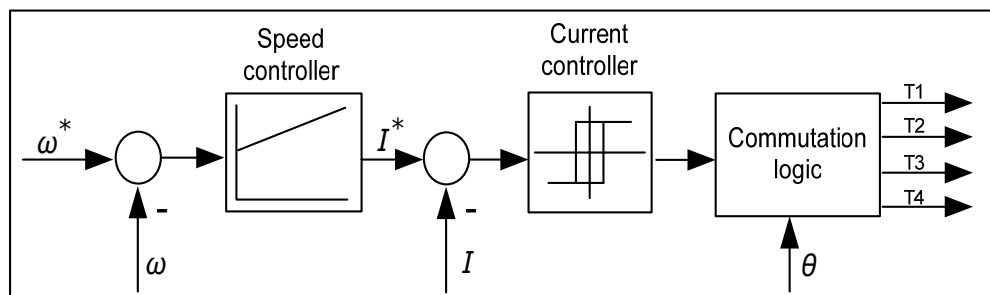


Figure 4. Speed control with hysteresis current control

Since the supply voltage is fixed, the hysteresis controller works at high variable chopping frequency to maintain the current between desired limits. The hysteresis control quality decreases as the chopping frequency decreases.

The PI controller is another viable solution for current control loop, and its principle of operation consist in minimizing the error between the reference and the

measured current by prescribing a duty cycle to the PWM block. This type of current controller will be used further in the current control loop for the implemented sensorless control.

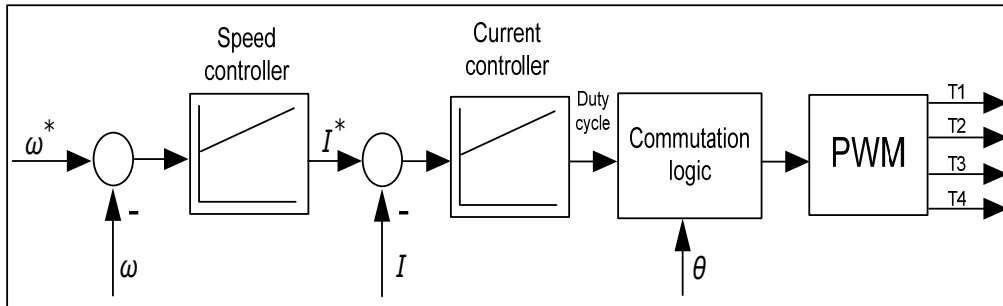


Figure 5. Speed control with inner PI current controller

3.3.2 Power electronic converter

To achieve variable speed a full bridge single phase PWM power electronic converter, as shown in figure 3 , is used.

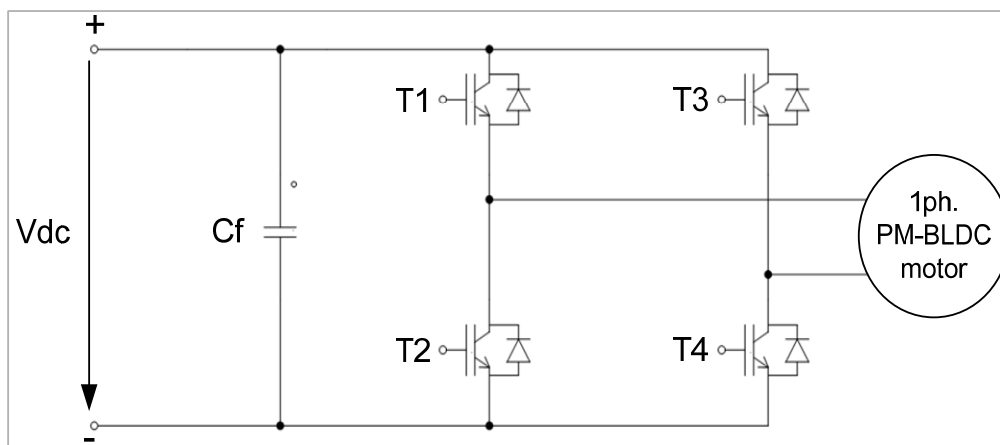


Figure 6. The full PWM converter drive for single phase PM-BLDC motor

This type of electronic converter is often used to increase the power density by fully utilizing the copper winding. This way the phase winding is conducting 180° for both negative and positive current cycles.

The main components of a VSI are the four transistor switches and the antiparallel diodes across each switch. Diodes are needed to allow for an alternative path when the power switches are turned off in order to maintain the current continuity.

Also, the presented H-bridge converter has the advantage of making possible bidirectional power flow operation.

Different methods to control a H-bridge converter are possible [25]-[27]. The hard chopping (fast decay) and the soft chopping (slow decay) are the most popular.

Hard chopping means that T1, T4, respectively T2, T3 switches are driven by the same chopping signal. This way the applied voltage at the motor terminals will be +Vdc and -Vdc (figure 5a).

If soft switching is applied only the upper or the lower switches are driven by the chopping signal while the other are left on for half a period. The values of the applied voltage are Vdc, 0, -Vdc (Figure 5b).

The soft switching method has the advantage that creates less current ripple, lower switching losses and noise than the hard chopping method, but it needs four independent control signals.

3.4. Matlab-Simulink simulation model

In order to validate the electrical motor model and to investigate the proposed sensorless control solutions, a Matlab-Simulink model for the control system was developed.

Both the hysteresis and the PI current controllers were implemented in the simulation model. First the hysteresis current control is employed in the inner current loop with the scope of validating the motor model under ideal rectangular current, and then an advanced simulation model containing a PI current controller is developed for further control purposes.

3.4.1 Single phase PM-BLDC motor model validation by hysteresis current control

The implemented digital simulation model is presented in figure 7.

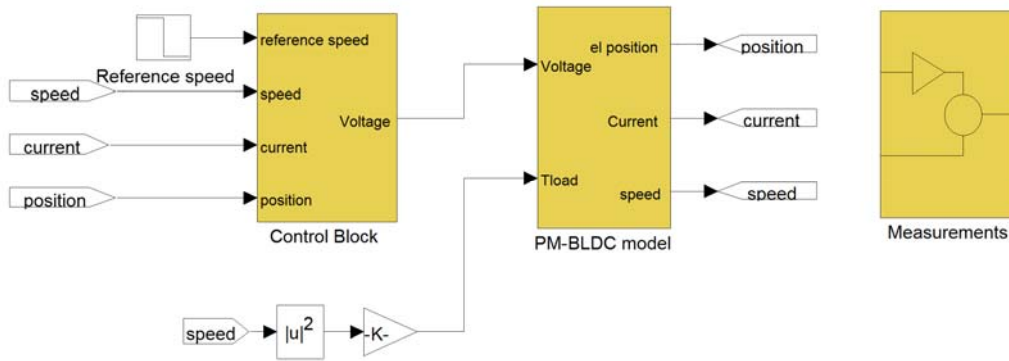


Figure 7. Single phase PM-BLDC motor simulated system overview

The hysteresis current control was mainly implemented for validating the machine model. In this case, for the correctness of the simulation, the overall simulation is working at 1 μs sampling time, while the control block from figure 7 is running at 10 μs in order to obtain acceptable current ripple.

The PM-BLDC model block from figure 7 contains the machine model from figure 2, while the control block consists of an outer speed control loop with an inner hysteresis current control loop.

For simplicity the H-bridge converter is considered ideal and is modeled to have a voltage output of $+V_{dc}$ or $-V_{dc}$ when hard switching is considered, respectively $-V_{dc}$, 0 , $+V_{dc}$ when soft switching is considered.

Figure 8 illustrates the control block containing the PI speed controller and the hysteresis current controller for both hard switching and soft switching cases.

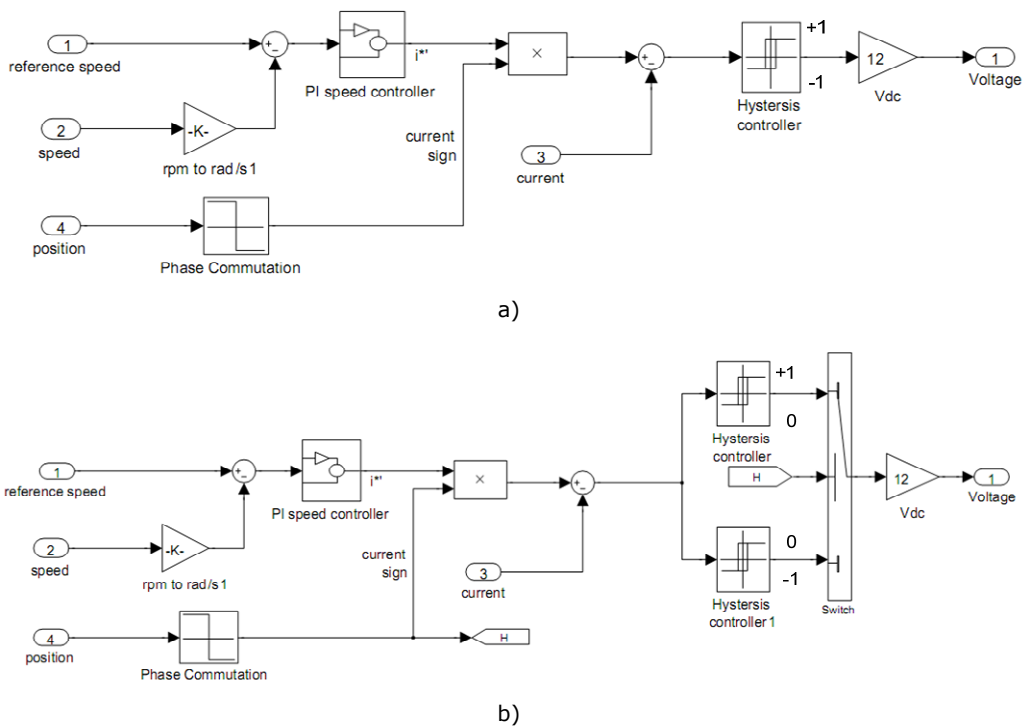


Figure 8. Control block content when Hysteresis current control is used: a) hard switching modeling, b) soft switching modeling

The control block from figure 8 generates the output voltage and is supplying a quasisquare current waveform whose magnitude is proportional with the electromagnetic torque by using either a two level or a three level PWM control.

Further some simulation results with both hysteresis and PI current control are presented.

Figure 9 illustrates the supplied voltage and current to the motor model for both hard switching and soft switching implementation. The reduced current pulsations in the soft switching method are visible.

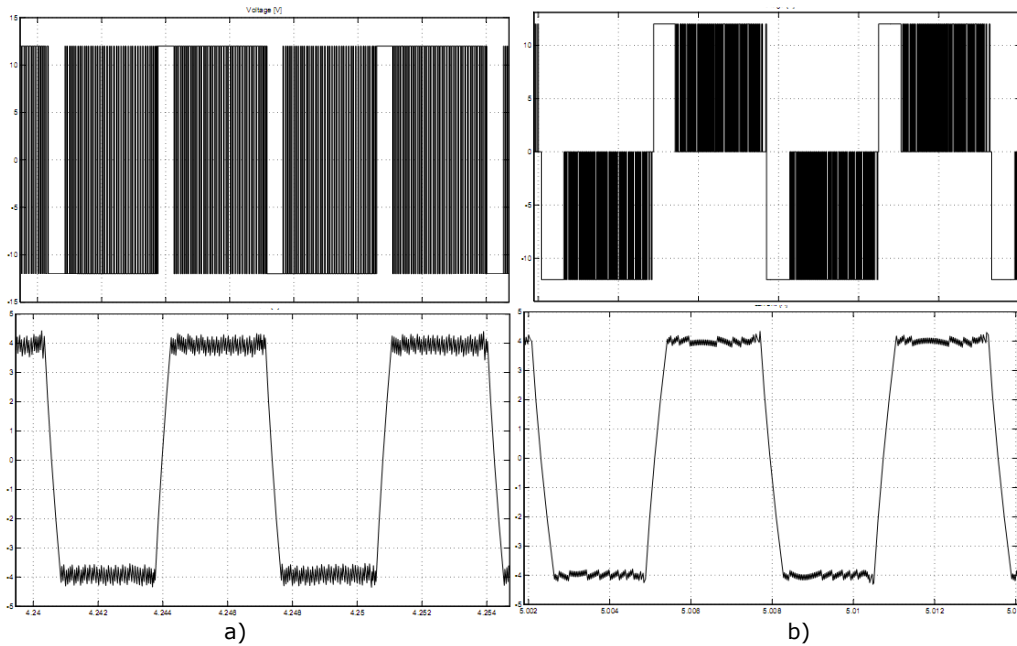


Figure 9 Supplied voltage and phase current during acceleration for: a) hard switching, b) soft switching

As mentioned before, higher current ripple is produced in the case of hard switching. Since the quality of the hysteresis controller is limited by the sampling time (figure 10), in order to have a cleaner image, without too much noise, over the produced torque, for the set sampling time of 20us, only the results obtained with soft switching method are presented.

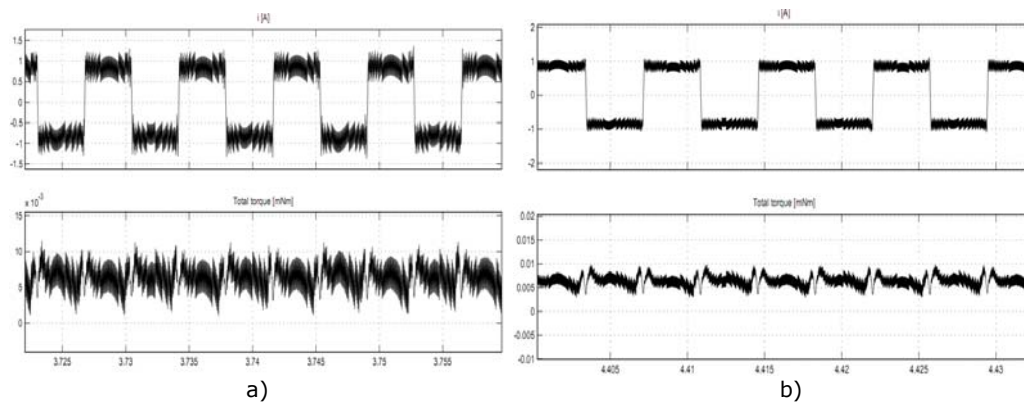


Figure 10 Phase current and developed torque with hysteresis current control and hard switching, using : a) sampling time $t_s = 20 \mu s$, b) sampling time $t_s = 10 \mu s$

Figure 11 shows some dynamical simulation results given in order to validate the motor model. First a transient from 0 to 4000 rpm is illustrated. The current is limited from control to 4A during transients. In the torque profile the safe starting is visible, and more, the torque envelope is almost always greater than zero

with small exceptions during transients. Due to current control, the obtained total torque $T(t)$ resembles the measured static torque (measured in chapter 2) and as shown startup is relatively smooth.

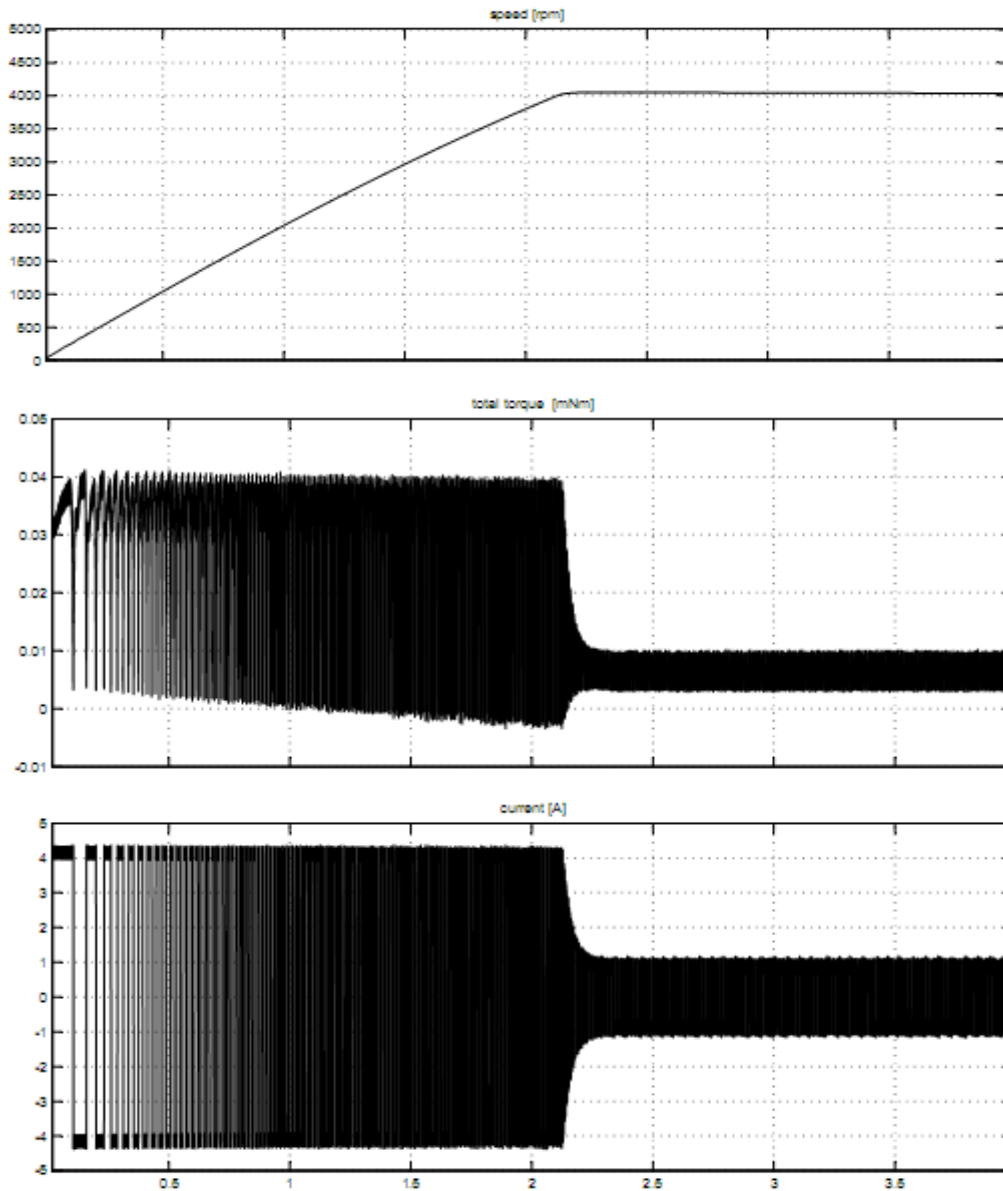


Figure 11 Simulation starting from zero to 4000 rpm with hysteresis current control

In order to confirm the quality of the motor model a zoom view over the starting region is presented in figure 12. The starting position is obtained from F E

software by analyzing the cogging torque profile and it was set as the initial integration condition in the speed integrator from PM-BLDC motor model (figure 2). By supplying with the proper current the developed torque is always positive.

The obtained results at 4000 rpm, respectively at 6000 rpm's steady state condition are presented in figures 13, 14.

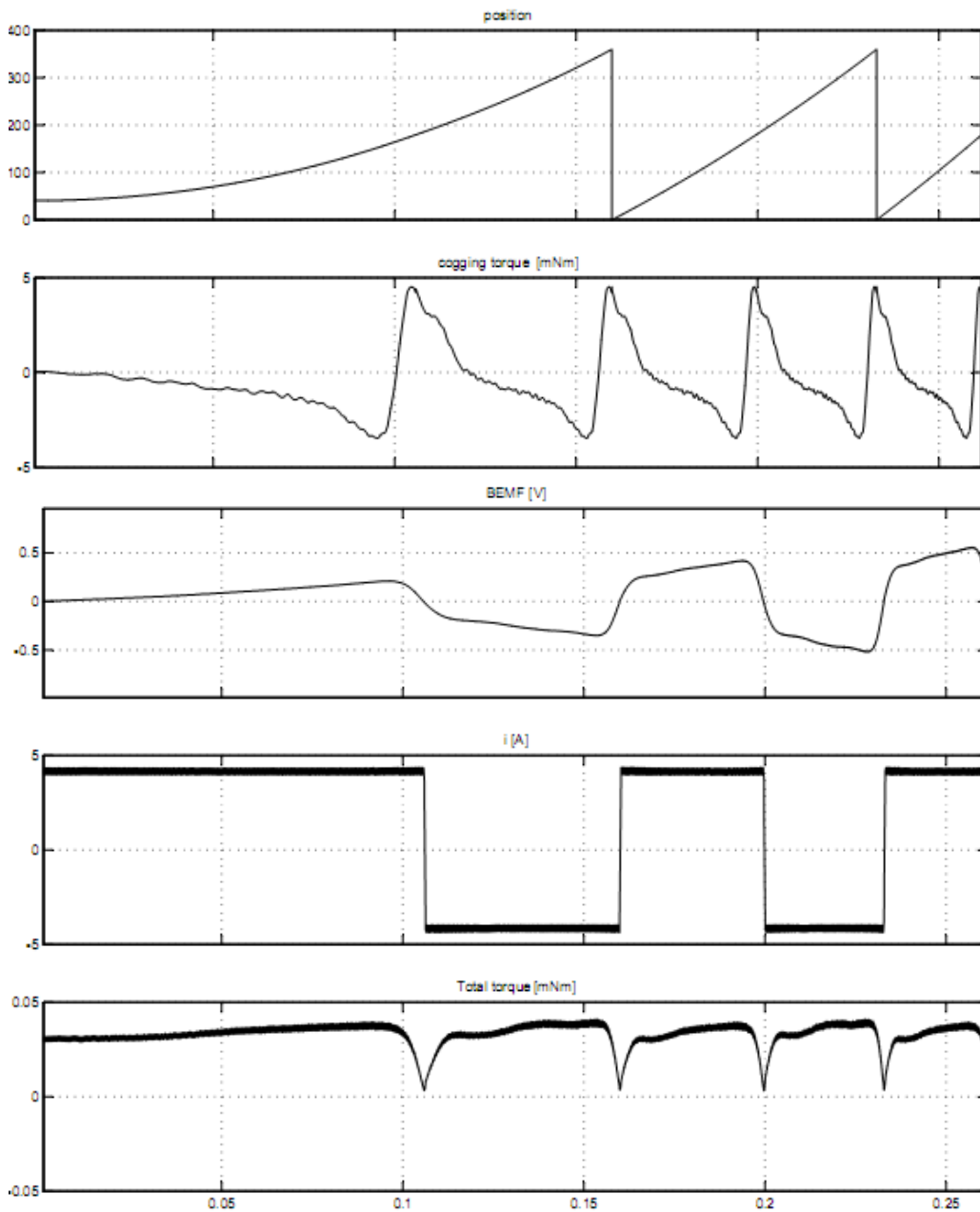


Figure 12 Detailed starting process: from top to bottom electrical position, cogging torque, BEMF, phase current and total torque

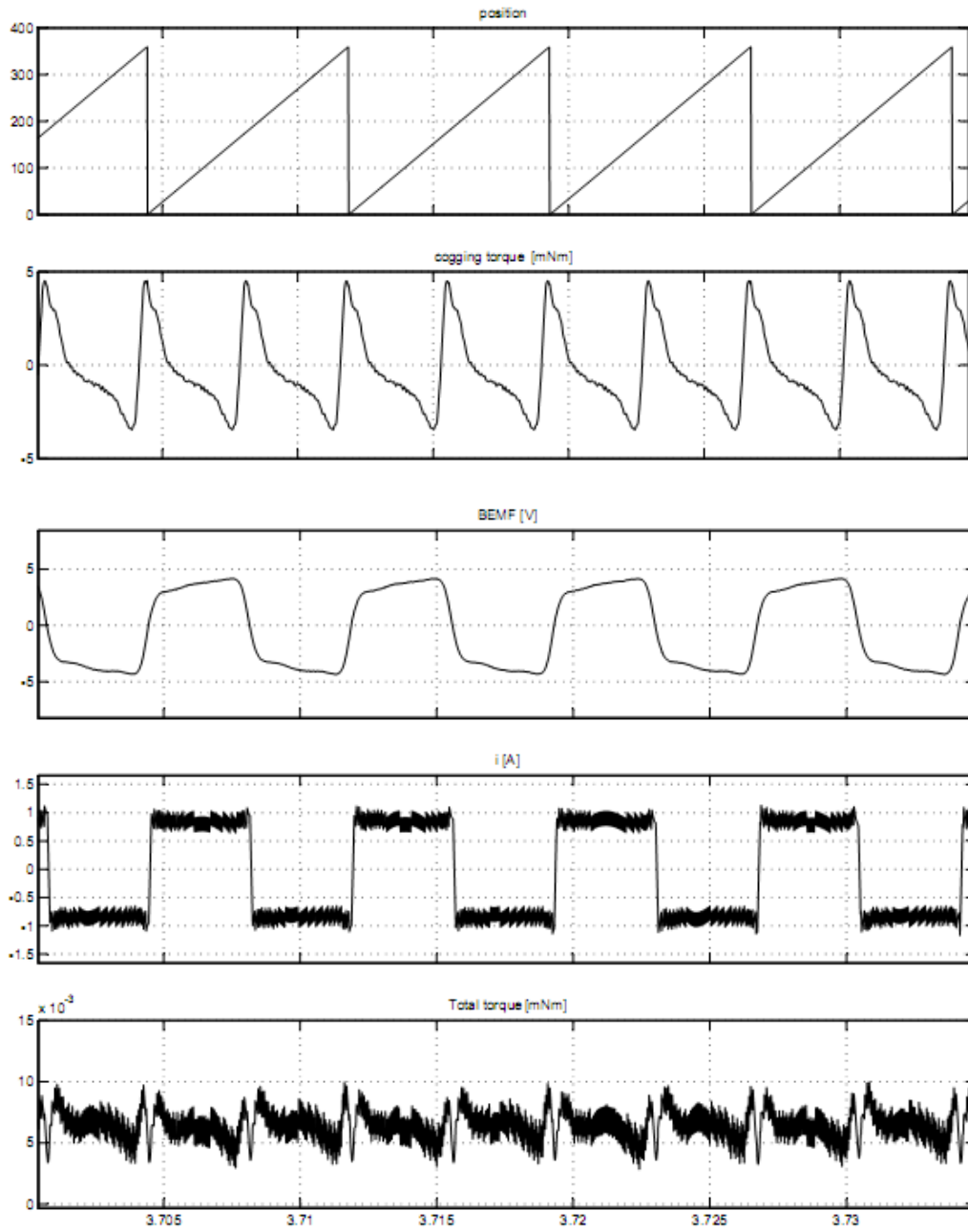


Figure 13 Simulation results at 4000 rpm steady state

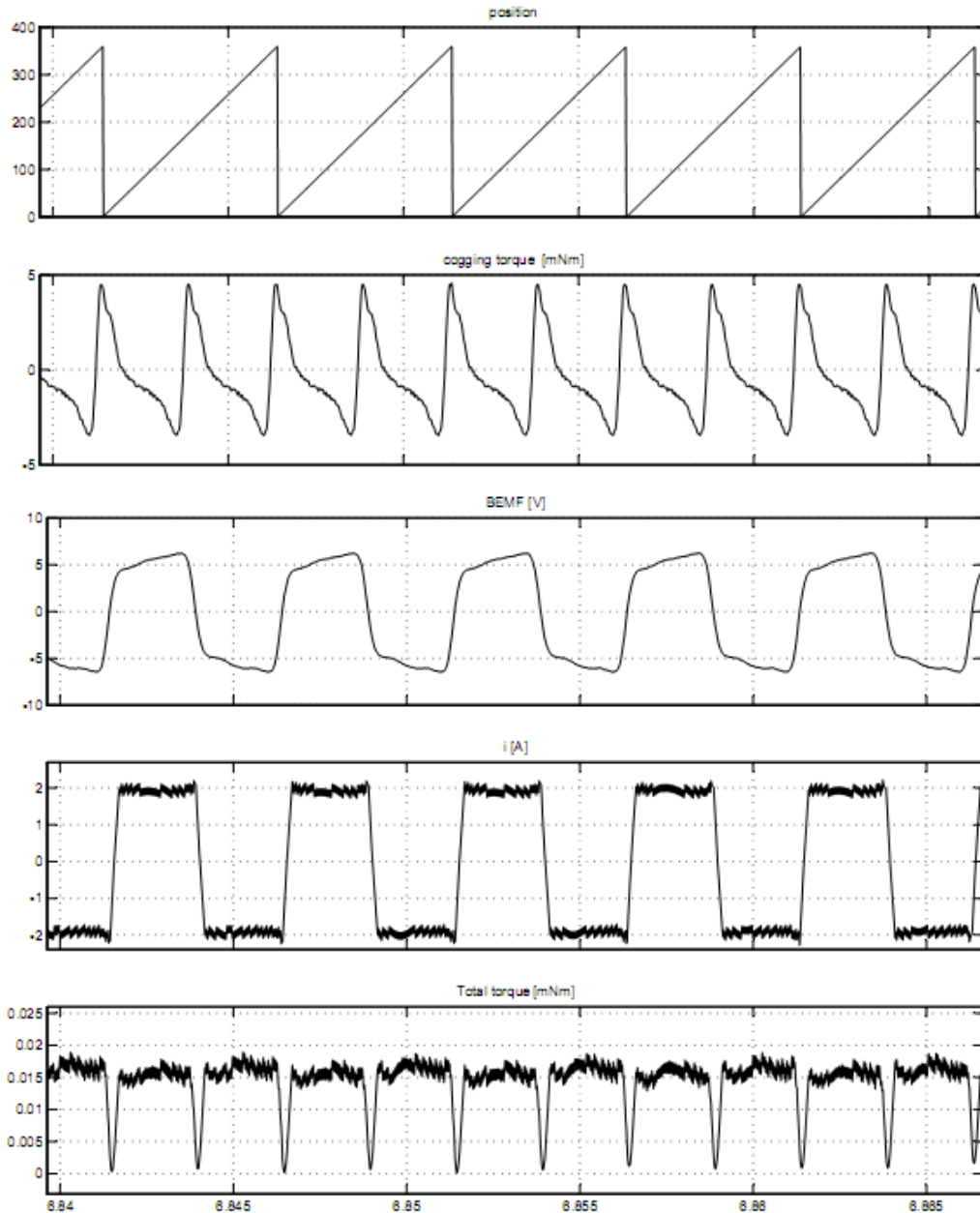


Figure 14 Simulation results at 6000 rpm steady state

The obtained torque from figure 12 is with its minimum value at 0, meaning that at this speed (6000 rpm) a small current delay is already present, making the current not to be in phase with the BEMF, and so the optimum torque/current is not obtained. This can be easily improved by implying a small commutation advance angle. The result is presented in figure 15.

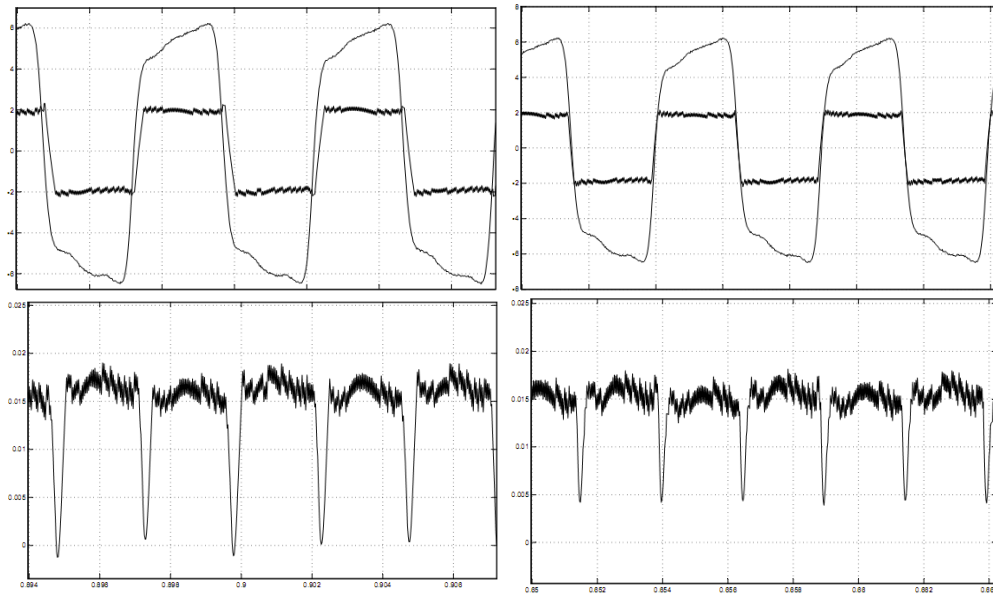


Figure 15. Torque improvement by using commutation phase advance angle

From figures 13, 14 a good correspondence with the FEM calculated and then measured torque is noticed which confirms the accuracy of the proposed model.

The hysteresis controller has better performances when implemented in analog scheme and the current can be easily kept in the hysteresis band. When implemented in digital form it is affected by the fixed sampling time [28]. For a digital implementation of the hysteresis controller the sampling time should be small enough to give good results.

Since high switching frequency and so high sampling frequency are needed for implementing the hysteresis current control, thus giving a long simulation time and higher timing restrictions in a digital practical implementation, only the speed closed loop control with inner PI current controller will be further used for the implementation of the proposed sensorless control strategies.

The analog hysteresis controller is also not considered because it implies extra circuits and the phase voltage is mandatory to be measured when state observers are used for sensorless control purposes.

The hysteresis current controller was chosen for single phase BLDC motor model validation due to its simple (not laborious design) implementation.

3.4.2 Advanced Simulink/ PSIM digital simulation control system model

In order to test and validate a sensorless control method for the single phase PM-BLDC motor, an in-depth simulation study is necessary.

A simulation model which gives a more insight over the inverter and the power devices gate signals logic, and allows a very close to reality simulation by running different parts of control model at different sampling times was developed and implemented here. In this model the control part is implemented basically in the same way, at the same sampling frequency, as in the real time dSpace rapid prototyping system used for experiments.

For a close as possible to reality simulation of the control system, and then for an easy experimental implementation on the dSpace prototyping system, the simulation model was build using the Simulink-Matlab and the PSIM softwares. This simulation model is based on coupling the Simulink and PSIM software and is constructed as follows:

-the inverter and the electrical part of the motor model are simulated in PSIM software at a sampling frequency of 1 μ s.

-the control structure and the mechanical part of the motor model are simulated in Simulink. This subsystem is running at 100 μ s as in the real dSpace platform.

Figure 16 shows the overall simulation model

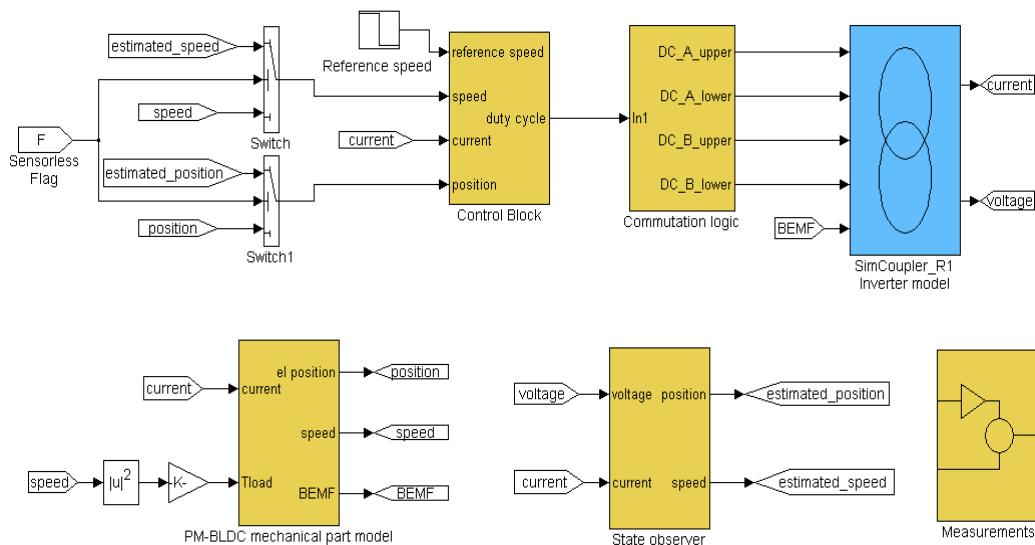


Figure 16. Overall simulated system

The control block from figure 16 contains an outer speed control loop and an inner current control loop, both implemented using PI controllers. The possibility to apply this closed loop control using the estimated speed, respectively position can

be also observed. The estimated speed and position are obtained from the State observer block, by calculations means using the applied voltage and phase current informations.

The connection signals between the two simulation software are the duty cycle, the phase current and the BEMF. The control block is executed once at 100us and the obtained duty cycle is sent to the PSIM where the comparison with the triangular signal is done. The obtained phase current is linked back to the Simulink model where it is used for torque calculation in the motor model and for control purpose. The calculated BEMF signal in Simulink is linked to the PSIM where it is used as a voltage control signal for a voltage source (Figure 17). Figure 16 illustrates the PSIM implemented H-bridge and the PWM pulse generator. The PWM pulses for each transistor are left independent so that the commutation logic to be handled from the Simulink with regard to the mentioned slow and fast decay commutation techniques.

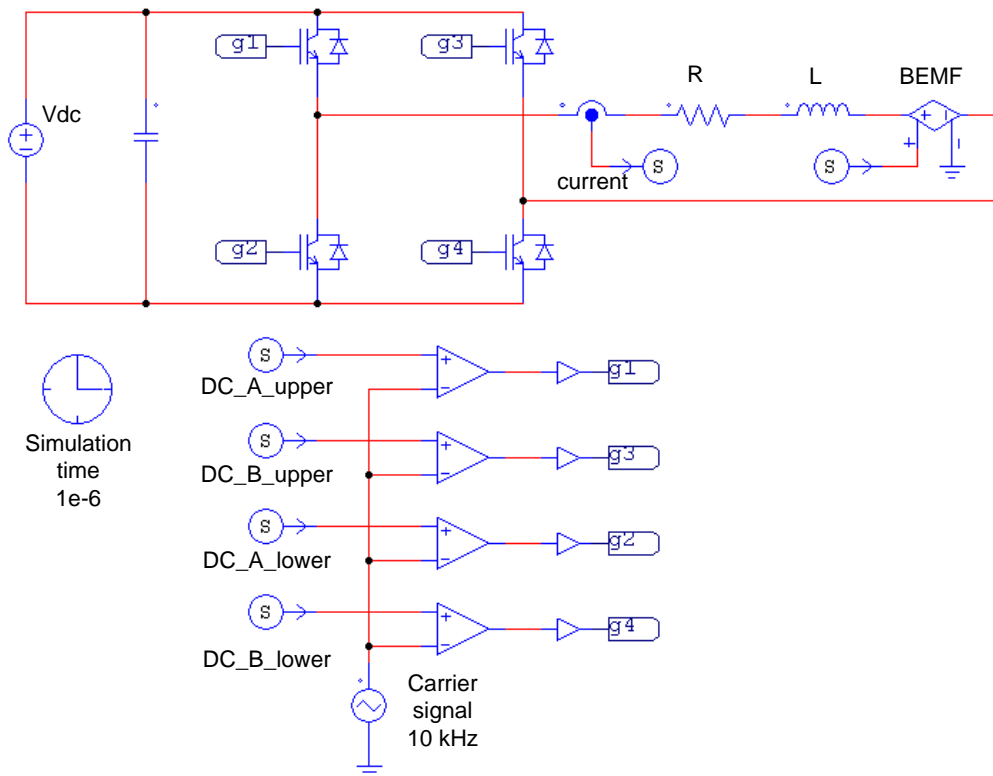


Figure 17. H-bridge converter simulation model

Since the considered load here is a blower or a fan, high dynamics are not needed and so, the soft switching (slow decay) PWM method is applied. Figure 18 shows the commutation logic block content.

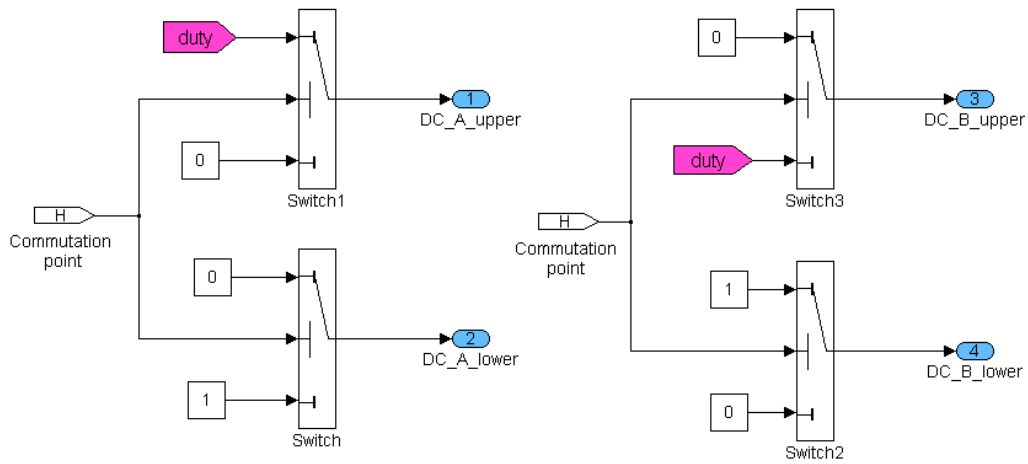


Figure 18. Soft switching block diagram

Only the upper transistors are commutated with the switching frequency, while the lower ones are commutated with the synchronous frequency.

3.4.2.1 Speed and torque closed loop control

Closed loop speed control with inner current control is employed here by using two PI controllers. A reference current (torque) is set by the PI speed controller based on speed error. To obtain the desired current an inner current control loop is used (Figure 19).

The current control loop employs a PI controller, which has the purpose to minimize the current error. The current error is fed to the PI current controller and the reference duty cycle is obtained. The duty cycle is applied to the power electronics switches using the PWM technique. In PWM control the motor is turned on and off at a high rate. The switching frequency is fixed but the length of duty cycle depends on the current error.

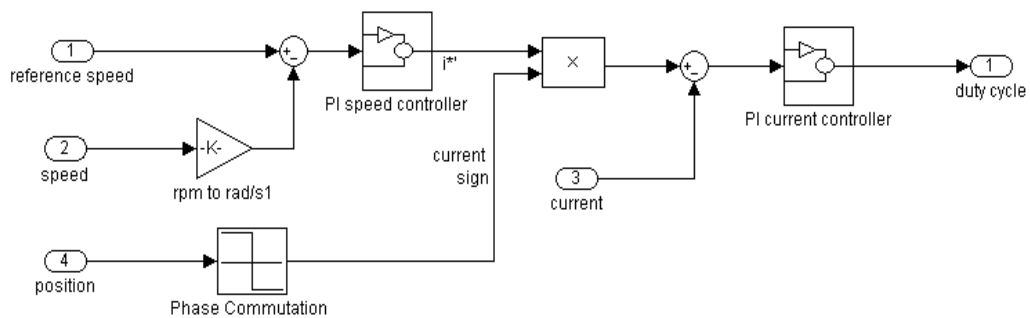


Figure 19. Speed and torque closed loop control overview

PI current controller design

Fast and accurate control of phase-winding current is possible only if the available supply voltage from the dc link is substantially greater than the BEMF, so that a surplus voltage is available to force current changes.

To design the PI current controller, first the zero-pole cancellation method was used. To simplify the analysis, the BEMF in the phase of the motor is neglected and so the motor can be approximated as a RL circuit.

By writing equation (1) in operational domain, the transfer function of a first order low pass filter is obtained, eq. (7):

$$H_p(s) = \frac{1}{L \cdot s + R} = \frac{K}{\tau_e \cdot s + 1} \quad (7)$$

$$K = \frac{1}{R}; \quad \tau_e = \frac{L}{R}$$

where K and τ_e are the gain and electrical time constant of the motor.

A PI controller with the transfer function given by (8) is used for a simplified tuning procedure.

$$H_{PI}(s) = k_p \left(1 + k_i \frac{1}{s} \right) = k_p \left(1 + \frac{1}{T_i \cdot s} \right) \quad (8)$$

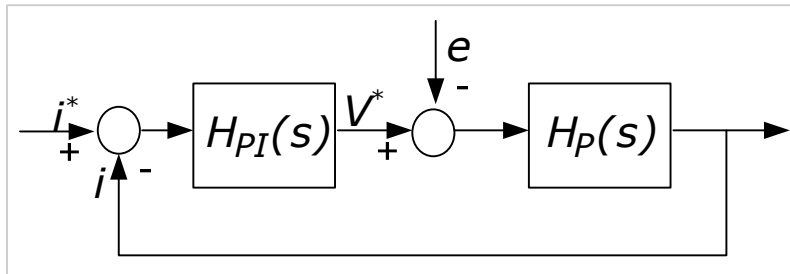


Figure 20. Current closed loop control

The closed loop transfer function of the current control loop (figure 20) is given by equation (9):

$$H_{CL}(s) = \frac{H_{PI}(s) \cdot H_p(s)}{1 + H_{PI}(s) \cdot H_p(s)} = \frac{k_p \left(\frac{T_i s + 1}{T_i s} \right) \cdot \frac{k}{\tau_e \cdot s + 1}}{1 + k_p \left(\frac{T_i s + 1}{T_i s} \right) \cdot \frac{k}{\tau_e \cdot s + 1}} \quad (9)$$

The integrator constant is chosen to eliminate the system highest time constant: $T_i = \tau_e$. Thus a 1st order system is obtained for the closed loop current control, given by the transfer function from equation (10):

$$H_{CL}(s) = \frac{\frac{k_p k}{T_i s}}{1 + \frac{k_p k}{T_i s}} = \frac{1}{\frac{T_i}{k_p k} s + 1} = \frac{1}{\frac{T_i R}{k_p} s + 1} = \frac{1}{\tau_{CL} s + 1} \quad (10)$$

For the obtained first order system the rise time t_r from 10% to 90% and the bandwidth $b = 1/\tau_{CL}$ are related as given by equation (11):

$$\tau_{CL} = \frac{1}{b} = \frac{t_r}{\ln 9} \approx 0.45 \cdot t_r \quad (11)$$

In order to increase the bandwidth of the current control loop, only the rise time t_r should be chosen and then the k_p can be determined from:

$$k_p = \frac{T_i \cdot R}{\tau_{CL}} = \frac{L}{\tau_{CL}} \quad (12)$$

In digital implementation the sampling and switching frequencies has to be considered when choosing the current closed loop time constant. In [28] the closed loop bandwidth is recommended to be selected at least 10 times smaller than the sampling frequency.

$$2 \cdot n \cdot f_s \geq 10 \cdot b \quad (13)$$

For the modeled motor with the electrical time constant $\tau_e = 2,2ms$ and for a chosen closed loop time constant $\tau_{CL} = 2 \cdot T_{PWM}$ ($T_{PWM} = T_s$) the obtained PI coefficients are:

$$k_i = \frac{1}{T_i} = \frac{1}{0.0022} \cong 450 \quad (14)$$

$$k_p = \frac{L}{2 \cdot T_{PWM}} = \frac{0.6 \cdot 10^{-3}}{2 \cdot 100 \cdot 10^{-6}} \cong 3 \quad (15)$$

For validation of current controller, the step response is presented in figure 21. The speed loop is disabled and a 1A reference current is set. The calculated torque from the motor model is fed back as load torque, which translates in zero speed and so the externally blocked rotor situation is simulated.

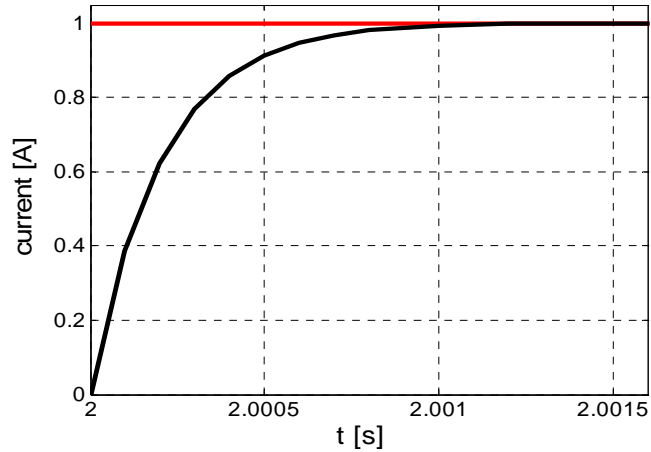


Figure 21. Current loop step response

In spite of its mechanical construction simplicity, the single phase bl dc motor imposes a few control problems. One is that the rotor position dependence of the BEMF impacts on the current control loop performance. Even at steady state the back EMF varies and is acting always as a disturbance.

In order to overcome this drawback, a BEMF compensation has to be added, or the PI controller has to be faster and its tuning has to be done based on parameters like rise time, settling time and overshoot, considering the closed loop system a second order system

Back-EMF compensation

Figure 22 illustrates the discrete time implementation of the PI current controller with BEMF compensation.

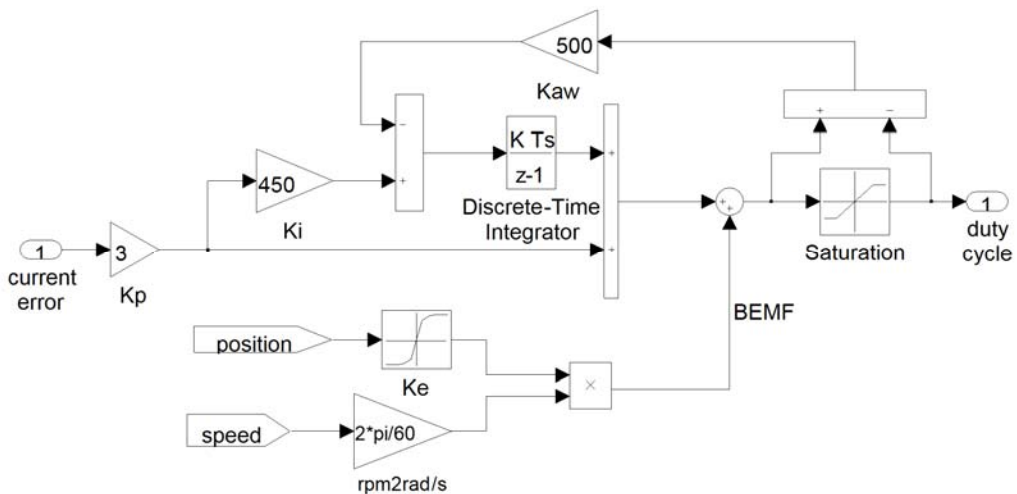


Figure 22. PI current controller with BEMF compensation

The scope of the BEMF compensation is to assure a better current regulation. For compensation the FE M based or the measured BEMF waveform dependence with position can be used. This is added to the output of the current controller resulting in smaller variations current controller output because the BEMF compensation term aim to assure the zero value for the current during any conditions. For BEMF compensation on the position and speed information is also needed.

The PI current controller contains also a saturation block which limits the duty cycle output to 1 in order for the comparison with the triangular carrier signal from PSIM to give correct resulting pulses. This limitation causes the integral part of PI controller to accumulate error, which will cause current overshoot because the integral part of the controller is still high when the current error becomes small. To avoid this, an anti windup back calculation is also used.

Figure 23 shows the current at 4000 rpm for both the situations with and without BEMF compensation. It is obvious that the usage of BEMF compensation helps the PI controller and the above design made by neglecting the BEMF can be applied.

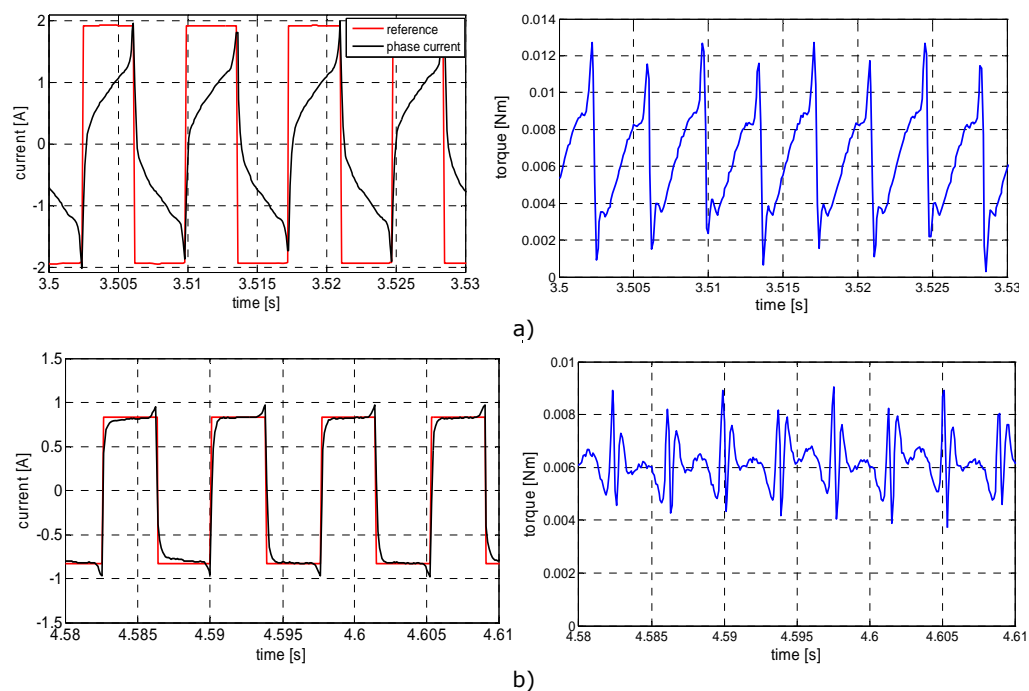


Figure 23. Simulation results for PI current (torque) control at a steady state speed of 4000 rpm: a) without BEMF compensation, b) with BEMF compensation

From figure 22 the improvement in the obtained torque waveform is visible. With the BEMF compensation also a current spike is noticed at each commutation point. This is caused by the introduced delay by inverter and by the fact that current controller is not quick enough, being limited by the switching frequency. Also it must be outlined that this is a medium current value, while the real current with the own switching pulsations visible is presented in figure 24.

3.4.2.2 Simulation results

A few simulation results for closed loop control based on measured position and speed from the machine model are illustrated further in order to demonstrate the digital simulation control system model accuracy.

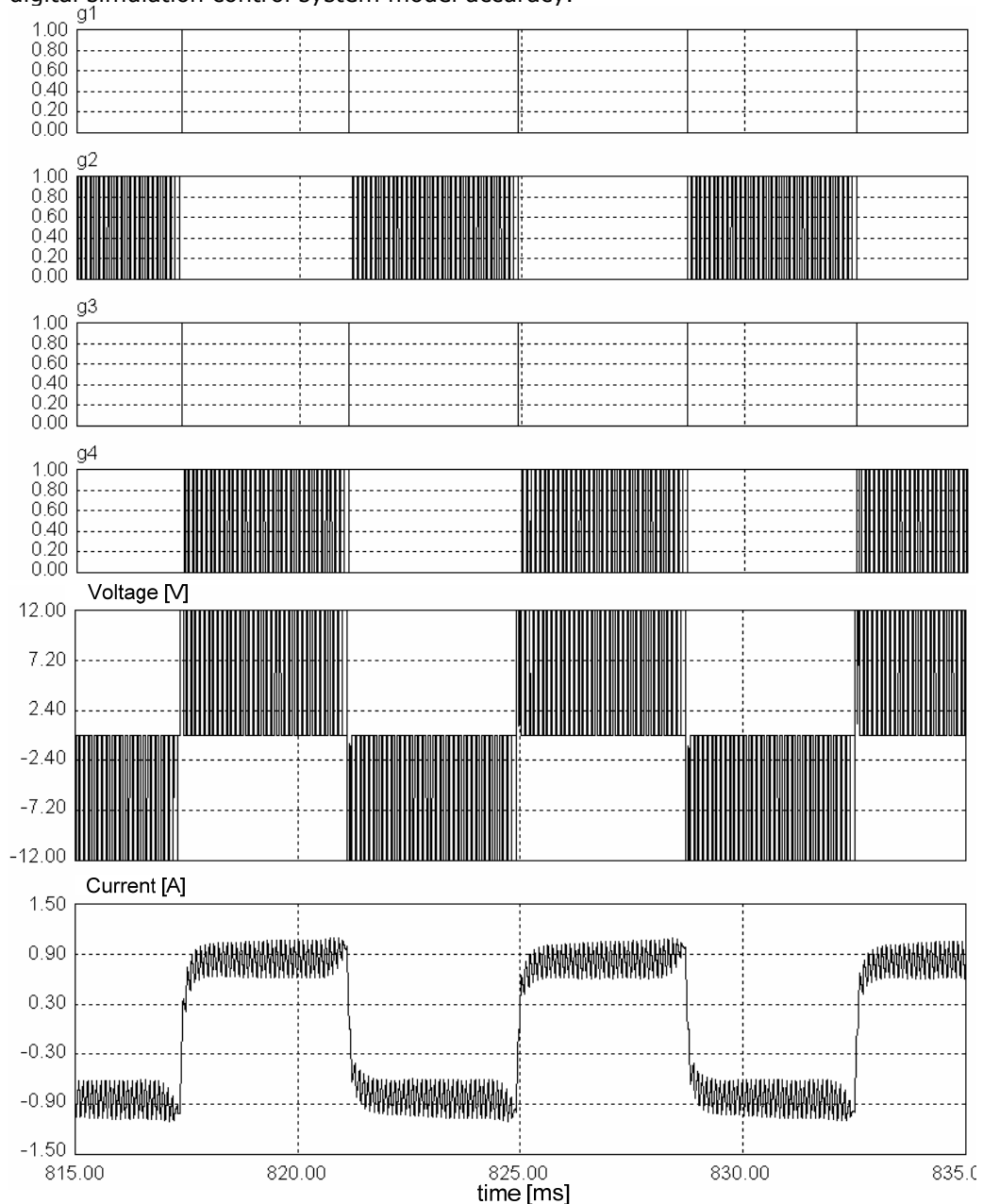


Figure 24. Simulation results from PSIM at 1us sampling period: from top to bottom, gate signals, phase voltage and phase current.

As mentioned before, the electrical part of the motor model and the inverter are running at 1 μ s sampling time, which allows us to have a better image over the system behavior. Figure 24 shows the transistors gate signals, the applied voltage and the phase current obtained from PSIM obtained from simulation for a steady state speed of 4000 rpm.

The high frequency current pulsation can be observed here due to the small sampling time. As in the experimental hardware implementation on dSpace test rig, this current is sampled in the connected Simulink model with 100 μ s. Figure 25 illustrates a comparison between the calculated phase current from PSIM and the received current by the control block from Simulink. The detailed image shows how the input current in the control is sampled and held at every PWM period.

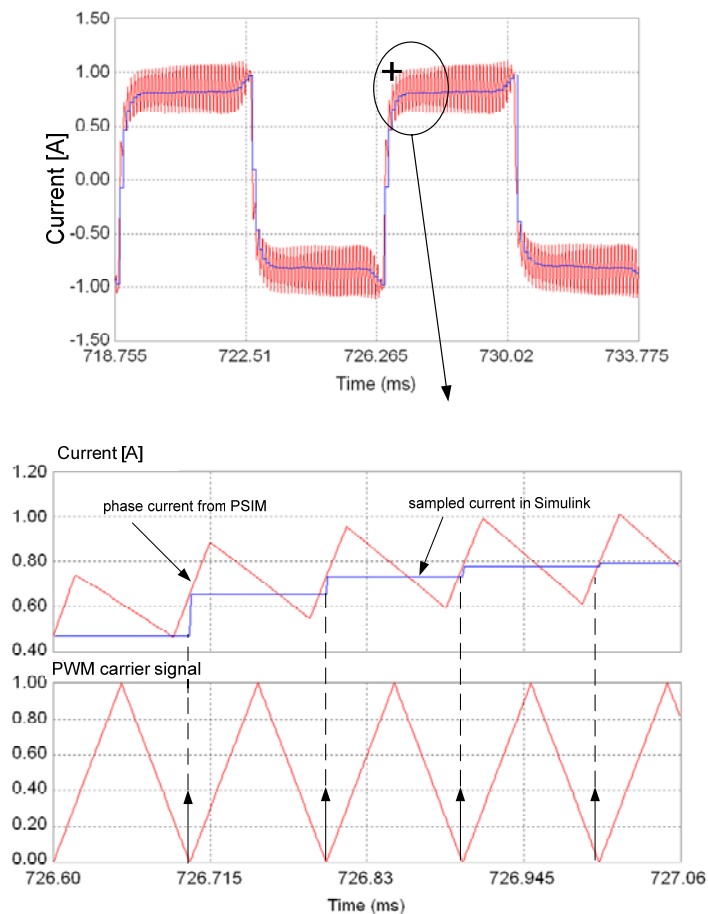


Figure 25. Phase current sample and hold

Further, a transient from 0 to 4000 rpm and then to 6000 rpm is illustrated (figure 26) and the obtained simulation results for the two steady state speed values are presented in figures 27 and 28. Due to the above presented sampling procedure of the current from PSIM at the input of the Simulink control block, the torque pulsations produced by PWM switching frequency are not visible anymore in

the simulation results. The same situation will be encountered when working on the dSpace platform.

As in the case of hysteresis current controller, the torque is again almost always positive, due to the accurate current control loop. It can be observed the the current, and so the developed torque is limited at the value of 4A.

From figures 27, 28 it can be noticed that the optimum torque is obtained due to the fact that the current is well regulated to be in phase with the back EMF. At 6000 rpm, this condition was accomplished by imposing an advanced commutation angle of 10 electrical degrees.

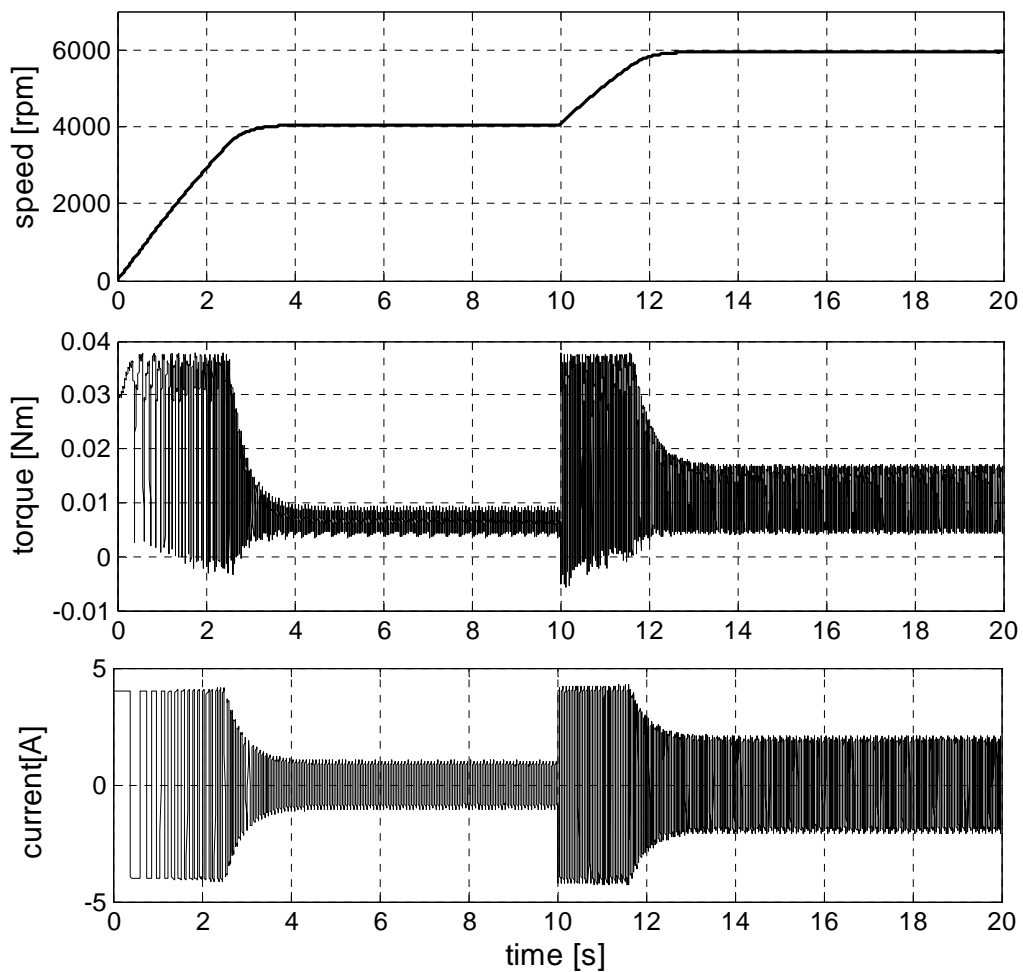


Figure 26. Digital simulation results for a speed step from 0 to 4000 rpm and then to 6000 rpm: a) speed, b) torque, c) phase current

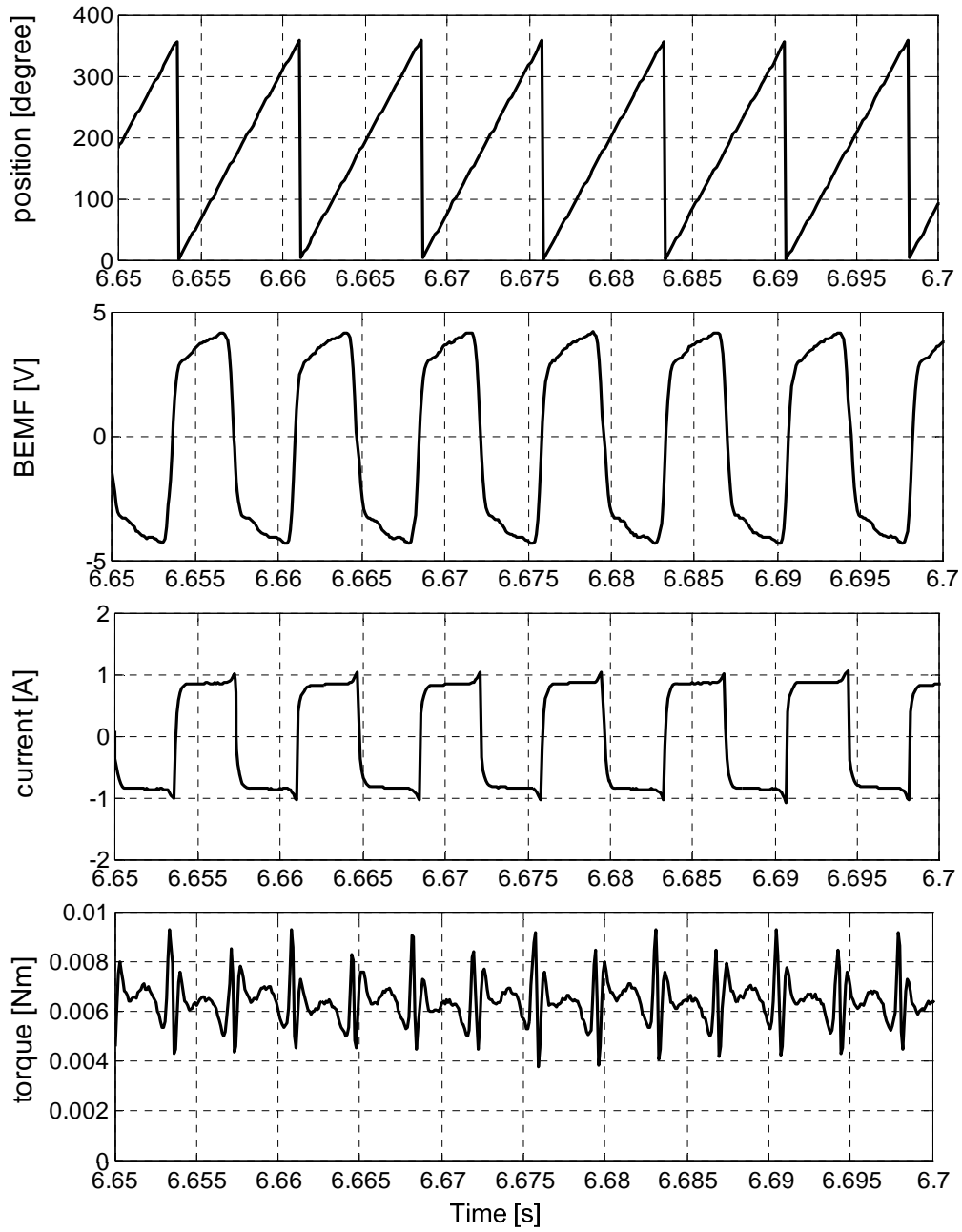


Figure 27. Digital simulation results for a steady state speed of 4000 rpm: position, BEMF, phase current and torque

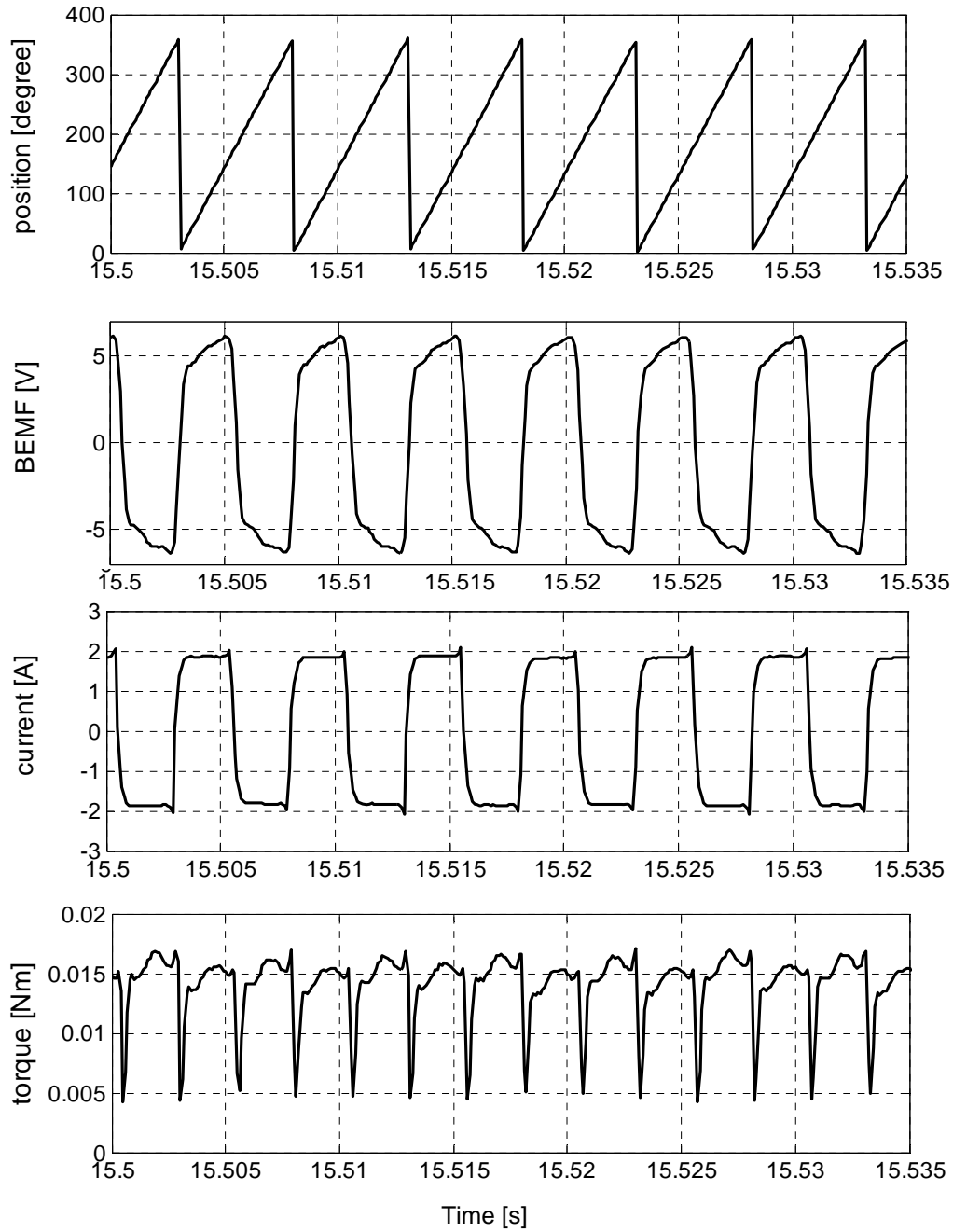


Figure 28. Digital simulation results for a steady state speed of 6000 rpm: position, BEMF, phase current and torque

3.5. Speed and position calculation from Hall sensor signal

In a practical implementation of a single phase PM-BLDC motor speed control usually one Hall sensor is used for current commutation in order to synchronize the BEMF and the phase current. If closed loop control is desired then the speed must be obtained from the Hall signal. In this case, the speed will be controlled by means of an outer speed loop that generates a speed error from the difference between the reference speed and the speed measured from Hall position sensor outputs using a PI regulator.

In order to test first a state observer for sensorless control purpose, the controlled motor must be run based on measured signals (speed, position).

Also, in order to validate a sensorless control, usually a high resolution position sensor is used.

In this section, continuous position information is obtained from the Hall sensor via a signal processing technique. In literature such a solution is presented in [25] for a 3 phase sinusoidal brushless drive. Improved solutions which allow also the starting of the motor with sinusoidal current are referred in [26], [27].

Here the calculated position from the Hall sensor is needed only as witness information in order to validate the proposed sensorless drive, but it also can offer an intermediate cost solution between encoder based and Hall based control when higher performance is needed without compromising the cost. Since this isn't the main topic of this thesis, only a simple signal processing method, based on zero order calculation algorithm, is applied here. If this solution is chosen for control, then the motor should be started based on Hall signal commutation fronts and then switch to the calculated position based control.

Basically the method consists in calculating the speed and then the position is calculated using as inputs the Hall signal and measured speed. Fig.29 shows the block diagram of speed and position computation based on Hall signal.

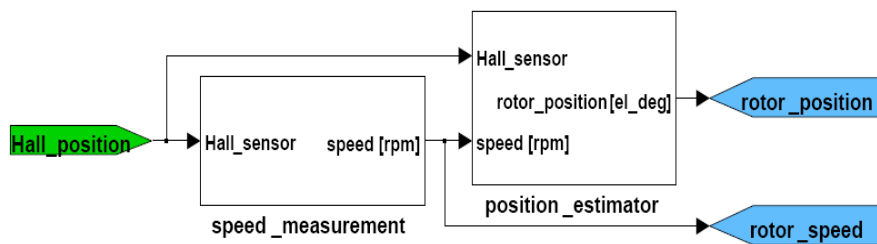


Figure 29. Speed and position computation block diagram

The speed calculation is done using the time difference between two consecutive Hall signal edges using equation .

$$\omega_{el} = \frac{\pi}{\Delta t} [\text{rad} / \text{s}] ; \omega_r = \frac{\omega_{el}}{p} \cdot \frac{60}{2 \cdot \pi} = \frac{60}{2 \cdot p \cdot \Delta t} [\text{rpm}] \quad (16)$$

where $\Delta t = k \cdot T_s$ represents the time interval between two consecutive edges given as a sum of sampling periods T_s , ω_r, ω_{el} are the rotor mechanical speed, respectively the electrical pulsation.

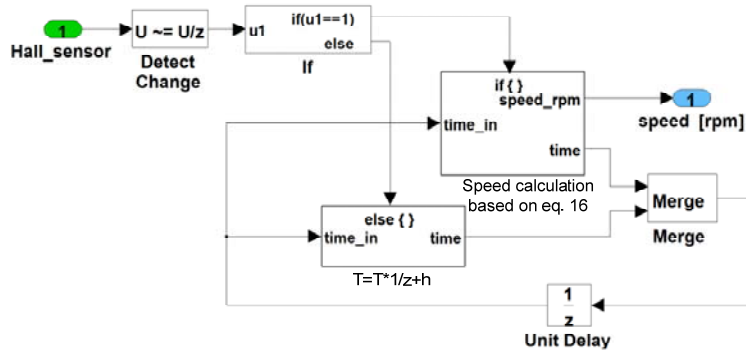


Figure 30. Speed calculation based on Hall signal edges.

Assuming a constant speed between this edge the position is further determined by integrating the calculated speed. The continuous position is corrected at every detected edge signal with the standard known position θ_k corresponding to 0 and π radians. Starting from the time moment t_k when a Hall edge is detected the position is further obtained by integrating the measured speed (eq. 17).

$$\theta(t) = \int_{t_k}^t \omega_{el}(t) \cdot dt + \theta_k \quad (17)$$

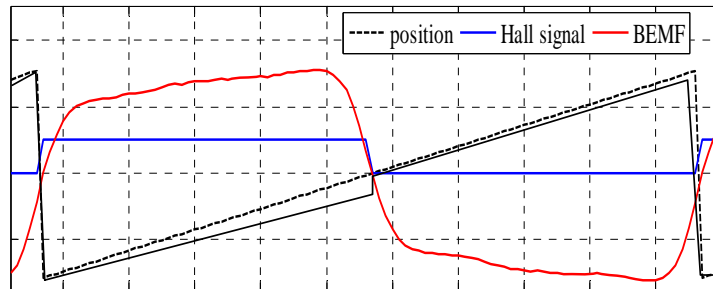


Figure 31. Detail on position calculation.

Figure 31 show the relation between the BEMF, Hall signal and the rotor position. It can be observed the way that the position is corrected on the encountered edge of Hall signal, as mentioned above. The case of a speed modification was chosen in order to make the correction visible. Under steady state condition the position is much better as will be seen.

For the real time implementation, the peculiarity of this method is that the integrator should be reset with proper initial condition on every edge of Hall signal in order to update the position information and to maintain the synchronization with the real rotor position. From figure 32 it can be observed that the digital integrator is

reset at every change detected in the Hall signal with different initial conditions if increasing or decreasing edge was detected.

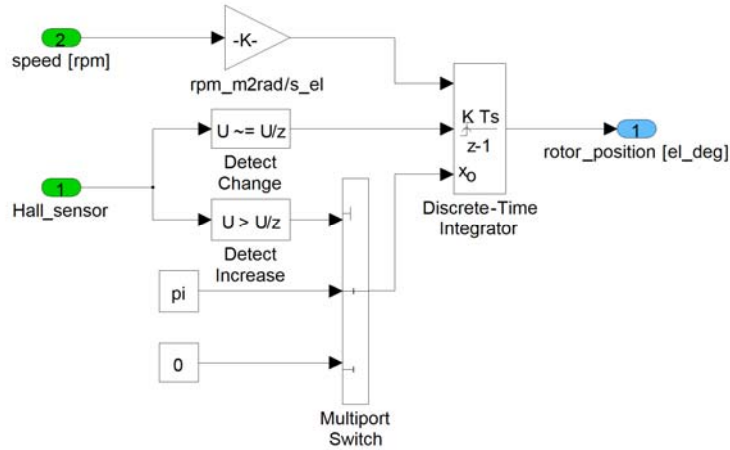


Figure 32. Position computation based on Hall signal edges

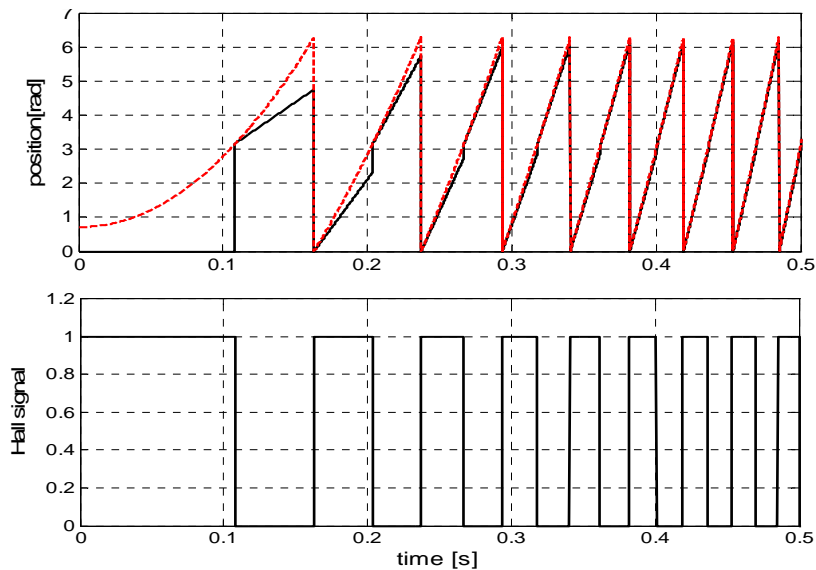


Figure 32. Simulation result during starting: a) real and calculated position, b) hall signal

The position extraction from Hall signal can be clearly seen during starting (figure 32), when low resolution speed information is obtained and so the position is not accurate. From figure 33.b a large position error can be noticed during starting.

This method of obtaining the speed has its limitation given especially by the low resolution of speed under starting and by the quantization errors caused by the limited sampling time. The combination of these two aspects produces less accurate information, which has to be considered when comparing with the estimated quantities for sensorless control purpose. Figure 32 illustrates by digital simulation the difference between the model speed and the Hall based calculated speed. In figure 32.a the above mentioned limitations are illustrated.

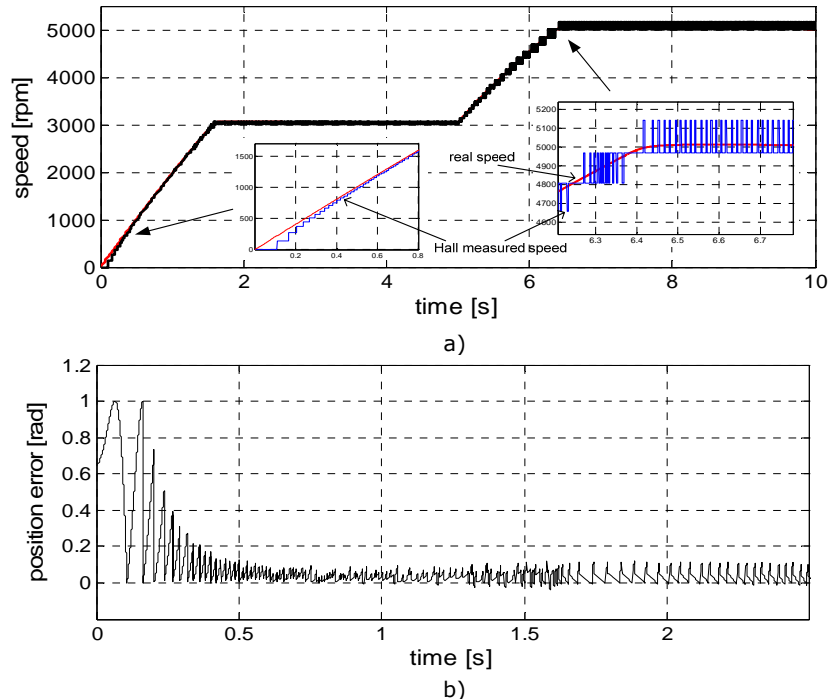


Figure 33. Simulation results for Hall based calculated : a) speed, b) position error

3.6 Conclusions

This chapter deals with the development of a detailed digital simulation environment for a single phase PM-BLDC motor drive system. The purpose of this chapter was to build a simple and accurate digital model, as close as possible to the real motor drive, for further control purposes.

First a methodology to accurately model the motor in Simulink environment using the FEM obtained characteristics (cogging torque, back EMF, inductance, and starting position) was presented and the model was validated under rectangular hysteresis current control. The benefits obtained by such a methodology are the ease of model construction and simulation.

Important aspects like sampling and switching frequency limitation, simulation time, power electronic commutation mode, practical implementation constraints like the need of additional external circuits for measuring the voltage are considered and the PI current controller was nominated to be used further in both, simulation and practical implementation of motor control system.

An advanced digital simulation model for the machine, power electronics converter and the control system was developed using a coupling between Simulink and PSIM software. A in-depth understanding of this model is necessary for further development and simulations of sensorless control schemes. This simulation environment was detailed and exemplified by simulation results for a closed loop speed control, based on the measured position and speed obtained from the machine model.

This model allows the user to simulate and implement the control algorithm and the state observer identically as it will be implemented on the realtime rapid

prototyping of software platform. This way the time consuming for real-hardware implementation can be reduced at minimum. In the same time it allows us to handle details as independent or complementary transistors gate PWM signals, dead time, sampling and switching frequency influence, soft switching or hard switching commutation influence etc..

In this work, from economical and technical constraints (the motor is under its natural load, being a blower and no place for encoder mounting is available) the speed and especially the position are obtained from the Hall sensor output using a signal processing technique. The limitations given by this method were detailed by simulation results.

It can be concluded that this chapter contributes to the simulation of electrical machines, power electronic converter and control system and that the developed digital model can produce a good prediction of drive behavior during both transient and steady state conditions, being adequate for implementing and testing the further proposed sensorless control methods.

References

- [1] P.J. Leonard and D. Rodger, "Modelling voltage forced coils using reduced scalar potential method," *IEEE Trans. on Magn.*, Vol. 28, No. 2, pp. 1615-1617, March 1992.
- [2] T. Dreher and G. Meunier, "3D line current model of coils and external circuits," *IEEE Trans. on Magn.*, Vol. 31, No. 3, pp. 1853-1856, May 1995.
- [3] F. Piviou and A. Razek, "Finite element analysis in electromagnetic systems accounting for electrical circuit," *IEEE Trans. on Magn.*, Vol. 29, No. 2, pp. 1669-1675, March 1993.
- [4] McDermott, T.E., Ping Zhou, Gilmore, J. and Cendes, Z., "Electromechanical system simulation with models generated from finite element solutions," *IEEE Trans. on Magn.*, Vol. 33, No. 2, pp. 1682-1685, March 1997.
- [5] Kay Hameyer, Johan Driesen, Herbert De Gerssem and Ronnie Belmans, "The Classification of Coupled Field Problems," *IEEE Trans. on Magn.*, Vol. 35, No. 3, pp. 1618-1621, May 1999.
- [6] J. Vaananen, "Circuit theoretical approach to couple two-dimensional finite element models with external circuit equations," *IEEE Trans. on Magn.*, Vol. 32, No. 2, pp. 400-410, March 1996.
- [7] Abe, N.M. and Cardoso, J. R. 1998: "Coupling Electric Circuit and 2D-FEM Model With Dommel's Approach for Transient Analysis", *IEEE Transactions on Magnetism*, Vol. 34, No. 5, September 1998, pp. 3487-3490.
- [8] Bedrosian, G. 1993: "A New Method for Coupling Finite Element Field Solutions with External Circuits and Kinematics", *IEEE Transactions on Magnetism*, Vol. 29, No. 2, March 1993, pp.1664-1668.
- [9] Fu, W.N., Zhou, P., Lin, D., Stanton, S., and Cendes, Z.J. 2004: "Modeling of Solid Conductors in Two-Dimensional Transient Finite-Element Analysis and Its Application to Electric Machines", *IEEE Transactions on Magnetism*, Vol. 40, No. 2, March 2004, pp. 426-434.
- [10] Preston, T.W., Reece, A.B.J., and Sangha, P.S. 1991a: "Analysis of Switched Reluctance Drives by the Finite Element Time-Stepping Method", *IEEE Fifth International Conference on Electrical Machines and Drives*. London, UK, September 11-13, 1991, pp. 81-85.
- [11] Sadowski, N., Carly, B., Le fevre, Y., La joie-Mazenc, M., and Astier, S. 1993: "Finite Element Simulation of Electrical Motors Fed by Current Inverters", *IEEE Transactions on Magnetism*, Vol. 29, No. 2, March 1993, pp. 1683-1688.
- [12] Oliveira, A.M., Kuo-Peng, P., Sadowski, N., de Andrade, M.S., and Bastos, J.P.A. 2002: "A Non-a priori Approach to Analyze Electrical Machines Modeled by FEM Connected to

- Static Converters", IEEE Transactions on Magnetics, Vol. 38, No. 2, March 2002, pp. 933-936.
- [13] Demenko, A. 1994: "Time-Stepping FEM Analysis of Electric Motor Drives with Semiconductor Converters", IEEE Transactions on Magnetics, Vol. 30, No. 5, September 1994, pp. 3264-3267.
- [14] Ahn, S.C., Lee, J.H., and Hyun, D.S. 2000: "Dynamic Characteristic Analysis of LIM Using Coupled FEM and Control Algorithm", IEEE Transactions on Magnetics, Vol. 36, No. 4, July 2000, pp. 1876-1880.
- [15] Ho, S.L., Fu, W.N., Li, H.L., Wong, H.C., and Tan, H. 2001: "Performance Analysis of Brushless DC Motors Including Features of the Control Loop in the Finite Element Modeling", IEEE Transactions on Magnetics, Vol. 37, No. 5, September 2001, pp. 3370-3374.
- [16] Jabbar, M.A., Phyu, H.N., and Liu, Z.J. 2004: "Analysis of the Starting Process of a Disk Drive Spindle Motor by Time Stepping Finite Element Method", IEEE Transactions on Magnetics, Vol. 40, No. 4, July 2004, pp. 3204-3206.
- [17] S. Kanerva, "Simulation of electrical machines, circuits and control systems using finite element method and system simulator", PhD. Dissertation, Helsinki University of Technology, Finland, 2005.
- [18] Z.Q. Zhu, S. Bentouati, D. Howe, "Control of single-phase permanent magnet brushless DC drives for high-speed applications", record of Power Electronics and Variable Speed Drives, 2000, pp. 327-332.
- [19] L. Iepure, L. Tutelea, I. Boldea, "FEM analysis and control of a tapered airgap single phase PMSM", record of OPTIM-2008, pp 241-248.
- [20] W.C. Chen, Y.Y. Tzou, "Efficiency optimization control for single-phase brushless dc fan motors", Record of IPEMC, May 2009, pp. 1913-1918.
- [21] J.S. Mayer and O. Wasynczuk, "Analysis and modeling of a single-phase brushless DC motor drive system", IEEE Trans. Energy Conversion, vol. 4, no. 3, pp. 473-479, Sep. 1989
- [22] Z.Q. Zhu, Y. Chen, Y. Li, D. Howe, J. H. Glemenn, "Dynamic modeling of a high-speed single phase PM brushless DC drive", record of PEMD, Mar. 2006, pp. 484-488
- [23] K. B. Jang, S. H. Won, T. H. Kim, Ju Lee, "Starting and High-Speed Driving of Single-Phase Flux-Reversal Motor for Vacuum Cleaner", Trans on Magnetics, vol. 41, no. 10, Oct. 2005, pp. 3967-3969.
- [24] J. Böcker, "Advanced Hysteresis Control of Brushless DC Motors", Deutsch-Koreanisches Symposium, Aachen, 2004
- [25] „Automotive full bridge mosfet driver“, Allegro, application note
- [26] "3953 Full bridge PWM motor driver", Allegro, datasheet
- [27] "BLDC motor control with Hall effect sensors using the 9S08MP". Freescale Semiconductor, Inc., document number AN4058.
- [28] M. P. Kazmierkowski, R. Krishnan, F. Blaabjerg, "Control in Power Electronics", Academic Press, 2002.
- [29] S. Morimoto, M. Sanada, Y. Takeda, "Sinusoidal Current Drive System of Permanent magnet synchronous motor with low resolution position sensor", Proc. of IEEE IAS Annual Meeting, pp. 9-13, Oct. 1996.
- [30] S. Morimoto, M. Sanada, Yoji Takeda, "High-performance current-sensorless drive for PMSM and SynRM with only low-resolution position sensor", IEEE Transactions on Industry Applications, vol. 39, no. 3, May/June 2003, pp. 792-801
- [31] F. G. Capponi, G. De Donato, L. Del Ferraro, O. Honorati, M. C. Harke, R. D. Lorenz, "AC brushless drive with low-resolution Hall-effect sensors for surface-mounted PM machines", IEEE Transactions on Industry Applications, vol. 42, no. 2, March/April 2006, pp. 526-535.

4. MOTION SENSORLESS CONTROL OF SINGLE PHASE BRUSHLESS D.C. PM MOTOR DRIVE BASED ON PRIOR KNOWLEDGE OF PM FLUX VS. POSITION

Abstract

A motion sensorless control for single phase permanent magnet brushless d.c. (PM-BLDC) motor drives, based on flux estimation and prior knowledge of the PM flux/position characteristic is proposed in this chapter and an adequate correction algorithm is adopted, in order to increase the robustness to noise and to reduce the sensitivity to accuracy of flux linkage estimation.

The chosen solution for estimating the PM flux linkage and the the rotor position and speed is detailed and exemplified using digital simulation results and then validated by experimental results.

For experimental validation, first, a speed and current closed loop control is employed based on the Hall signal and the motor is controlled at different speeds in order to validate the proposed estimation algorithm with satisfying results. The position correction effect is analyzed by examination of improvements in both position error and speed pulsations.

To further validate the proposed motion sensorless control system by experiments, the motor is runned on closed loop sensorless control and experimantal results are presented.

When running on sensorless closed loop control, an I-f strategy is used for starting, by prescribing a ramped reference frequency and a constant current, and then the seamless transition to closed loop sensorless control takes place.

4.1. Introduction

Typically one Hall sensor is used to control the current commutation in order to maximize the torque output by keeping the back EMF and the current in phase. This condition can not be achieved over a wide speed range without using the advance commutation angle technique as assessed in [1-3]. Also references [4-7] propose adaptive commutation angle methods for efficiency and torque improvement, requiring some extra hardware.

Under open loop PWM control, a current spike during each commutation appears. This results in acoustic noise, increased electronic cost, torque pulsations and low efficiency. One solution is to use the above mentioned phase advance technique, while reference [8] proposes a tail end current control. Also, in [9] the necessity of current shape control for improving the efficiency and to avoid the over dimensioning of the power electronics devices was referred to. Here the current is controlled based on one Hall output signal which is proportional to the intensity of the induced rotor field and so is identical with back-EMF. But, due to the fact that

the torque envelope is related to the winding current shape and the motor driving methods, a particular current shape (different from the BEMF shape) for smoothing the torque can be calculated based on a prior FEM analysis [10][11]. In [12] using the Lagrange multiplier an optimal current waveform for low copper losses and low torque ripple was introduced. For this purpose high resolution position information and a microcontroller are needed.

To reduce the cost and improve the reliability the position sensor can be eliminated. While numerous papers concerning position and speed estimation of 3 phase PMSM have been published, the field of single phase has not reached the same level of maturity. Like in the case of 3 phase BLDC motors, there are basically two types of sensorless control techniques. The first one is based on back EMF (BEMF) sensing using a second coil [13] or via the winding time-sharing method, as described in [14] while the second method is based on online flux estimation.

Considering the above, the sensorless estimation of a continuous position information could be an appreciable feature for customized applications, reducing the problem related to the Hall alignment procedure and the extra circuits needed for commutation phase advance angle and delivering a high resolution position for current shaping.

Although the cost is relatively higher in the case of sensorless control based on the on-line analysis of the voltages and currents in the machine winding, due to necessity of a DSP for the online computation, it has some advantages like higher torque/ current when using the whole 180 degrees interval, the possibility of torque pulsation reduction by current shaping and a higher resolution speed information.

In this chapter a novel motion sensorless control of a single phase brushless d.c. PM motor drive, based on a FEM assisted position and speed observer is presented and then validated by experimental results. The FEM assisted position observer is based on the online estimation of PM flux linkage.

4.2 PM flux estimator

The implemented PM flux estimator is based on a voltage model in stator reference. The estimator uses the applied voltage and the phase current for estimating the magnetic flux.

Starting from machine voltage equation 1, the PM flux linkage can be extracted from eq.2 by integrating the electromotive force (EMF), based on equation 3.

$$v = R \cdot i + L \cdot \frac{di}{dt} + e \quad (1)$$

$$v = R \cdot i + L \cdot \frac{di}{dt} + \frac{d\psi_{PM}}{dt} \quad (2)$$

$$\psi_{PM} = \int_0^t (v - R \cdot i) \cdot dt - L \cdot i \quad (3)$$

Where V is the input voltage, i is the phase current, R is the resistance, L is the winding inductance and ψ_{PM} is the permanent magnet flux linkage, respectively.

In practice, the flux estimation through an ideal integrator is problematic. Any dc offset in the measured current and voltage produces a ramp-drift which eventually lead the integrator into saturation, and also an incorrect initial value of the integrator produces a DC-offset on the output signal [15].

In this section, a flux linkage estimator based on an equivalent integrator using the voltage model is implemented. A PI correction feedback (V_{comp}) was used here together with an ideal integrator in order to overcome the above mentioned problems.

Using the compensation voltage, equation 3 becomes:

$$\psi_{PM} = \int_0^t (v - R \cdot i - V_{comp}) \cdot dt - L \cdot i \quad (4)$$

where:

$$V_{comp} = k_p \cdot \psi_s + k_i \cdot \int_0^t \psi_s \cdot dt \quad (5)$$

Transforming equation 4 and 5 from time domain to operational domain, the closed loop transfer function given by relation 6 is obtained.

$$H(s) = \frac{\hat{\psi}_s}{e} = \frac{s}{s^2 + k_p \cdot s + k_i} \quad (6)$$

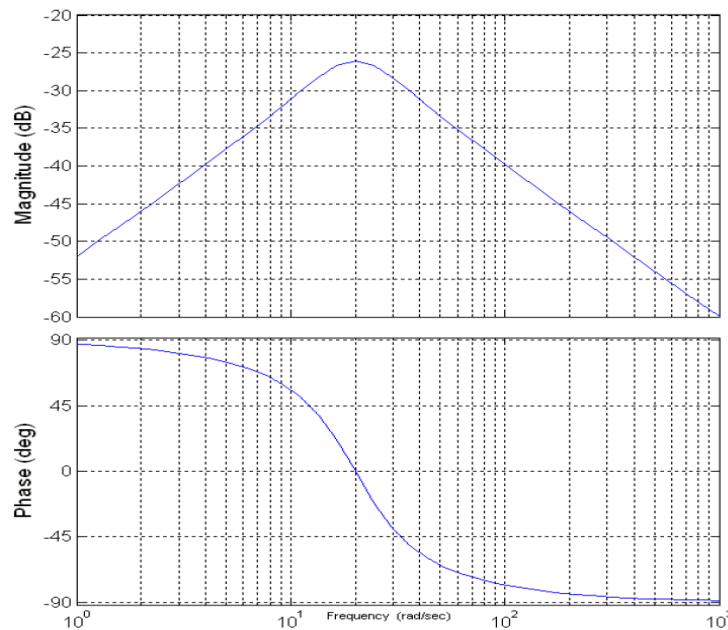


Figure 1. Bode characteristics of the flux estimator

Figure 1 shows the magnitude and phase frequency response of the resulting flux integrator transfer function. The PI constants are $k_p = 20[s^{-1}]$ and $k_i = 400[s^{-2}]$ so that the transfer function to behave like a pure integrator from an angular frequency of $\omega = 10 \cdot \omega_c$, where $\omega_c = 20rad/s$ is the cutoff pulsation.

The voltage information can be measured or it can be reconstructed from the PI current controller output and dc link voltage. Here, instead of using the measured phase voltage, the PI current controller output multiplied with the dc link voltage is used as voltage input for the flux estimator. This will reduce the cost and will improve the drive robustness to noise and also we won't need a LPF like in the case of measured voltage which can delay the signal. The drawback is that at low speed the voltage drop on the power switches has to be considered.

Considering the soft switching commutation method applied (as presented in chapter 3), it can be demonstrated that the output from the current controller can be used as voltage estimation.

For $sign(i_{reference}) > 0$ the phase voltage can be written as eq. 7 shows:

$$v(t) = \begin{cases} V_{dc}; 0 < t < t_{on} \\ 0; t_{on} < t < T \end{cases} \quad (7)$$

The medium voltage value over a PWM period is given in eq 8:

$$v = \frac{1}{T} \int_0^{t_{on}} v(t) \cdot dt = \frac{t_{on}}{T} \cdot V_{dc} = D \cdot V_{dc} \quad (8)$$

The same relation applies for $sign(i_{reference}) < 0$, the phase voltage can be written as eq. 9 shows:

$$v(t) = \begin{cases} -V_{dc}; 0 < t < t_{on} \\ 0; t_{on} < t < T \end{cases} \quad (9)$$

And the again the medium voltage over a PWM period is given by eq. 10:

$$v = \frac{1}{T} \int_0^{t_{on}} v(t) \cdot dt = -\frac{t_{on}}{T} \cdot V_{dc} = -D \cdot V_{dc} \quad (10)$$

Thus, for both current polarities, the phase voltage can be written as the product of the reference duty cycle and dc link voltage, and so, a final voltage estimation relation is given by equation 11.

$$v = sign(i_{reference}) \cdot D \cdot V_{dc} \quad (11)$$

Figure 2 shows, by simulation results, a comparison between the measured phase voltage and the estimated one, which in fact is the reference voltage.

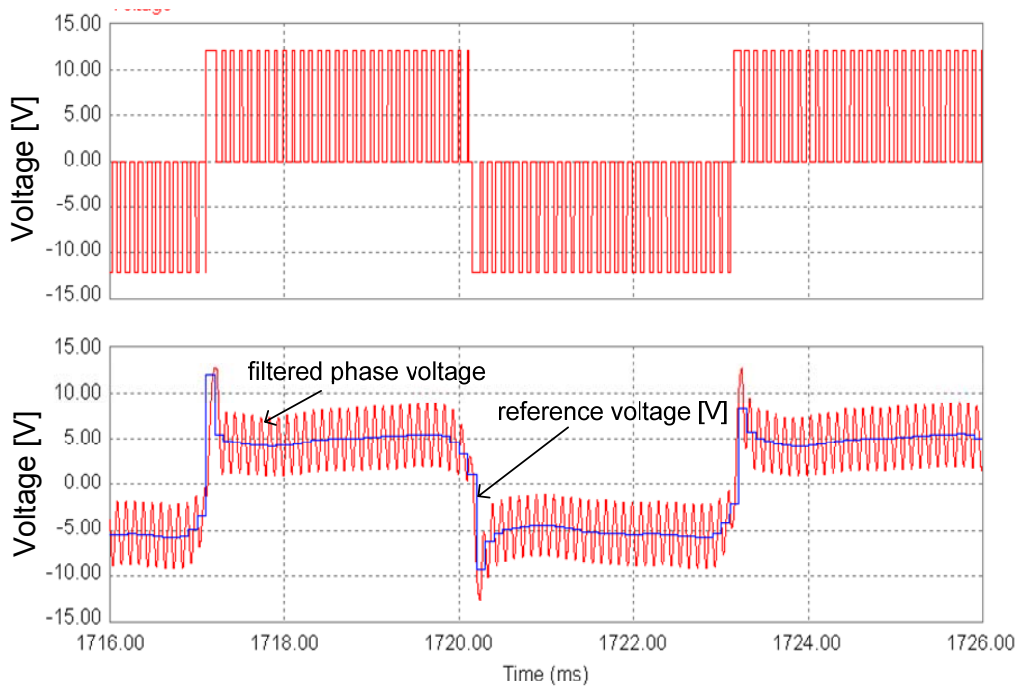


Figure 2 Simulation results for voltage estimation explicative

The resulting flux linkage estimator is in fact a reference voltage model in stator reference frame. Figure 3 presents the discrete-time implemented diagram of the PM flux estimator in Matlab/Simulink.

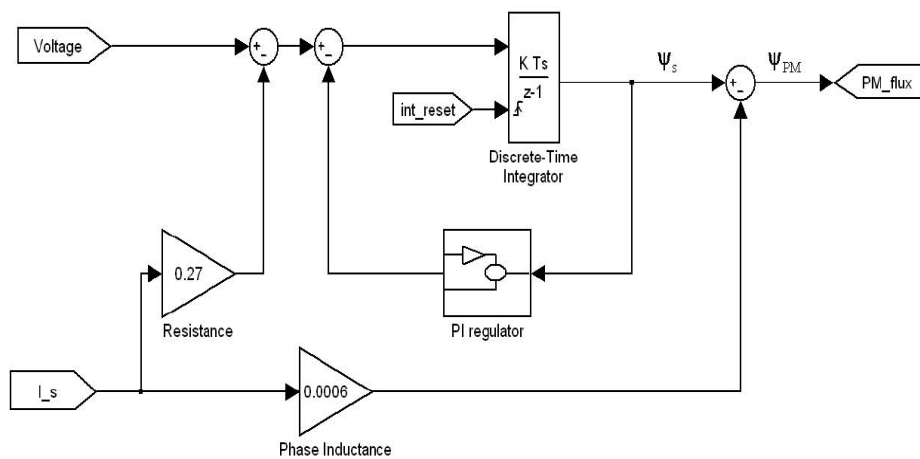


Figure 3. Flux estimator

Figure 4 illustrates the estimated total flux and PM flux obtained by simulation from the shown input voltage signal and phase current at a steady state speed of 5000 rpm.

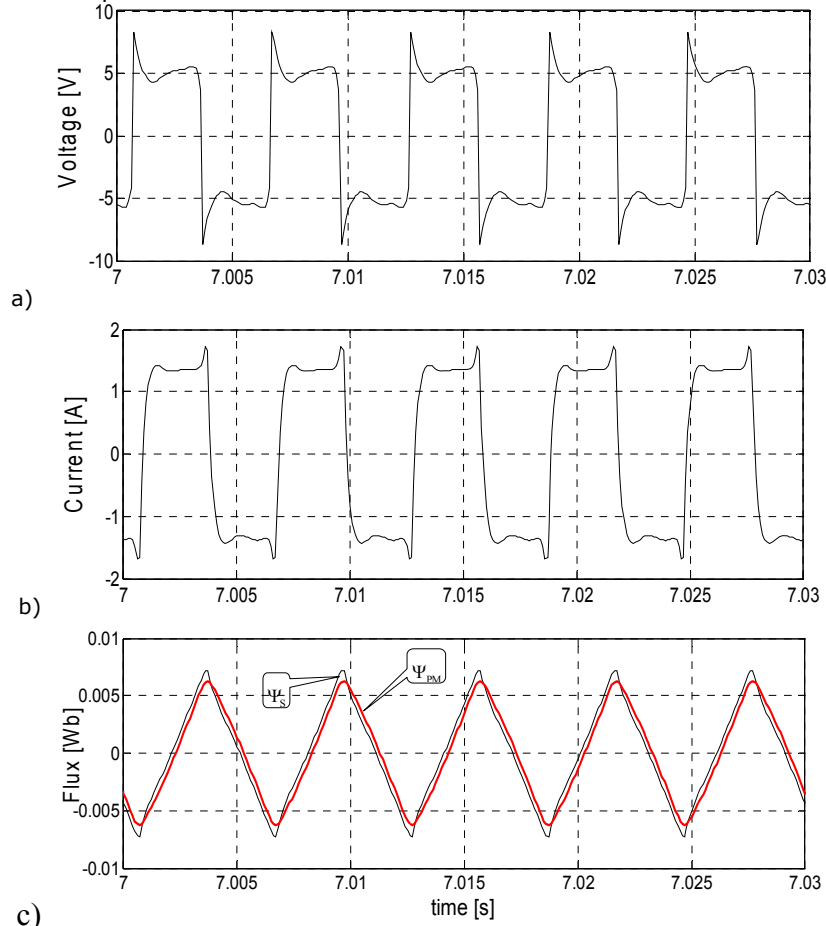


Figure 4. PM flux estimator inputs and output: a) applied voltage b) phase current, c) estimated total flux and PM flux

4.3 FEM based position estimator

The position estimator is based on the estimated PM flux dependence with position. In order to determine the PM position, a prior knowledge of the $\Psi_{PM}(\theta)$ characteristics of the motor is required. This is obtained either from a FEM based analysis in the design stage or by measuring the BEMF voltage and then integrate it. The BEMF can be measured by running the motor at high speed and then release the motor to free running, zero current value, and measure the terminal voltage. In [16] the electrical parameters and motor characteristics like back emf and PM flux linkage versus rotor position are determined by using both finite element method and measurements.

Basically the estimated position is extracted by comparing the estimated flux with a lookup table which contains the position versus the PM flux linkage.

Due to the fact that the flux linkage does not have a monotonous variation with rotor electrical position, the sign of estimated flux linkage derivative has to be considered also.

In order to avoid the errors caused by current measurement, the derivative of the total flux linkage ψ_s is used.

Figure 5 illustrates the block diagram of the proposed position estimator.

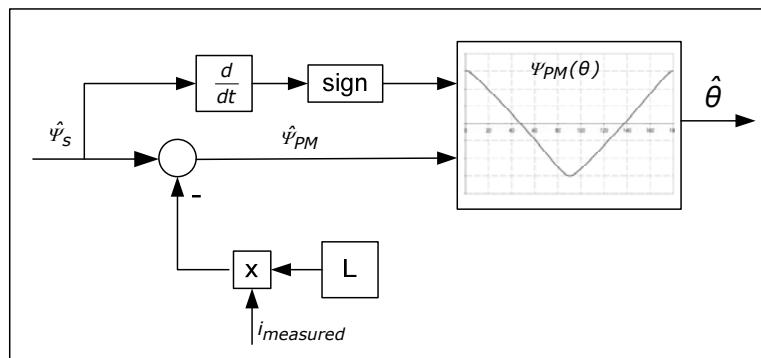


Figure 5. Position estimator

The estimated position obtained by digital simulation results using the structure from figure 5 is presented next in figures 6 and 7. The estimated and FEM measured PM flux linkage are presented in order to see the correspondence with the extracted position.

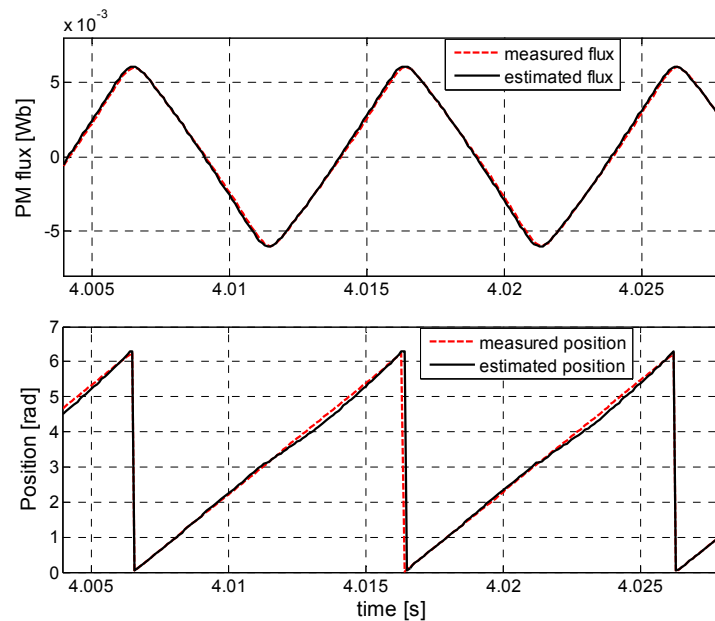


Figure 6. Digital simulation result at 3000 rpm: a) PM flux linkage, b) electrical position

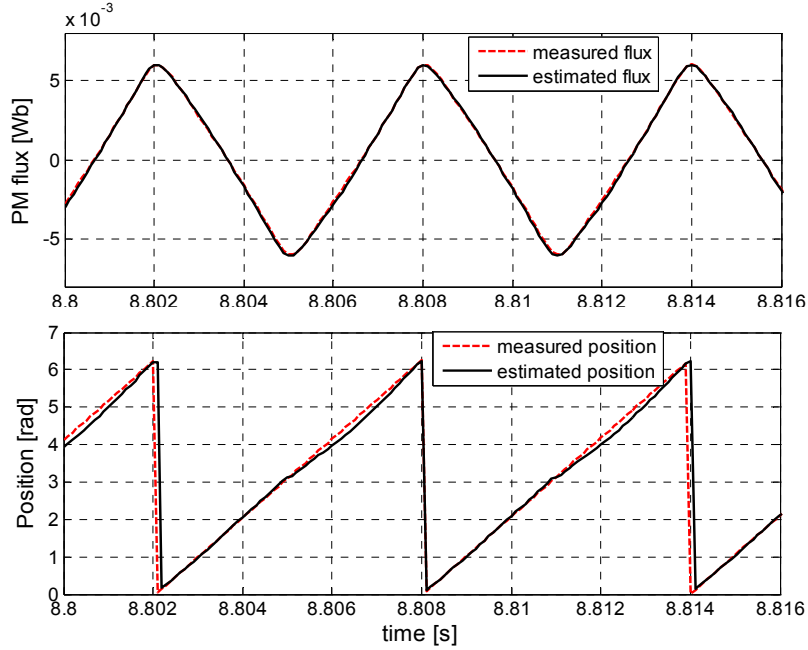


Figure 7. Digital simulation result at 5000 rpm: a) PM flux linkage, b) electrical position

It was noticed that this position estimation is very sensitive to the accuracy of the PM flux linkage estimation, including its amplitude and phase angle.

The most important problems in determining the PM position arises at the top values of the flux because the magnitude does not exactly match the one from lookup table and this produces discontinuities in the estimated position. Figure 8 shows the two cases that can occur.

In order to eliminate this problem and increase the estimator performance, a correction algorithm based on the estimated position derivative limitation is adopted.

Regarding the position estimation we can write equation (12)

$$\hat{\theta}_k = \hat{\theta}_{k-1} + \hat{\omega} \cdot T_s \quad (12)$$

where $\hat{\theta}_k$ is the present estimated position, $\hat{\theta}_{k-1}$ is the last estimated position and the estimated speed $\hat{\omega}$ and the sampling time T_s product gives the estimated position increment.

The correction basically consists in prescribing lower and upper bounds for the position derivative by using the position estimated increment, as in [17]. For this purpose the inequality (13) must be satisfied.

$$k_2 \cdot \hat{\omega} \cdot T_s < \hat{\theta}_k - \hat{\theta}_{k-1} < k_1 \cdot \hat{\omega} \cdot T_s \quad (13)$$

Where k_1 and k_2 decide how tight the position derivative limits should be.

The basic idea of this algorithm is that two parallel positions are build: if relation (13) and the flux derivative sign condition are satisfied then the position is extracted from lookup table (continuous lines from Fig.8) else each one of these two positions is constructed based on equation (12) (dotted lines from Fig.8). The final corrected position is the average of these two (the red line from Fig.8).

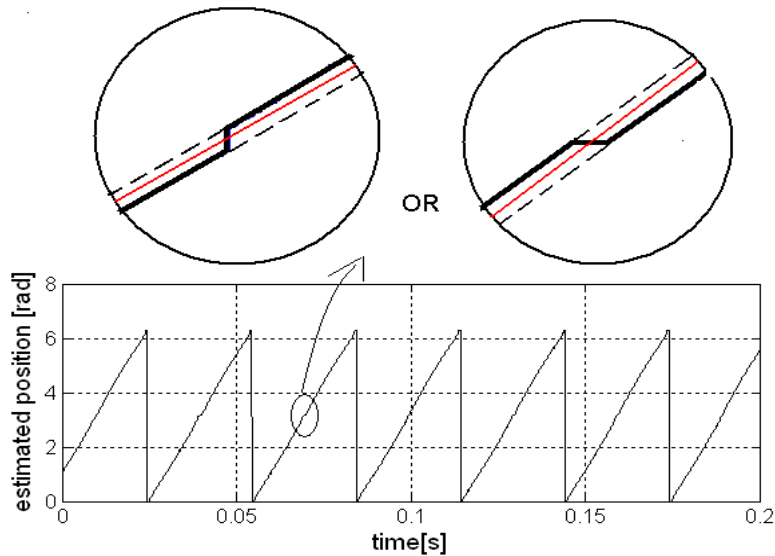


Figure 8. Possible position errors

Figure 9 shows the improvement on the estimated position at 1000 rpm, while Figure 10 presents the described correction algorithm implemented in Matlab/Simulink.

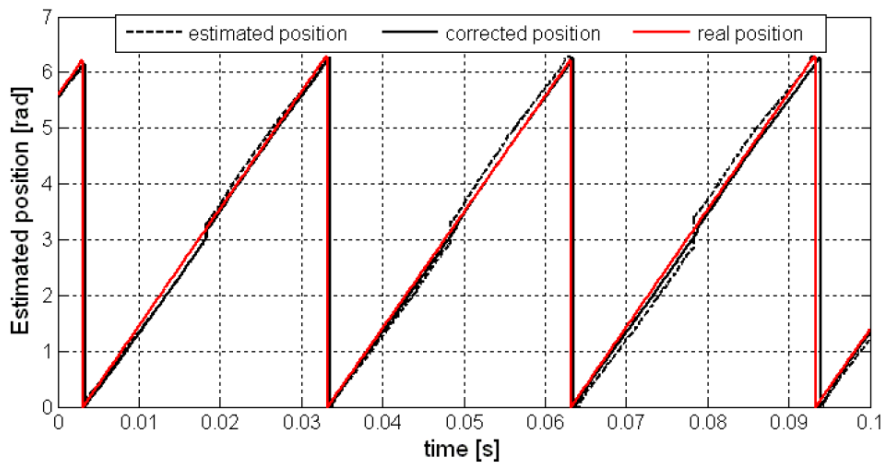


Figure 9 Estimated and measured position at 1000 rpm

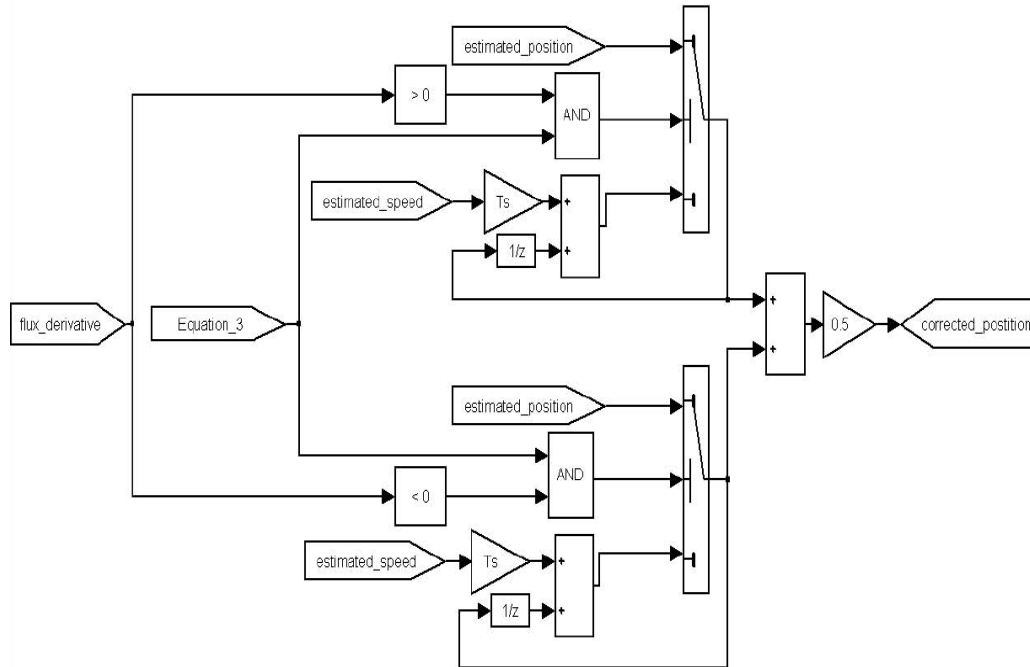


Figure 10. Position correction algorithm

Figure 11 presents the block diagram of the overall estimation algorithm, showing the interconnections between the described so far components.

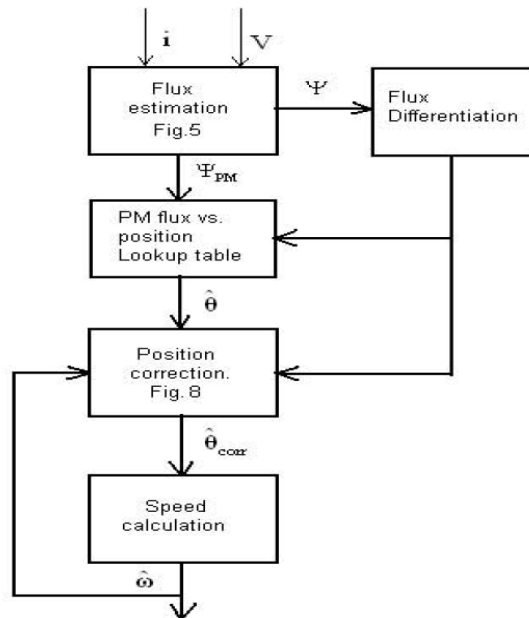


Figure 11. Block diagram of the proposed algorithm

We can see that, in fact, the block diagram consists in an autocorrecting position and speed closed loop estimator. The current estimated position depends on the last speed value and the next speed value depends on the calculated position. So the speed calculation further is mandatory, in order to have a good estimated position, even if the speed closed loop control in some simplified control schemes may not be needed.

4.4 Speed estimator

Two methods for speed estimation were used. In one case the speed information has the same resolution like that from the Hall sensor and in the other case the speed is actualized on each sampling period.

The first speed estimation method is based on a virtual Hall signal obtained from the estimated position. The rotor speed is calculated on the basis of time difference between two consecutive edges.

For speed calculation using this first method, the discrete time implementation makes use of equation (4).

$$n[rpm] = \frac{60}{N \cdot T_s \cdot 2 \cdot p} \quad (4)$$

Where N is the number of sampling periods between two consecutive edges, T_s is the sampling period and p represents the pole pairs number.

On the other hand, having continuous position estimation gives us the possibility to use speed information with a high refresh rate. The estimated speed information is obtained further by differentiating the estimated rotor position. The main disadvantages of obtaining the speed from position differentiation is the speed noise and oscillations, which highly depend on how good the estimated position is.

Figure 12 shows a simple discrete time speed calculation from the estimated speed.

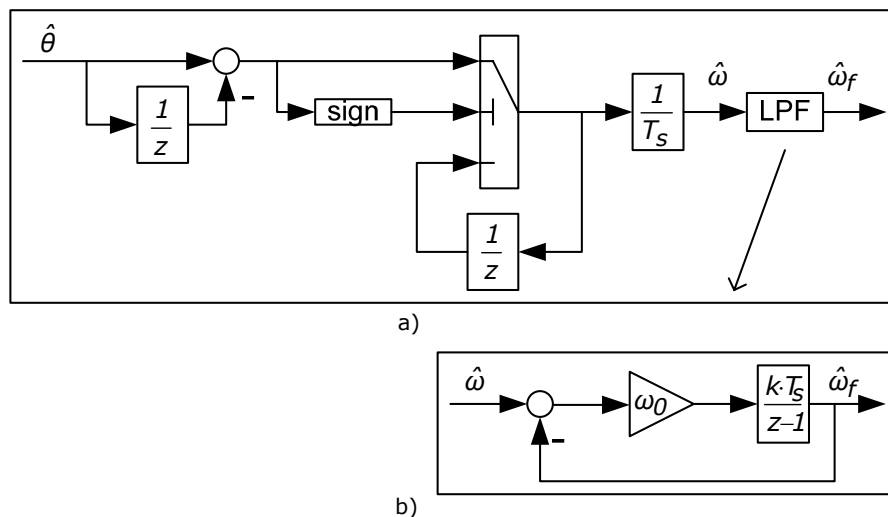


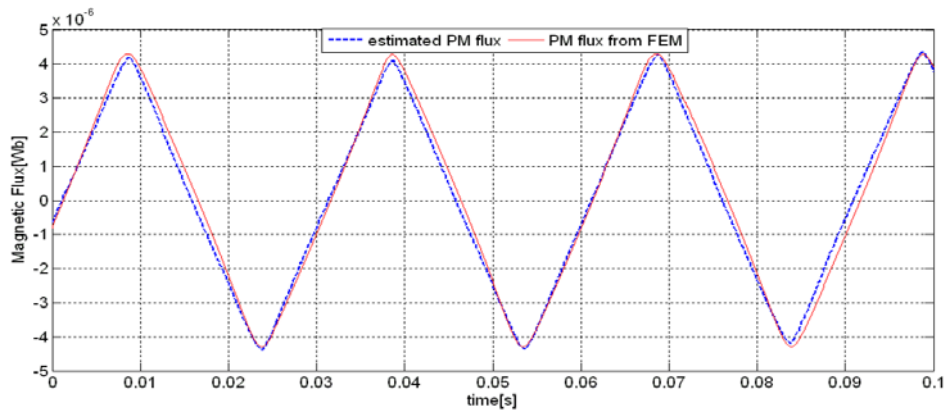
Figure12. Block diagram of speed estimator a), low pass filter detail implementation b)

4.5 Experimental validation of the proposed state observer

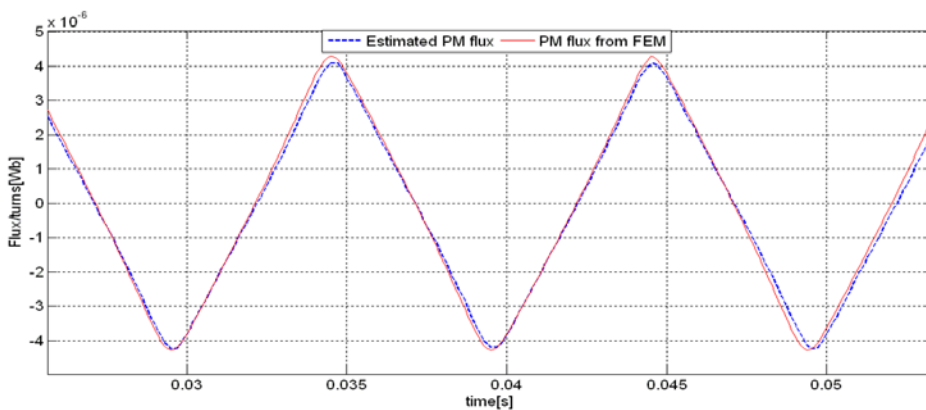
In order to first validate the flux estimator and the position and speed autocorrecting estimation algorithm the single phase PM-BLDC motor was run on closed loop speed control using the information from the Hall sensor, and the estimated quantities were analyzed.

4.5.1 PM flux estimator: experimental results

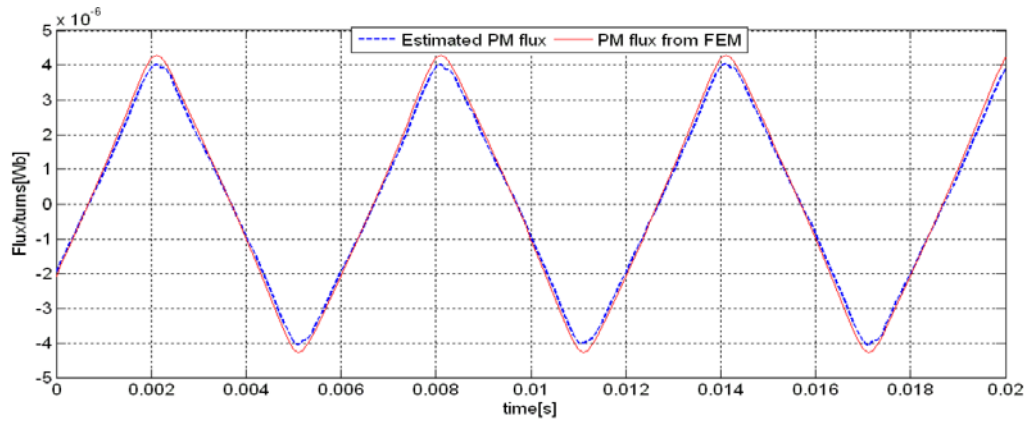
Figure 13 illustrates the estimated PM flux for different rotor speed in comparison with the PM flux obtained from FEM and imported as a lookup table.



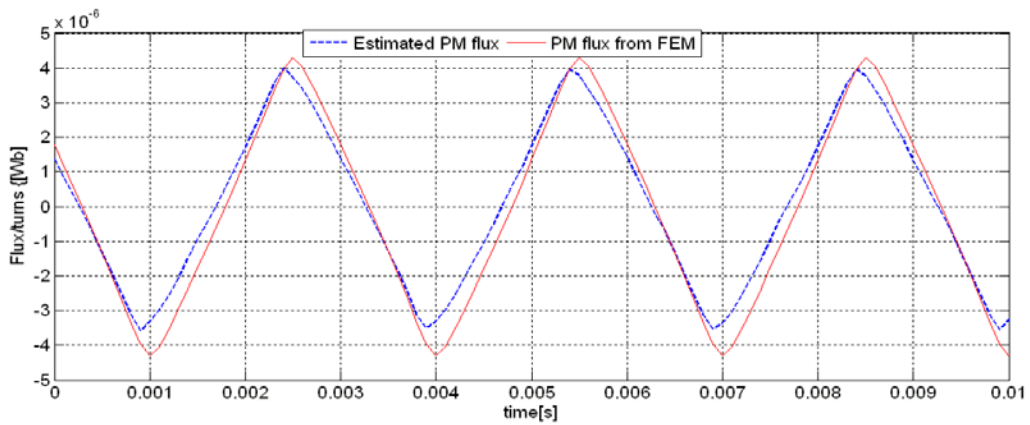
a)



b)



c)



d)

Figure 13. Estimated PM flux at a)1000rpm, b)3000rpm, c)5000rpm, d)10000rpm

Although a good agreement can be noticed, the amplitude and the phase difference can cause problems in the estimated position and speed and the presented correction method is necessary.

4.5.2 Estimated position: experimental results

Figure 14 shows experimental results at a given speed of 5000 rpm. The improvements of this correction method are visible. It may be noticed that, due to the differences in the fluxes, the position is not purely linear, but the result is better after the correction and the position error oscillations are reduced.

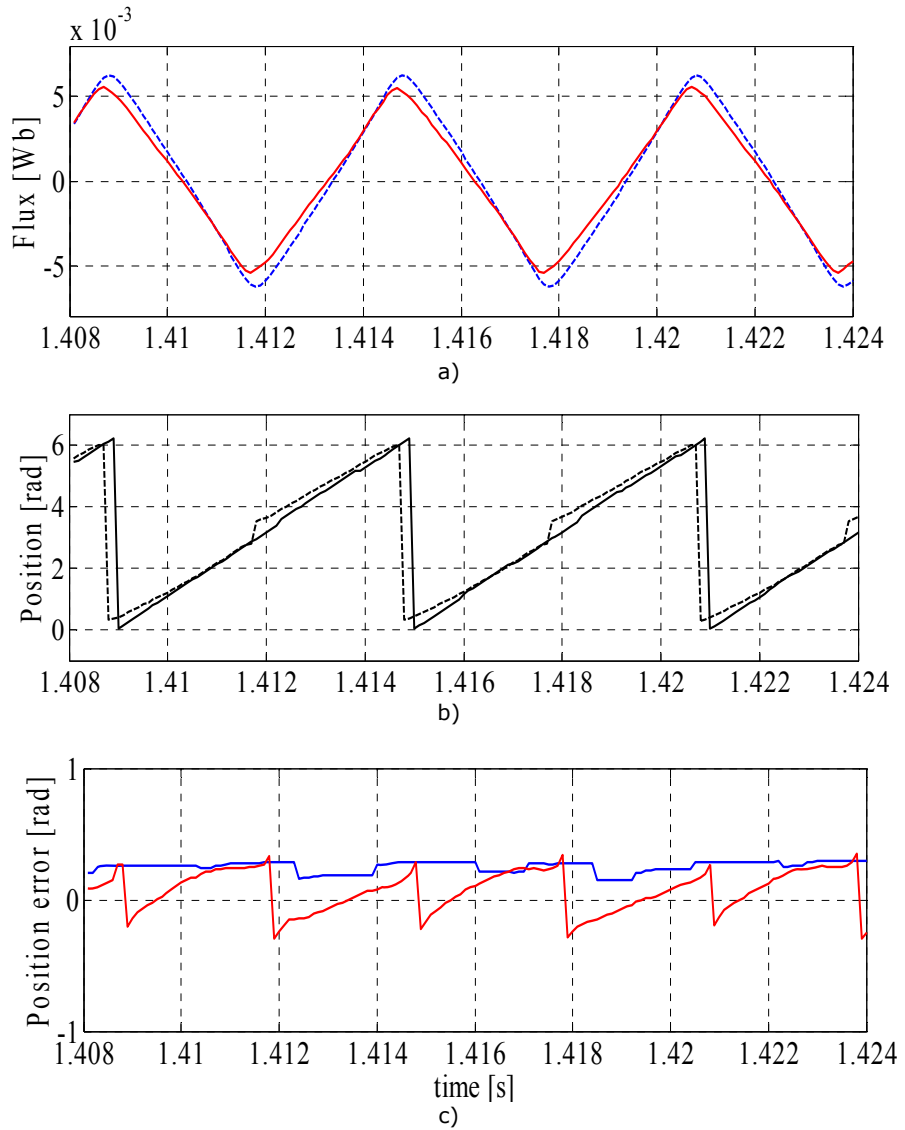
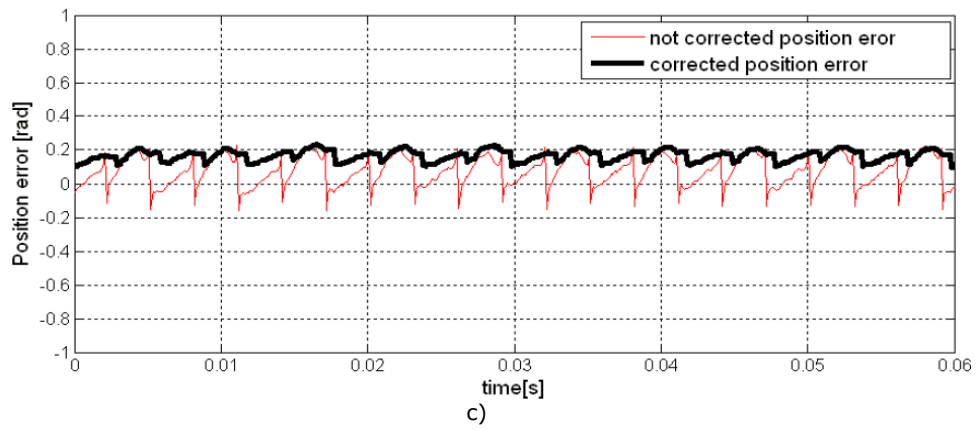
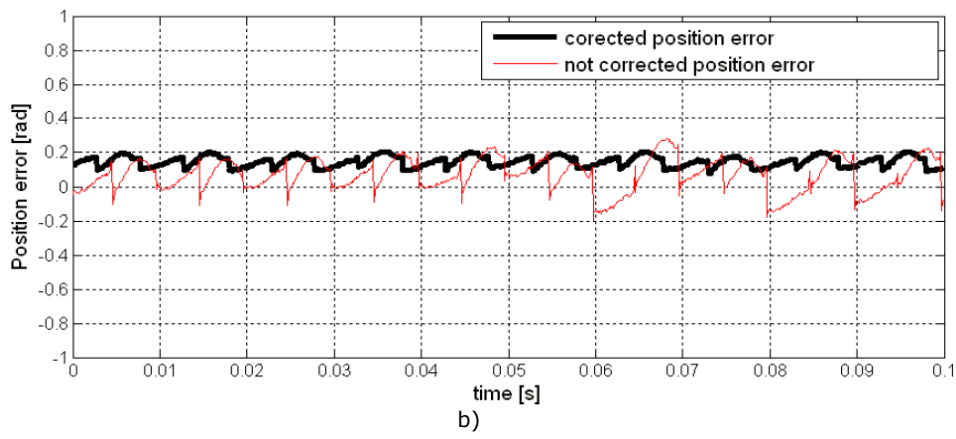
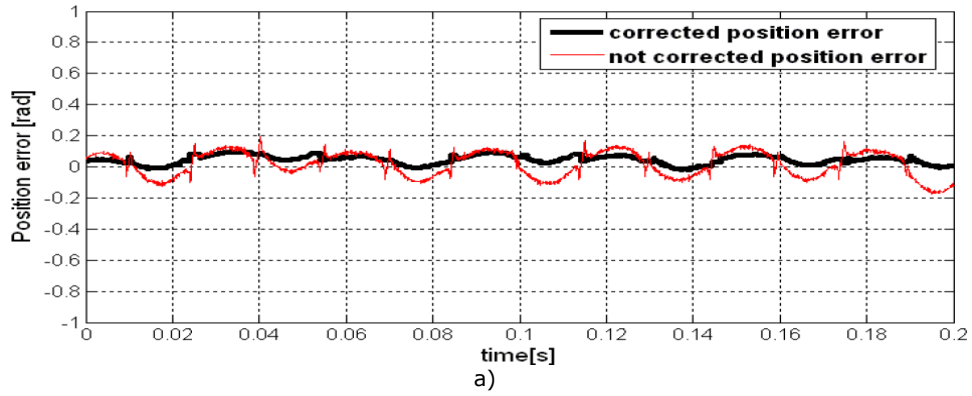


Figure 14. Experimental results at 5000 rpm with and without position correction: a) estimated and measured fluxes, b) estimated position, c) position error

In order to evaluate the improvement of the proposed correction solution over the estimated position, figure 15 shows the position errors at different running speeds for both the corrected and not corrected position. Notable improvements are visible.

4.5 Experimental validation of the proposed state observer 111



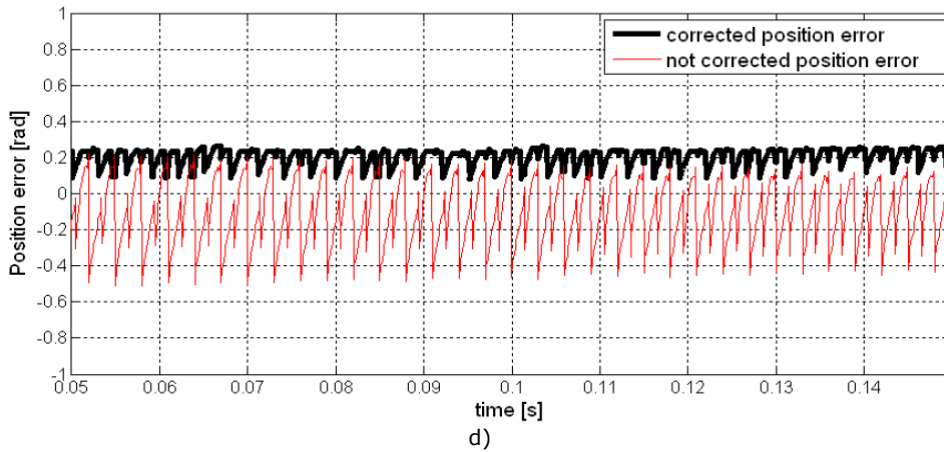


Figure 15. Position error at a)1000rpm, b)3000rpm, c)5000 rpm, d)10000rpm

4.5.3 Estimated speed: experimental results

In order to first appreciate improvement on speed also, of the proposed autocorrecting position and speed estimation algorithm, figure 16 shows a comparison between the calculated rotor speed by position differentiation for two cases: with position correction and without position correction.

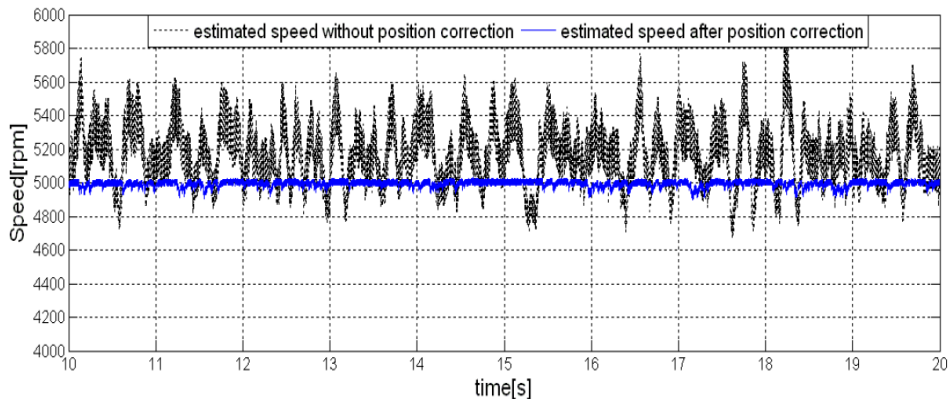


Figure 16. Speed comparison with and without position correction

For experimental validation Figure 17 illustrates estimated speed based on position derivative at different desired speeds at steady state.

4.5 Experimental validation of the proposed state observer 113

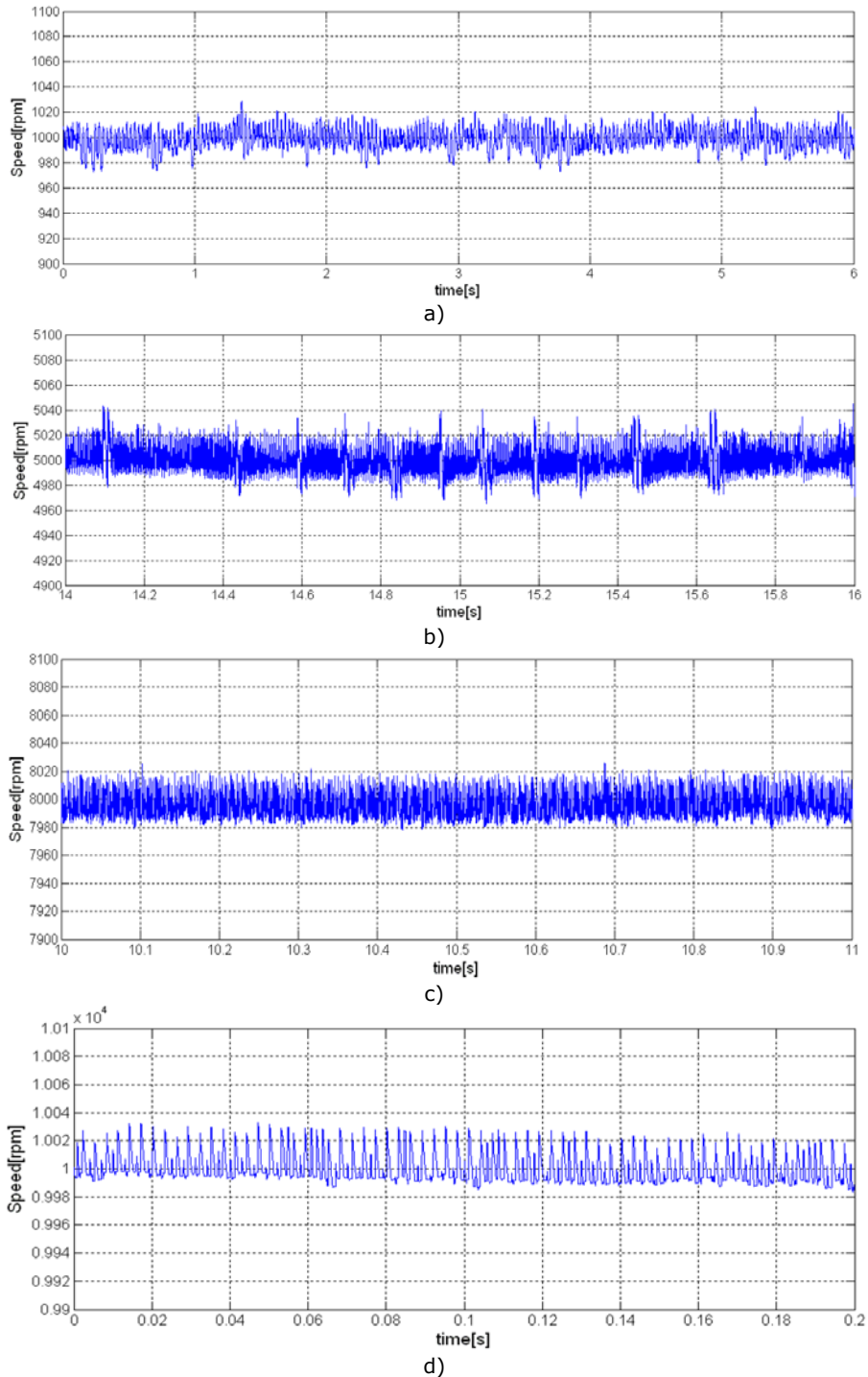


Figure 17. Experimental results under steady state at an expected speed of a)1000 rpm, b)5000 rpm, c)8000 rpm, d)10000 rpm

It should be noticed that some speed pulsations persist but in general, they are bellow 3% of average value.

These results are obtained after using a low pass filter with the corner frequency set at $\omega_c = 50$ rad/s at the output of the position differentiation.

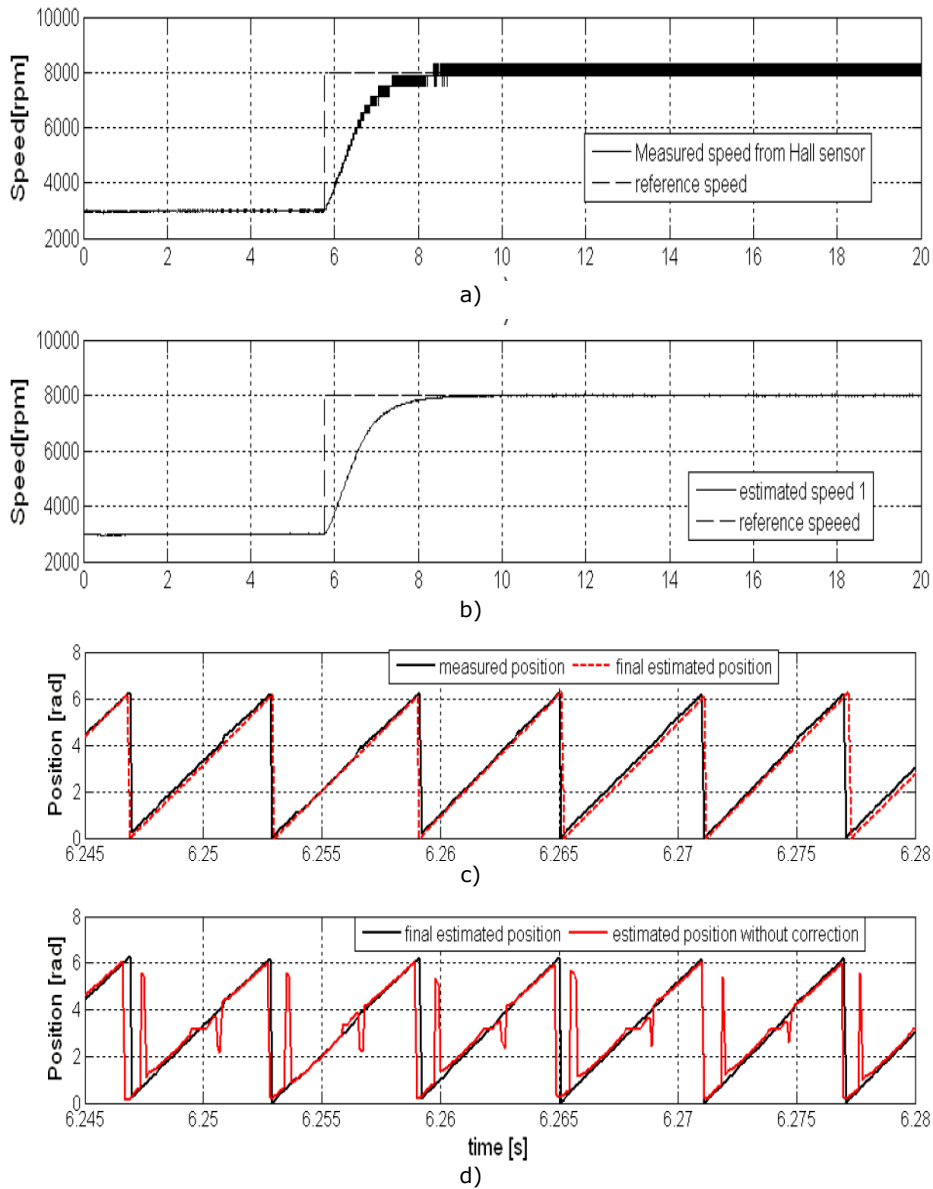


Figure 18. Experimental results at a step change in reference speed: a) measured speed b) estimated speed 1, c) measured and estimated position during acceleration, d) estimated position with and without correction during acceleration.

In order to further validate the proposed position and speed estimation algorithm, Figure 18 shows a reference speed step change from 3000 rpm to 8000 rpm.

If we examine the speed response, we can see that it is as quick as the real measured and unfiltered speed. This means that for this speed response the used filters don't insert any damaging delays.

Figure 18.c) shows a comparison between the estimated position and the real position during acceleration and a good agreement is noticed, while Figure 18.d) illustrates the estimated position without correction vs. the corrected one during the same time interval of speed increase. The beneficial effect of this correction solution over the final estimated position is acceptable due to the previous estimated speed used further for the next position value while the position extracted from lookup table is altered.

4.6 Motion sensorless control based on prior knowledge of PM flux vs. position

4.6.1 Control system overview

For motion sensorless control, a closed loop speed control with inner current control loop is used. The speed error between the reference and the estimated position is the input to the PI speed controller, while the output from the PI speed controller represents the reference current for the current controller. The current control loop also employs a PI controller, which has the purpose to minimize the current error. The current control is made through the measurement of the phase current which is forced to follow a waveform template (rectangular shape here).

Figure 19 illustrates the proposed sensorless control diagram. Basically the control contains the two PI controllers mentioned above, a state observer and a I-f starting sequence.

The state observer block from figure 19 contains three main interconnected parts: the PM flux estimator, the FEM based flux/position look-up table and the speed estimation.

Based on the measured current and the reference voltage, the permanent magnet flux linkage is estimated and then a preliminary rotor position is obtained from a look-up table. After applying a position correction algorithm the estimated position is further used in prescribing the current shape and for speed calculation. During starting these estimated quantities are not reliable so an open loop starting has to be applied.

To start the motor, an I-f starting sequence is employed here. The applied reference current frequency is ramped by using a first order delay filter while the reference current amplitude is maintained constant. From this frequency an imposed position is obtained and the prescribed phase current is commutated by using this feedforward signal. When running on this starting sequence, the speed controller is kept with zero input error by $flag_{I-f}$ in order to avoid error accumulation in the integral component (which would cause problems when crossing on the closed loop sensorless control). When the I-f frequency exceeds a certain threshold value, the $flag_{I-f}$ signal will make the transition to the state observer based sensorless control.

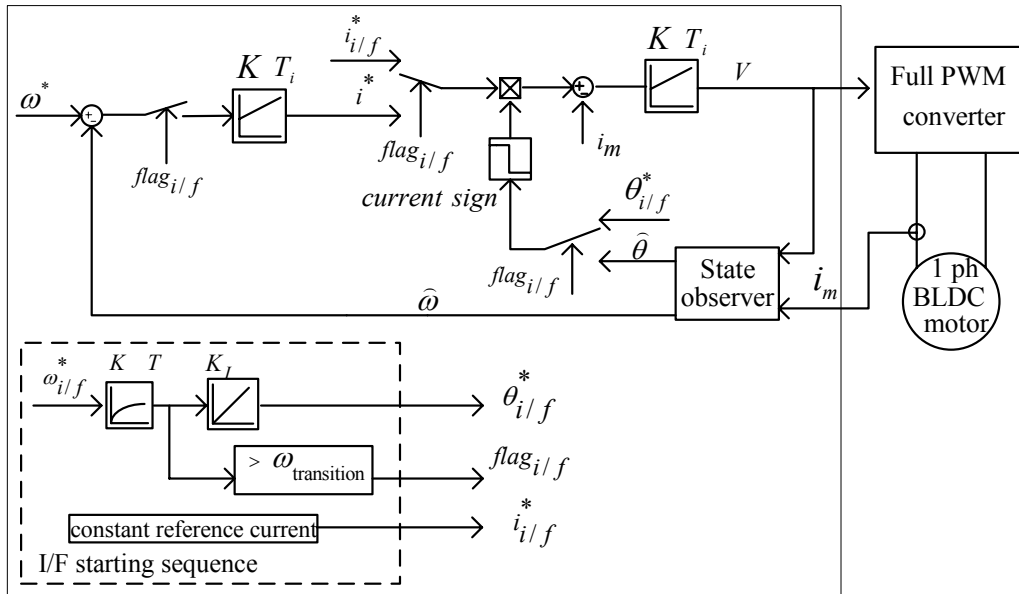


Figure 19. Motion sensorless control block diagram

Here the speed controller coefficients were determined by using the empirical Ziegler-Nichols tuning method and the values are: $K_{wp} = 0.06$ [As/rad] and $K_{wi} = 0.01$ [A/rad].

4.6.2 Experimental results

Further, figs. 20, 21, 22 shows some experimental results at a given constant speed of 2000 rpm, 5000 rpm, respectively 8000 rpm. We should mention that the prototype is provided with its blower and thus it is under its "natural" load all the time. The measured and estimated positions are intentionally shifted with 1 radian in order to avoid overlaps. From all figures a satisfactory agreement can be noticed between the estimated and measured position and speed. The measured speed is calculated by measuring the time difference between two consecutive edges in the Hall signal (as detailed in chapter 3) and filtered, which explains the smoother behavior compared with the estimated speed that is calculated at every sampling time from the estimated position.

4.6 Motion sensorless control based on prior knowledge of PM flux vs. position 117

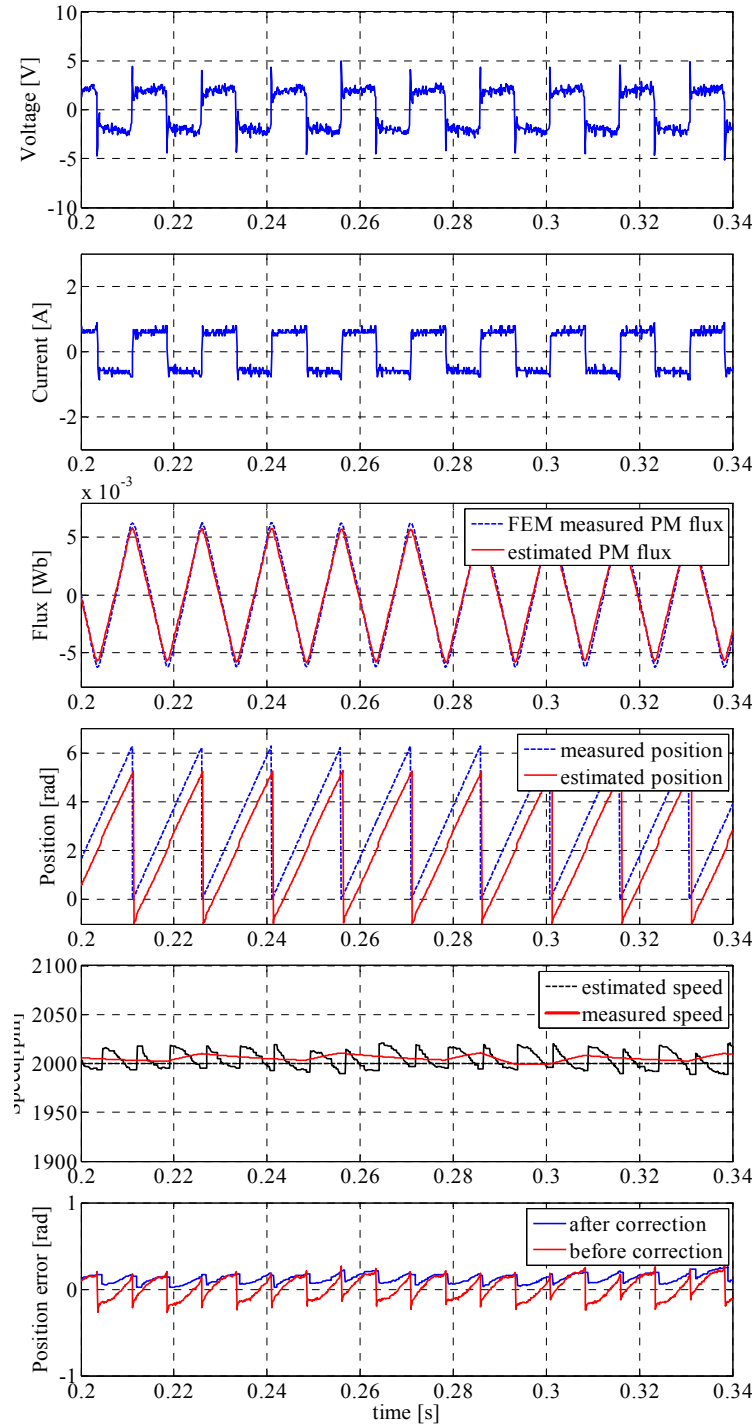


Figure 20. Experimental results for a given reference speed of 2000 rpm (from top to bottom: reference voltage, phase current, PM flux linkage, position, speed, position error)

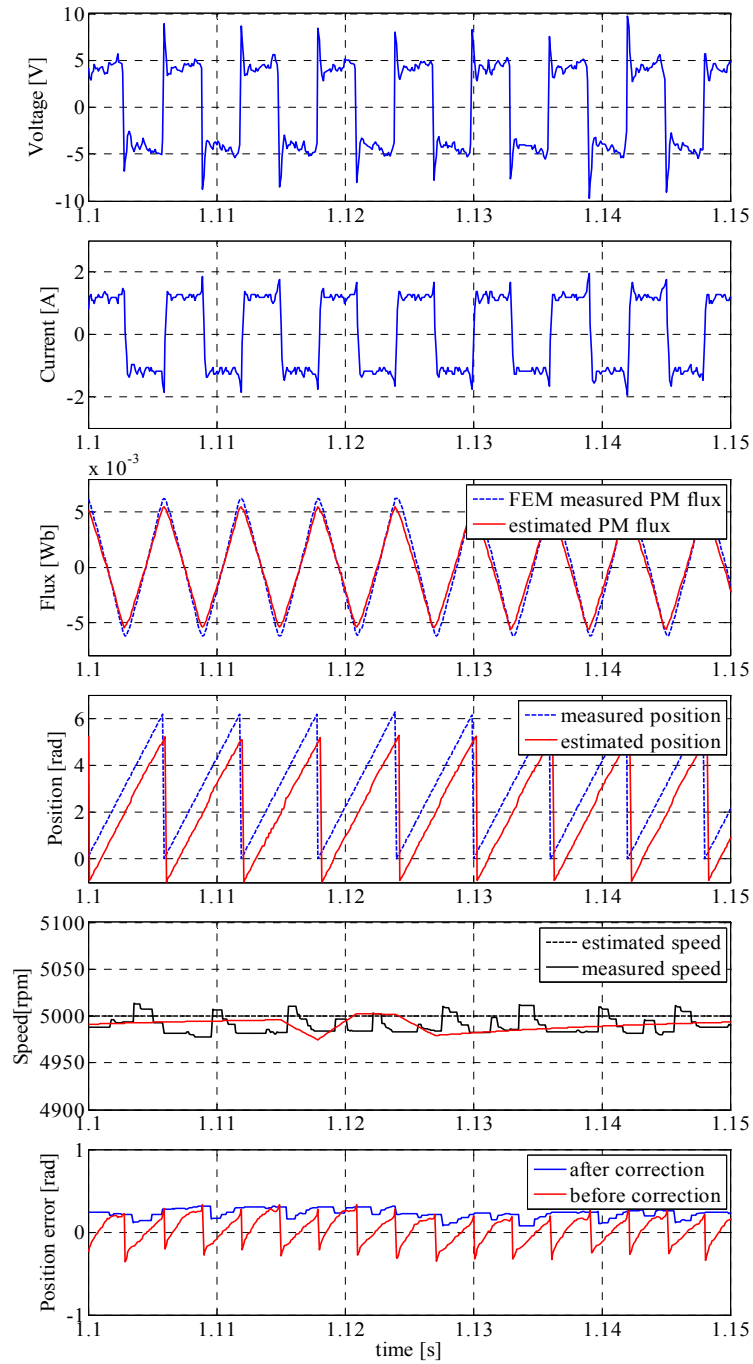


Figure 21. Experimental results for a given reference speed of 5000 rpm (from top to bottom: reference voltage, phase current, PM flux linkage, position, speed, position error)

4.6 Motion sensorless control based on prior knowledge of PM flux vs. position 119

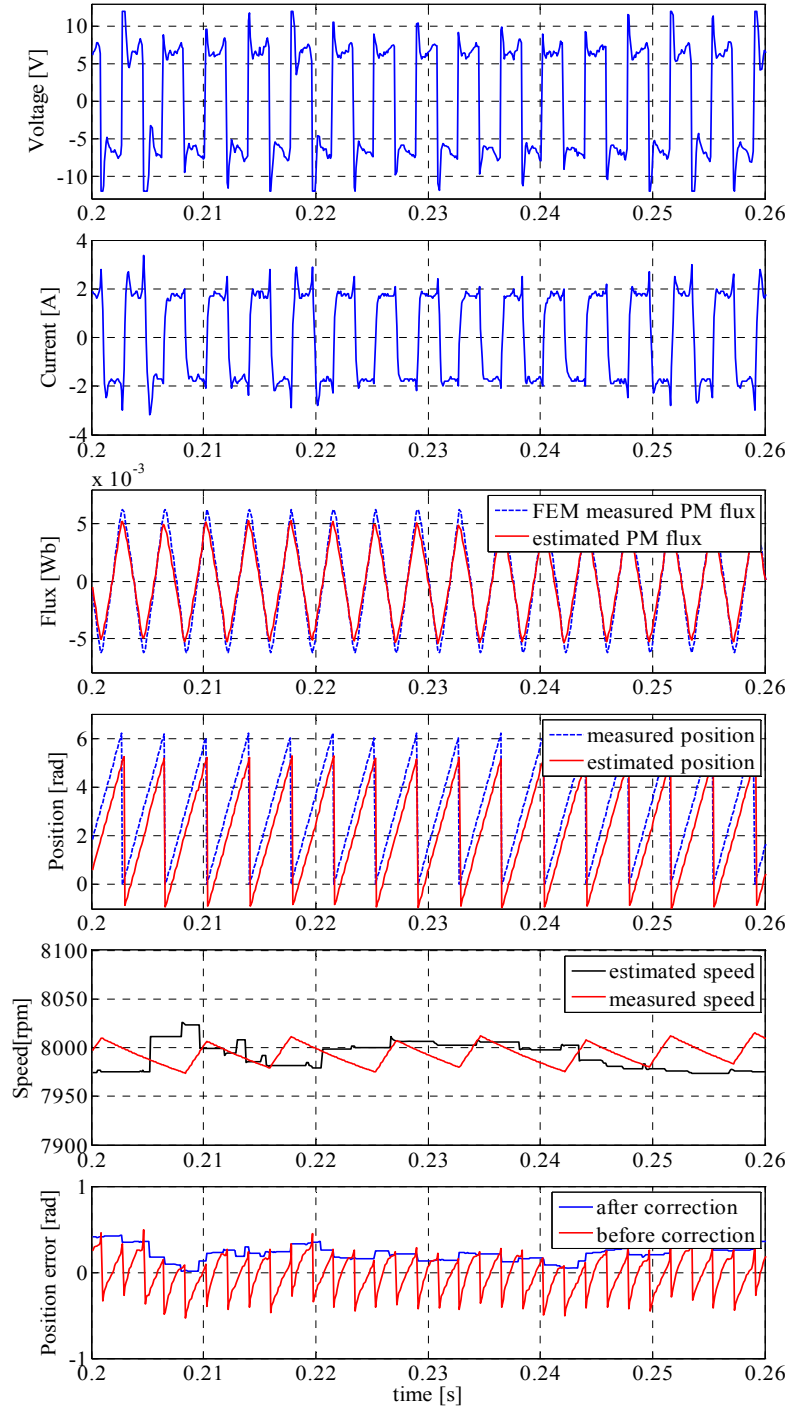


Figure 22. Experimental results for a given reference speed of 8000 rpm (from top to bottom: reference voltage, phase current, PM flux linkage, position, speed, position error)

Figure 25 illustrates the crossing moment from the I-f sequence to closed loop sensorless control. As explained in section 4.5.1 the PI speed controller has zero error and so the imposed reference current from it will be zero during I-f sequence.

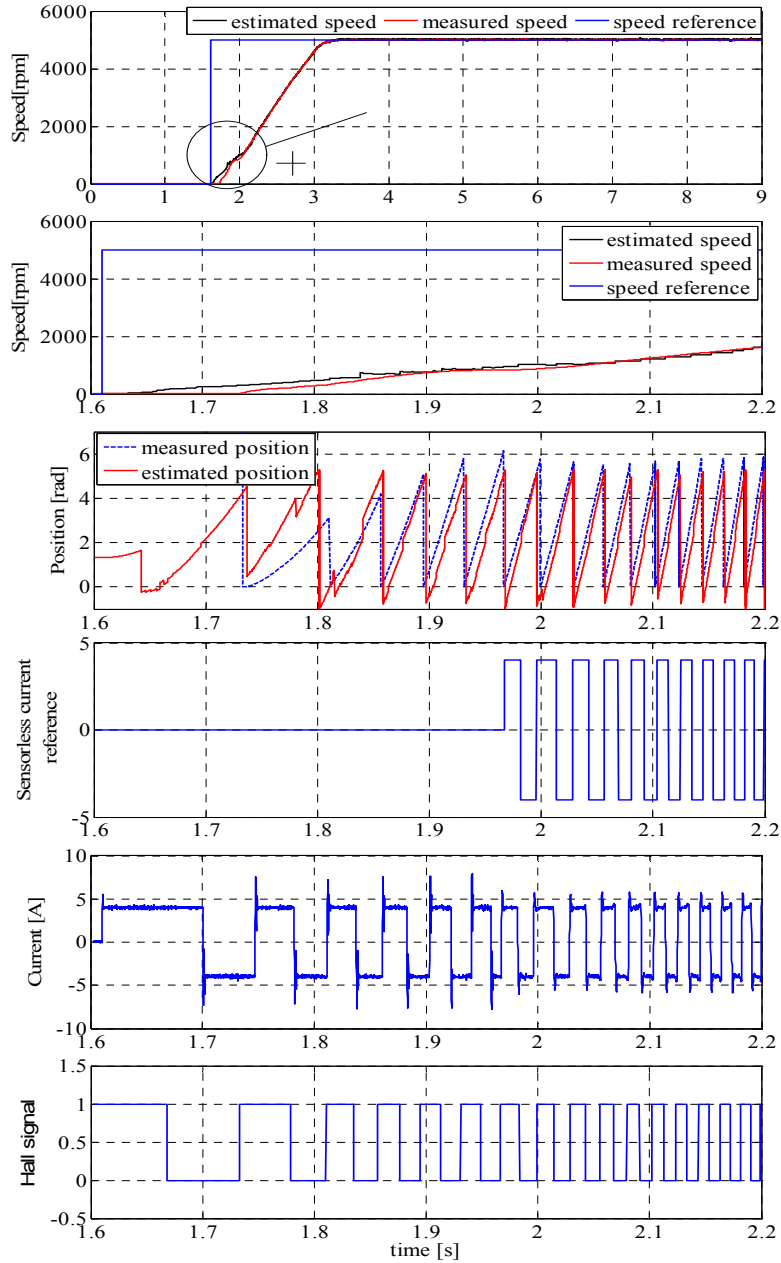


Figure 25. Zoomed view over the starting results for an acceleration from 0 to 5000 rpm (from top to bottom: speed, zoom on speed, position,, sensorless reference current, phase current, Hall signal)

During this sequence a constant current is commutated based on a feedforward position information. It is noticed that in spite of the fact that the current is not in phase with the Hall signal the state observer produces a satisfactory position before becoming active. When the reference frequency from I-f control is greater than the imposed threshold the sensorless control starts. Now, the speed controller produces a nonzero signal as the reference current and the current commutation is done based on the estimated position

It is visible that when running on FEM based sensorless control the current is in phase with the Hall signal, left active only for comparison. Also, at start, we can see that the continuous position calculated from the Hall sensor as mentioned above is not reliable for comparison.

4.7. Conclusions

A motion sensorless control system for a single phase PM BLDC motor based on a prior knowledge of the $\psi_{PM}(\theta)$ characteristic was introduced. The detailed step by step implementation was presented and illustrated by simulation results and then validated by experiments. First the motor was run in closed loop Hall based speed control in order to analyze the observer behaviour and then the closed loop motion sensorless control was performed.

Simple position and speed estimators were presented and an autocorrecting position and speed algorithm was proposed in order to reduce the sensitivity to PM flux estimator inaccuracy and experiments offered satisfying results. The autocorrecting effect was noticed when a ramp reference speed was imposed and the position remains satisfying in spite of the flux inaccuracy.

Also the proposed observer proved to be reliable when used in closed loop and good correspondence between measured and estimated speed was noticed. A position offset of approximately 0.25 rad was noticed and was compensated when running on closed loop sensorless control

The proposed method is using a I-f starting strategy with a simple switching to closed loop sensorless control. The important aspect related to the way that PI controllers are managed during switching was explained and demonstrated by experiments.

References

- [1] Zhu, Z.Q. Bentouati, S. Howe, D. "Control of single-phase permanent magnet brushless DC drives for high-speed applications", record of Power Electronics and Variable Speed Drives, 2000, pp. 327-332.
- [2] Ki B. Jang, S. H. Won, T. H. Kim, Lu Lee, "Starting and high-speed driving of single-phase flux-reversal motor for vacuum cleaner", IEEE Transactions on Magnetics, vol. 41, no. 10, Oct. 2005, pp. 3967-3969.
- [3] M. adriollo, M. De Bortoli, G. martinelli, A. Morini, A. Tortella, "Design Improvement of a single-phase brushless permanent magnet motor for small fan appliances", IEEE Transactions on Industrial Electronics, vol.57, no.1, Jan. 2010, pp. 88-95.

-
- [4] C.M. Chao, C.P. Liao, D.R. Huang and T.F. Ying "A New Automatic Phase Adjustment of Optical Drive Signal" *IEEE Transaction on Magnetics*, vol. 34, NO. 2, March 1998, pp. 417-419.
 - [5] D. R. Han g , C.Y. Fan, S.J. Wang, H.P. Pan, T.F. Ying , C.M. Chao and Eric G. Lean "A new type single phase spindle motor for HDD and DVD", *IEEE Transaction on Magnetics*, vol..35, no.2, March 1999, pp.839-844
 - [6] Jian Ni, Lijian Wu, Bo Zhang, Wanbing Jin, Jianping Ying " A novel adaptive commutation angle method for single phase bldc motor", *Proceedings of International Conference on Electrical Machines and systems*, Oct 2007, pp 446-449
 - [7] C. L. Chiu, Y. T. Chen, Y. Hsiang Shen, R. H. Liang, "An accurate automatic Phase Advance Adjustment of brushless DC motor", *IEEE Transactions on Magnetics*, vol 45, no. 1, Jan. 2009, pp. 120-126.
 - [8] L. Armstrong, "Current control removes brushless DC motor commutation spikes", *Application Note ZE0469*, Zetex Semiconductors, Aug. 2005.
 - [9] W. C. chen, Y.Y. Tzou, " Efficiency optimization control for single-phase brushless DC fan motors", *Proc. of Power Electronics and Motion Control Conference*, May 2009, pp. 1913-1918.
 - [10] M. Jagiela, E. A. Mendrela, R. Wrobel, "Current control for the smoothing of torque in a single-phase permanent-magnet disc motor using 3-D FEM", *Journal of Electrical Engineering*, vol. 87, no. 4, June 2005, pp.191-196.
 - [11] L. Sun, Qi Feng, J. Shang, "Drive of Single-Phase Brushless DC motors Based on Torque Analysis", *IEEE Transactions on Magnetics*, vol. 43, no. 1, Jan 2007., pp. 46-50.
 - [12] W. Amrhein, S. Silber, K. Nenninger, and G. Trauner"Mechatrical Design Studies on Small Brushless Motors" *International Journal of Rotating Machinery*,2003, pp.127-133.
 - [13] Atmel, "AVR440: Sensorless Control of Two-Phase Brushless DC Motor", *Application Note*.
 - [14] W. Wang, Z. W. Wanbing, J. J. Ying, "Sensorless control technology for single phase BLDCM based on the winding time-sharing method", *Record of Industrial Electronics Society*, Nov 2005, pp. 1732-1736.
 - [15] G. D. Andreescu, "Adaptive equivalent integrator for flux estimation in wide speed range for sensorless control of AC drives", *Record of EPE-PEMC 2002*, pp.1-9.
 - [16] L.Iepure, D.Iles-Klumpner, M.Risticovic, I.Boldea "Small blower PM single phase brushless d.c. motor drives: FEM characterization with experiments", in *CD-ROM Record of IEMDC*, may 2009, pp. 183-187.
 - [17] X.D. Xue, K.E.E Cheng, S.L. Ho "Sensorless Control Scheme for Continuously Estimating Rotor Position and Speed of Switched Reluctance Motor Drives Based on Two-Dimensional Least Squares", *Proceedings of Power Electronics Systems and Applications*, nov 2004, pp. 183-187.

5. MOTION SENSORLESS CONTROL OF SINGLE PHASE BRUSHLESS D.C. PM MOTOR DRIVE BASED ON A FICTITIOUS ORTHOGONAL FLUX SYSTEM

Abstract

A motion sensorless control for single phase PM-BLDC motor based on a I-f starting sequence and on real time flux estimation is proposed here.

Two methods of extracting the rotor position and speed for a sensorless single phase BLDC-PM motor drive by measuring only the phase current are presented here. The special calculation for extracting the position and speed used here implies the generating of an orthogonal flux system.

The first method extracts the position information by using the \tan^{-1} function and then an improved observer is created by adding a 4th order harmonic term in the estimated position, while the second method uses a phase locked loop observer.

The influence on position estimation of the harmonic content in the shape of the permanent magnet (PM) flux are presented by analytical expressions and digital simulation.

The proposed state observers are detailed using simulation results and then validated by experimental results. For testing and validation of the proposed sensorless control by experimental results, the required for comparisons information like real speed, position and torque are obtained using only a low resolution Hall sensor and the electromagnetic characteristics of the tested motor, without using any encoder or torque meter.

5.1. Introduction

As presented in the previous chapter, although for usual single phase BLDC motors, a precise determination of the rotor angle is not imperative because the rotor is commutated at every 180 degrees, in some cases, there could be necessary to have a more precise position information. For example, at lower speed, where there is enough voltage for current control, the current shaping could be appropriate for torque pulsation and noise reduction. This current shaping needs rather precise position information. Also, as referred in [1], even for trapezoidal BEMF motors, if the machine's torque producing capability is to be utilized over a wide range of speeds in the field weakening region, then high resolution position sensing is needed.

The investigation of techniques for eliminating the rotor position sensors for 3 phase permanent magnet synchronous motors was intensively adopted in many papers in the last years. While several publications on single phase BLDC-PM motors control have appeared, few so far considered the elimination of position sensor [2],[3].

In view of the above the present chapter aims to:

*Introduce a flux reference voltage-model PI compensated observer based sensorless control for single phase PM-BLDC motor drive.

*Develop a special calculation method for estimating the rotor position by generating an orthogonal flux system and by using the atan2 special trigonometric function.

*Analyze the peculiarity of using a flux waveform with harmonic content in the proposed position observer

Then, to improve the results, two position observers are derived:

* First, a position observer which consist in an injected harmonic term in the estimated position is applied based on a Fourier analysis and the improvements are proved by simulation and experimental results. When this method is used the speed will be calculated from the estimated position derivative

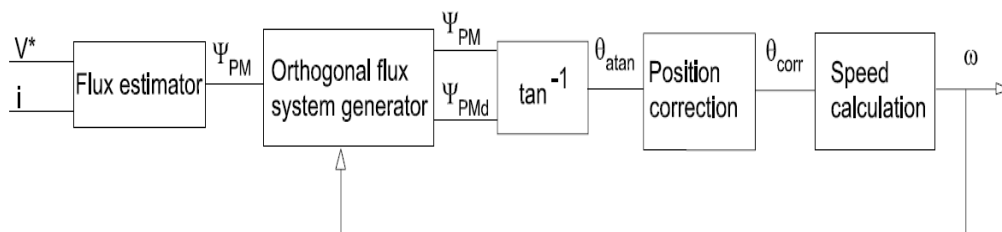
* A phase locked loop (PLL) observer based estimated position refining is the other solution, which can give also the estimated speed and so the noise produced by position differentiation is reduced.

*Combine the flux voltage-model observer based proposed sensorless control with an open loop I-f starting strategy with a simple transition to close loop sensorless control.

*Present the problems that arise when trying to validate the proposed sensorless control using the position/speed information from the existing Hall sensor for comparison. The use of other complementary qualitative information like current and Hall sensor signal relation and the torque information from the position dependent BEMF and cogging torque characteristics of the motor under test have the role to depict the sensorless control performance. Low torque ripple for a single phase PMSM is proved .

5.2 Proposed state observer structures

Two structures for rotor position and speed estimation, both of them based on a constructed orthogonal flux system, are proposed and tested. Figure 1 shows the proposed estimation diagrams. Both structures are composed of a PM flux estimator and an orthogonal flux system generator. The differences are in the manner by which the position and speed are extracted.



a)

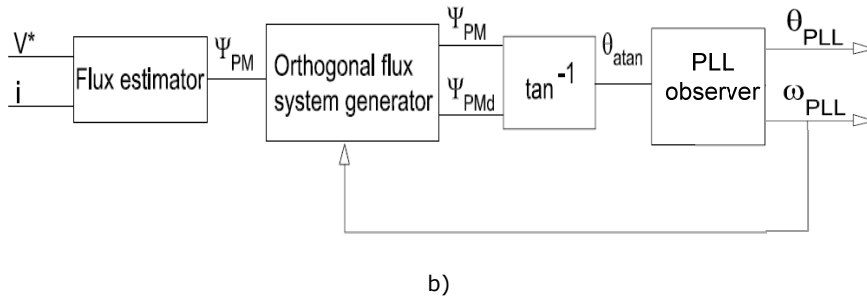


Figure1. Structure of the proposed state observers: a) Structure1, b) Structure 2

Both observers will be further presented and the component parts will be detailed.

5.3 PM flux estimator

The implemented PM flux estimator based on reference voltage model in stator reference is the same as the one presented in chapter 4. The estimator uses the output from the PI current controller as voltage information and the measured phase current for estimating the magnetic flux.

The same relation applies:

$$\psi_{PM} = \int_0^t (v - R \cdot i - V_{comp}) \cdot dt - L \cdot i \quad (1)$$

where:

$$V_{comp} = k_p \cdot \psi_s + k_i \cdot \int_0^t \psi_s \cdot dt \quad (2)$$

$$v = \text{sign}(i_{reference}) \cdot D \cdot V_{dc} \quad (3)$$

Where v is the input voltage, i is the phase current, R is the resistance, L is the winding inductance, ψ_{PM} is the permanent magnet flux linkage, and V_{comp} is a feedback compensation volatege, respectively. In equation 3, D represents the reference duty cycle and V_{dc} the DC link voltage.

5.4 Orthogonal PM flux system generator

In single phase BLDC-PM motors there is less information than in three phase motors, and so, some special calculations have to be done in order to estimate the rotor position. The idea of this sensorless drive is to create an orthogonal PM flux linkage system in order to employ it in rotor position/speed estimation. In the literature, the solution of generating two orthogonal signals is

also encountered in the field of single phase grid connected systems, and the delayed signal is the applied voltage [4]-[6].

In this paper, the adopted solution for real time generating of the imaginary PM flux component is based on delaying the estimated PM flux with a number of sampling periods equivalent to 90 electrical degrees. The number of sampling periods used for the delay is obtained from the estimated speed using equation (4):

$$N = \frac{2\pi}{4 \cdot \omega \cdot p \cdot T_s} \tag{4}$$

Where ω is the estimated speed in [rad/s], p is the number of pole pairs and T_s is the sampling time.

Note that for calculating the necessary number of sample periods for the delay the estimated speed is fed back into the orthogonal flux system generator block, thus making the the estimation to be autituning with speed.

Thus having two orthogonal fluxes, the rotor position can be calculated using the \tan^{-1} function. Figure 2 illustrates the orthogonal PM flux system and the estimated position obtained by simulation at a speed of 5000 rpm, while Figure 3 shows the Simulink implemented block diagram of the position estimator.

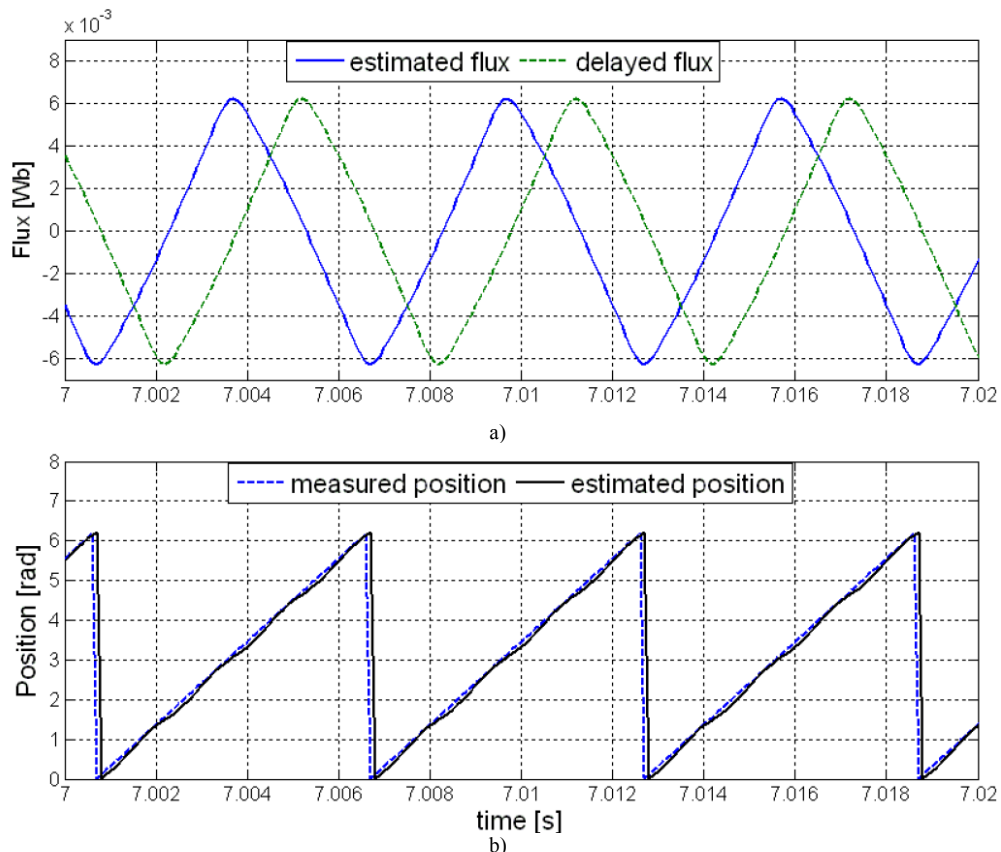


Figure 2 a) Orthogonal fluxes, and b) estimated position at 5000 rpm by digital simulations

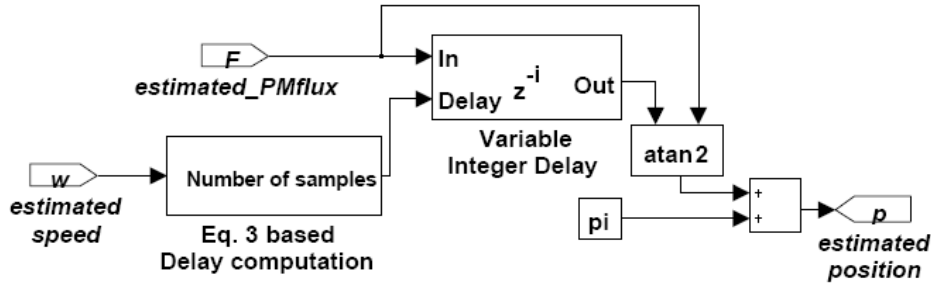


Figure 3 Simulink implementation of position estimator

As expected, some oscillations are visible in the estimated position due to the nonsinusoidal waveform of the estimated PM flux. This can cause further problems in prescribing a proper current shape and in speed calculation and some measures must be taken.

5.5 Offline Fourier analysis based position refining and speed estimator

5.5.1 Fourier analysis and state observer implementation

Considering an ideal sinusoidal flux distribution as in eq (5), a flux phasor can be assigned, eq. (6), where the estimated PM flux is $\text{Re}\{\underline{\psi}\}$

$$\psi(\theta) = \Psi \cdot \cos(\theta) \quad (5)$$

$$\underline{\psi} = \Psi \cdot e^{j\theta} = \Psi \cdot \cos(\theta) + j \cdot \Psi \cdot \sin(\theta) \quad (6)$$

Where $\psi(\theta)$ is the instantaneous value of PM flux in stator frame coordinates and Ψ is the PM flux amplitude. From equation (6) the phasor phase angle, and so the PM position, can be determined by using relation (7), which, under steady state conditions, equals $\omega \cdot t$.

$$\theta = \arctan\left(\frac{\text{Im}\{\underline{\psi}\}}{\text{Re}\{\underline{\psi}\}}\right) = \omega \cdot t \quad (7)$$

This means that the obtained position from a sinusoidal flux waveform is linear and has no pulsations as those referred in figure 5.

Further, the estimated flux was approximated by Fourier series as function of θ through a curve fitting algorithm in order to analytically illustrate the peculiarity

of using nonsinusoidal flux distribution in the proposed position and speed estimation.

Equation (8) shows the obtained analytical approximation.

$$\psi_{PM} = \sum_{k=1,3,5} A_k \cdot \cos(k \cdot \theta) + B_1 \cdot \sin(\theta) \tag{8}$$

where ψ_{PM} is the instantaneous estimated PM flux, and the terms A_k, B_1 are the coefficients of the Fourier series, listed in Table I.

Starting from eq.(5-7), the nonsinusoidal PM flux shape is implied in estimating the rotor position and the peculiarities of this method are noticed. By using an identical flux shape delayed with $\frac{\pi}{2}$ the imaginary component of the PM flux phasor is created. Having the PM flux approximation from equation (8) the delayed PM flux analytical approximation is expressed by equation (9):

$$\psi_{PMd} = \sum_{k=1,3,5} A_k \cdot \cos(k \cdot \theta - \frac{\pi}{2}) + B_1 \cdot \sin(\theta - \frac{\pi}{2}) \tag{9}$$

In the case of the real PM flux, due to the harmonic content in its shape, the PM flux phasor amplitude is not constant with its position and is not always equal with the PM flux amplitude as Fig. 4 shows. Due to this aspect some error can occur in extracting the position.

Figure 4 illustrates the flux locus of the ideal sinusoidal flux respectively of the real PM flux determined using eq. (8) and (9).

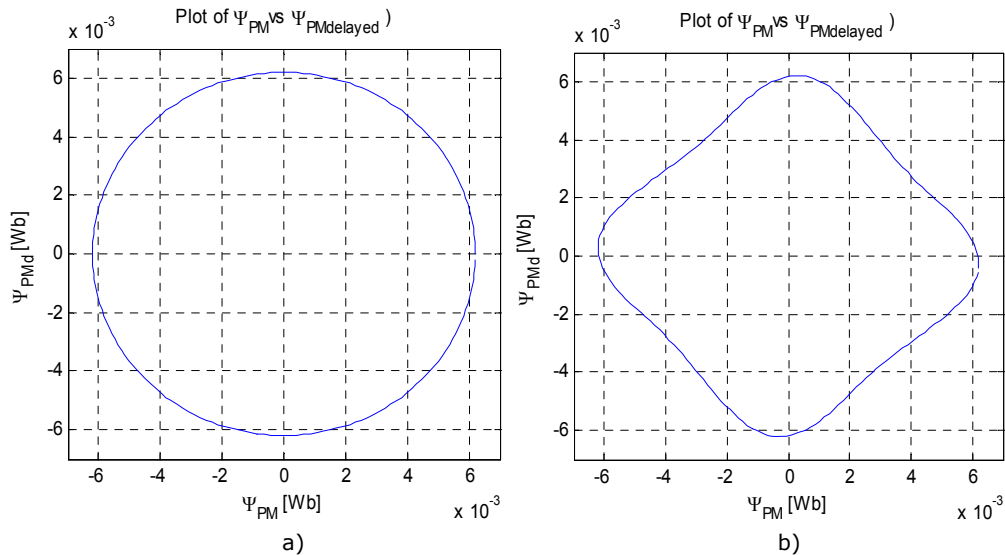


Figure 4 Locus of PM flux phasor: a) ideal sinusoidal shape; b) real flux shape

Thus having two orthogonal fluxes as the real and imaginary components of a flux phasor, eq.(10), the position can be extracted using the special function atan2 as eq (11) shows:

$$\underline{\Psi}_{PM} = \Psi_{PM} + j \cdot \Psi_{PMd} \quad (10)$$

$$\theta_{atan} = \arctan\left(\frac{\text{Im}\{\underline{\Psi}_{PM}\}}{\text{Re}\{\underline{\Psi}_{PM}\}}\right) = \text{atan2}\left(\frac{\Psi_{PMd}}{\Psi_{PM}}\right) \quad (11)$$

In order to avoid the complex mathematical operations for analytical expression of the position, eq. (11) was numerically computed using the fluxes from equations (8) and (9) and the result was also expressed using the Fourier series. Equation (12) represents the Fourier series based approximation of the calculated position for steady state conditions, and some 4th order harmonics are noticed additionally to the linear dependency with speed. The C_0 , C_1 and C_2 are the coefficients of the Fourier series, listed in Table I.

$$\theta_{atan} = \omega \cdot t + C_0 + C_1 \cdot \cos(4\omega t) + C_2 \cdot \sin(4\omega t) \quad (12)$$

Considering the obtained truncated Fourier series approximation coefficients, a feed-forward position correction can be applied. For simplicity, this position refining employs only the most dominant term, the 4th order sinusoidal harmonic term which is applied to the \tan^{-1} based estimated position (Fig.2b) by using relation 13:

$$\theta_{corr} = \theta_{atan} + K \cdot \sin(4 \cdot \theta_{atan}) \quad (13)$$

where θ_{atan} is the position obtained from the atan2 function, θ_{corr} is the refined estimated position and the correction amplitude is $K = 0.07 \cong -C_2$.

Table I contains the obtained Fourier series coefficients.

TABLE I
Fourier series coefficients

A_1	$5.518 \cdot 10^{-3} \text{ Wb}$
A_3	$0.548 \cdot 10^{-3} \text{ Wb}$
A_5	$0.146 \cdot 10^{-3} \text{ Wb}$
B_1	$-0.387 \cdot 10^{-3} \text{ Wb}$
C_0	-0.0442 radians
C_1	0.0091 radians
C_2	-0.0726 radians

Figure 5 illustrates the content of the position and speed calculation blocks from figure 1.a), while Figure 6 proves by digital simulation results the position improvements of the described correction at 3000 rpm.

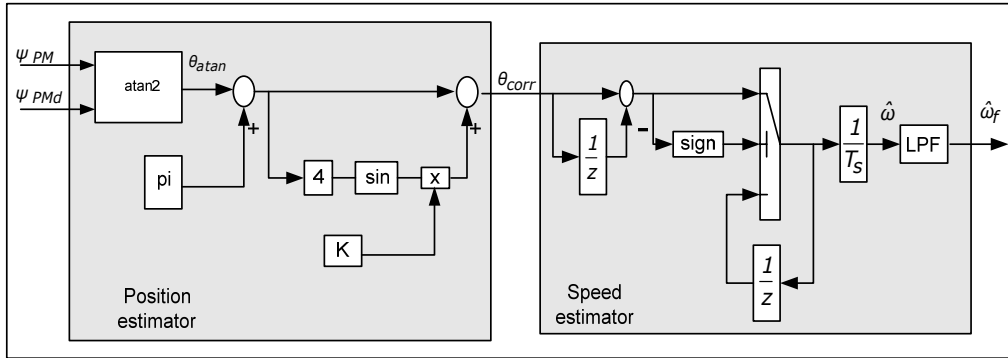


Figure 5 Position and speed estimation algorithms

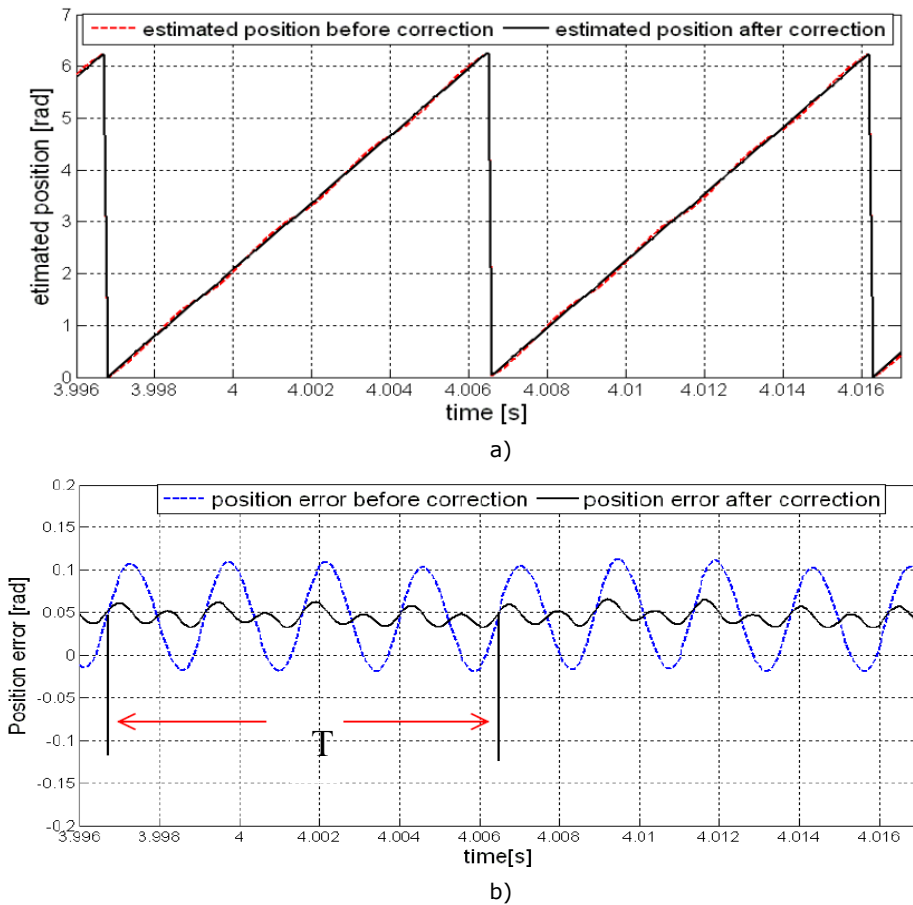


Figure 6 Simulation results at 3000 rpm after correcting the estimated position: a) position b) position error

5.5.2 Experimental results

For experimental validation the motor was still run using the hall sensor only for the proposed observer to be detailed and tested in open loop.

The presented state observer was tested at various steady state speed values in order to experimentally validate the improvements on estimated position error (Fig.7) and speed pulsations (Fig.8).

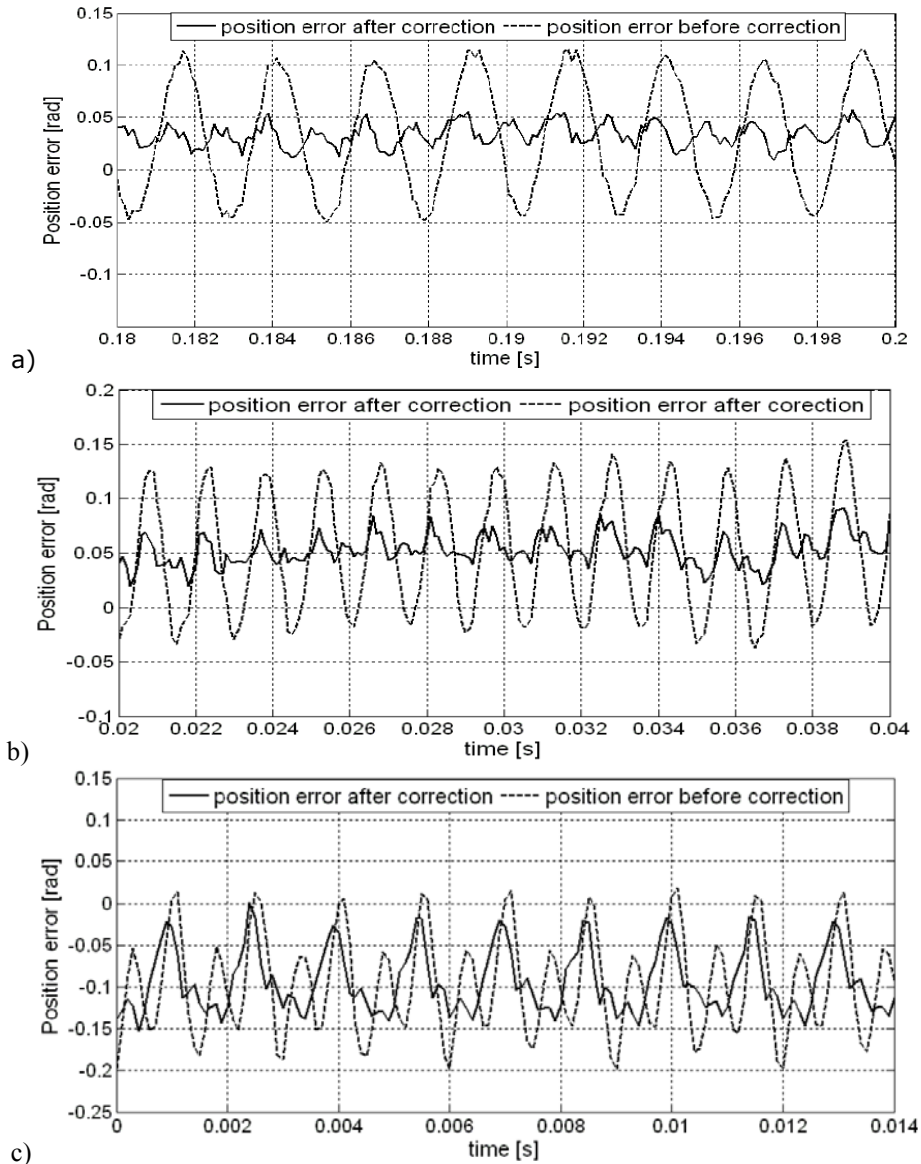


Figure 7 Position error with 4th order harmonic correction at a) 3000 rpm, b) 5000rpm, c) 10000rpm, by experiments

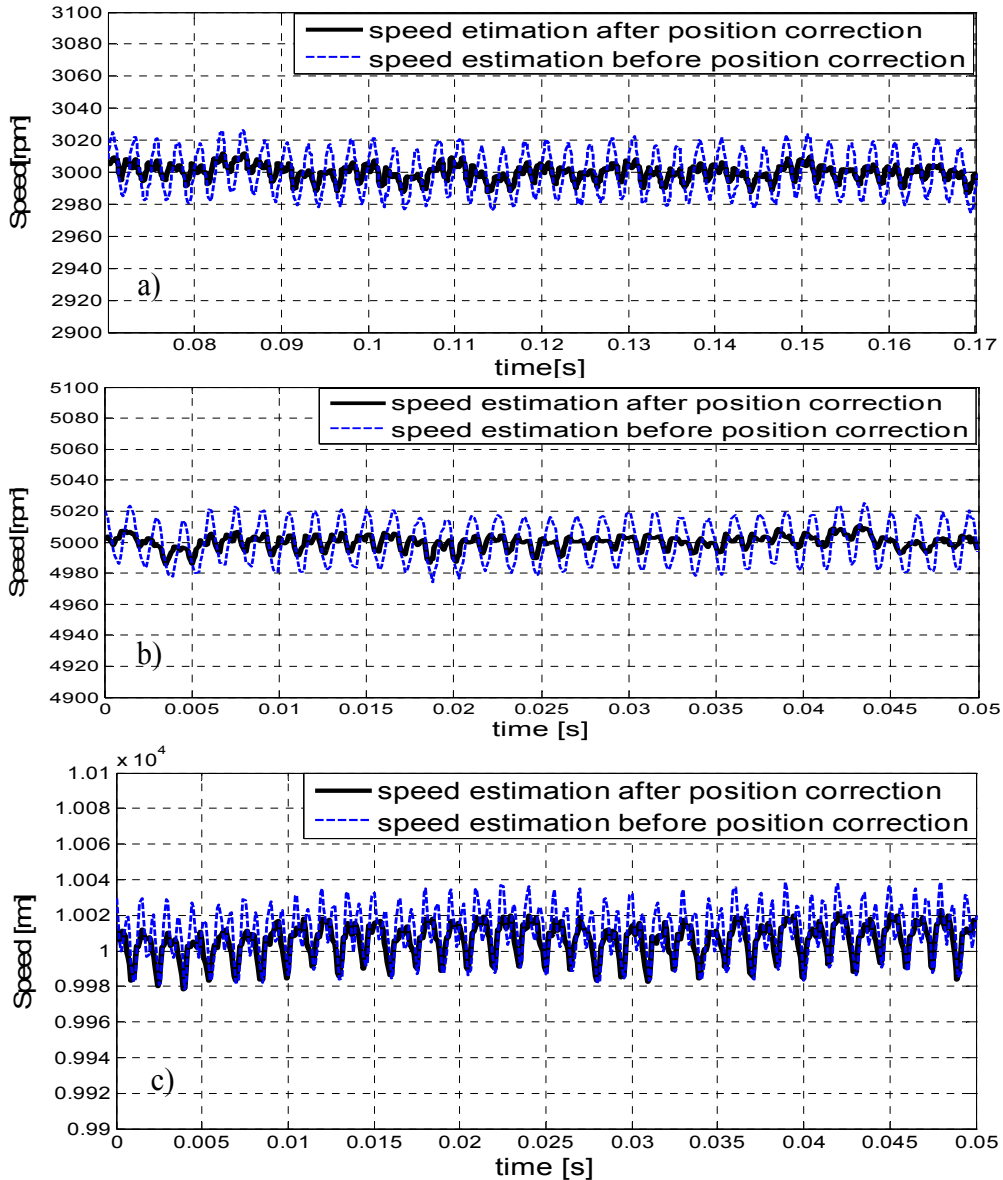


Figure 8. Experimental speed results a) 3000rpm, b) 5000rpm, c) 10000rpm

The illustrated experimental results show a good filtering of the initial position. When calculating the position error using as reference the calculated position from Hall sensor different position error may appear due to the fact that the Hall calculated position is sometimes reset before the 2π radian value. This is the explanation for negative position error illustrated at 10krpm. Fig 8 shows the estimated speed obtained from the \tan^{-1} based estimated position (θ_{atan}) versus the estimated speed obtained from the corrected estimated position (θ_{corr}).

The reduced speed pulsations are noticed, as expected, due to the improvement of estimated position. It can be noticed that at 10krpm this correction method is not very effective any more, but at 5000 rpm is still very effective.

5.6 PLL based position refining and speed observer

5.6.1 PLL behavior analysis

In general, the calculation of speed from the estimated rotor position by differentiation is problematic because it results in significant noise. Here we use a phase locked loop (PLL) in order to both estimate the speed and to filter the estimated position.

The PLL system was intensively studied and in [7],[8] a simplified model is presented and some tuning recommendations are given. So far PLL observer have been widely used in high performance servo drives for speed calculation from resolver or encoder signals or for position and speed estimation in sensorless control of three phase motors [9]-[13]. Regarding the single phase PLL observer, various structures were usually used for single phase grid connected applications [14]-[16], but no applications for single phase PM-BLDC motor sensorless drives are known.

Based on the PLL characteristic to cause one signal to track another one, the rotor speed and position are further refined by using such a PLL structure.

Figure 9 presents the PLL structure which improves the atan2 based estimated position (θ_{atan}). PLL structure basically consists of a phase detector (PD), a loop filter (LF) and a voltage-controlled oscillator (VCO). Here, the loop filter is a proportional plus integral controller (PI) and the VCO function is represented as an integrator. The essential relations are given by eq.(14)-(16).

The error between the previous atan2 position and the estimated position is the input to a PI controller and the output from the PI controller is the estimated speed.

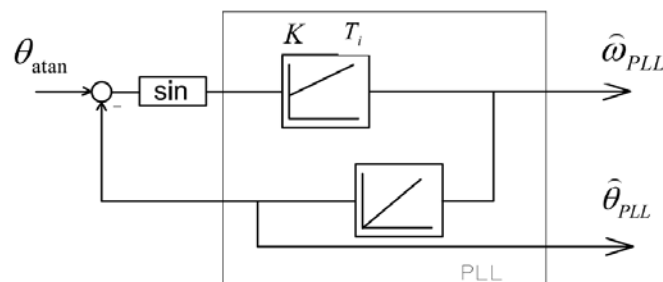


Figure 9 Equivalent PLL based position and speed estimator

The PI controller coefficients were set to $K_p = 25$ and $K_i = 4000$ in order for the PLL to track the input but not exactly. The target was that the PLL to behave like a filter for the positions oscillations.

$$\hat{\omega}_{PLL} = \left(K_p + \frac{K_i}{s} \right) \cdot \varepsilon \quad (14)$$

$$\varepsilon = \sin(\hat{\theta}_{atan} - \hat{\theta}_{PLL}); \quad (15)$$

$$\hat{\theta}_{PLL} = \hat{\omega}_{PLL} / s \quad (16)$$

Compared with the offline Fourier analysis based position and speed observer, a few advantages reveals:

-Simple observer structure which eliminated the speed noise produced by the position derivative

-It does not need any previous analysis to obtain the correction coefficient

-Theoretically, by just adapting the PI controller coefficients, it can be applied to any PM flux shape from linear to sinusoidal

Figure 10 shows by simulation results how the PLL output position tracks the input position and behaves like a very efficient LPF for the noticed position oscillations.

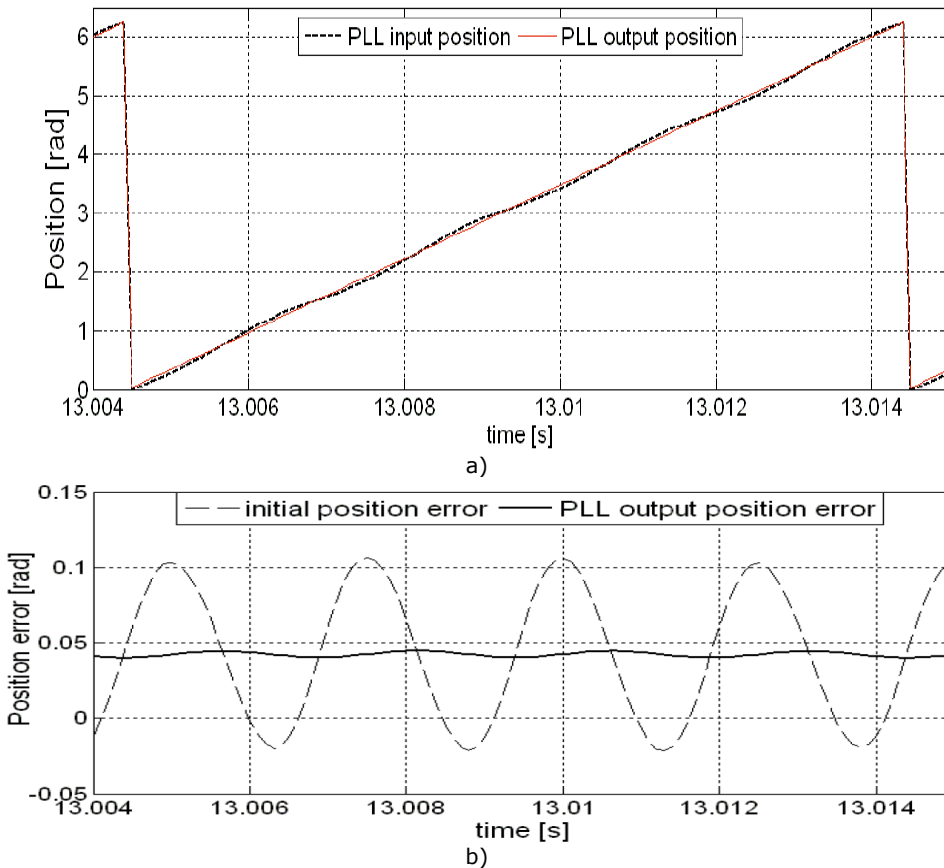


Figure 10 Simulation results at 3000 rpm: a) estimated position, b) position error

The presented PLL based observer (Fig.9) is attractive because of its simple construction which outlines the filtering behavior of the PLL algorithm over the position obtained from nonsinusoidal flux linkage waveform.

A modified state observer, derived from the one from figure 1.b was also implemented and tested. It eliminates the \tan^{-1} function and uses a modified PLL structure for position and speed extraction. The difference from the previous PLL observer is concentrated in the PD section.

In order to simplify the demonstration, for the PM flux, a sinusoidal waveform is first considered. Thus, the flux phasor $\underline{\psi}_{PM}$ can be written as in eq. (17)

$$\underline{\psi}_{PM} = \psi_{PM} \cdot e^{j\theta} = \psi_{PM} \cdot \cos(\theta) + j \cdot \psi_{PM} \sin(\theta) \quad (17)$$

Considering the unitary phasor given by equation 18, the PLL error can be extracted starting from eq. 19, which in fact represents the product of the two $\underline{\psi}_{PM}$ and $\underline{\psi}_{PLL}$ phasors.

$$\underline{\psi}_{PLL} = e^{-j\theta_{PLL}} = \cos(\theta_{PLL}) - j \cdot \sin(\theta_{PLL}) \quad (18)$$

$$e^{j\Delta\theta} = e^{j(\theta - \theta_{PLL})} = \cos(\Delta\theta) + j \cdot \sin(\Delta\theta) \quad (19)$$

Knowing that for small values an angle can be approximated with its sinus value, the PLL error can be written as:

$$\varepsilon \cong \psi_{PM} \cdot \sin(\Delta\theta) = \text{Im}(\underline{\psi}_{PM}, \underline{\psi}) \quad (20)$$

Which yields to eq 21 :

$$\varepsilon \cong \psi_{PM} [\sin(\theta) \cdot \cos(\theta_{PLL}) - \cos(\theta) \cdot \sin(\theta_{PLL})] \quad (21)$$

Considering the above, the PLL observer is implemented based on equation 22 where $\psi_{PM}(\theta)$ and $\psi_{PMd}(\theta)$ are the real flux distribution function, approximated by eq. 8, 9.

$$\varepsilon \cong \psi_{PMd}(\theta) \cdot \cos(\theta_{PLL}) - \psi_{PM}(\theta) \cdot \sin(\theta_{PLL}) \quad (22)$$

Based on eq. 19, the inputs of PLL observer are the outputs from the orthogonal flux system generator block. Since in a PMSM the rotor flux is locked to the rotor position, the proposed PLL structure estimates the rotor position and speed from the nonsinusoidal flux functions given by the flux observer.

Figure 11 illustrates the derived state observer structure, while figure 12 presents the modified PLL observer.

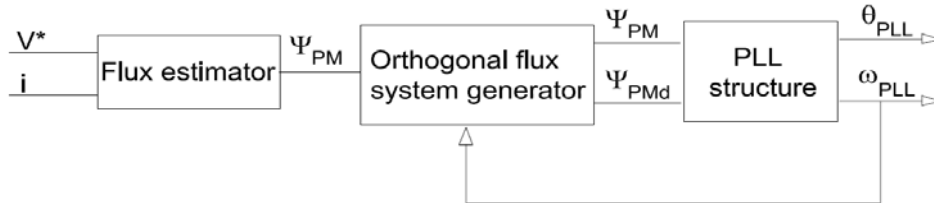


Figure 11. Derived State observer

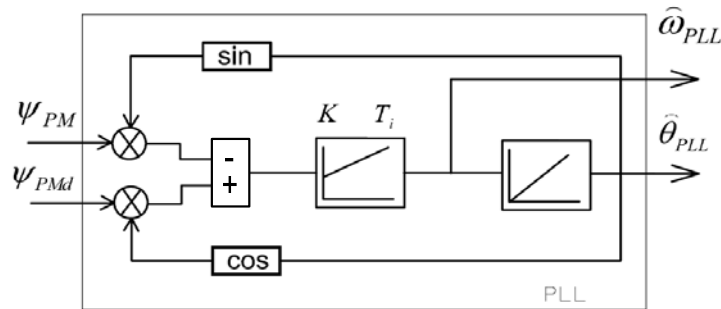
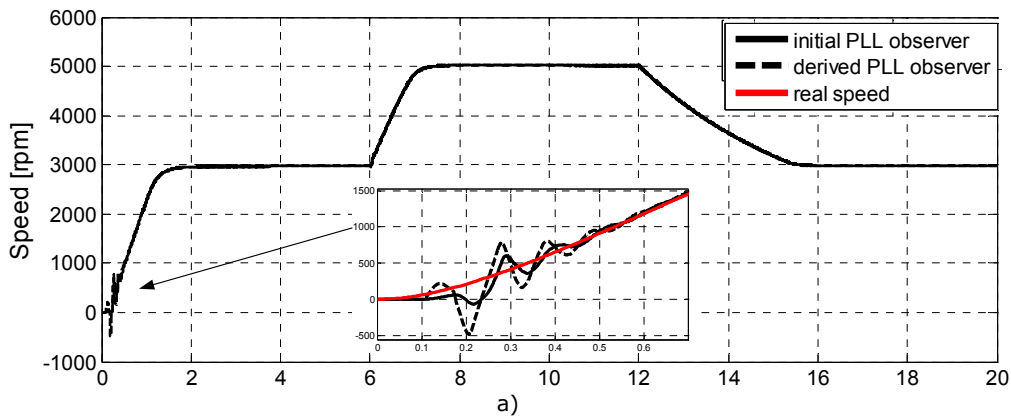


Figure 12. Modified PLL observer

The PI controller from this structure has the same coefficients as mentioned for the other one, and in spite of the nonsinusoidal waveforms of the flux, the obtained speed and position proved to be satisfying. In order to use the same coefficients as for the previous PLL observer, it is necessary that the estimated flux, respectively the delayed PM flux to be used in per unit.

The behavior of both presented PLL based position and speed observers was almost the same in simulation and also in experiments. Figure 13 shows the open loop digital simulation results for the two PLL observers. A good behavior is noticed for both of them with a slight advantage for the first PLL structure.

As expected, at starting some oscillations are visible until the phase is locked. These oscillations won't affect the sensorless control because during this time interval the motor will be drive with open loop speed, by using an I-f strating sequence.



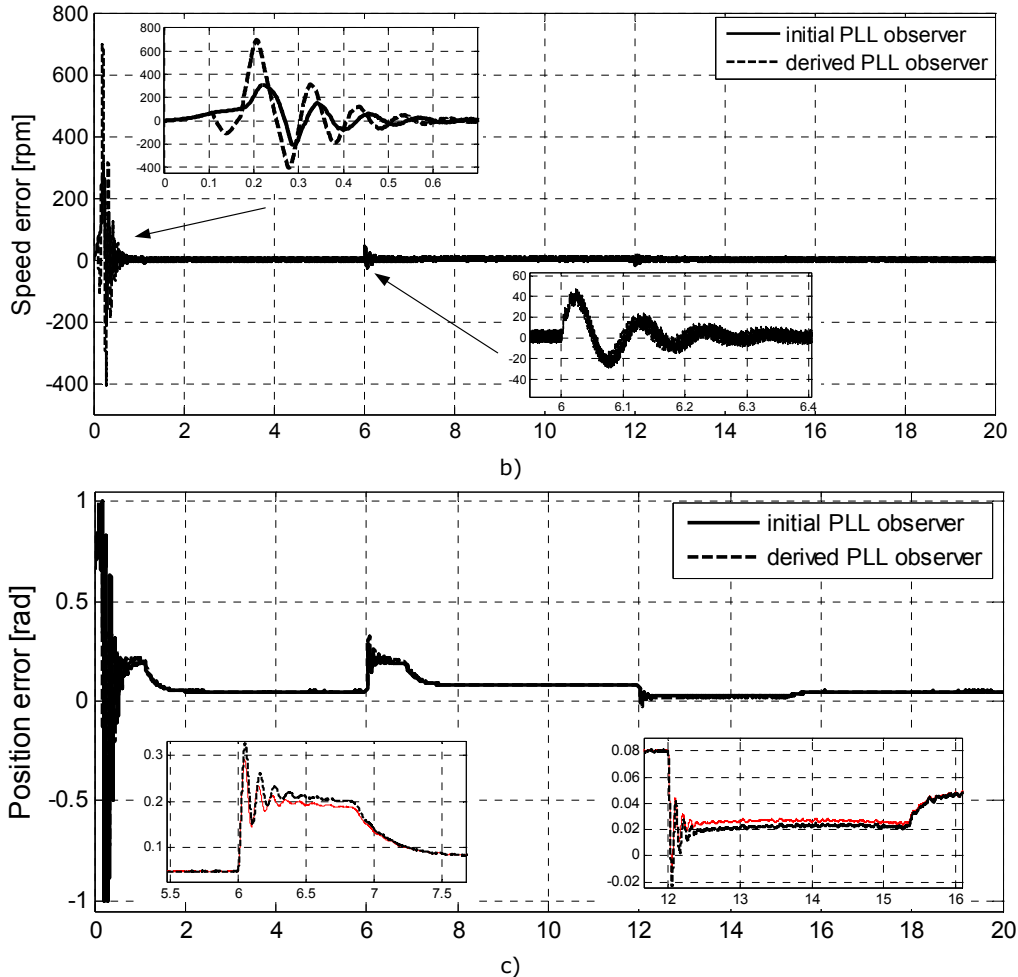


Figure 13. Simulation results for PLL observers open loop validation

As it was shown in chapter 4, a decrease in the flux amplitude with speed increase it is noticed due to the PMs demagnetization caused by the corroboration of eddy currents and temperature. Also during transients the estimated PM flux suffers amplitude changes. The derived PLL observer presents the drawback that it is affected by these PM flux amplitude and may require retune of PI controller to render the same experimental performance as in simulation. Considering the above, because it is not affected by the PM flux amplitude modification with speed, the first PLL solution is further used for sensorless control.

5.6.2. Experimental results

In order to compare the proposed state observer behavior with the one predicted from simulations, in what follows some experiments for the chosen PLL scheme (Fig.9) are run. The motor is still run by using the position and speed

information from the Hall sensor only for the proposed observer to be analyzed in open loop.

Figures 14-16 presents the experimental results three different constant speed values. The measured and estimated positions are intentionally shifted with 1 radian in order to avoid overlaps, in Fig.14-16.

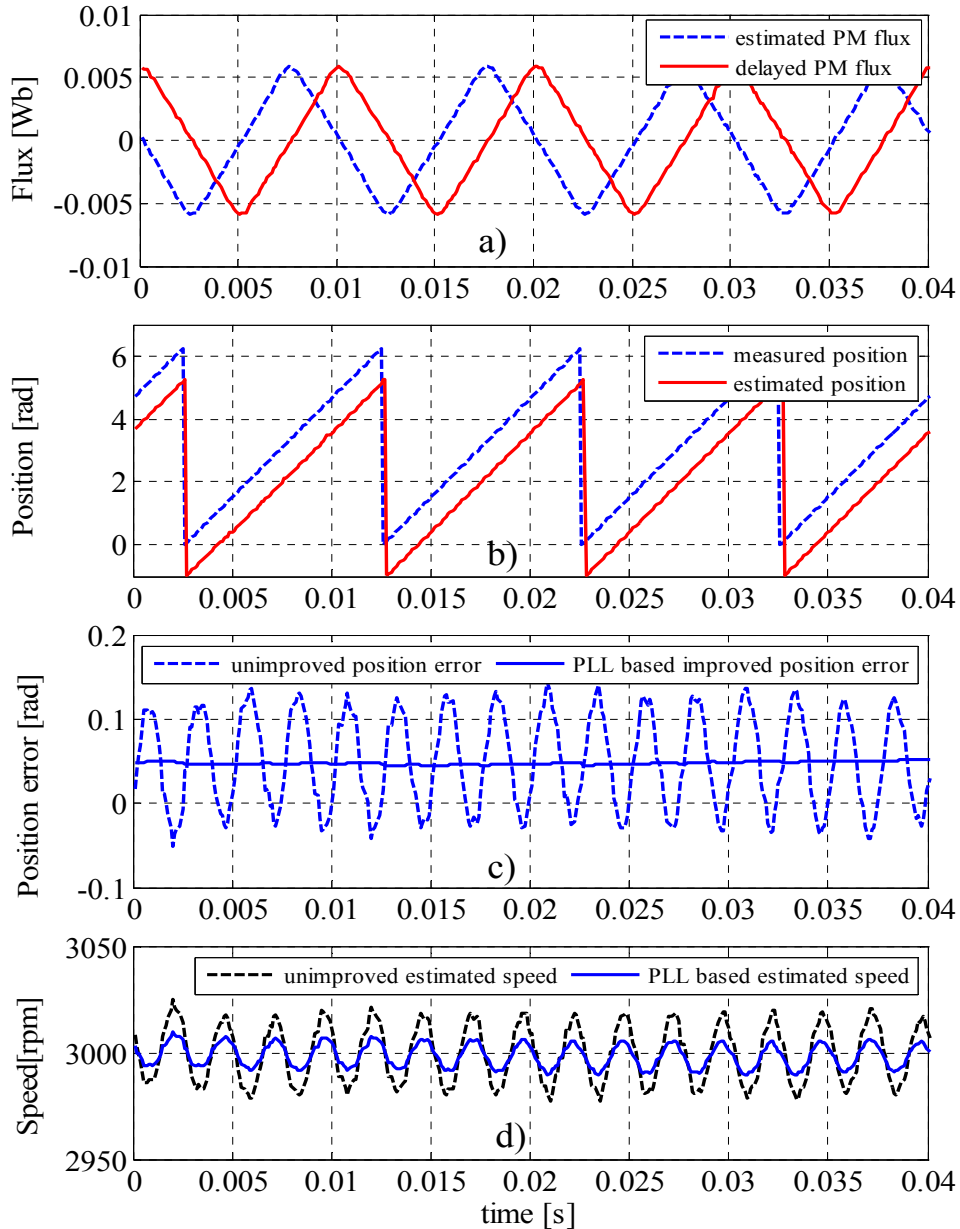


Figure 14. Experimental results at 3000rpm: a) estimated and delayed flux, b) measured and PLL based estimated position, c) position error d) speed

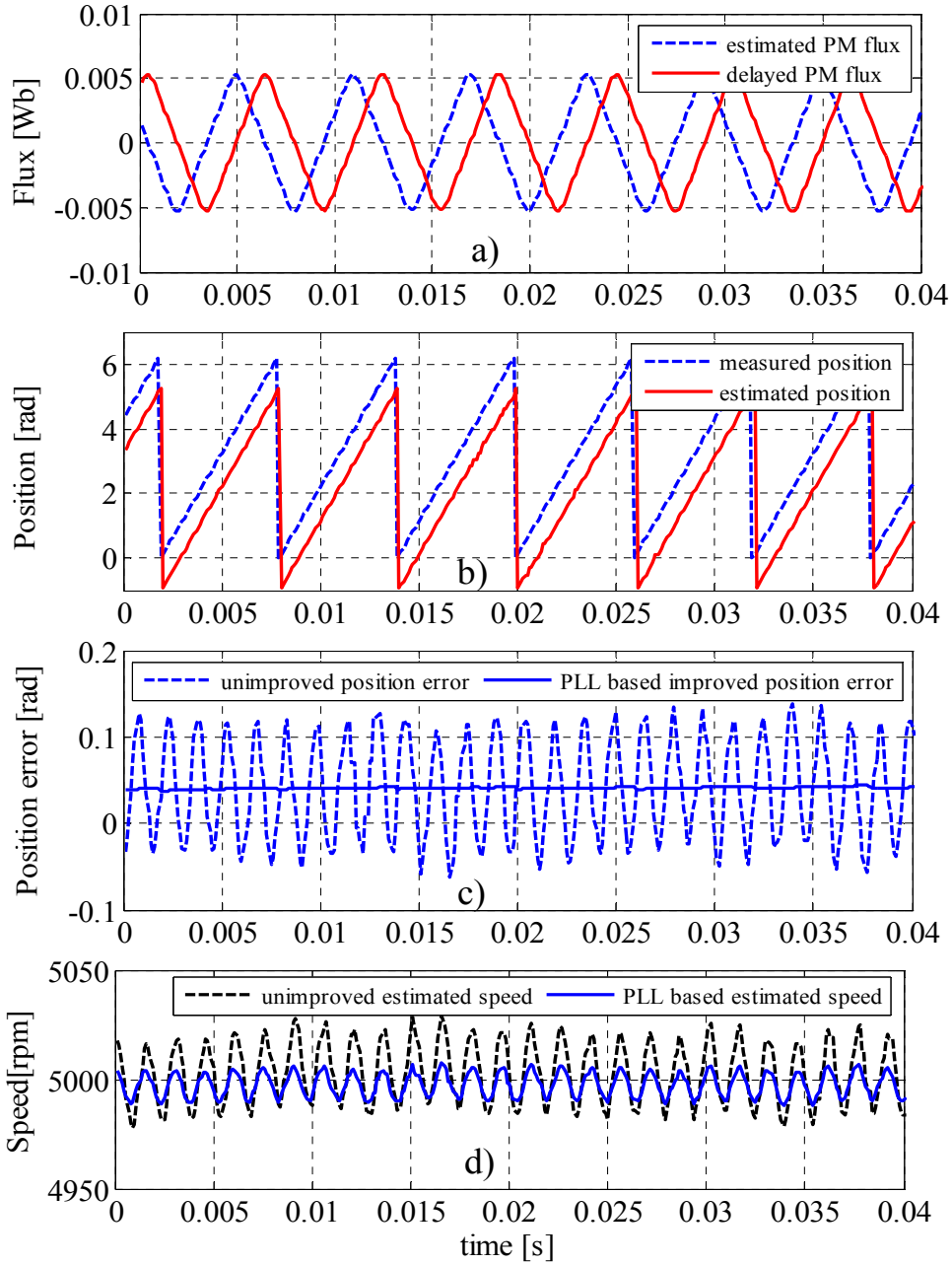


Figure 15. Experimental results at 5000rpm: a) estimated and delayed flux, b) measured and PLL based estimated position, c) position error d) speed

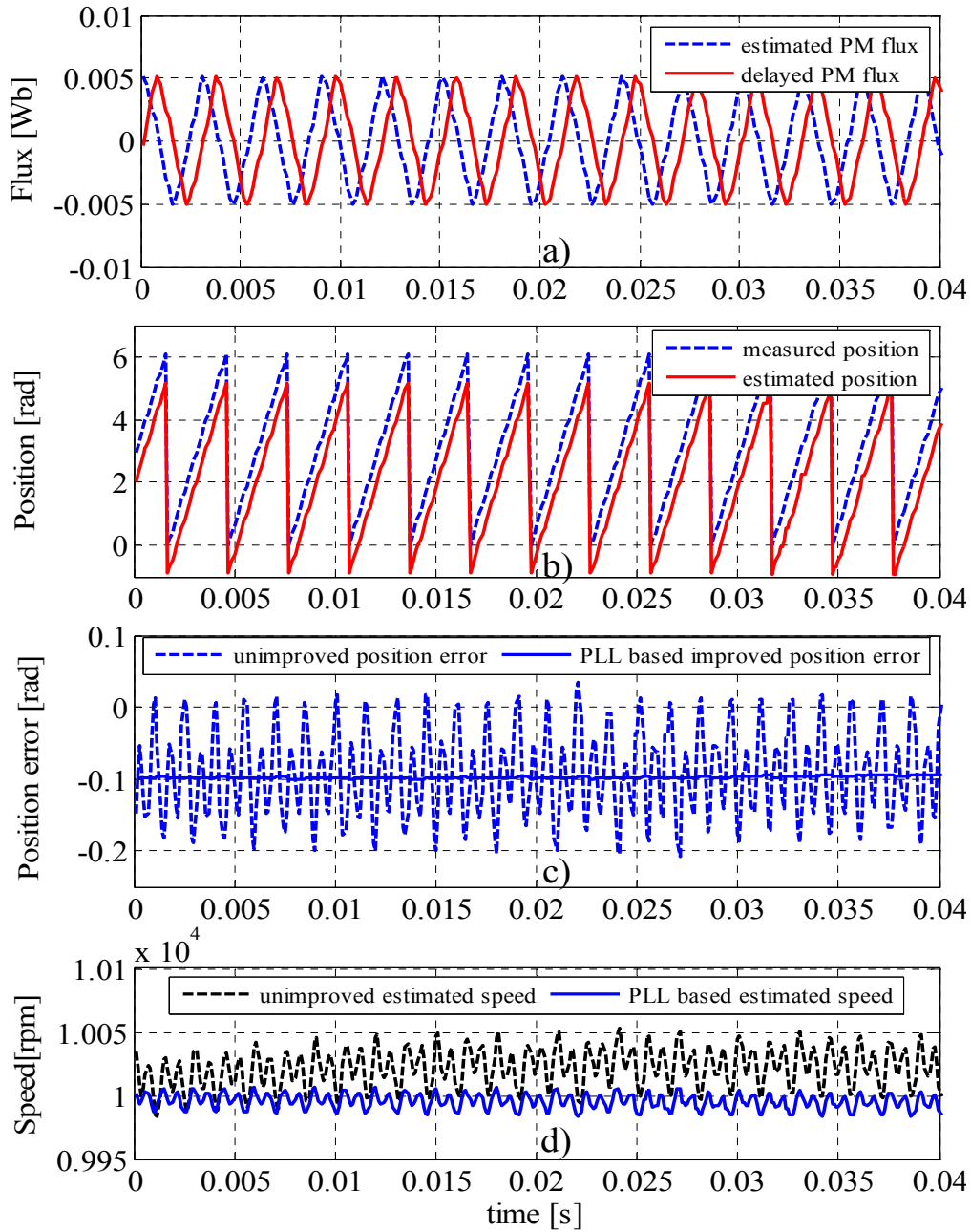


Figure 16. Experimental results at 10krpm: a) estimated and delayed flux, b) measured and PLL based estimated position, c) position error d) speed

The filtering behavior of the PLL structure over the estimated position and the speed pulsations reduction are visible. Again, the different offset position error at 10krpm is due to the fact that the so called measured position is, in fact,

calculated from the Hall sensor and at high speed some computational error appears, but in spite of this aspect, it offer a good enough information over the filtering behavior of the PLL observer.

5.6.3 Offline Fourier analysis based state observer vs. PLL based state observer: short experimental comparison

Although both state observer structures gave good results regarding estimated position and speed pulsations, by using the PLL based observer a smother estimated position was obtained (this can be better noticed in the position error, which is also smother).

Also, in Figure 17 a good tracking behavior is noticed for both structures when the speed reference changes from 1000 rpm to 8000 rpm.

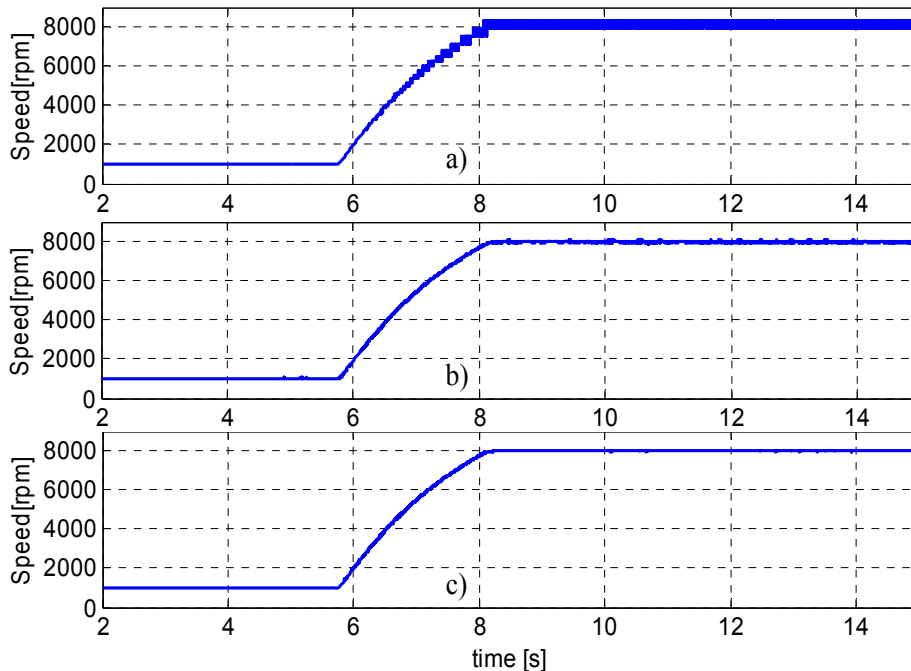


Figure17. Experimental results for 1000 to 8000 rpm speed transient: a)Hall based measured speed, b)Offline Fourier based speed observer speed c)PLL based speed observer

Figure 18 shows a comparison between the two presented state observer structures (Fig.1) results at 10krpm and, again better results are noticed for the PLL based state observer. It can be noticed that at higher speed the PLL based observer seems to be more reliable due to smoother position and lower speed pulsations.

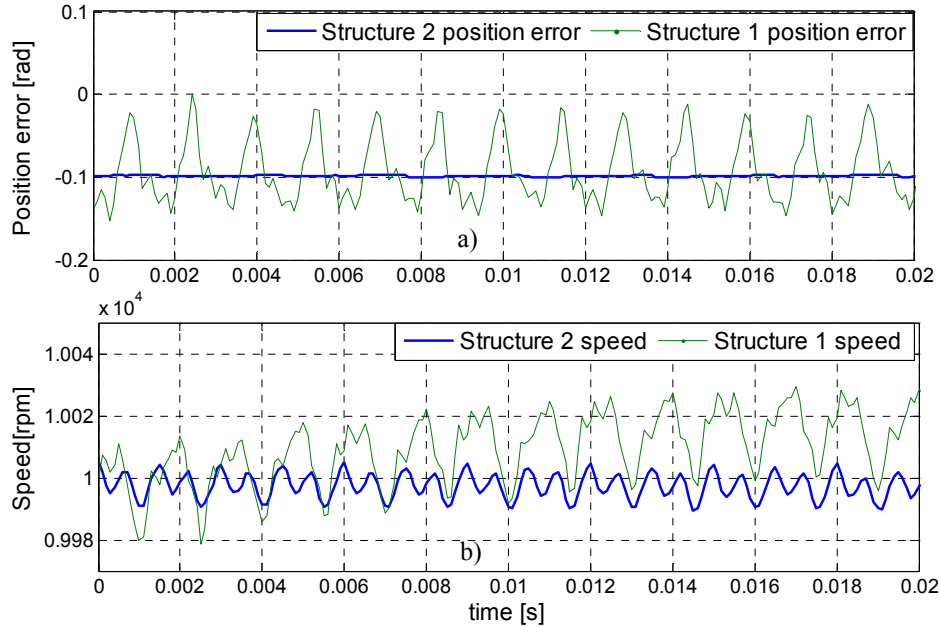


Figure 18. Experimental comparison results between: the two proposed observer structures at 10 krpm a) position error, b) speed

5.7. Hybrid I-f starting and observer based motion sensorless control: experimental results

In order to test the motor in close loop sensorless control, basically the same close loop control as presented in chapter 4 applies.

To start the motor, an I-f starting sequence is employed here. The applied reference current frequency is ramped by using a first order delay filter while the reference current amplitude is maintained constant. From this frequency an imposed position is obtained and the prescribed phase current is commutated by using this feedforward signal. After starting the sensorless control is done based on the estimated position and speed obtained from the state observer.

Figure 19 illustrates the proposed sensorless control diagram, which contains the two PI speed and current controller, the I-f starting sequence and the state observer.

The PI speed controller coefficients were determined by using the empirical Ziegler-Nichols tuning method and the values are: $K_{wp} = 0.06$ [As/rad] and $K_{wi} = 0.01$ [A/rad]. The applied PI current controller is exactly the one described in chapter 3, with the $K_{ip} = 500$ [V/A] and $K_{ii} = 3$ [s^{-1}] and BEMF compensation. The PI controller used for the I-f strategy has the form : $K_{pI-f}(1 + K_{iI-f}/s)$, with

$K_{pI-f} = K_{ip} = 500$ [V/A] and $K_{ii-f} = K_{ii} = 3[s^{-1}]$; no bemb compensation is needed.

In what follows detailed experiments for the proposed sensorless drive are run.

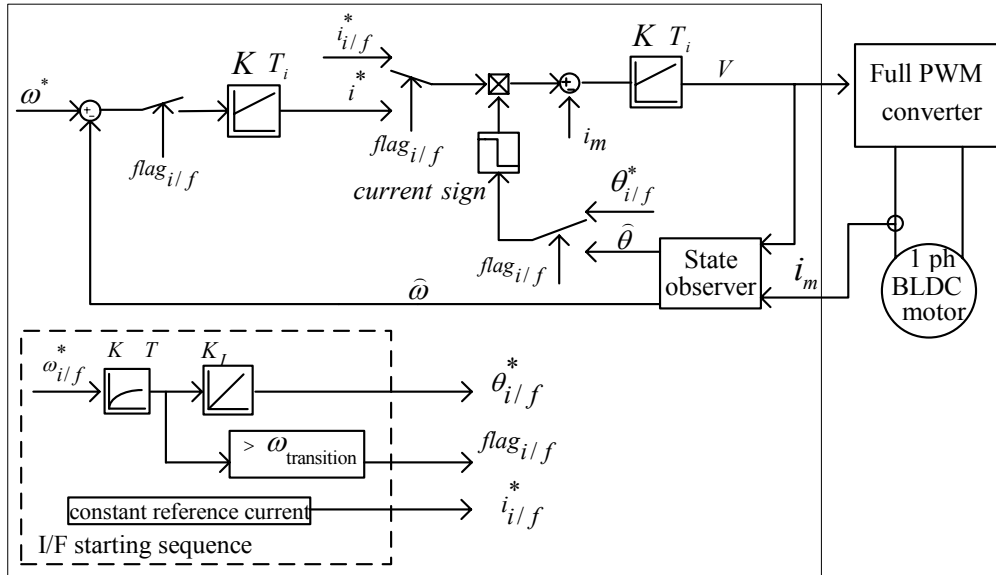


Figure 19. Sensorless control block diagram

5.8. Experimental results

Due to better results under open loop experimental testing, only the PLL observer is considered further for close loop sensorless control experiments.

Fig. 20, 21, 22, shows the experimental results at a given constant speed of 3000 rpm, 5000 rpm, respectively 10000 rpm. The reference volatage, phase current, generated orthogonal fluxes, position and speed informations are depicted for a qulitative overview of the close loop sensorless control under steady state. The measured and estimated positions are intentionally shifted with 1 radian in order to avoid overlaps. A good agreement between measured (calculated from hall signal) and estimated position can be observed and the speed pulsation are very good for a single phase motor. At 10000 rpm a speed offset is noticed, which may be minimized by a more carefully tuning of the PI speed controller.

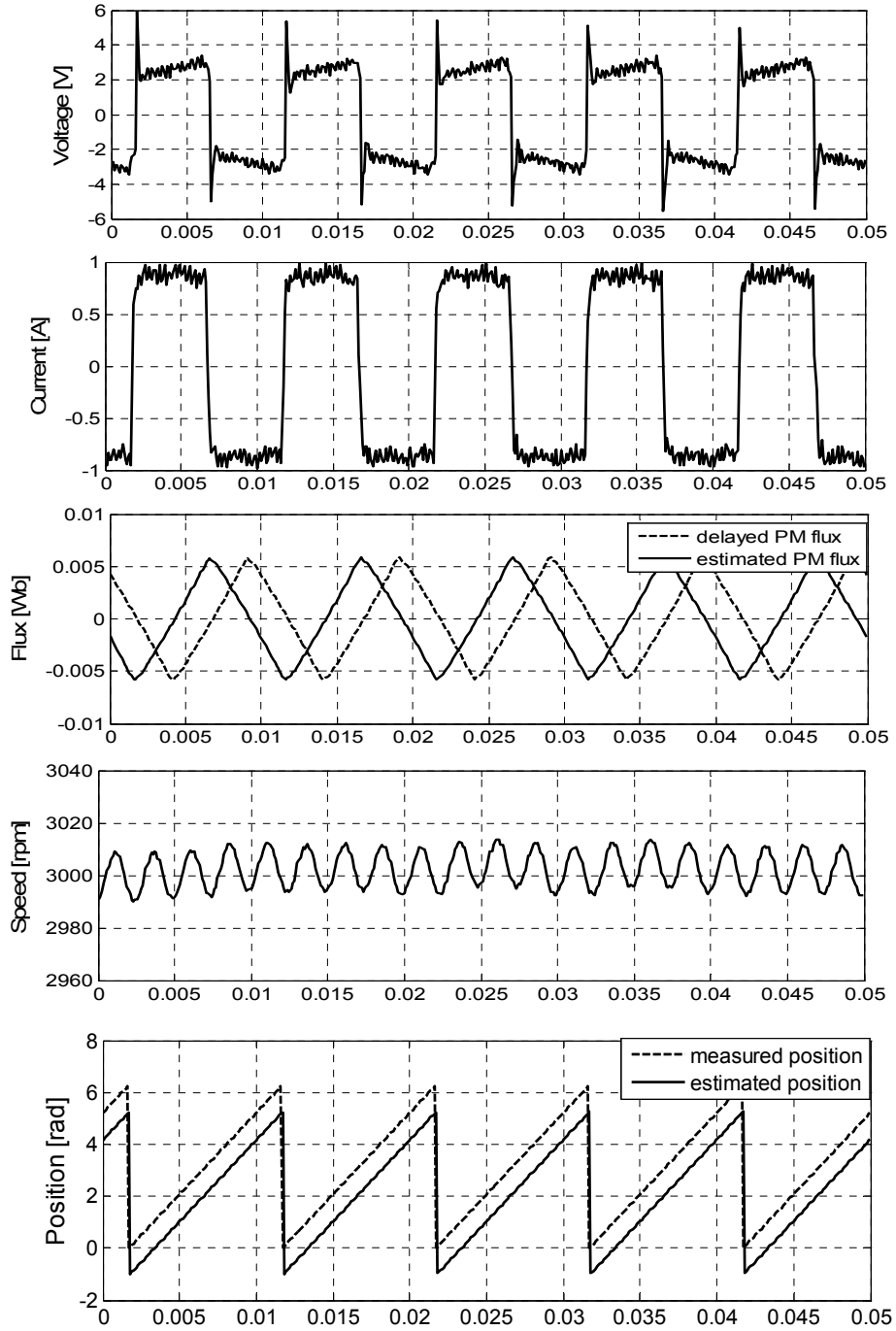


Figure 20. Sensorless control experimental results at 3000 rpm : a)reference voltage, b)current, c) flux, d) speed, e) position

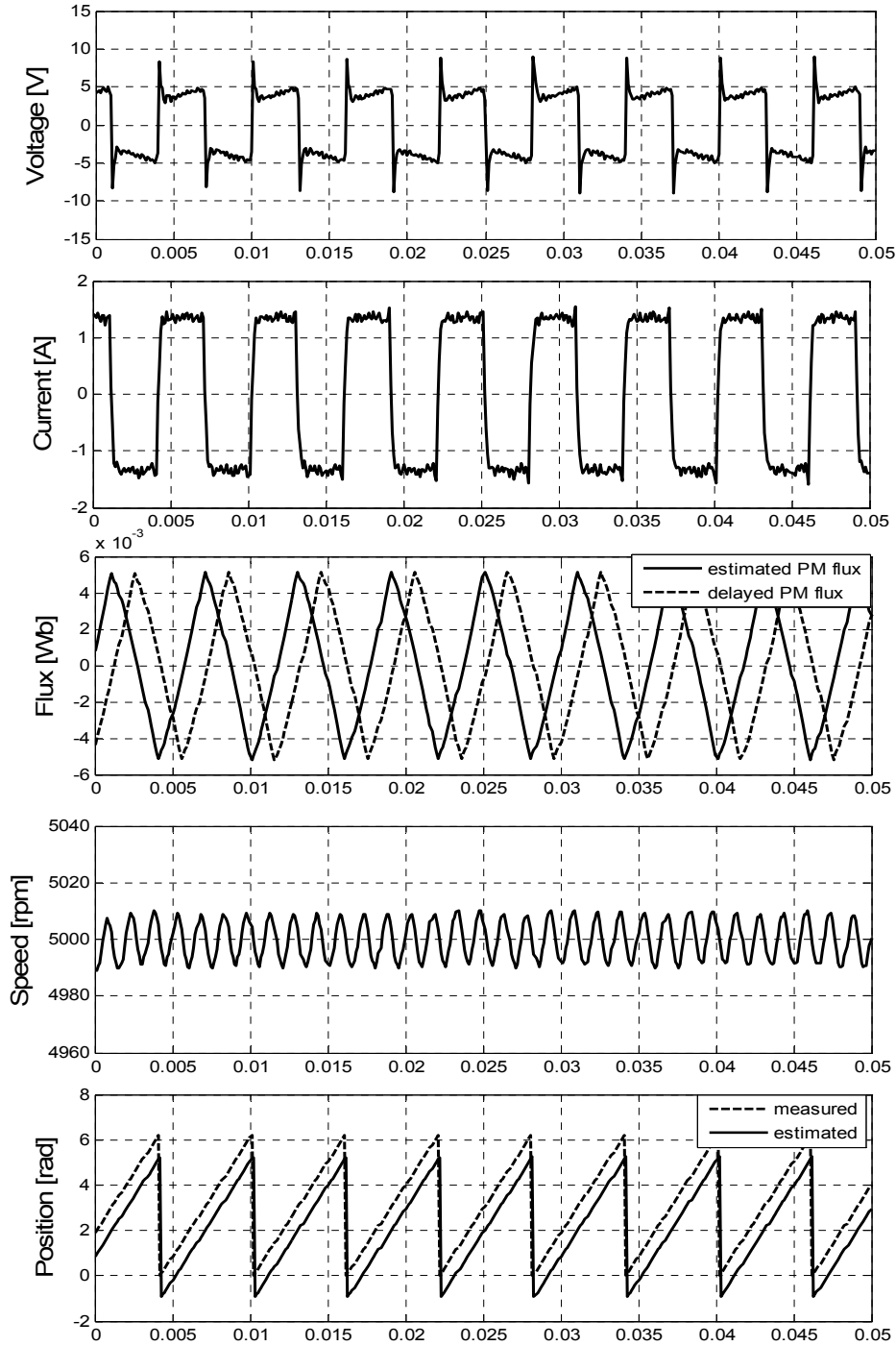


Figure 21. Sensorless control experimental results at 5000 rpm : a)reference voltage, b)current, c) flux, d) speed, e) position

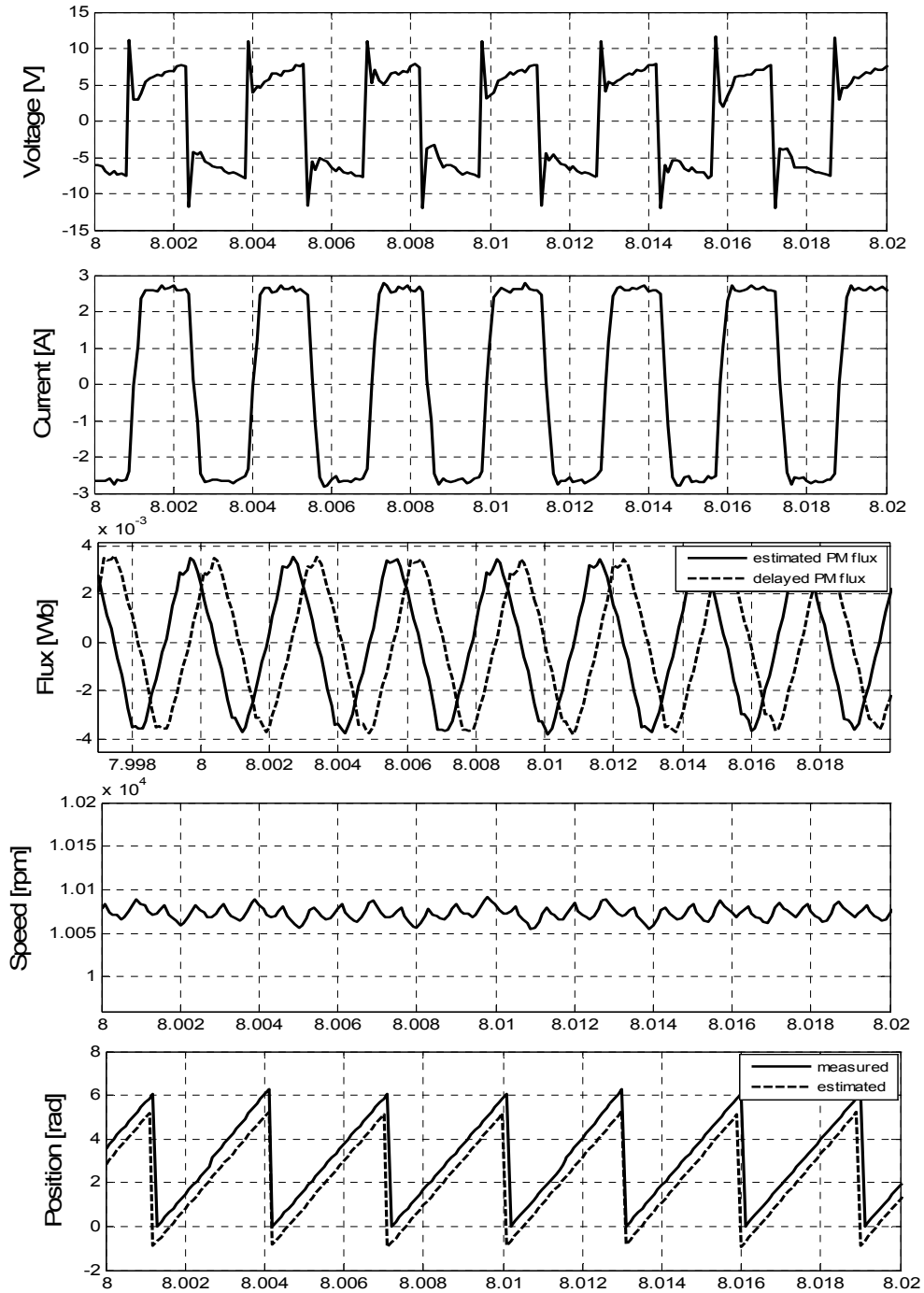


Figure 22. Sensorless control experimental results at 10000 rpm : a)reference voltage, b)current, c) flux, d) speed, e) position

Figure 23 shows a sensorless speed control from standstill to 10 krpm. The starting from zero speed is achieved with the proposed I-f strategy. As in simulation results, some oscillations are noticed in the estimated speed, but those imposes no problems since the open loop starting is used in this time interval, and the reference speed is reached.

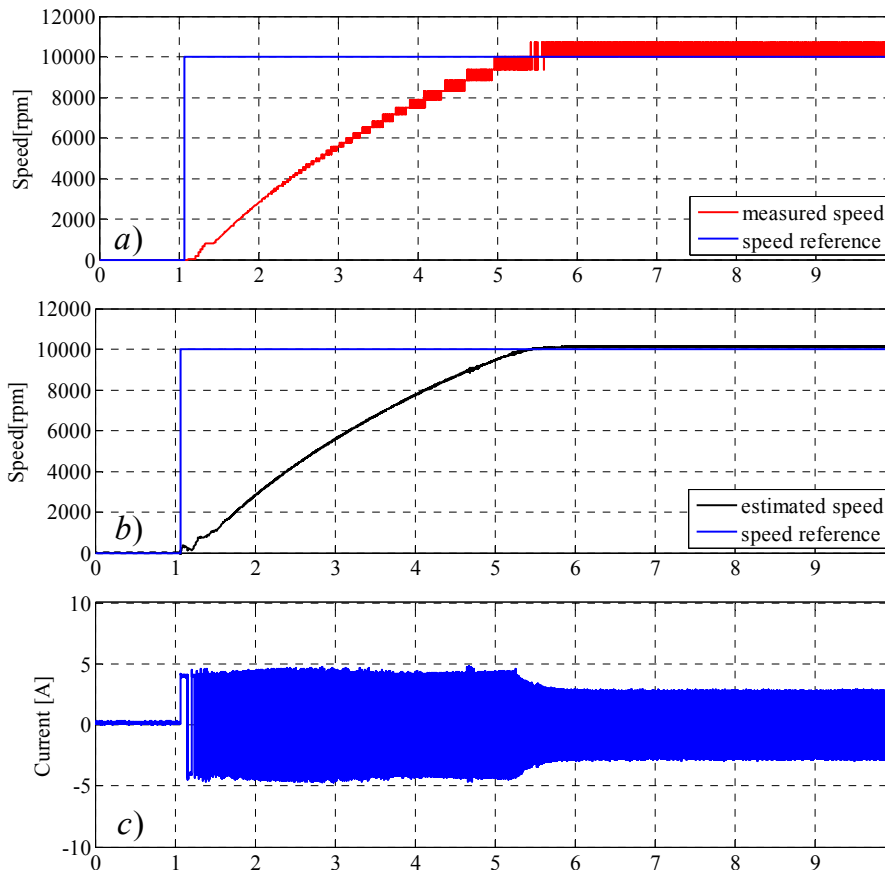


Figure 23. Experimental results for 0 to 10 krpm speed transient: a) measured speed, b) estimated speed, c) current

Figure 24 shows a deceleration from 8000 rpm to 5000 rpm. Note that the the estimated speed is in good correspondence with the measured one under both acceleration and deceleration, and as expected is more smother under transients because it is updated on every sampling period, while the so called measured speed is updated on every encountered edge of hall signal.

During deceleration, the minimum current reference value was limited in order to avoid zero current because it causes important problems for the flux estimation. If zero current is required the controller will produce also a zero duty cycle, and so, based on equation 11 (section 4.2) the estimated voltage becomes zero. Thus, the flux estimator has no information for integration and the sensorless control fails. But, for the given load here, a blower, considering that no quick speed

changes are needed, it may be enough to decelerate by only reducing the duty cycle and thus the motor slowly reduces speed. This is a simple solution when low noise level achieved through soft switching and not high dynamics requirements are desired.

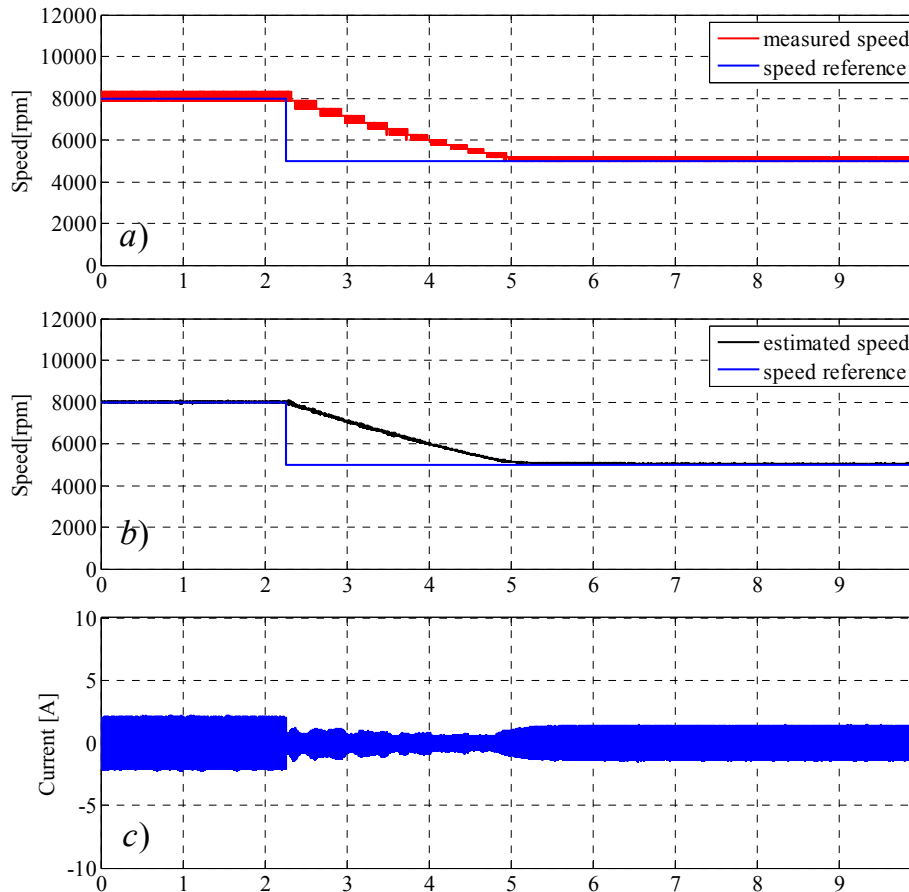


Figure 24. Experimental results for 8000 to 5000 rpm speed transient: a) measured speed, b) estimated speed, c) current

The position offset from figure 14, 15, 16 is compensated when running on speed close loop sensorless control, and more, a speed dependent phase advance commutation angle was applied in order to obtain an always positive torque. Since the position error is not very reliable information due to the problems that arise in the position information computation from hall signal, additional informations are needed for performance evaluation of the proposed sensorless control.

The relation between hall signal and the current is used to verify the motor behavior under transients. Figure 25 illustrates a transient behavior for speed steps of 1000 rpm. Comparing figures 25.e and 25.f a delay between the current and the hall signal is noticed under transient. Because the current is prescribed using this estimated position, it means that the error between the estimated and the real

position is increasing under speed variations but not alarming. Such delay between current and BEMF are often obtained with hall control.

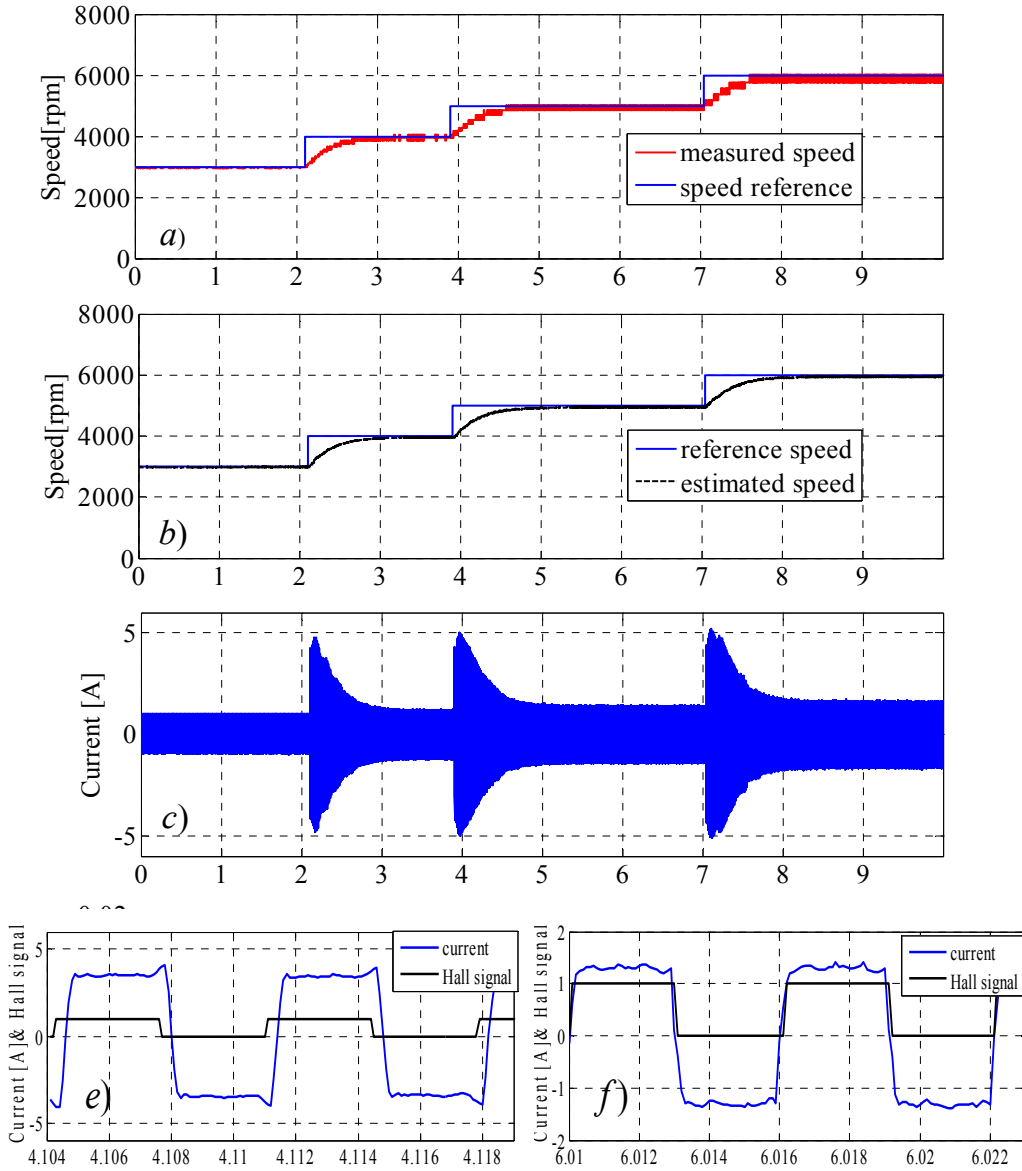


Figure 25. Experimental results for speed transient: a) measured speed, b)estimated speed, c) current, d) current and hall signal under speed transient e) current and hall signal for constat speed

Figure 26 presents a detailed view over the crossing moment from the I-f sequence to close loop sensorless control.

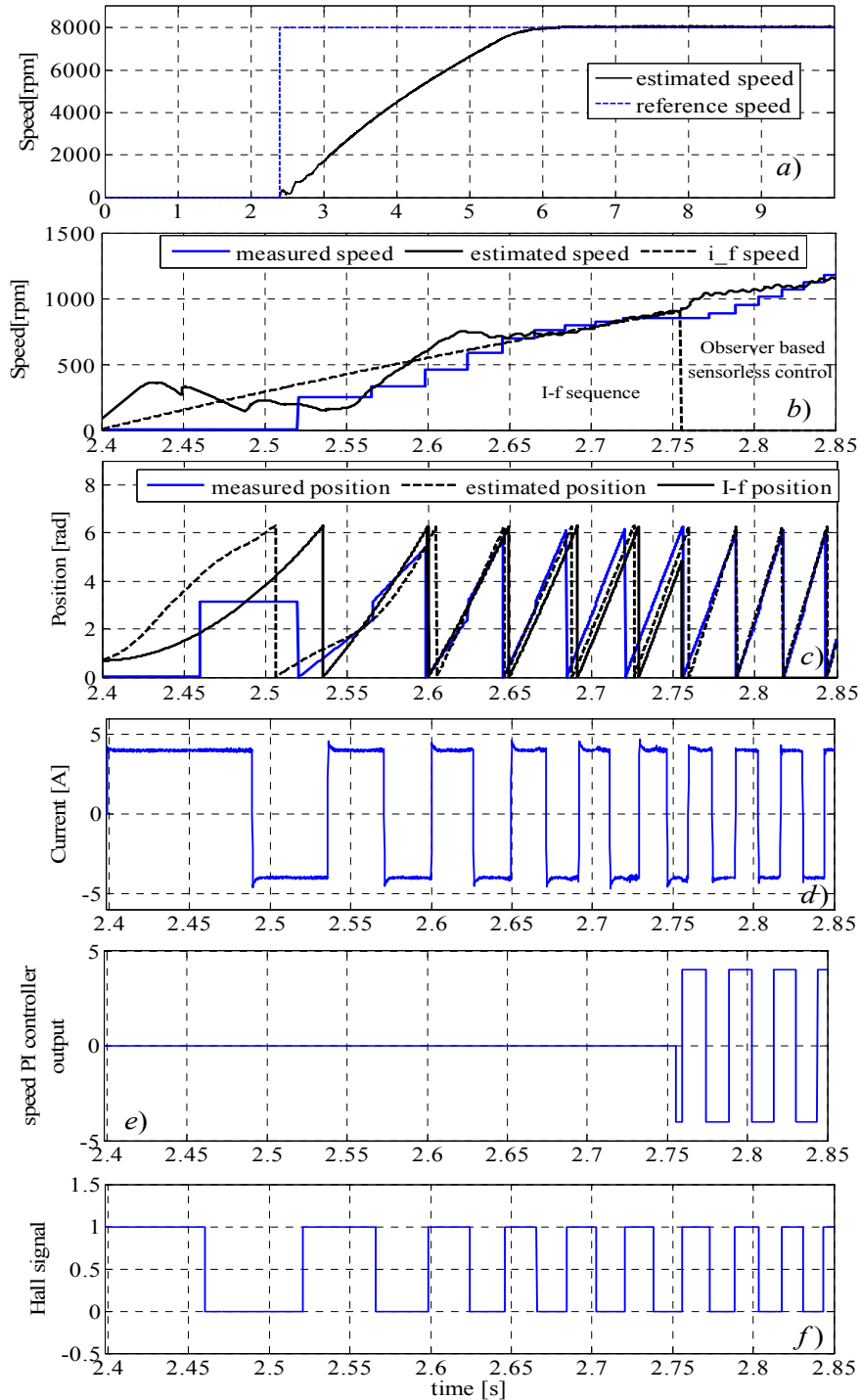


Figure 17. Experimental results for starting: a) estimated speed, b) speed comparison, c) position, d) current, e) output from speed controller, f) hall signal

As explained above, the PI speed controller sees zero speed error at the input, and so the imposed reference current from it will be zero during I-f sequence. During this sequence a constant current is commutated based on a feedforward position information. When the reference frequency from I-f control is greater than the imposed threshold the sensorless control passes to the close loop sensorless control and the current commutation is done based on the estimated position (Fig.26.d), while the I-f position and speed becomes zero. Now, the speed controller produces a nonzero signal as reference current (Fig.26.f). In Fig.26.c good speed estimation is obtained, with some oscillations at the start around the prescribed I-f speed. Figure 26.d shows that for both the estimated and I-f position the initial position is considered to be the parking position. To start in the desired direction, the PM polarity must be known. A solution for starting based on rotor pole discrimination is presented in [17]. Another solution based on cogging torque exploiting is presented in [18]. As shown in [18], by applying a proper positive pulse before I-f sequence, the starting position will always be appropriate for starting with positive current as used here (Fig. 17.e).

In order to further validate this proposed sensorless control a short analysis of developed torque is done. Based on a previous FEM analysis and laboratory measurements, the BEMF and the cogging torque characteristic of the motor are used as look-up tables. The input to these look-up tables is the calculated position from the hall signal. Using this information the torque was calculated using equation (23) under steady state.

$$J \cdot \frac{d\omega}{dt} = k_e \cdot i + T_{cogg} - T_{load} \quad (23)$$

Figure 18, 19 shows the experimental results for a constant speed of 4000 rpm, respectively 10000 rpm. It can be noticed that the current is in phase with the BEMF and so the torque required by the blower load at the mentioned speeds is obtained with minimum current. The obtained instantaneous torque is always positive due to the proper control.

Due to the errors that can appear when calculating the position from the hall sensor in dynamics, only the torque under steady state speed is reliable and presented. Only rectangular current shape control was used here at small speed, but any current shape can be prescribed, while at 10000 rpm only the phase advance technique has used.

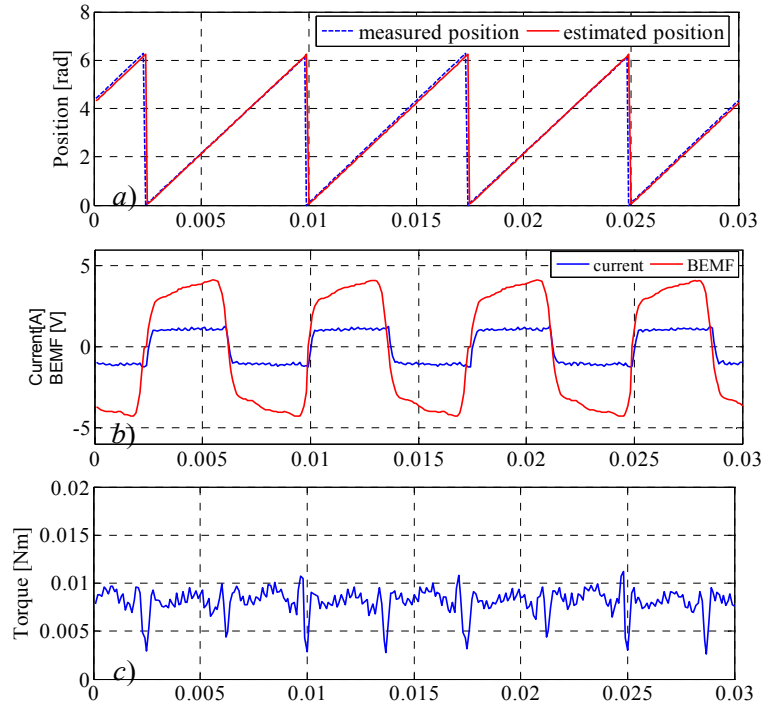


Figure18. Experimental results at 4000 rpm: a)position, b) BEMF and current, c)calculated torque

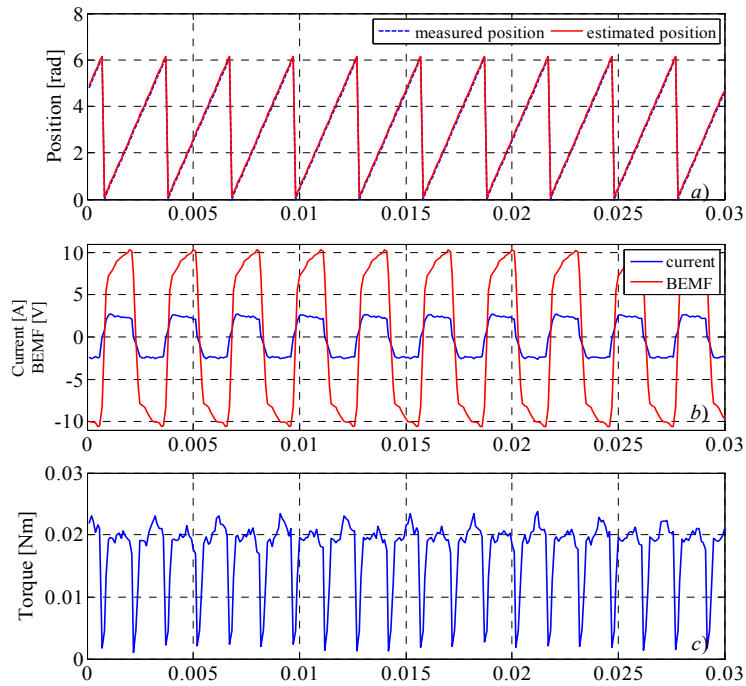


Figure19. Experimental results at 10000 rpm: a)position, b) BEMF and current, c)calculated torque

5.9 Conclusions

A hybrid I-f starting and observer based motion sensorless control for a single phase PM BLDC motor was introduced here.

A real time PM flux estimator is implemented and some special calculations are done in order to extract the position/speed information. These imply a generated orthogonal flux system whose outputs are used in estimating the position using the atan2 function.

The peculiarity of using a PM flux with harmonic content for extracting the position in this way is explained and detailed by Fourier series analytical approximation and by simulations.

Based on this Fourier analysis a position refining method is proposed, detailed by simulation and validated by experimental results.

As another solution for position and speed improvement, two PLL observers were presented and compared by simulation results. The difference between them is located in the phase detector part. The first one was used for speed estimation and for filtering the obtained position from atan2 function, while the second one eliminates the atan2 function and estimates the speed and position from the estimated and the delayed fluxes. The first PLL observer is chosen for further sensorless control tasks and its effectiveness was demonstrated by experimental results. The PLL strategy is totally independent from any amplitude variation of the estimated PM flux.

The proposed sensorless control was validated by exhaustive experimental results. The possibility to apply this control for different solution for smoothing the torque, increase the efficiency or other improvement by control was suggested by combining the current control and the phase advance technique.

The steady state torque results are good with no negative values. Also, the difficulties that arise when low cost resources (existing Hall sensor) are used to apply and test the sensorless control were referred here and its limitations were mentioned. The real position and speed were measured from the Hall sensor without using a high resolution position sensor like an encoder and the torque was calculated using the motor characteristics without using a torquemeter.

References

- [1] Paul P. Acarnley, John F. Watson, "Review of Position-Sensorless Operation of Brushless Permanent-Magnet Machines", *Transaction on Industrial Electronics*, vol. 53, no.2, April 2006, pp. 352-362.
- [2] Weizi Wang Zhigan Wu Wanbing Jin Jianping Ying "Sensorless control technology for single phase BLDCM based on the winding time-sharing method", *record of Industrial Electronics Society*, Nov 2005, pp. 1732-1736.
- [3] H. Ohta, T. Satou, K. Matsuse, "Principle and analysis of simple starting method for new single-phase PM motor without position sensor", pp.1103-1108
- [4] Silva, S.M., Lopes, B.M., Filho, B.J.C., Campana, R.P., Bosventura, W.C. "Performance evaluation of PLL algorithms for single-phase grid-connected systems", *Record of the Industry Applications Conference*, oct.2004, vol.4, pp.2259-2263.

- [5] Ciubotariu, M., Teodorescu, R., Blaabjerg F. "A new single-phase PLL structure based on a second order generalized integrator", Power Electronics Specialists Conference, June 2006, pp.1-6.
- [6] S. Shinnaka, "A robust single phase PLL system with stable and fast tracking", Transactions on Industry Applications, vol. 44, no.2, March/April 2008, pp. 624-633
- [7] Kaura, V.; Blasko, V "Operation of a phase locked-loop system under distorted utility conditions", Conference proceedings of Applied Power Electronics Conference and Exposition, Mar.1996, pp.703-708.
- [8] F. D. Freijedo, J. Doval-Gandoy, O. Lopez, E. Acha, "Tuning of phase-locked loops for power converters under distorted utility conditions", Transactions on Industry Applications, vol. 45, no. 6, Nov/Dec 2009, pp.2039-2047
- [9] L. Harnefors, H.P.Nee, "A general algorithm for speed and position estimation of AC motors", IEEE Transactions on Industrial electronics, vol. 47, no.1, Feb. 2000, pp.77-83
- [10] M. Comanescu, L. Xu, "An Improved Flux Observer Based on PLL Frequency Estimator for Sensorless Vector Control of Induction Motors", IEEE Transactions on Industrial Electronics, vol. 53, no.1, Feb 2006, pp.50-56
- [11] M. Fatu, R. Teodorescu, I. Boldea, G.D.Andreescu, F. Blaabjerg, "I-f starting method with smooth transition to EMF based motion- sensorless vector control of PM synchronous motor/generator", Power Electronics Specialists Conference, June 2008, pp. 1481-1487
- [12] G. D. Andreescu, "Position and speed sensorless control of PMSM drives based on adaptive observer", EPE 1999, Lausanne, Switzerland,.
- [13] J-K. Lee, J-K. Seok, D-C Lee, "Sensorless speed control of non-salient permanent magnet synchronous motor using rotor position tracking PI controller", IEEE Power Electronics Specialists Conference, Aachen, Germany, 2004, pp. 4024-4029.
- [14] M. Cacciato, A. Consoli, V. Crisafulli, G. Scarcella, G. Scelba, "Robustness Evaluation of Phase-Locked Loop Algorithms for Single-phase Distributed Generation Systems", record of SPEEDAM 2010, Pisa, Italy, June 2010
- [15] S. A. Oliveira da Silva, R. Novochadlo, R. A. Modesto, "Single-Phase PLL Structure Using Modified p-q Theory for Utility Connected Systems",
- [16] R. M. Santos Filho, P. F. Seixas, P. C. Cortizo, L. A. B. Torres, A. F. Souza, "Comparison of Three Single-Phase PLL Algorithms for UPS Applications", IEEE Transactions on Industrial Electronics, vol 55, no. 8, August 2008, pp.2923-2932.
- [17] H. Ohta, T. Sato, I. Masugane, K. Matsuse, " Rotor pole discrimination and simple starting method of new single-phase PM motor without position sensor", pp.616-621
- [18] Weizi Wang Zhigan Wu Wanbing Jin Jianping Ying, "Starting methods for Hall-less single phase BLDC motor", Proc. of IEEE Industrial Electronics Society, Nov. 2005, pp. 1605-1609.

6. ENHANCED MOTION SENSORLESS CONTROL INCLUDING REGENERATIVE BRAKING

Abstract

An enhanced sensorless control, allowing also regenerative braking for more demanding, customized applications, is presented in this chapter. It basically uses the same hybrid I-f starting and PLL observer based sensorless control presented in chapter 5. The main differences are in the way that the power devices are controlled by PWM and in the way that the estimated voltage, used for reference voltage model based flux estimator, is obtained.

For current control and voltage estimation considerations under regenerative braking mode, the soft switching (slow decay) mode used until now for controlling the H-bridge power devices under PWM, is replaced by the hard switching (fast decay) mode with synchronous rectification.

6.1. Introduction

A full bridge power converter can be controlled with soft PWM switching or with hard PWM switching. These switching strategies are also known as slow and fast decay modes, based on the current dynamics, caused by the current path during recirculation.

The slow decay is the simplest and the most common control. In slow decay mode, current recirculation can be done through the high side or low side transistor, corresponding to low side PWM or high side PWM [1],[2].

By turning on the complementary power devices during current recirculation, to short the reverse diode, the so called synchronous rectification mode (sometimes called active freewheeling) is obtained. This feature can be used on both slow decay and fast decay modes.

When using this commutation mode, power losses can be minimized and the efficiency can be increased when the inverter is made of MOSFETs with small on resistance (R_{dson}) because current can flow in both directions through a MOSFET. Thus, during the current decay period, the current can flow through the Mosfet, rather than through the body diode. The diode will conduct only during the dead time interval [3],[4].

The slow decay mode is suitable for two quadrant motor control, while using fast decay mode, the four quadrant motor control can be achieved. [3]

When fast and controlled braking is desired the use of a four quadrant control is needed.

In order to achieve the regenerative braking for single phase PM- BLDC motor some special aspects have to be treated further.

6.2. Braking methods for single phase PM-BLDC motor

An easy way of braking a single phase PM-BLDC motor is obtained by applying a short circuit at motor terminals. In the literature, this method is encountered under the name of dynamic braking. It often uses a resistor for dissipating the stored kinetic energy in form of the heat. This braking is achieved by forcing the power bridge to apply a short across the load, by turning on either low side or high side switches. Thus the shorting path is always present and allows the BEMF to generate a braking torque during both polarities. If the back-EMF voltage is large, the load current can increase to high values given by $i = E / R_s$, where R_s is the phase resistance.

This braking method has the drawback that the braking torque is not controlled and it can be used only for rapid emergency braking.

In order to control the current in the II quadrant, the regenerative braking is employed. Under regenerative braking, the motor is driven by the stored mechanical energy of the load and the electric energy is returned to the DC link. This feeding back of the energy to dc source increases the dc link voltage. The dc link capacitor should be large enough to assure almost constant voltage.

For rapid braking, the torque has to reverse, while the motor continues to rotate in the same direction with a decreasing speed. Thus, the phase current and the BEMF must have opposite signs. For an effective regenerative braking system, both the current direction and magnitude have to be controlled.

For controlled braking torque under sensorless control the relation between the BEMF and the applied voltage is of interest for estimation purposes.

For a simplified overview over the regenerative braking of a single phase motor, sinusoidal waveforms (only the first harmonic) are considered for voltages and current. Thus the motoring and the generating situations can be treated as for a sinusoidal synchronous motor.

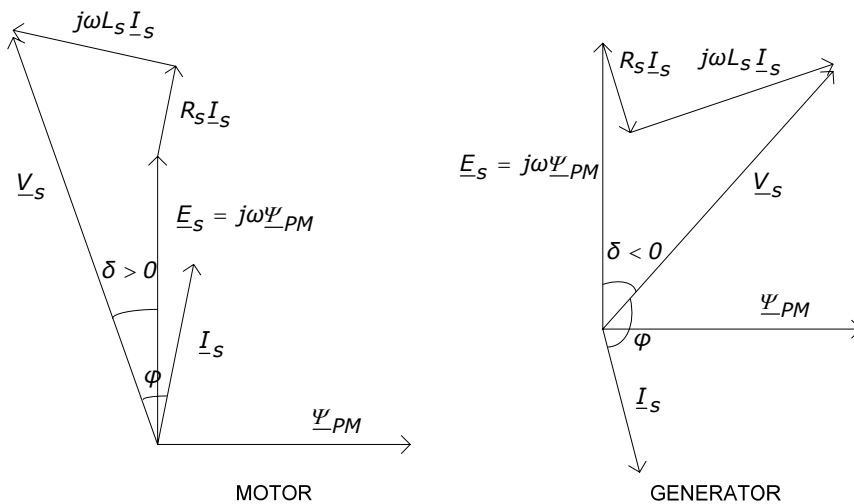


Figure 1. Phasor diagram for single phase PMSM

For steady state , the voltage equation in the phasor form is:

$$\underline{V}_S = R_S \underline{I}_S + j\omega L_S \underline{I}_S + E_S ; E_S = j\omega \underline{\Psi}_{PM} \quad (1)$$

where V_S, I_S , stator voltage and current, L_S, R_S stator inductance and resistance, Ψ_{PM} - the PM flux linkage.

Based on equation (1) the phasor diagram for both motor and generator is constructed in figure 1.

For both motoring and generating situations the current is not considered in the ideal position, in phase with BEMF, respectively in opposition. For example a small delay compared with the BEMF is considered, as usually happens when no phase advance is used. If phase advance has to be considered under steady state, the current phasor has to be rotated in counter clockwise direction.

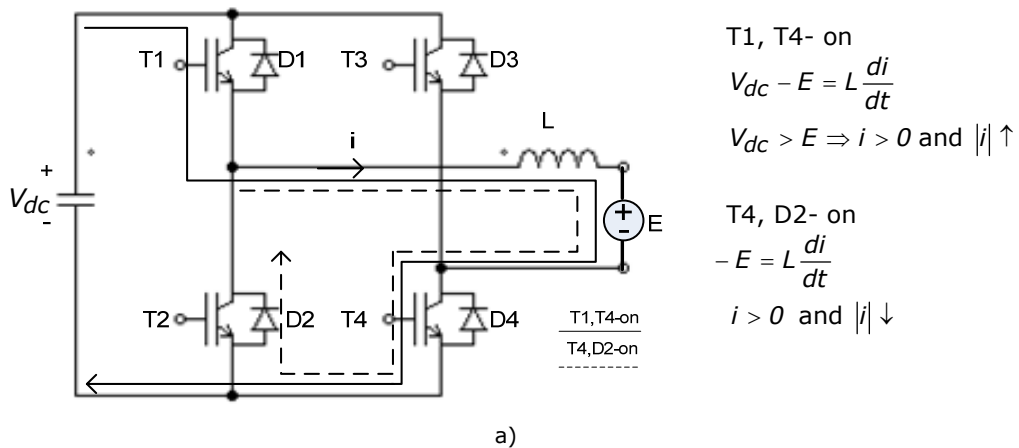
In figure 1, δ represents the power angle which is positive for motoring and negative for generating.

Thus, it is expected that, for regenerative braking, the applied voltage to be delayed compared with the BEMF. This is a very important aspect when voltage reconstruction from the duty cycle and V_{dc} is desired.

6.3. Current control with soft switching PWM mode

A comparison between the current control possibility with soft switching PWM mode under motoring and braking situations is presented next. Its purpose is to outline the necessity of using a modified switching strategy when braking.

In the exemplified situation, the upper transistors are controlled by PWM while the lower ones are on during the corresponding half period. For analysis, the voltage drop on phase resistance is ignored and the current control during a PWM period is examined.



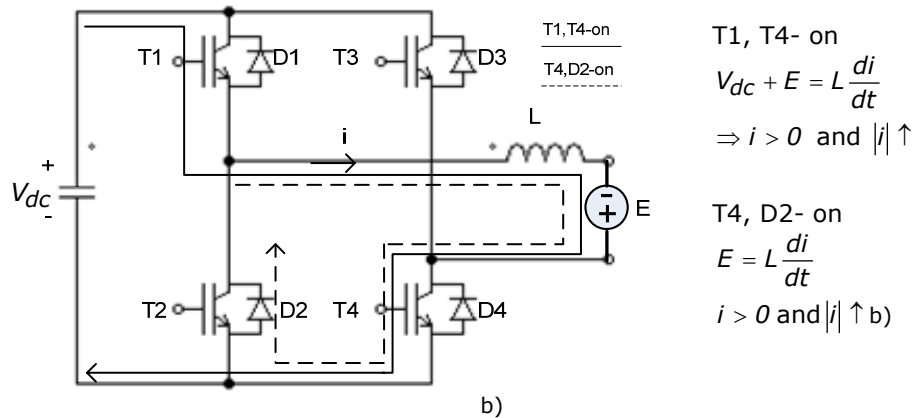


Figure 2. Single phase converter states and current behaviour with soft switching for :
 a) motoring, b) generating

Figure 2 illustrates the current behavior during a PWM period for positive current situation in both motoring and braking modes.

During motor mode, when the phase current and BEMF are positive, while PWM on the motor terminals voltage is V_{dc} and the current is increasing. During PWM off the applied voltage is zero and the current is decreasing due to opposing BEMF.

During brake mode, when the phase current is positive and BEMF is negative, while T1 is on, the motor terminals voltage is V_{dc} and the current is increasing. When T1 is off, the applied voltage is zero, but the current still increases during this freewheeling due to the BEMF.

Therefore, by using the soft switching commutation the phase current is uncontrollable during braking.

In order to allow current control under braking mode, a modified switching logic has to be applied.

6.4. Regenerative braking modes

There are two possibilities of obtaining a regenerative braking. The first one is using only the BEMF to produce the current, while the second one helps current to reach the reference by adding an external voltage. Both methods are detailed next in order to examine which is more feasible to be applied in the presented sensorless control.

6.4.1. Regenerative braking using only the BEMF

Since the BEMF is not higher than the dc link voltage, in order to make the current flow from motor into the dc link during regenerative braking, it must pull high the BEMF potential of the motor and provide a path to connect the motor and the dc link [5-7]. If during the motoring mode the H bridge can be analyzed as a buck converter for each BEMF polarities, during the regenerative mode it can be

viewed as a boost converter.

Starting from the above presented soft switching control under motor mode, a modified commutation pattern is derived next, which allows the current control during regenerative braking.

The control method which allows regenerative braking consists in applying the PWM signal only at one transistor, while the others are kept off. If in the case of motoring, for a given BEMF polarity, a transistor is controlled with PWM, in generating, needs not to be switched on and the other transistor controlled with PWM is conducting.

Figure 3 illustrates the obtained converter states during a PWM period, by using the above described control under regenerative braking:

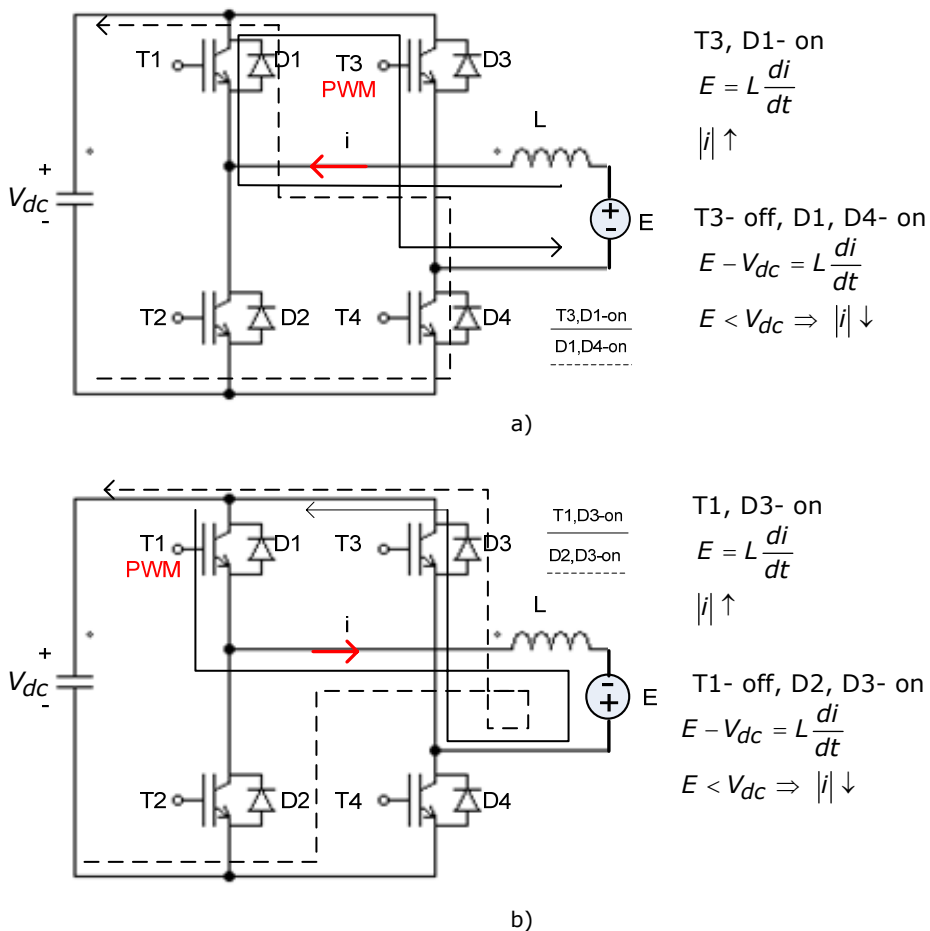


Figure 3. Current control during one PWM period: a) positive BEMF polarity, b) negative BEMF polarity

Basically the motor phase inductance is used for energy storage during PWM on and then, during PWM off, the stored energy is discharged into the load supply through the freewheeling diodes, charging the capacitor and causing the motor current to decay. From figure 3 it can be observed that current control is possible

during both BEMF polarities. The current increases during PWM on and decreases during PWM off, thus is directly proportional with the duty cycle.

Table 1 synthesizes the full bridge converter switching commands during driving and regenerating modes:

TABLE I Power converter switching commands

	MOTOR MODE				REGENERATIVE BRAKING			
BEMF	T1	T2	T3	T4	T1	T2	T3	T4
>0 P	WM	OFF	OFF	ON	OFF	OFF	PWM	OFF
<0 OF	F	ON	PWM	OFF	PWM	OFF	OFF	OFF

Other combinations are possible but it was chosen to make PWM during braking at the same transistors which are chopped during driving mode in order to keep the same control circuit.

Since the regenerative braking under sensorless control is the main task, the voltage reconstruction from the reference duty cycle is presented further.

For $sign(i_{reference}) > 0$ the phase voltage can be written as eq. 2 shows:

$$v(t) = \begin{cases} 0; & 0 < t < t_{on} \\ -V_{dc}; & t_{on} < t < T \end{cases} \quad (2)$$

The medium voltage value over a PWM period is given in eq. 3:

$$v = \frac{1}{T} \int_{t_{on}}^T v(t) \cdot dt = -\frac{T-t_{on}}{T} \cdot V_{dc} = -(1-D) \cdot V_{dc} \quad (3)$$

The same relation applies for $sign(i_{reference}) < 0$, the phase voltage can be written as eq. 4 shows:

$$v(t) = \begin{cases} 0; & 0 < t < t_{on} \\ V_{dc}; & t_{on} < t < T \end{cases} \quad (4)$$

And the again the medium voltage over a PWM period is given by eq. 5:

$$v = \frac{1}{T} \int_0^{t_{on}} v(t) \cdot dt = \frac{T-t_{on}}{T} \cdot V_{dc} = (1-D) \cdot V_{dc} \quad (5)$$

Thus, the final voltage estimation relation is given by equation 11.

$$v = -sign(i_{reference}) \cdot (1-D) \cdot V_{dc} \quad (6)$$

Thus using the PWM switching command presented in Table I, the estimated voltage from the reference duty cycle is given by equation 6 during regenerating and by equation 7 (introduced in chapter 4) during motoring.

$$v = \text{sign}(i_{\text{reference}}) \cdot D \cdot V_{dc} \quad (7)$$

In order to evaluate this regenerative braking method and to analyze the possibility of using it into a motion sensorless control, digital simulation results are presented. The motor was driven in close loop speed control based on the measured speed and position and the reconstructed voltage from the reference duty cycle and the estimated flux were analyzed.

Figure 4 shows, by simulation results, a comparison between the measured phase voltage and the estimated one during regenerative braking. The measured voltage is obtained from PSIM model by using a not too strong low pass filter at the motors terminals, in order to avoid the delay. The regenerative regime can be noticed, since the measured voltage is delayed compared with the BEMF from the motor model (negative power angle). Also the braking current and the BEMF have opposite signs as expected resulting in a negative torque.

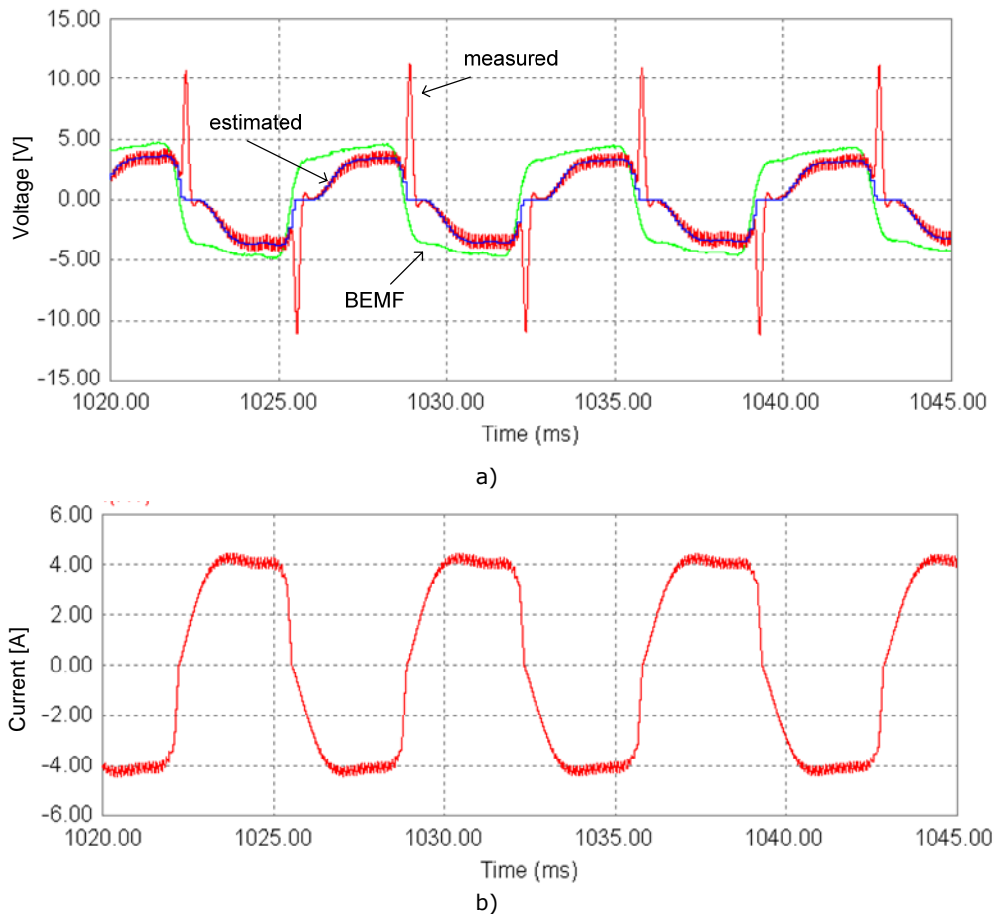


Figure 4. Simulation results for a regenerative braking : a) measured and estimated voltage, b) phase current

The reconstructed voltage approximates the measured one, excepting the region when the current decays at the end of each polarity.

Also, using this braking solution for the proposed sensorless control based on a reference voltage model flux estimator imposes difficulties in reconstructing the voltage at zero current.

For both motoring and generating, when zero current is desired, the reference duty cycle decreases to zero. If equations (11) and (12) are analyzed, it can be noticed that when the duty cycle is zero the following cases will appear:

For motor mode, if $D \rightarrow 0$ then $v \rightarrow 0$ and measured current will also be zero as a consequence that it has no path for circulating. Thus, the flux estimator loses the needed information for integration resulting in zero flux estimation.

For generative braking mode, if $D \rightarrow 0$ then $v \rightarrow V_{dc}$ and a gain wrong flux estimation is obtained.

Figure 5 shows the voltage estimation problem that occurs at the crossing moment from generative braking to motor mode. It can be noticed that the estimated voltage is no longer the same with the measured one.

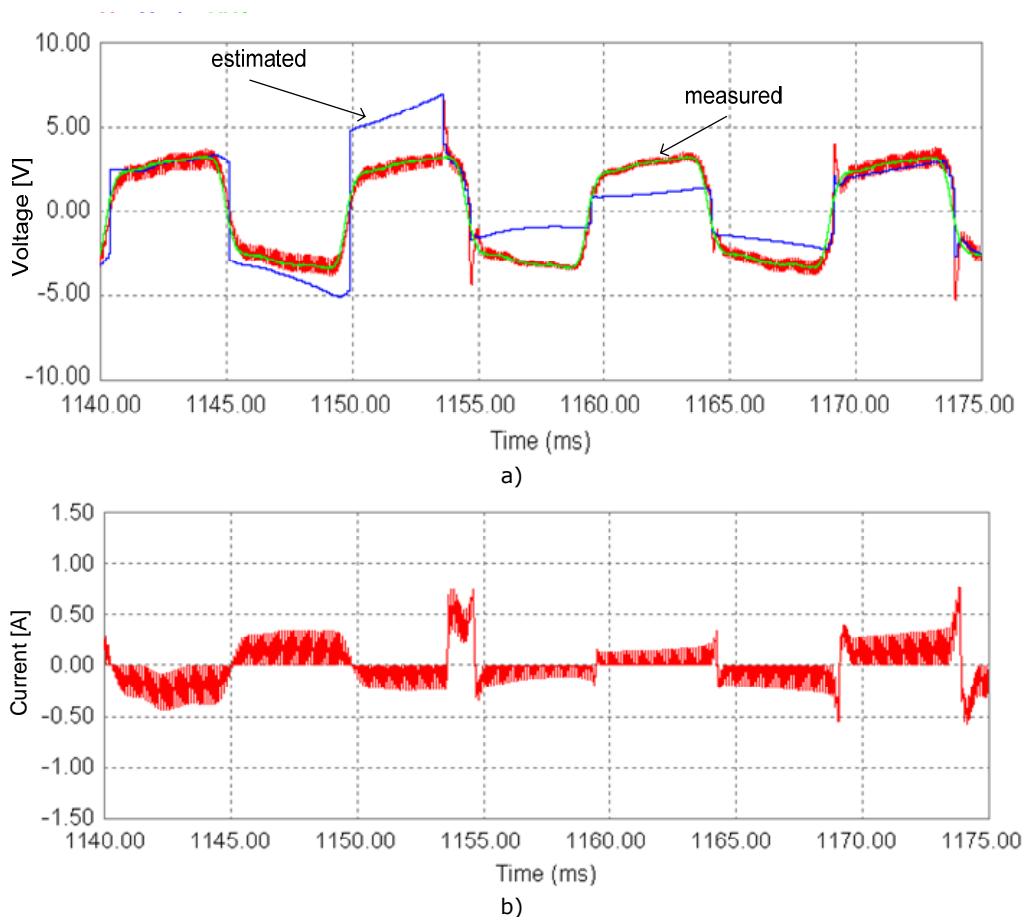


Figure 5. Simulation results when crossing from generator to motor: a) voltage, b) current

This wrong voltage estimation causes further problems for flux estimation. Figure 6 shows the simulation results for a regenerative braking from 5000 to 3000 rpm. It is visible that during the time interval where the current is almost zero (the crossing moments from braking to motor) the estimated flux obtains wrong values

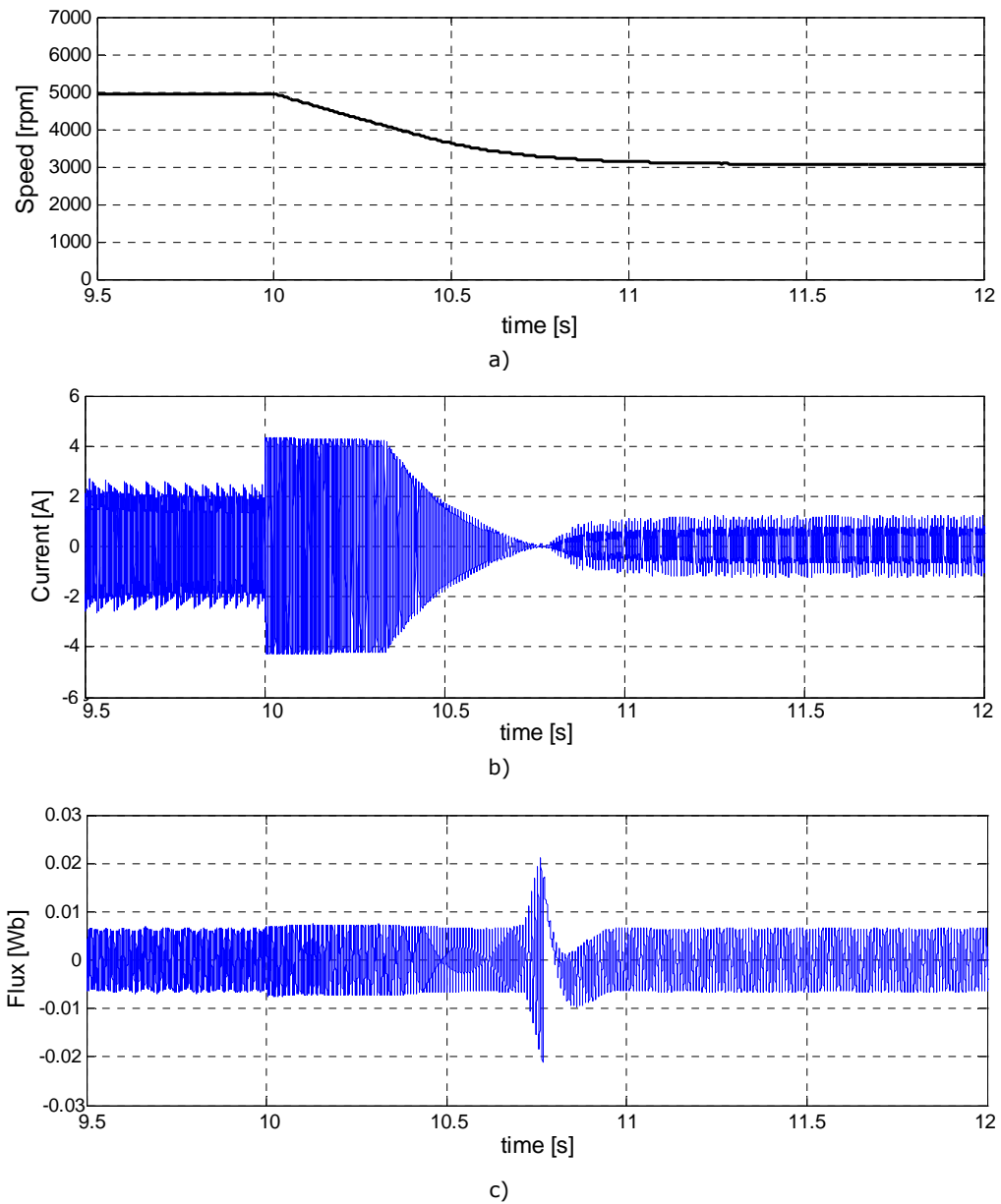


Figure 6. Simulation results for a regenerative braking from 5000 rpm to 3000 rpm: a) speed, b) current, c) estimated flux

Due to the above presented problems, when small current pulsations and low noise level are important requirements, the use of this method should be conditioned by a few "tricks". In order to avoid the problem which seems to appear at the crossing moment from braking mode to motor running, a quick crossing has to be done. A discontinuity in the current reference should be inserted, so that when the speed is around the reference the controller to cross to the motor mode with an enough duty cycle. But this will produce speed oscillations around the prescribed speed. Also, a more careful tuning the PLL observer, used in the sensorless control, could provide satisfactory position information during the crossing moment.

If the measured phase voltage is available and a proper compensation of the delay produced by the low pass filter is done, than this regenerative braking method should not impose any important problem under motion sensorless control.

6.4.2. Improved regenerative braking by complementary PWM signals

To overcome the problems of the previous presented regenerative braking method, an improved solution is presented. During braking the converter is now controlled so that the dc link voltage it adds to BEMF when phase current changes sign, thus allowing a much better current control. To achieve this, a PWM commutation pattern which implies the hard switching mode with synchronous rectification is applied here.

To realize the synchronous rectification, the PWM on high and low side MOSFET must be complementary.

Although the hard switching mode is not as popular as the soft switching mode due to the higher torque ripples and bad electromagnetic noise [8], [9], it will be seen that it allows an improved sensorless control under regenerative braking. The use of hard switching under regenerative braking is also assessed in [10]-[12].

By using complementary switching of the top and bottom transistors, an average zero voltage is obtained for a 50% duty cycle. The synchronous rectification mode behaves like the fast decay with freewheeling current recirculation mode until current reaches zero, and then it forces it in the opposite direction.

Considering the above, the main difference from the soft switching mode and hard switching with diode recirculation is that the transition from motoring to braking and vice versa, is done by just modifying the duty cycle. There are no different commutation patterns for the power running and regenerative modes as in the previous case.

6.4.2.1. Analysis of current control during motor and braking mode

The current control over a PWM period is analyzed in both motor mode and regenerative braking mode. For simplicity, the voltage drop is neglected in the presented analysis. Also during the short time interval of a PWM period, the inverter states can be treated as electrical dc circuits. Considering each polarity of the current as a distinct dc state the analysis with equivalent dc circuits under a PWM period gives a good insight over the current control capability.

As figure 7.a) shows, in motor mode, when T1 and T4 are conducting the current flows through loop 1 and increases since the dc link voltage is greater than

the BEMF. During PWM off, the current flows through loop 2 and decreases due to the corroboration of the dc link voltage and BEMF voltage.

The same current control behavior is obtained during the negative polarity of the current (fig. 7.b). When T2, T3 switches are on the current flows through loop 1 and its absolute value is increasing. When T2, T3 are off the current circulates through loop 2 and its absolute value is decreasing.

The signs of both phase current and BEMF are mentioned in each case and the current loops are symbolical drawn to suggest the receptor and generator sign conventions.

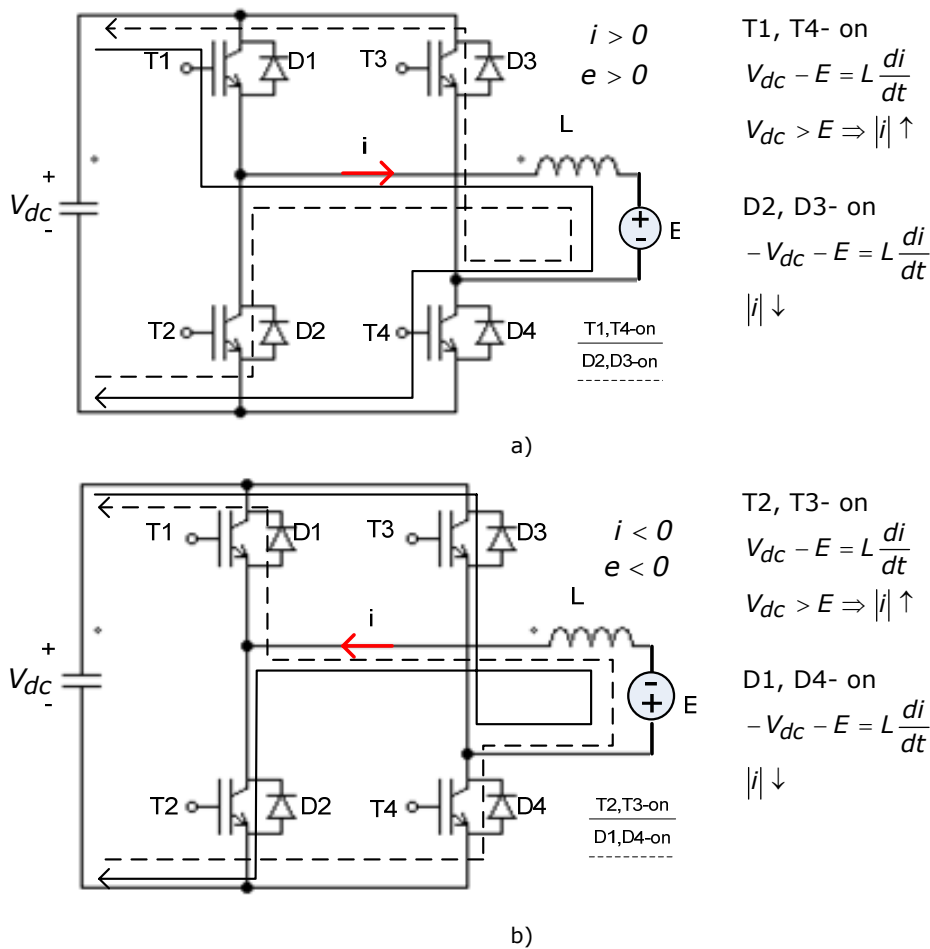


Figure 7 The two possible current paths during a PWM period for motor mode: a) positive current, b) negative current

If regenerative braking is considered, for the negative polarity of the current, shown in figure 8.a), when T2, T3 switches are on current flows through loop 1 and its absolute value is gradually increasing. This current is fed from the dc link into the winding and it produces braking torque. When T2, T3 are turn off, the

current flows through loop 2 charging the d.c. link capacitor and its absolute value is decreasing. Now the motor is in the regenerative braking state.

The same behavior is noticed for positive current polarity. When T1, T4 switches are conducting, the current flows through loop 1 and its absolute value is gradually increasing. When T1, T4 are turned off, the current flows through loop 2 charging the d.c. link capacitor and its absolute value is decreasing.

As observed, the BEMF and the phase current have opposite signs, and thus negative power is obtained.

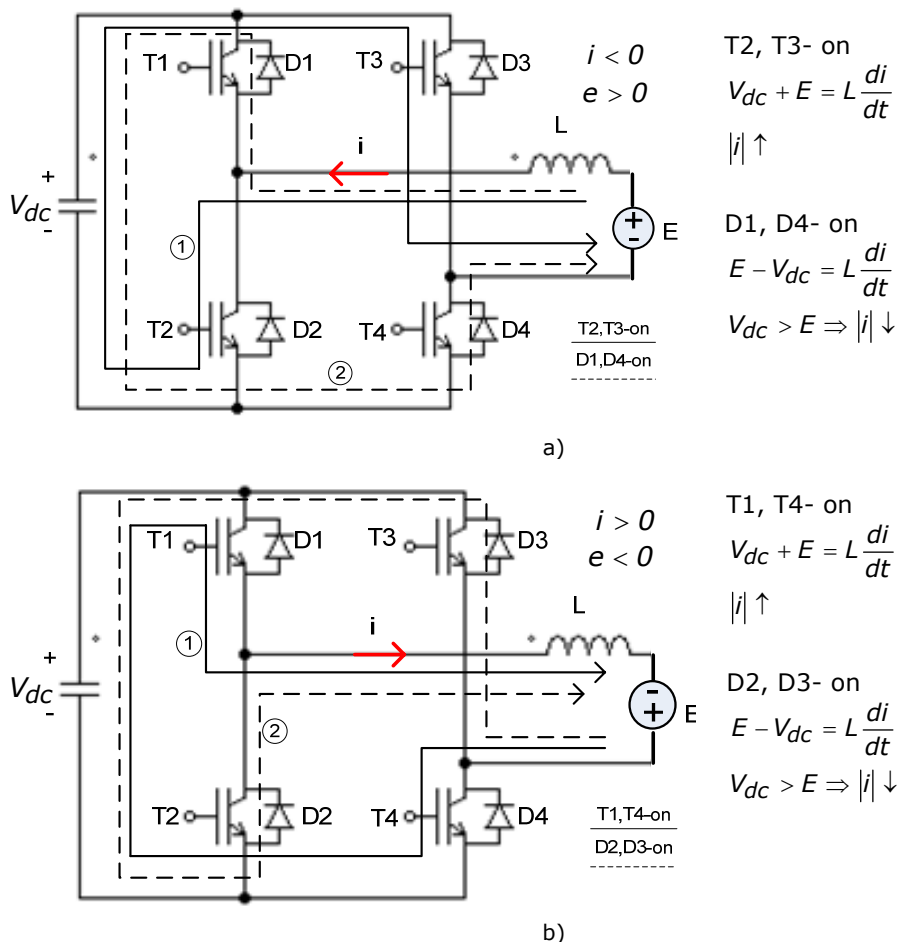


Figure 8 The two possible current paths during a PWM period for regenerative braking mode: a) positive current, b) negative current

Considering the above, using the hard PWM switching, the current phase is controllable in either of the motor or generator states.

During PWM off time, the current flow through the complementary power device. It can flow either through the body diodes or through the transistors, if synchronous rectification is chosen. Here, the current path is drawn through the diodes during current decay in order to avoid any confusion.

Since here complementary control is done and MOSFETs are used, the current flows through the body diodes only during the dead time, and then it goes through the MOSFETs. This complementary commutation can be used even if no MOSFET switches are used, only for voltage estimation considerations.

In both motor and generator states, during one PWM period the current is either pulled from or pushed into the dc link. The difference is given by its medium value.

6.4.2.2. Phase voltage estimation when using complementary PWM

For phase voltage information reconstruction from the reference duty cycle, the same methodology as used until now is used. By complementary control of power devices the voltage at motor terminals during a PWM period is given by equation (8).

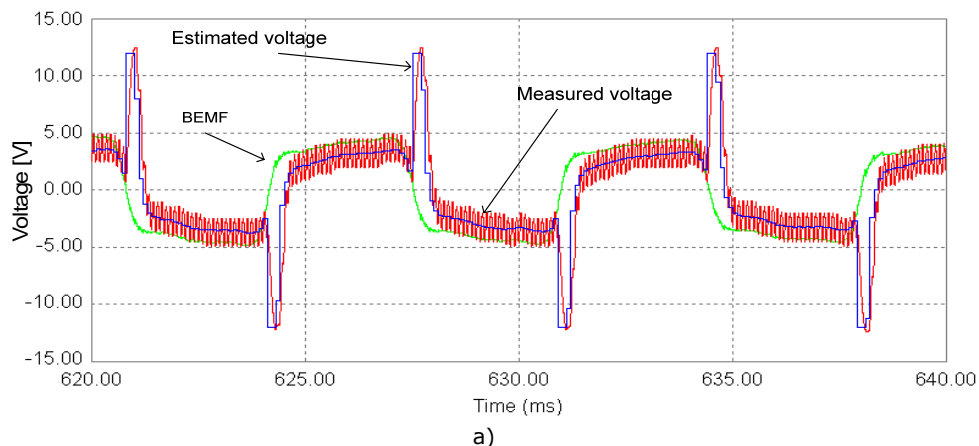
$$v(t) = \begin{cases} +V_{dc}; & 0 < t < t_{on} \\ -V_{dc}; & t_{on} < t < T \end{cases} \quad (8)$$

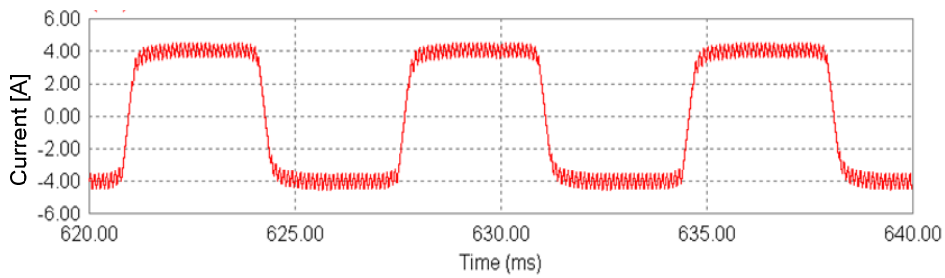
The medium voltage value over a PWM period is given in eq. (9):

$$v = \frac{1}{T} \int_0^T v(t) \cdot dt = \frac{1}{T} \left(\int_0^{t_{on}} V_{dc} \cdot dt + \int_{t_{on}}^T (-V_{dc}) \cdot dt \right) \quad (9)$$

$$v = \left(2 \frac{t_{on}}{T} - 1 \right) \cdot V_{dc} = (2 \cdot D - 1) \cdot V_{dc}$$

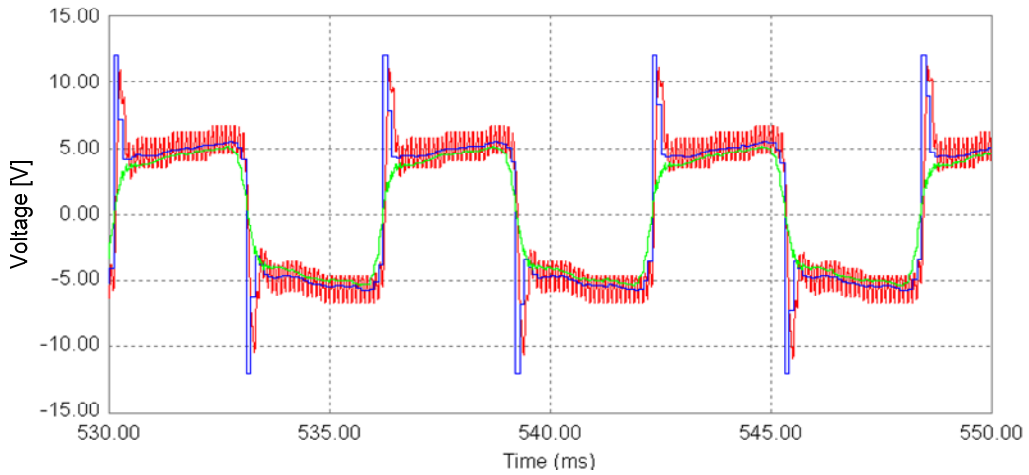
Thus for a duty cycle of 50%, the zero voltage is applied at the motor terminals during a PWM period. Equation 9 is valid for both motor and braking states. The PI current controller has just to adjust the duty cycle in order to reach the reference current in either motor or generator mode. Figure 8, 9 illustrates by simulation results the voltage estimation during both situations.



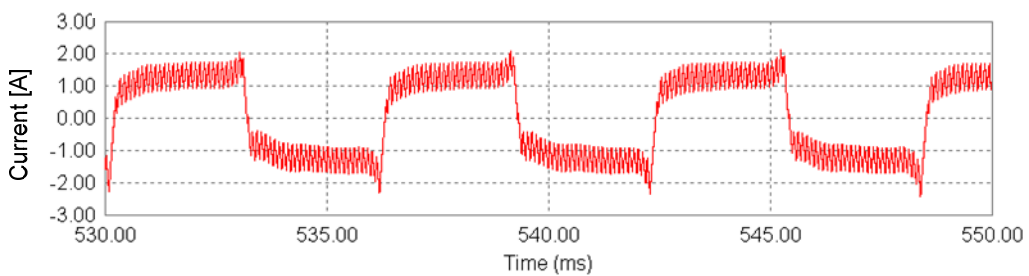


b)

Figure 9. Simulation results during regenerative braking: a) BEMF, measured and estimated phase voltage, b) phase current



a)



b)

Figure 10. simulation results when running as motor: a) BEMF, measured and estimated phase voltage, b) phase current

It can be observed that, when in power running mode, the BEMF have the same sign while during braking opposite signs are noticed, resulting in negative torque. Also, as presented in section 6.2, the phase delay between the phase voltage and BEMF during braking is visible, while in motor situation these signals are almost in phase. In motor mode, with a proper commutation phase advance, the

phase voltage can be advanced more, compared with the BEMF, so that the phase current to be in phase with the BEMF for an optimum torque production.

Comparing with the previous regenerative braking method, here the estimated voltage can reconstruct the voltage during the current decay when this changes the sign.

Also, the encountered problem at the transition from regenerative braking to motoring that was reported for the previous case, does not appear here. This can be shortly explained by the fact that when zero current is desired the control tries to achieve it by supplying a voltage equal with the BEMF. Figure 11 shows a detail view over the above mentioned transition.

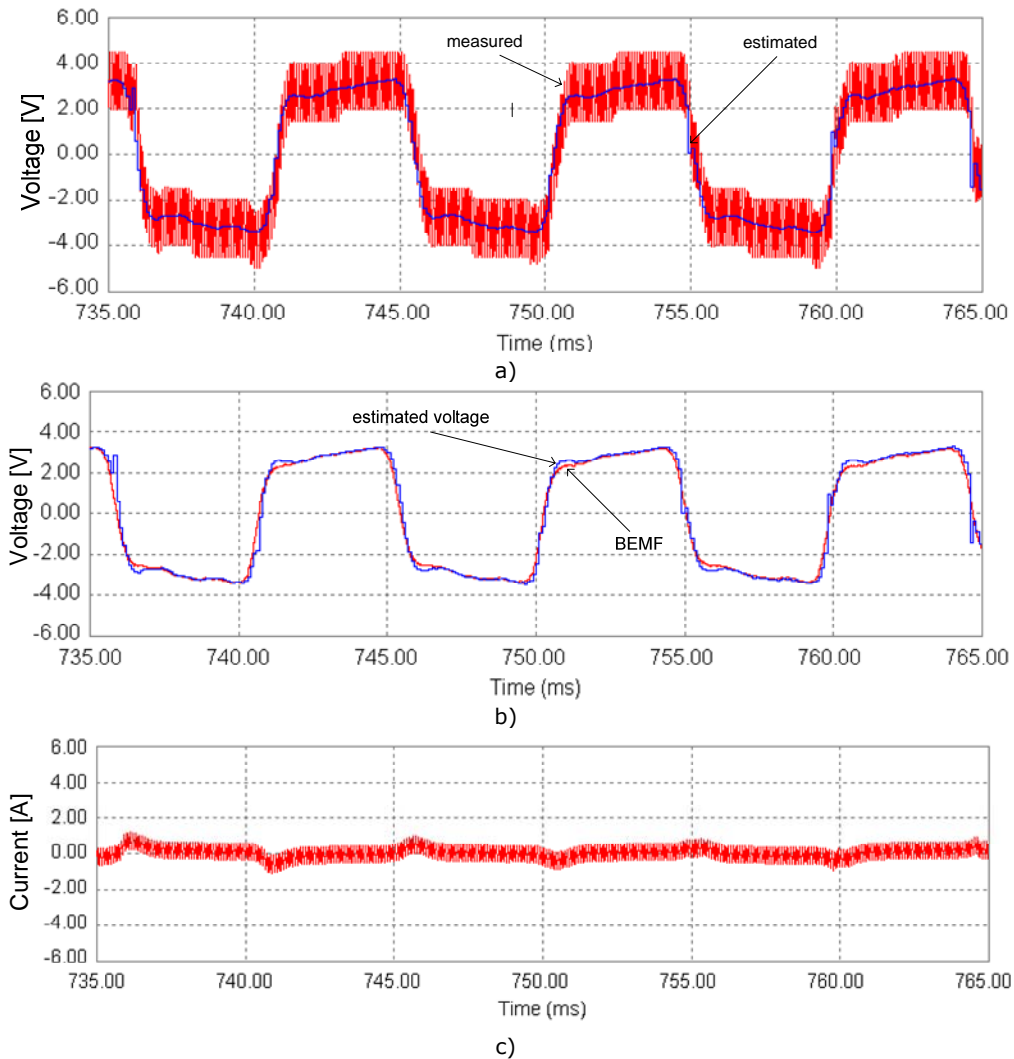


Figure 11. Transition from braking to motoring, digital simulation results: a) measured and estimated voltage, b) estimated voltage vs. BEMf, c) phase current

Since during the transition, the supply voltage at motor terminals equals the BEMF, and so does the estimated voltage also, the flux estimator integrates this voltage and does not manifest the same issues as for the other regenerative method.

Figure 12 shows how the flux estimator remains reliable under this regenerative braking, behaviour which makes it proper for sensorless control.

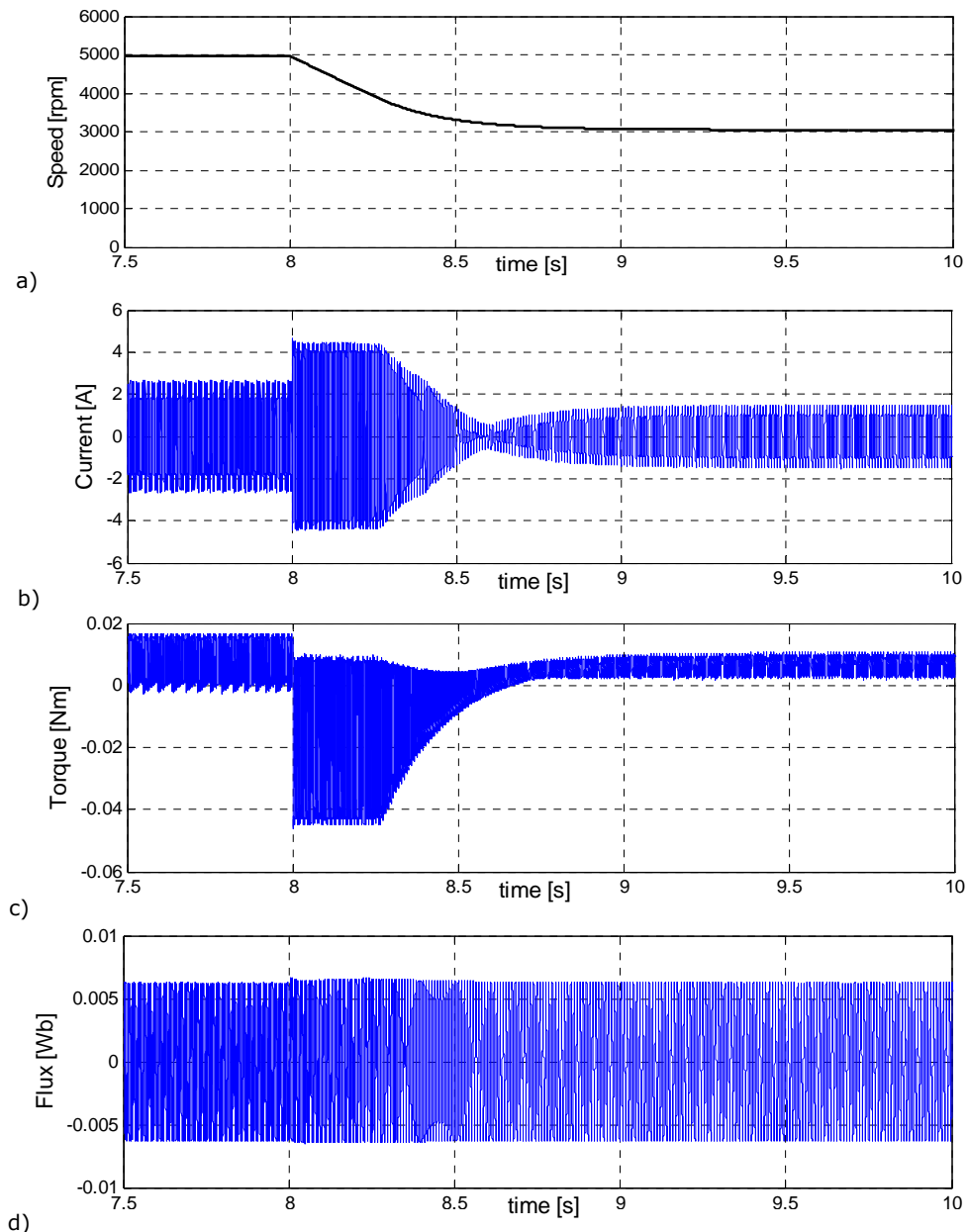


Figure 12. Simulation results for a regenerative braking from 5000 rpm to 3000 rpm: a) speed, b) current, c) torque, d) estimated flux

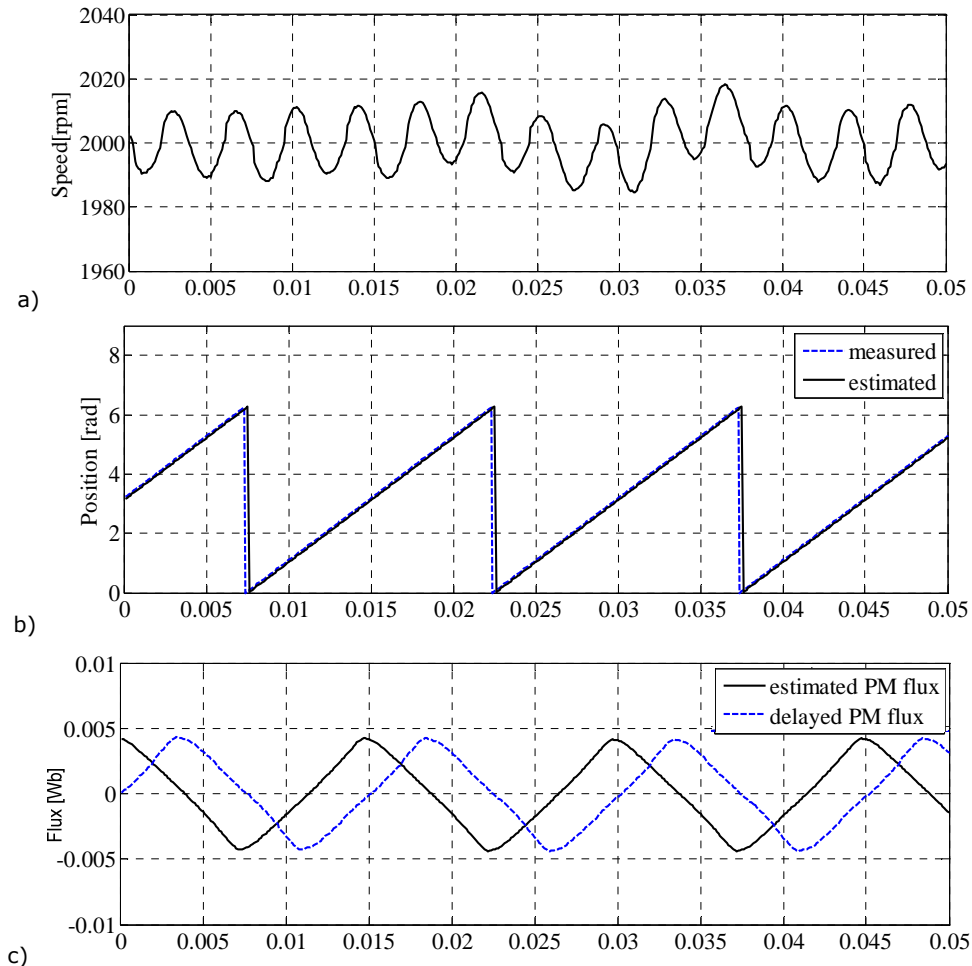
6.5. Experimental results

Experimental results for validating the regenerative braking under motion sensorless control are further presented.

The motion sensorless control method is the one presented in Chapter 5. The motor is driven in close loop speed control by using the estimated position and speed from the PLL observer.

The PWM commutation mode was modified from the soft switching to hard switching with active freewheeling. As a consequence of this modification the phase voltage estimation from the reference duty cycle was also modified.

Figures 13, 14 illustrate the experimental results for two steady state speeds for power running mode. The same satisfactory behavior as in chapter 5 is noticed. The main estimated quantities are illustrated. The estimated voltage is presented together with the BEMF in order to see the difference between motoring and braking.



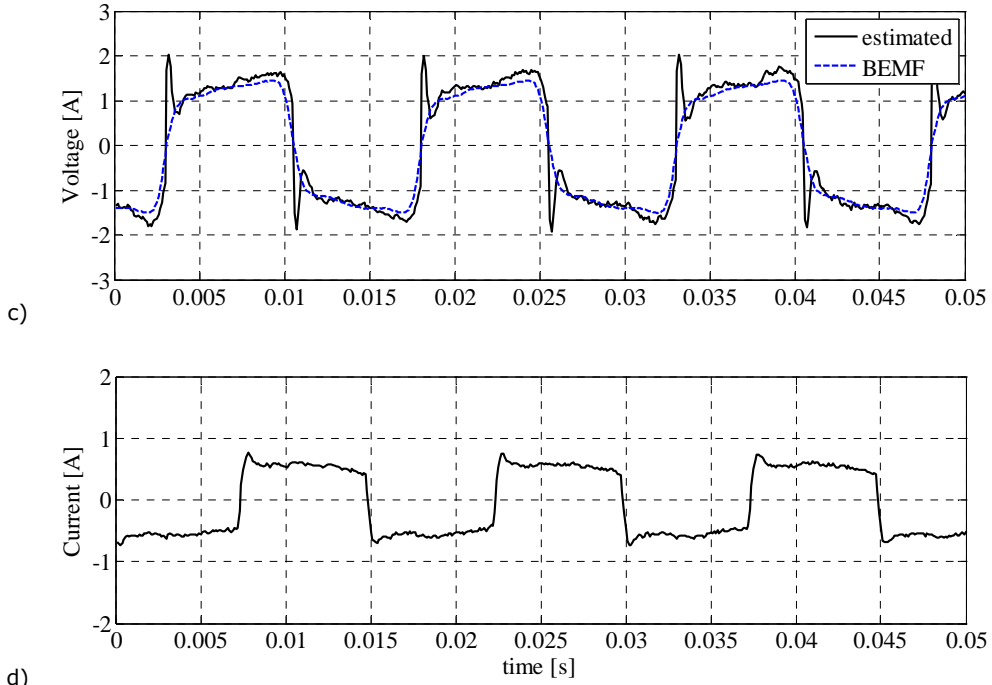
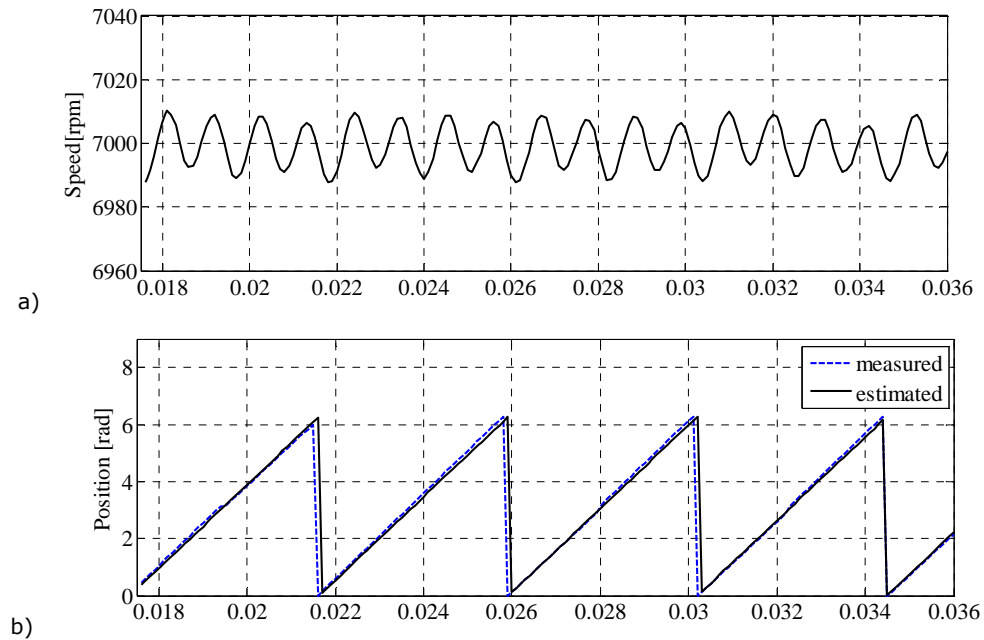


Figure 13. Experimental results at 2000 rpm: a) speed, b) position, c) flux, d) voltage, e) current



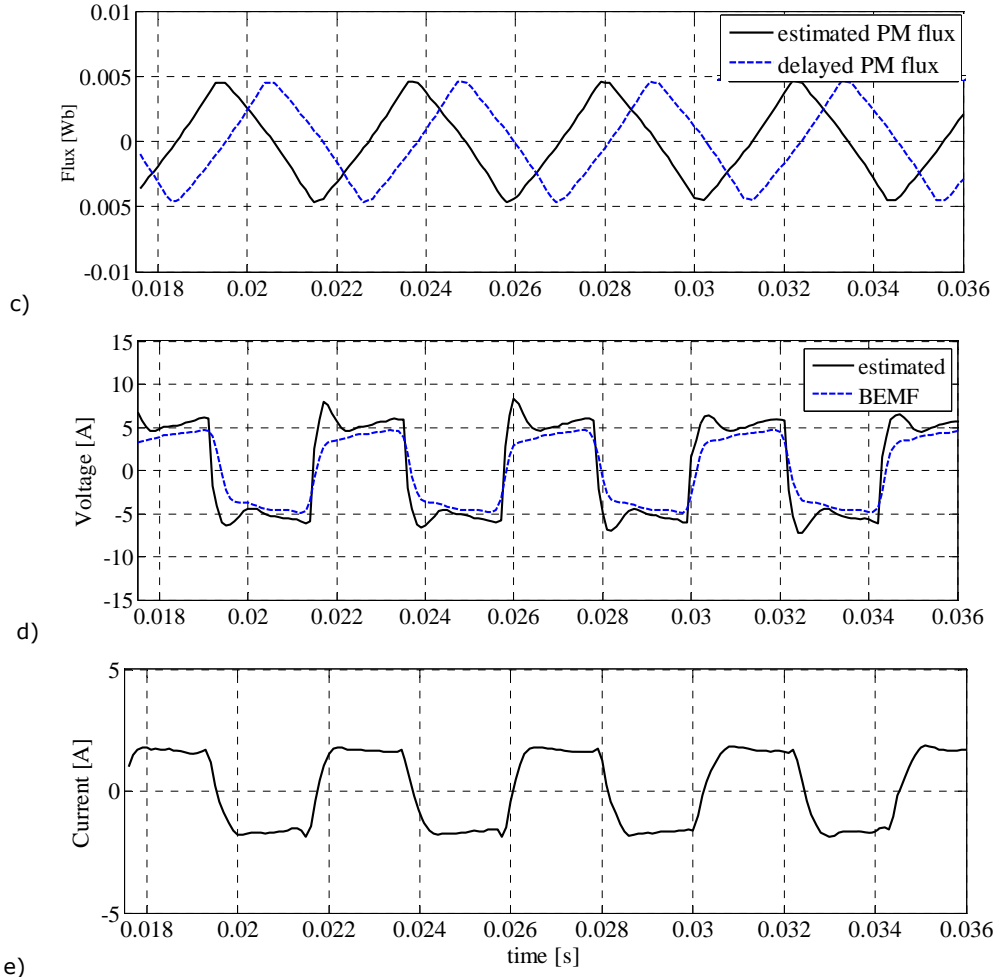


Figure 14. Experimental results at 7000 rpm: a) speed, b) position, c) flux, d) voltage, e) current

Since the main subject of this chapter was to present an enhanced sensorless control which to allow also regenerative braking, experimental tests were carried out for this purpose and representative results are illustrated next.

Figures 15, 16 show the obtained experimental results for a regenerative braking from 5000 rpm to 3000 rpm, respectively from 8000 rpm to 6000 rpm. Satisfactory results are obtained. The speed response is visibly improved compared with the one from chapter 5.

A drop in the estimated flux amplitude during the braking process is noticed. This flux decrease can be explained by the fact that during the braking time period the dc link voltage increases. A laboratory dc voltage source was used for experiments and it does not allow reverse current. Thus the current is forced to circulate through the capacitor.

For the same reference current, with an increased dc link voltage, a smaller reference duty cycle results. Since the dc link voltage is not measured either, the

estimated phase voltage will be smaller also, and so causing a decrease in the estimated flux.

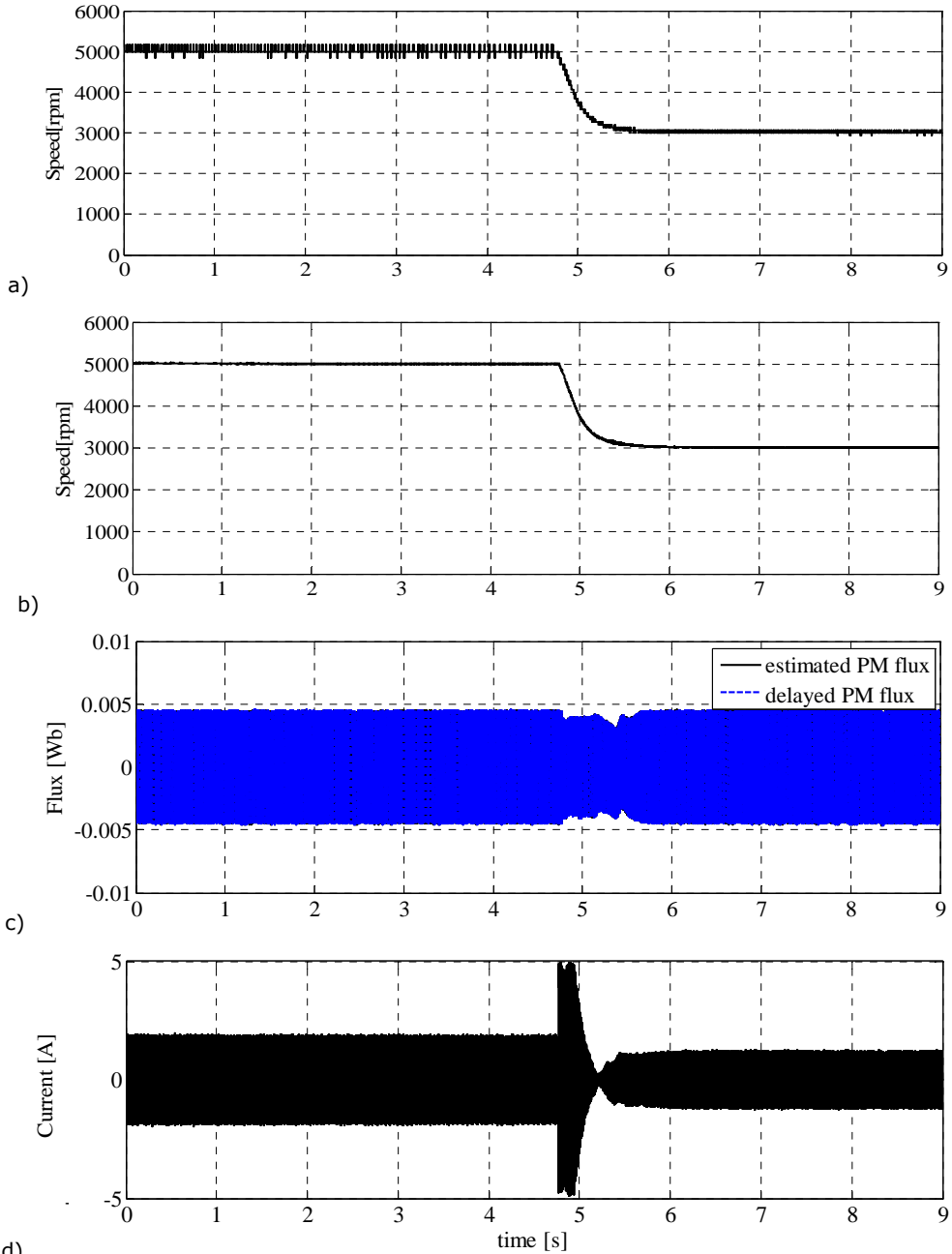


Figure 15. Experimental results for a regenerative braking from 5000 rpm to 3000 rpm

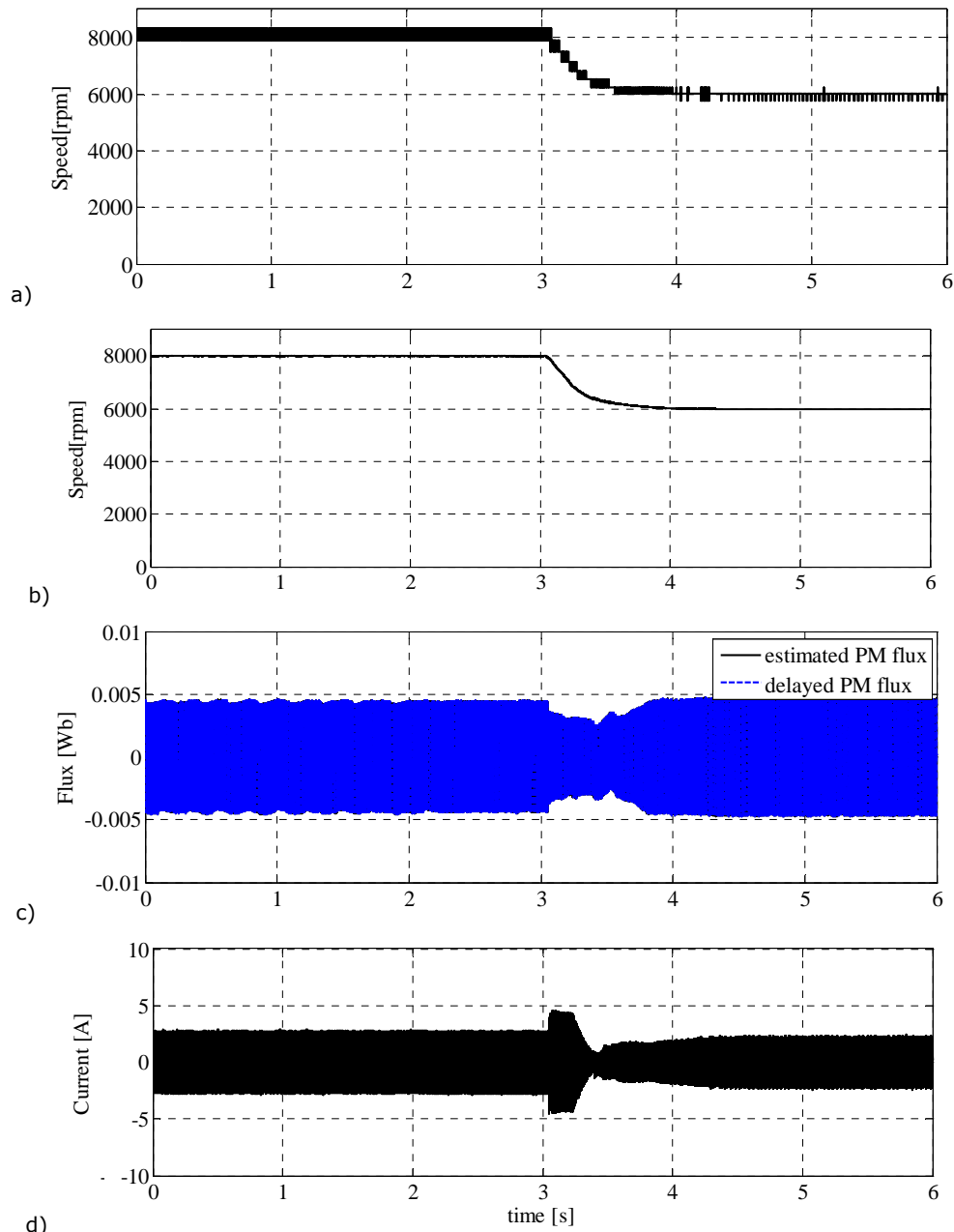


Figure 16. Experimental results for a regenerative braking from 8000 rpm to 6000 rpm

As already assessed in chapter 5, the involved PLL state observer in the sensorless control is not affected by the flux amplitude modifications. Thus, in spite of this estimated flux amplitude decrease the speed control performs the same. This can be observed if figure 17 is analyzed. The estimated position which remains close to the measured one and the current waveform confirm the control effectiveness.

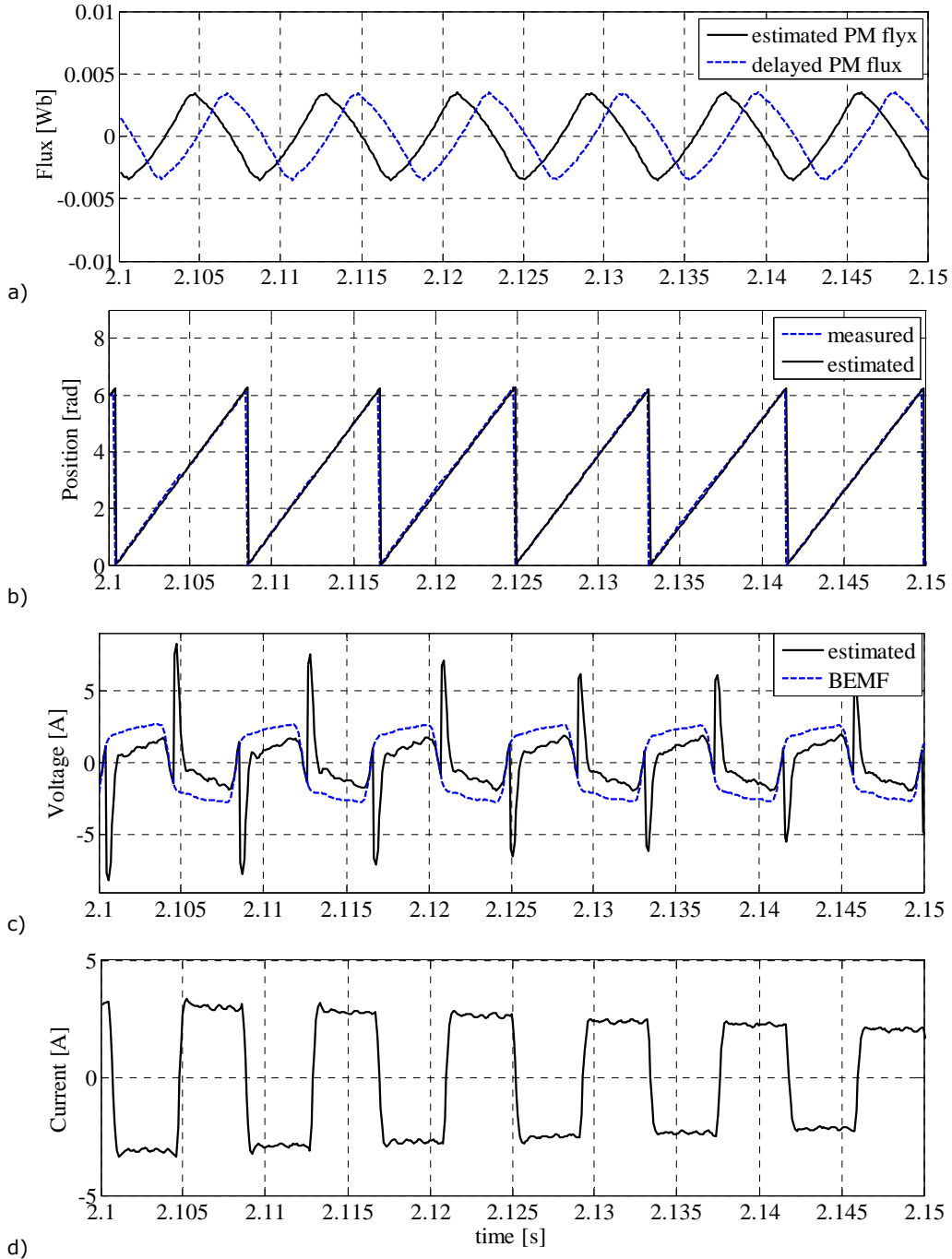


Figure 17. The representative signals during braking : a) orthogonal flux system , b) estimated and measure position, c) estimated voltage vs. BEMF, d) phase current

The estimated voltage is shown again in comparison with the BEMF. The BEMF shape from the FEM analysis is used and the speed and position from hall sensor was used to obtain the BEMF at various speeds.

Also a good correspondence with the digital simulations results can be noticed.

6.6 Conclusions

The importance of PWM commutation mode on current control was analyzed for both situations: when running as a motor and when running as brake. The possibility to include a controlled braking, in order to realize a complete sensorless motion control for a single phase PM-BLDC motor, was studied.

Two solutions for a regenerative controlled brake were detailed and exemplified by simulation results. Both methods were analyzed in order to see which is more reliable for the implemented sensorless control.

First it was shown that when soft switching PWM mode is used, the same commutation logic can not be applied if current control under braking is needed. More, in order to obtain regenerative braking, starting from the soft switching mode, a modified commutation logic was presented. The current control capability using this commutation pattern was analyzed for both motor and brake mode. A relation which allows the voltage estimation using the reference duty cycle was deduced, and then the possibility to use it in the proposed reference voltage model based sensorless control was detailed.

A second regenerative braking method was presented and detailed and its effectiveness when used in the motion sensorless control was demonstrated by experimental results. This eliminates the problems that the previous one has at the transition from motor to regenerative brake and has the same equation for the estimated voltage in both regimes. The transition from motor to generating is done by just modifying the duty cycle.

Thus, an enhanced motion sensorless control for single phase PM-BLDC motor drive which allows controlling the current during regenerative braking was obtained.

A good correspondence between the experimental and digital simulation results can be observed. Also, the robustness of the proposed motion sensorless control was again proved. The speed and current control were not affected by the amplitude modifications in the estimated flux caused by the dc link voltage increase during braking process.

References

- [1] "Automotive full bridge Mosfet driver", Allegro, Application Note
- [2] "DSP Solutions for BLDC Motors", Texas Instruments, Application note
- [3] "BLDC motor control with Hall effect sensors using the 9S08 MP", Freescale Semiconductor, Application Note
- [4] "Using CCU6E for BLDC control with synchronous rectification (active freewheeling)", Infineon, Application Note
- [5] M. Marchesoni and C. Vacca, "New DC-DC Converter for energy storage system interfacing in fuel cell hybrid electric vehicles," IEEE Trans. on Power Electronics, vol. 22, no. 1, pp. 301-308, January 2007.

- [6] P. Bajec, B. Pevec, D. Voncina, D. Miljavec and J. Nastran, "Extending the low-speed operation range of PM Generator in automotive applications using novel AC-DC converter control," *IEEE Trans. on Industrial Electronics*, vol. 52, no. 2, pp. 436-443, April 2005.
- [7] J. R. Rodriguez, J. E. Dixon, J. R. Espinoza, J. Pontt and P. Lezana, "PWM regenerative rectifiers: state of the art," *IEEE Trans. on Industrial Electronics*, vol. 52, no. 1, pp. 5-22, February 2005.
- [8] Z. Xiang-jun, C. Bo-shi, "Influence of PWM modes on commutation torque ripples in sensorless brushless DC motor control system", *Journal of Shanghai University*, vol. 5, no.3, Sep. 2001, pp. 217-223.
- [9] Z. Xiang-jun, C. Bo-shi, "A new method for reducing commutation torque ripples in bldc motors", *Journal of Shanghai University*, vol. 5, no.1, Mar. 2001, pp. 71-75.
- [10] A. Komatsuzaki, T. Banba, I. Miki, "A position sensorless drive using estimation of turn-off angle under regenerative braking in switched reluctance motor", *Proc. of International Conference on Electrical machines and Systems*, Oct. 2007, Seoul, Korea, pp. 450-455.
- [11] J. Bocker, "Advanced hysteresis control of brushless DC motor"
- [12] Y. Xu, Yu tang, J. Zhu, J. Zou, C. Ma, "Control of a BLDC motor for electromechanical actuator", *Proc. of International Conference on Electrical Machines and Systems*, Oct 2008, pp. 3266-3269.

7. EXPERIMENTAL SETUP

Abstract

In this chapter a short description of the laboratory equipment used for the carried out measurements is done. Also, the experimental platform used for the implementation of sensorless control is presented and the main aspects related to software implementation are pointed out.

7.1. Tested motor

The used motor for laboratory measurements and then for sensorless control development is a tapered airgap blower motor as presented in figure 1. Table I contains the motors main parameters.

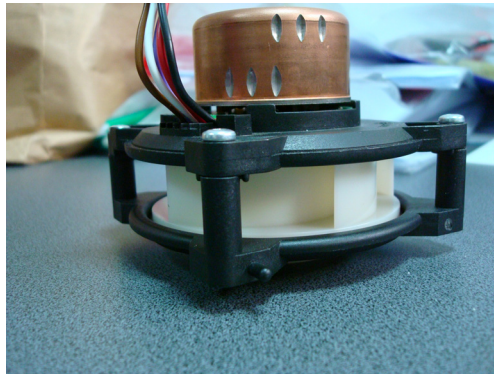


Figure 1 Experimental motor

TABLE I
Motor Parameters

Voltage	12 V
Nominal Power	40 W
Resistance	0.27 Ohm
Inductance	0.6 mH
K_e	0.008 Vs/rad
Number of poles pairs (p)	2
Viscous friction coefficient (B)	$2.2 \cdot 10^{-5}\text{ Nms / rad}$
Blower load coefficient	$4.56 \cdot 10^{-9}\text{ Nms}^2 / \text{rad}^2$
Inertia of rotating system (J)	$15 \cdot 10^{-5}\text{ kg} \cdot \text{m}^2$

7.2. Measuring laboratory equipment

In order to validate the FE analysis, the BEMF, inductance, cogging torque and total torque were measured on dedicated test rigs. All measurements were carried out in the research and development laboratory for electric drives from ebm papst GmbH St. Georgen Germany.

The inductance was measured using an INSTEK RLC bridge. For this, the rotor was fixed in different positions using a mechanical rotor positioning device as presented in figure 2.

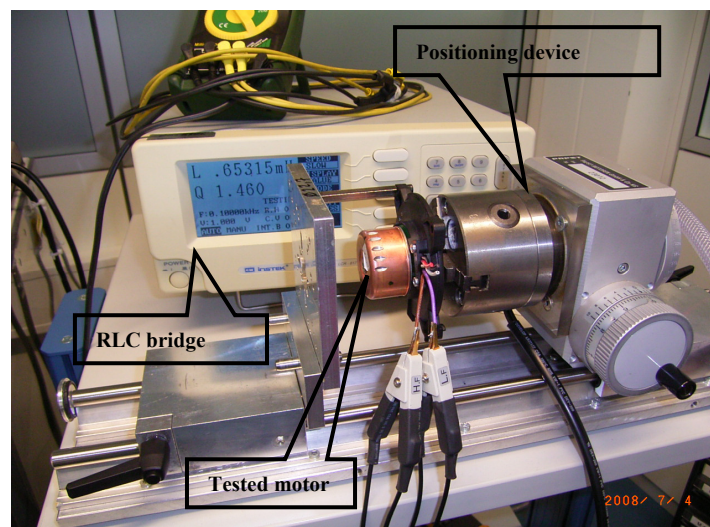


Figure 2. Test equipment for inductance measurements

The static torque measurements were done with a torquemeter on a dedicated motor test rig with the PMSM fed with dc. current and driven at constant very low speed (7 rpm), by a speed controlled drive.

Figure 3 presents the equipment for bemf, cogging torque and total torque measurements.

The main component parts are the drive motor, the torque sensor, an encoder with index, dc power supply, the data acquisition system from Tektronix and the LabView software from National Instruments.

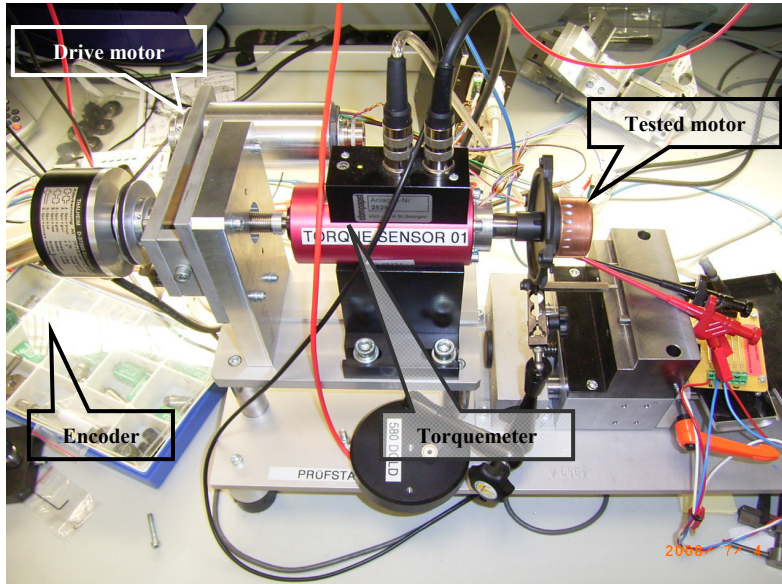


Figure 3. Measurement equipment for bEMF and torque

7.3. Experimental platform

The experimental rig basically consists on a mosfet inverter, a current sensor, the tested motor and the dspace platform (figure 4).

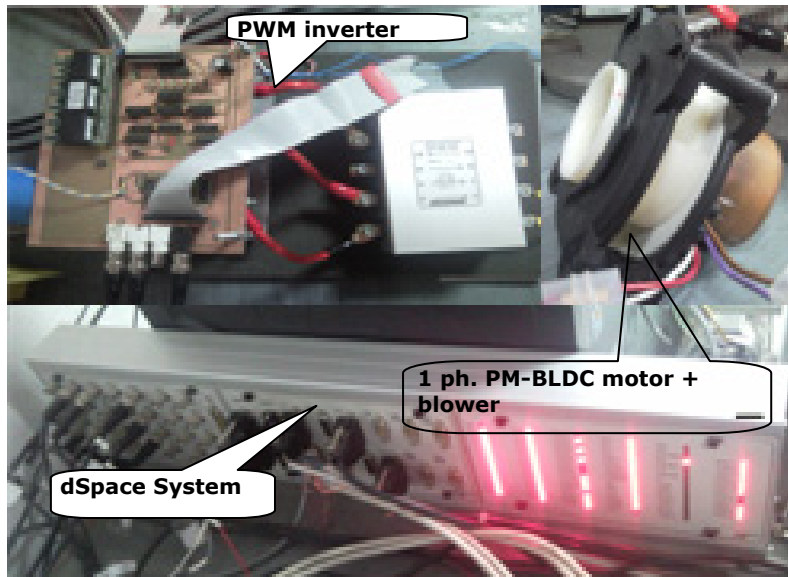


Figure 4. Experimental rig

The implementation of the digital control, position and speed estimator and finally, of the close loop motion sensorless control was carried out with the rapid prototyping and real time interface system dSpace DS1103. The DS1103 PPC is a very flexible and powerful system featuring both high computational capability and comprehensive I/O peripherals. Additionally, it features a software SIMULINK interface that allows the control applications to be developed in Matlab/Simulink friendly environment.

The DS1103 is a single board system based on the Motorola PowerPC 604e/333MHz processor, which forms the main processing unit. The DSP subsystem, based on the Texas Instruments TMS320F240 DSP fixed-point processor, is especially designed for the control of electric drives. Among other I/O capabilities, the DSP provides 6 complementary PWM channels and 4 independently PWM channels, making the subsystem useful for drive applications. From the available resources the 16 bit resolution/ 4 μ s sampling time and the 12 bit /800 ns sampling time ADC converters has to be mentioned also since an ADC channel was used for current measurements.

The dedicated software for realtime control allows an easy acquisition of informations through the provided virtual control panel with instruments and scopes. Figure 5 illustrates the virtual panel used for the experiments.

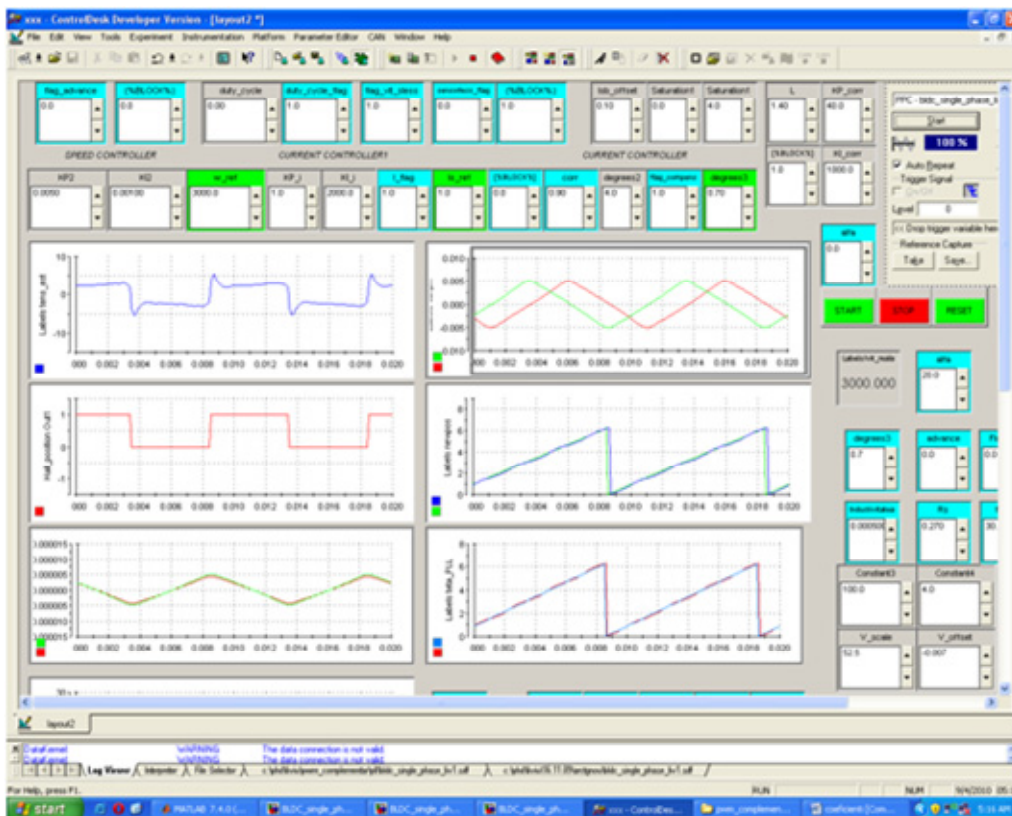


Figure 5. dSpace Control Desk real-time interface

7.4. Software implementation

The control algorithm was implemented in Matlab/ Simulink environment. Basically the control consists in exactly the same block used in simulation, due to the accurate digital model used. What is particular for the practical implementation is the way that information is exchanged with the periphery. Thus, in figure 5 it can be seen that the hall signal is read from the digital input port, the current is read from the ADC channel 17, while the enable signal to the inverter is sent through bit C14 from the digital I/O. Figure 6 shows how the duty cycle is send to the two converter legs.

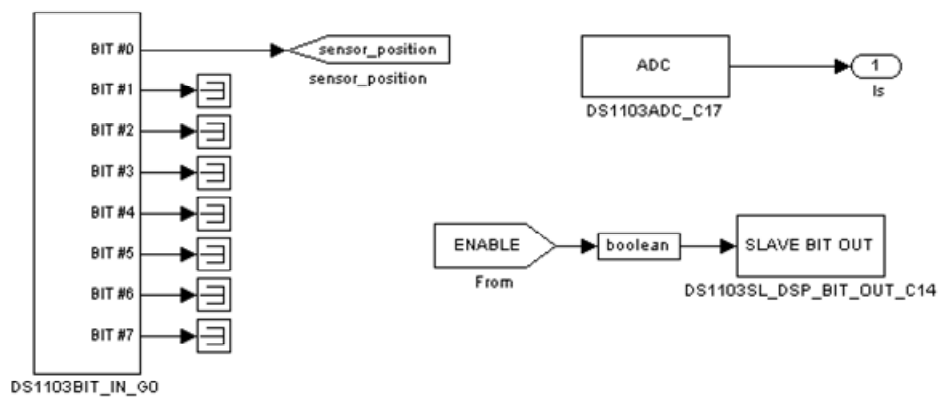
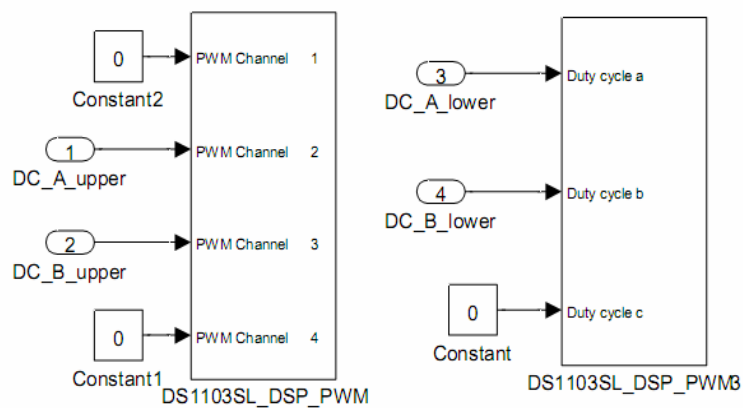
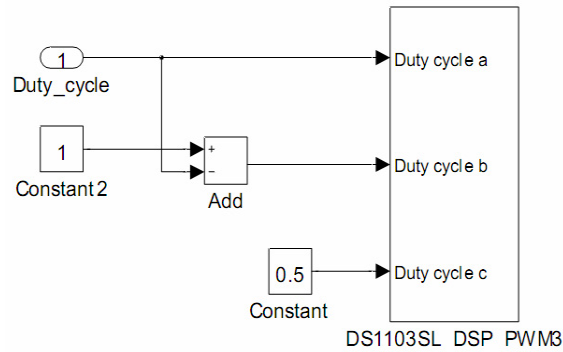


Figure 6. Control interface with the inverter and motor



a)



b)

Figure 7. PWM interface block and their use: a) for soft switching, b) for complementary PWM signals

7.5. Conclusions

The used equipment for laboratory measurements and the experimental test platform used for sensorless implementation of the single phase PM-BLDC motor was presented in this chapter.

Also, an overview on the software implementation was offered. The software was implemented in Matlab Simulink and with Real Time Workshop an automatic code was generated and downloaded into the microprocessor.

8. CONCLUSIONS AND CONTRIBUTIONS

The present work is dedicated to single phase permanent magnet brushless dc motor drives. Based on the results presented in the thesis, the main conclusions can be summarized as bellow.

- For small power, small starting torque applications, the single phase permanent magnet brushless DC motor presents a growing interest, especially in the residential and automotive industry, where it is more efficient than rival motors. It is used in order to cut the costs of the power electronics converter for variable speed, by reducing the number of power switches and the number of Hall sensors.
- For obtaining a competitive single phase PM brushless dc motor drive, an in-depth characterization by finite element method, validated by laboratory measurement is needed.
- The corroboration of stator and rotor geometry, dimensions, materials, permanent magnet magnetization affects the motors parameters such as BEMF, cogging torque, phase inductance and starting capability.
- Finite element magnetostatic solvers can include these effects, resulting a more accurate estimate of the motor bemf and excitation torque constant, phase inductance, cogging torque and flux linkage.
- For accurate dynamical modeling, the above mentioned effects can be considered by using the FEM obtained characteristics (cogging torque, back EMF, inductance, and starting position).
- An accurate simulation model that simulates the motor, the power electronics converter and the control simplifies the transition from simulation work to experimental implementation.
- Important aspects like sampling and switching frequency limitation, simulation time, power electronic commutation mode, practical implementation constraints like the need of additional external circuits for measuring the voltage have to be considered when a sensorless control method is implemented.
- In order to eliminate the phase voltage measurement a reference voltage model flux estimator can be implemented by using the reference duty cycle and the dc link voltage.
- The PM flux vs. position characteristic of a single phase PM brushless dc motor can be used to extract the rotor position.
- In single phase BLDC-PM motors there is less information than in three phase motors, and so, some special calculations have to be done in order to estimate the rotor position. The idea of another sensorless method is to create an orthogonal PM flux linkage system in order to employ it in rotor position/speed estimation.
- When implementing a reference voltage flux estimator the phase voltage estimation is an important aspect. The power electronic commutation mode has to be considered when the phase voltage is reconstructed.

- An enhanced motion sensorless control for single phase PM-BLDC motor drive which allows controlling the current during regenerative braking can be obtained if complementary PWM signals are used.

The main contributions in the thesis, from the author point of view, can be summarized as below:

- A quasi-exhaustive FEM characterization supported by experimental measurements, of a single phase PM BLDC motor was done.
- Using the obtained characteristics from FEM, an accurate and complete motor dynamical model was built. Also, a complete simulation model for the whole drive system, which allows the user to simulate and implement the control algorithm and the state observer identically as it will be implemented on the realtime rapid prototyping dSpace hardware platform, was presented.
- The problems which arise when trying to validate a sensorless control by using only the existing Hall sensor were also detailed by simulation results, and during experiments, the limitations given by this method were mentioned.
- A motion sensorless control system for a single phase PM BLDC motor based on a prior knowledge of the flux vs. position characteristic was introduced. The detailed step by step implementation was presented and illustrated by simulation results and then validated by experiments.
- Starting from the real time PM flux estimator, a position and speed observer which imply a generated orthogonal flux system, the atan2 function and two position refining methods was detailed and validated by experiments.
- An enhanced motion sensorless control for single phase PM-BLDC motor drive which allows controlling the current during regenerative braking was presented and detailed and its effectiveness was demonstrated by experimental results.
- Both proposed motion sensorless control methods were complemented by a I-f starting strategy with a simple switching to observer based close loop sensorless control. The important aspect related to the way that PI controllers are managed during switching was explained and demonstrated by experiments.

Author's papers related to the Ph.D. thesis

- [1] L. Iepure, L. Tutulea, I. Boldea, "FEM analysis and control of a tapered airgap of single phase PMSM", *OPTIM 2008*, May 2008, Brasov, Romania, (ISI Proceedings, IEEE Explore, INSPEC, Compendex).
- [2] L. Iepure, D. Iles-Klumpner, M. Risticvic, I. Boldea, "Small blower PM single phase brushless d.c. motor drives FEM characterization with experiments", on the *CD-ROM IEEE-IEMDC 2009 Proceedings*, ISBN: 978-1-4244-4252-2, May 2009, Miami, Florida, USA.
- [3] L. Iepure, G.D. Andreescu, D. Iles, F. Blaabjerg, I. Boldea, "Novel Position and Speed Estimator for PM Single Phase Brushless D.C. Motor Drives: Validation with Experiments", *ISIE 2010 Conference*, Bari, Italy, (ISI Proceedings, IEEE Explore, INSPEC, Compendex).
- [4] L. Iepure, I. Boldea, G.D. Andreescu, D. Iles, F. Blaabjerg, "Novel Motion Sensorless Control of Single Phase Brushless D.C. PM Motor Drive, with experiments", *OPTIM 2010 Conference*, May 2010, Braşov, Romania, (ISI Proceedings, IEEE Explore, INSPEC, Compendex).
- [5] L. Iepure, I. Boldea, G.D. Andreescu, F. Blaabjerg, "Improved state observers for sensorless single phase BLDC-PM motor drives" accepted for *IECON 2010*, Nov.2010, Phoenix, Arizona, USA, (ISI Proceedings, IEEE Explore, INSPEC, Compendex).
- [6] L. Iepure, I. Boldea, F. Blaabjerg, "Hybrid I-f starting and observer based sensorless control of single phase BLDC-PM motor drives", pending for *IEEE Transaction on Industrial Electronics, Fractional Horsepower Electric Drives*, (ISI Journal)

Author's CV

Liviu Ioan Iepure

Office: University Politehnica of Timisoara, Romania

Blvd. Vasile Parvan, no. 2, room D108

Tel: +40 256403463

Email: liviu.iepure@yahoo.com

Home Address: Bd-ul Pacii, no. 8

Lupeni, Hunedoara, Romania

Mobile: +40 723171696

EDUCATION

- 2007-2010 Ph.D. student at University "Politehnica" of Timisoara,
Faculty of Electrical and Power Engineering,
Dept. of Electrical Machines and Drives, Timisoara, Romania
- 2007 Dipl. degree in Electrical Engineering
- 2002-2007 University "Politehnica" of Timisoara, Timisoara, Romania
Faculty of Electrical Engineering
- 1998-2002 High School of Informatics, Petrosani, Romania

PERSONAL EXPERIENCE

- July-Oct. 2009 Guest Researcher at Institute of Energy Technology, Aalborg
University Denmark,
- July-Sep. 2008 Guest Researcher at EBM-Papst St. Georgen GmbH&Co. KG., St.
Georgen, Germany,
- Mar.-Oct. 2007 Electrical engineer at S.C. ELTREX SRL, Timisoara, Romania.

PERSONAL INFORMATION

Born: January 31, 1984

Family: Unmarried